SAPIENZA
Università di Roma

Scuola di Dottorato “Vito Volterra”
Dottorato di Ricerca in Astronomia– XXIV ciclo

Globular Clusters and Galactic Nuclei

Thesis submitted to obtain the degree of
Doctor of Philosophy (“Dottore di Ricerca”) in Astronomy

by

Alessandra Mastrobuono Battisti

Program Coordinator
Prof. Roberto Capuzzo Dolcetta

Thesis Advisor
Prof. Roberto Capuzzo Dolcetta

Anno Accademico 2010-2011

Abstract

Dynamical evolution plays a key role in shaping the current properties of star clusters and star cluster systems. We present the study of stellar dynamics both from a theoretical and numerical point of view. In particular we investigate this topic on different astrophysical scales, from the study of the orbital evolution and the mutual interaction of GCs in the Galactic central region to the evolution of GCs in the larger scale galactic potential.

Globular Clusters (GCs), very old and massive star clusters, are ideal objects to explore many aspects of stellar dynamics and to investigate the dynamical and evolutionary mechanisms of their host galaxy. Almost every surveyed galaxy of sufficiently large mass has an associated group of GCs, i.e. a Globular Cluster System (GCS). The first part of this Thesis is devoted to the study of the evolution of GCSs in elliptical galaxies. Basing on the hypothesis that the GCS and stellar halo in a galaxy were born at the same time and, so, with the same density distribution, a logical consequence is that the presently observed difference may be due to evolution of the GCS. Actually, in this scenario, GCSs evolve due to various mechanisms, among which dynamical friction and tidal interaction with the galactic field are the most important. On the other side, the collisionless stellar halo component stands unchanged, thus the difference between the two profiles may correspond to mass lost by the GCS to the galactic center. There the GCs merge and they contribute to the formation/accretion of a luminous and compact central Nuclear Star Cluster (NSC). This is known as the “merger model” for the formation of NSCs, observed at the center of many galaxies and also in the Milky Way (MW) center.

In the second part of this work a new high performance code, NBSymple, is presented. NBSymple is an efficient N-body integrator implemented on a hybrid CPU+GPU platform, exploiting a double-parallelization on CPUs and on the hosted Graphic Processing Units (GPUs). The precision is guaranteed by direct summation for force evaluation, and on the use of high order, symplectic time integration methods. The code allows the choice between two different symplectic integrators: a second-order algorithm (commonly known as leapfrog) and a much more accurate (but also time consuming) sixth-order method. The effect of the external galactic field is represented as an analytical approximation of its gravitational potential. The code has been widely tested and benchmarked. Moreover, it has been used for various applications (globular clusters quasi-radial orbit through a galactic massive central object, primordial evolution of young stellar clusters, etc.).

NBSymple and another, publicly available, direct summation code, ϕGRAPE, have been used to explore the the previously described merger mode for the Galactic NSC formation. In particular, we used self consistent N-body simulations where the Galaxy was modeled using observational data about the Milky Way, and including the presence of the Galactic central supermassive black hole. We let decay 12 GCs

initially located on different circular orbits at the same galactocentric distance. The merging of clusters in the central zone of the Galaxy and its following evolution due to two-body relaxation generates a NSC that actually resembles the one observed at the center of the MW.

By mean of numerical simulations carried on with NBSymple, we investigated more in detail the dynamical evolution of GCs in the MW potential with particular attention to the formation of clumpy structures in the tidal tails that arise around the orbiting cluster. Although various hypothesis have been proposed, the formation process of these clumps is not yet clearly understood. Through a statistical analysis of the orbital properties of the stars that "escape" from the cluster we aimed to a better understanding of the on going process. Studying and comparing such simulations with observational data we could gain to a deeper knowledge of the shape Galactic potential and, more generally, of the Galactic dynamics.

Contents

Introduzione

Nel 1971 l'astronomo francese Charles Messier pubblicò un catalogo di oggetti celesti nebulosi brillanti. Il primo oggetto del catalogo, M1, era la Nebulosa del Granchio; il secondo, M2, era un ammasso globulare, ovvero un ammasso sferico autogravitante di centinaia di migliaia di stelle. Degli oggetti catalogati, 28 sono oggi riconosciuti come ammassi globulari; ad oggi, un totale di 150 ammassi globulari è stato osservato nella nostra Galassia. Dopo questa scoperta l'importanza dello studio degli ammassi globulare è cresciuta in maniera significativa.

Gli Ammassi Globulari (AG) sono i soggetti principali di questa Tesi. Qui tratteremo la loro evoluzione su diverse scale spaziali (dalla loro interazione nei nuclei galattici alla loro evoluzione nel campo galattico) e sotto diversi punti di vista; in particolare utilizzeremo sia l'analisi di dati osservativi sia metodi numerici.

Questi ammassi sono sistemi stellari estremamente antichi e massicci; essi sono oggetti ideali per l'esplorazione di molti aspetti della dinamica stellare e per investigare i meccanismi dinamici ed evolutivi della loro galassia di appartenenza. Sono infatti sistemi dove alcuni processi dinamici fondamentali hanno avuto luogo su un tempo scala più breve dell'età dell'Universo. A differenza delle galassie, questi ammassi rappresentano laboratori unici per lo studio del rilassamento a due corpi, della segregazione di massa dovuta all'equipartizione dell'energia, delle collisioni e fusioni stellari e dei collassi centrali. Tuttavia solo recentemente, dalla maggior parte degli studi teorici ed osservativi, è emersa la reale complessità della dinamica degli ammassi globulari. Questi lavori hanno chiaramente mostrato la stretta interazione tra dinamica stellare, evoluzione stellare, contenuto stellare degli ammassi e la dinamica e le proprietà della galassia ospite (Heggie, 1992). Come mostreremo largamente, l'evoluzione degli AG potrebbe essere collegata alle proprietà dinamiche e morfologiche della regione centrale della loro galassia ospite. L'introduzione relativamente recente di strumenti ad alta risoluzione, sia terrestri che spaziali, ha incrementato le conoscenze riguardanti queste regioni peculiari. In particolare, le osservazioni effettuate dall'Hubble Space Telescope hanno rivelato la presenza di ammassi stellari densi al centro di molte galassie; questi ammassi sono noti come ammassi stellari nucleari (NSC, dall'inglese Nuclear Star Cluster). I NSC sono stati osservati in galassie di qualsiasi tipo di Hubble, e ciò suggerisce una stretta connessione tra la loro formazione e l'evoluzione della galassia in cui essi risiedono. Un'altra classe di oggetti la cui presenza è stata rivelata al centro delle galassie è quella dei buchi neri supermassicci (SMBH), la cui massa può essere maggiore di 10^9 $M_\odot$. I SMBH sono tipicamente osservati nelle galassie massicce ($M \geq 10^{10}$ $M_\odot$), mentre i NSC sono presenti in quelle meno massicce (Böker, 2010b). Sembra che i NSC obbediscano a una relazione di scala con le proprietà della galassia ospite simile a quella seguita dai SMBH; inoltre, la media della funzione di frequenza del rapporto tra la luminosità del nucleo e quella della galassia, $\langle \log \eta \rangle = -2.49 \pm 0.09$ dex ($\sigma = 0.59 \pm 0.10$), è indistinguibile da quella trovata per il rapporto di massa tra SMBH e bulge della galassia, $\log(M/M_{gal}) = -2.61 \pm 0.07$ dex ($\sigma = 0.45 \pm 0.09$), calcolata in 23 galassie di tipo primordiale contenenti un SMBH (Côté *et al.*, 2006). Questi risultati hanno suggerito che i NSC possano essere le controparti meno massicce dei SMBH. Se questa interpretazione fosse corretta, si dovrebbe pensare in termini di un "oggetto centrale massiccio" sia esso un SMBH o un nucleo stellare compatto che accompagna la formazione di quasi tutte le galassie di tipo antico e che contiene una frazione media pari a $\sim 0.3\%$ della massa totale del bulge. In alcune galassie, tra cui la Via Lattea (VL) il NSC coesiste con il SMBH, e quindi questa affermazione non può essere ritenuta conclusiva.

L'evoluzione dinamica degli ammassi stellari considerati come sistemi isolati è stata studiata approfonditamente a partire da Plummer (1911), che fu il primo a suggerire una legge analitica che rappresentasse la distribuzione di densità degli AG. Con questo lavoro si aprì la strada agli studi di King che portarono ad una migliore approssimazione analitica delle proprietà degli AG per mezzo dell'assunzione della distribuzione di velocità Maxwelliana troncata alla velocità di fuga locale (King, 1963). Il ruolo del campo esterno è però importante perché accelera la dinamica interna e il rilassamento e quindi anche la conseguente instabilità degli ammassi debolmente legati, causandone, eventualmente, la dissoluzione. Ne consegue che, per ottenere risultati affidabili, è necessario studiare la dinamica stellare prendendo in considerazione l'effetto del potenziale esterno. L'evoluzione dei sistemi stellari è dunque un problema molto complicato da affrontare, tuttavia, con buona approssimazione, la dinamica interna degli ammassi a cui siamo interessati può essere considerata come un problema ad N-corpi, in cui le stelle sono considerate come punti di massa. Le forze dominanti che governano il loro moto interno sono le mutue forze gravitazionali e quelle dovute al campo mareale della galassia. Nella nostra analisi trascureremo l'effetto della perdita di massa dovuta all'evoluzione stellare e non considereremo l'evoluzione primordiale degli ammassi e la presenza del gas, il cui effetto, come è noto, cessa presto durante l'evoluzione dell'ammasso, ossia quando le stelle più massicce terminano la loro evoluzione (Aarseth and Heggie, 1998).

Il problema degli N-corpi non è però risolubile analiticamente per $N > 2$; dobbiamo quindi affidarci a metodi numerici. Ad ora, numerose sono le tecniche e gli algoritmi sviluppati. Uno dei più popolari, noto come Fokker-Plank, tratta le stelle nell'ammasso come un gas; gli incontri gravitazionali tra le stelle sono considerati come collisioni in un gas ideale. Questo è un approccio piuttosto approssimativo; i metodi diretti a N-corpi sono molto più accurati e affidabili per studiare l'evoluzione dinamica dei sistemi stellari. Questi modelli a N-corpi sono infatti privi di assunzioni semplificative, al contrario di quello che accade per le altre tecniche. La loro debolezza principale consiste nel tempo di calcolo richiesto che può essere enorme quando un ammasso viene rappresentato con un grande numero di particelle. Motivati dal grande numero di problemi aperti nello studio della dinamica stellare (sia puramente astrofisici che computazionali) abbiamo svolto il nostro lavoro i cui risultati sono raccolti in questa Tesi, che è organizzata come segue.

- Il **Capitolo 1** raccoglie alcune informazioni di base sui sistemi stellari. Parleremo brevemente di associazioni, “stream” stellari e ammassi aperti. Forniremo inoltre dettagli sugli AG e sui NSC.

- Ogni galassia osservata contiene un insieme di AG: il Sistema di Ammassi Globulari (SAG). Nel **Capitolo 2** focalizzeremo l’attenzione sul problema a larga scala dell’evoluzione dei SAG in galassie ellittiche effettuata utilizzando dati osservativi. I SAG evolvono principalmente a causa di due meccanismi: l’attrito dinamico e l’interazione mareale con il campo galattico. Questi meccanismi causano il decadimento orbitale degli AG al centro della galassia. Un risultato osservativo significativo è che, in molte galassie, il SAG sembra essere meno concentrato, nella regione centrale della galassia di appartenenza, rispetto alle stelle di alone. Una delle possibili spiegazioni di questa differenza potrebbe essere la nascita contemporanea dei due sistemi, seguita dall’evoluzione del profilo di densità del SAG, fino alla distribuzione attuale. Poiché le stelle di alone costituiscono un sistema non collisionale, il loro profilo rimane invariato, quindi la loro distribuzione attuale rappresenta il profilo di densità iniziale del SAG. Con questa premessa è possibile valutare il numero degli AG decaduti orbitalmente nella regione centrale della galassia come l’integrale della differenza tra i due profili. Per mezzo di ipotesi sulla massa media degli ammassi decaduti è possibile dare una stima della massa persa dal SAG. Dopo un breve riassunto dei risultati trovati in letteratura mostreremo in dettaglio i risultati originali da noi ottenuti per un nuovo insieme di galassie ellittiche: NGC 1400, NGC 1407, M 49, NGC 3268, NGC 3258, NGC 4374, NGC 4406 e NGC 4636.

- Nel **Capitolo 3** introdurremo il problema degli N-corpi e le sue proprietà principali. Descriveremo anche i possibili algoritmi e le soluzioni hardware adottate.

- In particolare, una delle possibili classi di integratori temporali usati nel problema degli N-corpi è quella costituita dai metodi simplettici. Questi metodi sono largamente utilizzati in meccanica celeste essendo caratterizzati da una elevata precisione. I metodi simplettici di ordine elevato sono molto affidabili ma anche pesanti dal punto di vista computazionale. La recente introduzione delle schede grafiche programmabili (Graphic Processing Units, GPU) come acceleratori di calcolo a basso costo ci ha permesso di introdurre questi metodi in un nuovo codice a somma diretta per sistemi ad N-corpi, NBSymple, caratterizzato da alte prestazioni e doppiamente parallelo (sia su CPU che su GPU). Questo codice verrà descritto nel **Capitolo 4**; NBSymple è stato testato su diverse architetture e in numerosi contesti astrofisici e i risultati di questi test saranno mostrati in questo stesso capitolo.

- Il **Capitolo 5** è dedicato allo studio della formazione e dell'evoluzione dei NSC nelle galassie ed in particolare nella VL. Dall'ipotesi descritta nel Capitolo 2 segue che una grande quantità di massa può arrivare al centro di una galassia in forma di AG orbitalmente decaduti. Questi ammassi, fondendosi, possono formare il NSC centrale della loro galassia ospite. Questo scenario è noto come "merger model" della formazione dei NSC. Esploreremo la possibilità che un problema a larga scala sia collegato all'evoluzione su larga scala degli AG. In particolare, verificheremo se il decadimento degli AG al centro della galassia può dare luogo ad un sistema simile ai NSC osservati per mezzo di simulazioni a N-corpi auto-consistenti (mai realizzate in precedenza), in cui al centro della galassia viene considerata la presenza di un SMBH. Rivolgeremo poi la nostra attenzione alla nostra Galassia, il cui modello è basato sui più recenti dati osservativi sulla VL, considerando, per la prima volta, il SMBH centrale. Seguiremo l'evoluzione dell'ammasso stellare che si forma al centro della Galassia, intorno al SMBH, tramite la fusione di AG e confronteremo i risultati della simulazione con le proprietà morfologiche e cinematiche osservate per il NSC Galattico.

- Nel nostro studio dell'evoluzione dinamica dei sistemi stellari, usando NBSymple, esploreremo un problema aperto dell'evoluzione degli AG in campi mareali: la formazione ed evoluzione delle code mareali e della loro struttura con sovradensità ("clump"). Nel **Capitolo 6** riporteremo i risultati di uno studio ancora aperto su queste code mareali, effettuato per mezzo di simulazioni ad N-corpi ad alta precisione. In particolare focalizzeremo la nostra attenzione sull'origine e l'evoluzione dei clump.

- Tracceremo infine le nostre conclusioni.

Il contenuto dei Capitoli 2, 4, 5 and 6 è basato sui seguenti articoli e contributi a conferenze:

- Capuzzo-Dolcetta, R., Mastrobuono-Battisti, A., 2009, "Globular cluster system erosion in elliptical galaxies", A&A, vol. 507, p. 183;

- Capuzzo-Dolcetta, R., Mastrobuono-Battisti, A., Maschietti, D., 2011, "NBSymple, a double parallel, symplectic N-body code running on Graphic Processing Units", New Astron., vol. 16, p. 284;

- Capuzzo-Dolcetta, R., Arca-Sedda, M., Mastrobuono-Battisti, A., Montuori, M., Punzo, D., Spera, M., 2011, "High performance astrophysics computing", to appear in Proceedings of "Advances in Computational Astrophysics: methods, tools and outcomes", ASP Conference Series, R. Capuzzo-Dolcetta, M. Limongi and A. Tornambè eds.;
- Antonini, F., Capuzzo-Dolcetta, R., Mastrobuono-Battisti, A., Merritt, D., "Dissipationless Formation and Evolution of the Milky Way Nuclear Star Cluster", eprint arXiv:1110.5937, submitted to ApJ;
- Capuzzo-Dolcetta, R., Antonini, F., Mastrobuono-Battisti, A., 2011, "The Milky Way Nuclear Star Cluster", eprint arXiv:1107.0484v1, to appear in Proceedings of "Stellar Clusters and Associations - A RIA workshop on GAIA", 23-27 May 2011, Granada, Spain;
- Mastrobuono-Battisti, A., Capuzzo-Dolcetta, R., 2011, eprint arXiv:1109.6620, "The Formation of the Milky Way Nuclear Cluster", to appear in Proceedings of "Advances in Computational Astrophysics: methods, tools and outcomes", ASP Conference Series, R. Capuzzo-Dolcetta, M. Limongi and A. Tornambè eds.;
- Montuori, M., Capuzzo-Dolcetta, R., Mastrobuono-Battisti, A., 2011, "Globular Cluster clumpy tidal tails", to appear in Proceedings of "Advances in Computational Astrophysics: methods, tools and outcomes", ASP Conference Series, R. Capuzzo-Dolcetta, M. Limongi and A. Tornambè eds.

Introduction

In 1791 the French astronomer Charles Messier published a catalogue of bright nebulous celestial objects. The first object of the catalogue, M1, was the Crab Nebula; the second one, M2, was a globular cluster (GC), i.e. a self-gravitating spherical cluster of hundred of thousands of stars. A total of 28 objects from that catalogue are now known to be galactic GCs, but a total of about 150 GCs have been observed in our Galaxy up to now. Since this discovery, the importance of studying globular clusters has increased significantly.

GCs are the main characters of this Thesis; here their evolution is faced across different spatial scales, from their interaction in the (small scale) galactic nuclei to their evolution in the (large scale) galactic field, and from different points of view. In particular we both analyse observational data and use numerical tools.
These clusters are old and massive star systems; they are ideal object to explore many aspects of stellar dynamics and to investigate the dynamical and evolutionary mechanisms of their host galaxy. They are indeed systems where many fundamental dynamical processes have taken place on time scales shorter than the age of the Universe. In contrast with galaxies, these clusters represent unique laboratories for learning about two-body relaxation, mass segregation from equipartition of energy, stellar collisions, stellar mergers, and core collapse.

Only recently, however, the actual complexity of globular cluster dynamics has emerged from most of the observational and theoretical studies that have clearly shown the close interplay between stellar dynamics, stellar evolution, the clusters' stellar content and the dynamics and properties of the host galaxy (Heggie, 1992).

As we will widely show, the evolution of GCs may be directly connected to the dynamical and morphological properties of the central region of galaxies where the recent observations made by mean of the Hubble Space Telescope revealed the presence of dense stellar clusters. These cluster are known as Nuclear Star Clusters (NSCs). NSCs have been observed in galaxies belonging to every Hubble type, and this reveals a strong correlation between their formation mechanism and the one of their host galaxy. Another class of objects found at the center of the galaxies are the Supermassive Black Holes (SMBHs), whose mass can exceed 10^9 $\mathrm{M}_\odot$. SMBHs has been typically observed in massive galaxies ($M \geq 10^{10}$ $\mathrm{M}_\odot$), while NSCs have been revealed in less massive galaxies (Böker, 2010b). It seems that NSCs obey to a scale relation with the properties of the host galaxy similar to the one followed by SMBHs; moreover, the mean of the frequency function for the nucleus-to-galaxy luminosity ratio in nucleated galaxies, $\langle \log \eta \rangle = -2.49 \pm 0.09$ dex ($\sigma = 0.59 \pm 0.10$), is indistinguishable from that of the SMBH-to-bulge mass ratio, $\log(M/M_{gal}) = -2.61 \pm 0.07$ dex ($\sigma = 0.45 \pm 0.09$), calculated in 23 early-type galaxies with detected SMBHs (Côté *et al.*, 2006). These results suggested that NSCs could be the less massive counterparts of SMBHs. If this interpretation is correct, then one should think in terms of "central massive objects" either SMBHs or compact stellar nuclei that accompany the formation of almost all early-type galaxies and contain a mean fraction $\sim 0.3\%$ of the total bulge mass. In some galaxies, including the Milky Way, the NSC coexists with a central SMBH, thus this statement cannot be considered definitive.

The dynamical evolution of star clusters as isolated systems has been deeply investigated since pioneering works of Plummer (1911) who was the first to suggest an analytical law to represent the density distribution of globular clusters. He opened the way to the King's work that lead to a better fit of globulars by mean of the assumption of a Maxwellian velocity distribution truncated at the local escape velocity (King, 1963). However, the role of the external field is important because it accelerates the internal dynamics, speeding up relaxation and the consequent instability of loose clusters and their possible dissolution into the stellar background. Thus to obtain reliable results, star cluster dynamics must be studied taking into account the effect of the external potential.

From these early studies it was apparent that the investigation of the dynamical evolution of star clusters is a very complicate issue. However, at a very good approximation, the internal dynamics of clusters to which we are interested can be considered as an N-body problem, where stars are represented as point masses. The dominant forces that govern the internal motions are the mutual gravitational (point-mass) forces of the stars and the tidal field exerted by the host galaxy. In our analysis we neglect the effect of the individual star evolution and mass loss, and we explore the mutual gravitational interactions of the stars and the action of the tidal field of the galaxy. We do not consider the early evolution of the clusters and the presence of gas, whose effect is known to cease very early on during the evolution of the cluster, i.e. by the time the most massive stars have evolved (Aarseth and Heggie, 1998).

As well known, the N-body problem is not analytically soluble if $N > 2$; thus we have to resort on numerical methods. A lot of techniques and algorithms have been developed so far. One of the most popular is the Fokker-Plank one, which treats a cluster of stars like a gas; the gravitational encounters between stars are considered as collisions between particles in an ideal gas. This is a rough approach and the direct N-body method, that we will adopt, is much more accurate and reliable to study the dynamical evolution of stellar systems. These N-body models are, indeed free of simplifying assumptions than are other techniques. However their main problem is the computing time required in the calculations that can be overwhelming when using a large number of particles to represent the cluster.

We started our work motivated by the great number of open issues (both purely astrophysics and computational) in the study of the dynamical evolution of stellar systems and this Thesis, where the results obtained are collected, is organized as follows.

- **Chapter 1** provides some basic information about stellar systems. We briefly talk about associations, stellar streams and open clusters. Then we enumerate some more details about GCs and NSCs.
- Every observed galaxy contains a set of GCs: the Globular Cluster System (GCS). In **Chapter 2** we focus our attention on the large scale issue represented by the evolution of GCSs in elliptical galaxies. GCSs orbitally evolve due to two main mechanisms: dynamical friction and tidal interaction with the galactic field. These mechanisms cause the decay of CGs toward the galactic center. A significant observational result is that, in many galaxies, the GCS seems to be less concentrated respect to the halo stars in the central region of their parent galaxy. One of the possible explanations of this difference is the coeval birth of both the systems, followed by the evolution of the density profile of the GCS, up to the present distribution. Since halo stars constitute a collisionless system, their profile remains almost unchanged and so their distribution is representative of the initial GCS density profile. With this premise it is possible to evaluate the number of GCs orbitally decayed in the central region of the galaxy as the integral of the difference between the two density profiles. By mean of hypothesis on the mean mass of decayed GCs is possible to estimate the mass lost by the GCS. After a brief review of the literature results we show some new results about a new set of elliptical galaxies: NGC 1400, NGC 1407, M 49, NGC 3268, NGC 3258, NGC 4374, NGC 4406 e NGC 4636.
- In **Chapter 3** we introduce the N-body problem along with its main properties. Both the possible algorithms and the hardware solutions adopted are described in this Chapter.
- In particular, one of the possible classes of time integrators used in the N-body problem is the symplectic one. These methods are widely used in celestial mechanics and they are characterized by a high accuracy. High order symplectic methods are very reliable but also time consuming. The recent introduction of Graphic Processing Units (GPUs) as efficient and cheap accelerators allowed us to introduce such methods in a new high performance double parallel (both on CPUs and GPUs) code, NBSymple. This direct summation code is described in **Chapter 4**; NBSymple has been tested on different architectures and in several astrophysical scenarios. The results of these tests are also shown in this Chapter.

- **Chapter 5** is devoted to the study of the formation and evolution of NSCs in galaxies and in particular in the MW. From the hypotheses described in Chapter 2 it follows that a great quantity of matter can reach the center of a galaxy in form of orbitally decayed GCs. These clusters can merge and form the central NSC of their host galaxy. This in known as the "merger model" of the NSCs formation. Here we consider a small scale problem and its connection to the large scale evolution of GCs. Running self-consistent N-body simulations we try to verify if the GCs decay to the galactic center, where for the first time we put an SMBH, give rise to a system which features resemble those observed in NSCs. Then, we turn our attention to our Galaxy, whose model is based on the most recent MW observational data, considering the presence of the central Galactic SMBH. We follow the evolution of the massive cluster, formed through the merging of GCs, around the massive black hole and and we compare the results of the simulation with the Galactic NSC observed morphological and kinematical properties.

- In our study of the dynamical evolution of stellar systems we also used NBSymple to explore an open (large scale) issue in the GCs evolution in tidal fields: the formation and evolution of clumpy tidal tails around these systems. In **Chapter 6** we report preliminary results of this on-going study on tidal tails by mean of high precision N-body simulations. In particular, we focus on tail substructure (clumps) origin and evolution.

- Finally, we draw our conclusions.

The content of Chapters 2, 4, 5 and 6 is based on the following papers and conference proceedings:

- Capuzzo-Dolcetta, R., Mastrobuono-Battisti, A., 2009, "Globular cluster system erosion in elliptical galaxies", A&A, vol. 507, p. 183;

- Capuzzo-Dolcetta, R., Mastrobuono-Battisti, A., Maschietti, D., 2011, "NBSymple, a double parallel, symplectic N-body code running on Graphic Processing Units", New Astron., vol. 16, p. 284;

- Capuzzo-Dolcetta, R., Arca-Sedda, M., Mastrobuono-Battisti, A., Montuori, M., Punzo, D., Spera, M., 2011, "High performance astrophysics computing", to appear in Proceedings of "Advances in Computational Astrophysics: methods, tools and outcomes", ASP Conference Series, R. Capuzzo-Dolcetta, M. Limongi and A. Tornambè eds.;

- Antonini, F., Capuzzo-Dolcetta, R., Mastrobuono-Battisti, A., Merritt, D., "Dissipationless Formation and Evolution of the Milky Way Nuclear Star Cluster", eprint arXiv:1110.5937, submitted to ApJ;

- Capuzzo-Dolcetta, R., Antonini, F., Mastrobuono-Battisti, A., 2011, “The Milky Way Nuclear Star Cluster”, eprint arXiv:1107.0484v1, to appear in Proceedings of “Stellar Clusters and Associations - A RIA workshop on GAIA”, 23-27 May 2011, Granada, Spain;

- Mastrobuono-Battisti, A., Capuzzo-Dolcetta, R., 2011, eprint arXiv:1109.6620, “The Formation of the Milky Way Nuclear Cluster”, to appear in Proceedings of “Advances in Computational Astrophysics: methods, tools and outcomes”, ASP Conference Series, R. Capuzzo-Dolcetta, M. Limongi and A. Tornambè eds.;

- Montuori, M., Capuzzo-Dolcetta, R., Mastrobuono-Battisti, A., 2011, “Globular Cluster clumpy tidal tails”, to appear in Proceedings of “Advances in Computational Astrophysics: methods, tools and outcomes”, ASP Conference Series, R. Capuzzo-Dolcetta, M. Limongi and A. Tornambè eds.

Chapter 1

A brief introduction to Stellar Systems

A stellar system is a gravitationally bound group of stars. Stellar systems vary over some fourteen orders of magnitude in size and mass, from binary stars to star clusters containing 10^2 to 10^6 stars, through galaxies containing 10^{10} to 10^{12} stars, and vast clusters containing thousands of galaxies, to superclusters, or filaments, which contain tens of clusters and appear to be the last level of aggregation hierarchy. The behaviour of these systems is determined by Newton's laws of gravitation. The study of the dynamics of stellar systems is the branch of theoretical physics called stellar dynamics and this Thesis will deal with different aspects of this topic. Thus it is worth to briefly resume some general aspects regarding stellar systems in our Galaxy and in the Universe to better understand and to develop the following Chapters.

1.1 Associations and stellar streams

In our brief survey of stellar systems, we can start from very weakly bounded stellar systems: associations and stellar streams. An *association* is a widely distributed star cluster. Observations show that associations are nearly always found enclosed within giant molecular clouds, suggesting that they formed from this material. The member stars are all the same ages and so they must have been born at the same time from the same raw material. After these groupings have formed, the gas and dust is eventually removed, and the association is left behind. On an average, the associations contain between 10 and 100 stars, but a few candidates such as Cygnus OB-2 contain up to ~ 1000 members, or more. Since they are weakly bounded they are fairly short-lived phenomena lasting on average only a few million years. Currently, there are two basic types of association, OB or O Associations, and T Associations with an average size of 80 pc. O or OB associations, as the name suggests, are groups of massive hot stars with spectral types O and B that are typically spread over an area of more than 100 pc in diameter. Their component

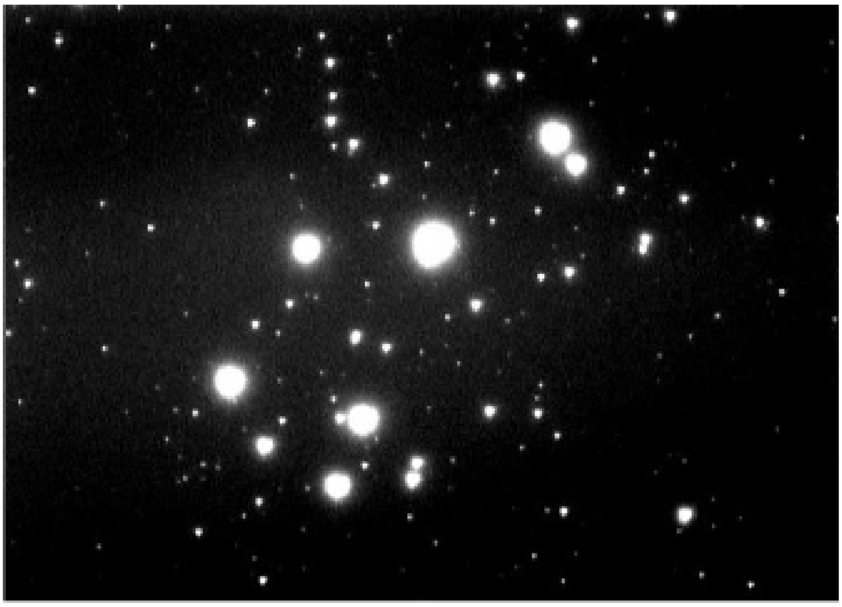

Figure 1.1. M 45, the Pleiades.

stars are very luminous. T associations are similar in nature to OB associations but they contain low mass, T Tauri type stars. T Tauri stars are newborn stars, or protostars, that are still evolving and undergoing contraction. They are variable stars with an irregular period, and are nearly always found in groups or associations, with temperatures ranging from 3,500 to 7,000 K. Associations disperse with time becoming no more apparent and they finally form *moving groups of stars*.
It is also worth to introduce a particular kind of associations: *stellar streams*. A stellar stream is a group of stars that orbits a galaxy and was once a globular cluster (see Section 1.3) or dwarf galaxy that has now been torn apart and stretched out along its orbit by tidal forces (see Chapter 3 and Chapter 6). Recent years have seen a tremendous advance in the quality and quantity of observational data for substructure in the halo of our Galaxy. Of particular note is the outstanding success of the Sloan Digital Sky Survey (SDSS, York *et al.* 2000), which has uncovered large numbers of streams in the halo of the Milky Way (Odenkirchen *et al.*, 2003; Majewski *et al.*, 2003; Yanny *et al.*, 2003; Belokurov *et al.*, 2006a, 2007; Grillmair, 2006; Grillmair and Dionatos, 2006b; Grillmair and Johnson, 2006; Grillmair, 2009; Newberg *et al.*, 2009).

1.2 Open clusters

The next level in the hierarchy of gravitationally bound systems are the *open clusters*. Open clusters are loosely associated groupings of physically attracted stars, bound together by gravity (see Figure 1.1). Gas and dust is commonly found within these clusters, and many open clusters are surrounded with nebulosity left over from star birth within the cluster. Open clusters are unevenly distributed and are often found clumped together within and around the central plane. All the stars in an open cluster orbit around one another, and are affected by each other's gravity. Open clusters often have no determinable shape or structure, and are generally irregular and loosely formed, as opposed to globular clusters, which are spherical in nature and tightly packed with stars (see Section 1.3).

The stars within a cluster formed together and are mainly dwarf stars. They had origin from the gas and dust which contracts rapidly under gravity, and fragments, with any fragment eventually forming a star. Young clusters use up most of the dust and gas over time, or this dust and gas can be dispersed by interactions from other massive stars. Clusters form throughout the life of the Galaxy and, due to their distribution, they can be used to scrutinize the galaxy on a large scale. From observation, many open clusters appear to have two distinct regions, a nuclear one surrounded by an extended area, called corona. The nucleus contains the most massive bright stars, whereas the corona, which is less well understood, hosts the fainter stars. There is an ongoing debate over whether open clusters started life with such two regions or if they evolved this way (see Section 4.8). Regarding the age, most open clusters are between 1 Myr and 10^4 Myr old. Many clusters are less than 50 Myr old. Due to the difficulties in the definition of their edges, the size of open clusters is not well given. Roughly, their diameters can be in the range from 1 to 25 pc. Typical clusters contain 150 to 200 $M_\odot$, but this figure can be anywhere from 50 to 600 $M_\odot$.

Open clusters are short lived, as the tidal interaction with the gravitational potential of the Galaxy cause their disruption. Encounters with massive binary stars can force out the more remote members of a cluster, and over a period of time they begin to loosen up and drift apart. Eventually, all the member stars within a cluster are dispersed to become part of the general stellar population. Many lone stars were once members of such clusters and our own Sun once belonged to an open cluster. Clusters that reside further out from the central bulge of the Galaxy appear to live longer, so must be less affected by tidal forces from the Galaxy itself.

1.3 Globular Clusters

The usual definition of a Globular Cluster (GC) describes it as an old star cluster (with an age larger than about 10 Gyr) found in the bulge and halo regions of the Galaxy. GCs are very compact and almost spherical groups of old stars; they usually contain between 10^5 and 10^6 stars, their mass can reach 10^6 $M_\odot$ and their size can vary significantly between ~ 10 pc and ~ 100 pc with an error due to contours definition.

The spatial density of these clusters decreases from the center to the outskirts and they eventually contain only a negligible quantity of gaseous material. GCs are more stable and persistent than open clusters, although they can be conspicuously affected by evaporation. The gravitational interactions among stars may cause a gravitational collapse of the cluster, which leads to an increasing density of the core and a dilution of the surrounding halo.

A precise determination of the absolute age of the oldest galactic globular clusters is still an elusive cosmological problem. According to Gratton *et al.* (1997) the most likely age is of about 12.1 Gyr, but calibrations through stellar evolution models are uncertain. Contrary to absolute ages, the relative ages of some galactic globular clusters are more precisely known. They are obtained by comparison of their color-magnitude diagrams, which display clear differences in age of about 3 Gyr (Bolte and Hogan, 1995). Chaboyer *et al.* (1996), on more recent age estimates for 43 globular clusters, argue that their sample has a statistically significant age spread of at least 5 Gyr.

Although most galactic globular clusters are located within 20 kpc from the galactic centre, it is worth mentioning the existence of a few very remote galactic clusters.

It is also worth remembering that, already in our Galaxy, globular clusters differ strongly from one to the other, e.g., in integrated absolute magnitude and total mass, which range from $M_V^{int} = -10.1$ and $M_{tot} = 5 \times 10^6$ M$_\odot$ (Meylan *et al.*, 1994, 1995) for the giant galactic globular cluster ω Centauri down to $M_V^{int} = -1.7$ and $M_{tot} = 10^3$ M$_\odot$ for the Lilliputian galactic globular cluster AM-4 (Inman and Carney, 1987). AM-4 is located at $\simeq$ 26 kpc from the galactic centre, and at $\simeq$ 17 kpc above the galactic plane and cannot be considered to be an old open cluster. The uncertainties on the above total mass estimates, perhaps as large as 10%, do not alter the fact that, in our Galaxy, the individual masses of globular clusters range over three orders of magnitude.

It is interesting to note that, in the MW, two different populations are observed, disk and halo GCs. Each of these two populations may contain a fraction of GCs accreted from satellite galaxies (Forbes and Bridges, 2010), which contributed, over time, to build the MW halo, in agreement with a ΛCDM scenario of structure formation (Bullock and Johnston, 2005; Abadi *et al.*, 2006; Font *et al.*, 2006).

For example, the comparison of the spatial distribution of the tidal tails of the Sagittarius galaxy, as deduced by N-body models, with those of halo GCs (Law and Majewski, 2010) has suggested that a number of them (5) are almost certainly associated with Sagittarius, and that four others are likely to be as well, thus confirming the early findings of Bellazzini *et al.* (2003). Some others halo GCs may be probable accreted systems, (Pal 1, for example, whose relatively young ages and chemical composition can be hardly explained with an in situ origin, see Marín-Franch *et al.* (2009); Sakari *et al.* (2011). A number of other systems have been shown to be distinctly younger than typical old halo globular clusters at similar metallicities, suggesting that 25 to 50 globular clusters could have been accreted from 7-8 different dwarf galaxies (Forbes and Bridges, 2010; Mackey and Gilmore, 2004).

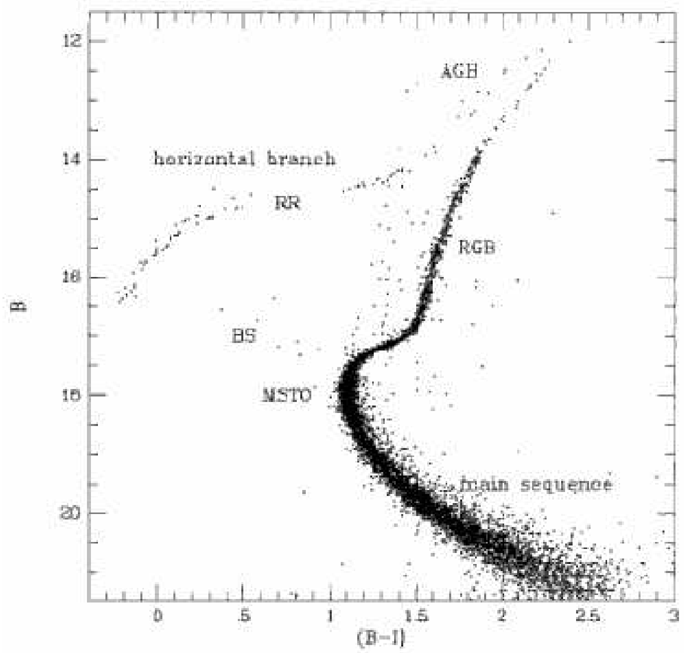

Figure 1.2. Color-magnitude diagram for the GC M 5. The horizontal branch and the main sequence are shown. The RR Lyrae gap (RR), the red giant branch (RGB), the turn-off of the main sequence (MSTO) and the blue stragglers are also shown. [Ashman and Zepf 1998]

Globular clusters are observed in other galaxies of the Local Group and beyond. The major difference with the galactic globular clusters resides in the fact that the above definition based on the age only (larger than ∼ 10 Gyr) is no longer sufficient. Rich stellar systems with ages smaller than the threshold are observed. Anyway, every sufficiently massive galaxy in the Local Group has an associated group of globular clusters, and almost every large galaxy surveyed has been found to possess a Globular Cluster System (GCS, Harris 1991 and Chapter 2).

In the following paragraphs some of the general features of the Galactic GCs are summarized.

1.3.1 Color-Magnitude diagram

Globular clusters, like most of the astronomical objects, are characterized by several properties which, in some cases, are common to all of them. The Color-Magnitude (or H-R) diagram is very useful in the description of these features as it resumes the properties of the stars belonging to the cluster. Moreover, as opposite to open clusters, different GCs have very similar color-magnitude diagrams. As an example, Figure 1.2 (Ashman and Zepf, 1998) shows the H-R diagram for the Galactic GC M 5. Here we describe the different regions characteristic of such diagrams. The main sequence (MS) is included between the turn-off (MSTO) and the fainter mag-

nitudes and the redder colors; the red giant branch (RGB) goes from the subgiants, that provide a connection with the MS, to the more luminous magnitudes and the redder colors. The horizontal branch (HB) is an almost horizontal strip of stars located between the turn-off (MSTO) and the red giant region; the stars that populate the horizontal branch are bluer than that belonging to the RGB and brighter than the main sequence ones. Usually, the variable are omitted from the horizontal branch, so this region is characterized by the presence of the so-called "RR Lyrae gap". The asymptotic giant branch (AGB) elongates up to the maximum luminosity point of the giants, and the blue stragglers (BSs) that seem to be an extension of the main sequence beyond the turn-off.
The comparison between the features of the stars observed in the globular clusters and the theoretical models allows to study the stars found in the various branches in terms of internal structure and evolutionary stage. Following the timeline of the evolution of stars of growing mass we have that:

- the main sequence stars have masses up to ~ 0.75 $M_\odot$ and are burning hydrogen in their cores;
- in the subgiant and in the red giant branch the burning of hydrogen takes place in an intermediate layer of the stars;
- stars which are at the red giant peak have masses ~ 0.8 $M_\odot$ and are about to undergo the helium flash in their center. The horizontal branch stars are quietly burning helium into their central nucleus and hydrogen in an intermediate shell;
- the horizontal branch morphology in the observed globular clusters suggested the hypothesis that the stars suffer a significative mass loss during the red giant phase. From the horizontal branch models and from the pulsation features of the RR Lyrae variables its possible to infer that the stars in the HB have masses between 0.5 and 0.6 $M_\odot$;
- the asymptotic branch stars are burning hydrogen and helium in two different concentric layers.

At present no more stars massive enough to burn carbon into the core can be found in GCs, and the initially most massive stars evolved in neutron stars and white dwarfs. The probably numerous white dwarfs are very faint and so they are very difficult to be detected. Stars with an initial mass bigger than 8 $M_\odot$ may have been exploded as supernovae, leaving neutron stars as remnants.

1.3.2 Dynamical and structural properties

1.3.2.1 Surface brightness profile

In GCs, a significant fraction of stars is concentrated into a small central "core" with the remainder of the stars populating a tenuous envelope. The high stellar density in the central region of globular clusters is one of the properties which differentiate them from lower-density (and lower-mass) open clusters (see Section 1.2).

The surface brightness profile of most globular clusters is well fitted by a King model; specifically the density profile which results from the following distribution function:

$$f(E) = \begin{cases} 0 & E > E_0 \\ K[e^{-\beta(E-E_0)} - 1] & E < E_0 \end{cases} \tag{1.1}$$

(King, 1966; Michie, 1963), where K, β, and E_0 are constants, $E = (1/2)v^2 + \phi(r)$, $\phi(r)$ is the potential, and $f(E)d\mathbf{r}d\mathbf{v}$ is the mass within $d\mathbf{r}d\mathbf{v}$. In this model the core radius is defined as

$$r_c = \sqrt{\frac{9}{4\pi G\rho_0\beta}} \tag{1.2}$$

where ρ_0 is the central density of the cluster. The model has a cut-off at r_t, where ϕ is set equal to 0, and the concentration, c, of such a distribution is defined to be:

$$c \equiv log_{10}(r_t/r_c). \tag{1.3}$$

Observationally, globular clusters are sometimes described in terms of the half-light radius, $r_{1/2}$, i.e. the radius containing half of the projected integrated light of the cluster. Although the core radius is often numerically similar to the half-light radius, the two quantities are not identical.

King models form a sequence of models that can be specified by c. At any value of c there is a set of models generated by different values of r_c. In a lot of calculations, it is convenient to characterize the concentration through a dimensionless parameter $W_0 = -\beta\phi_0$, where ϕ_0 is the value of the potential at the cluster center. All dimensionless quantities, such as the ratio of the central to the mean density, are determined by W_0. There are other models which at various times have been called King models in literature (see Richstone and Tremaine 1986). One of these is an empirical fit to the observed surface brightness profiles of clusters introduced by King (1962). As discussed in King (1966), these original empirical fits are similar to those derived from the distribution given above. The King (1966), model substitutes the earlier work, as it fits the surface brightness profiles equally well and has a dynamical basis. Another model which is sometimes called a King model (or more commonly, a modified Hubble profile) has the form $I(r) = I_0[1 + (r/r_c)]^{-2}$ (Rood *et al.*, 1972a), where I_0 is the central surface brightness. This profile doesn't give a good fit to the most of the observed GCs.

All these models assume that GCs are spherical systems. Observations of the Milky Way globular clusters have found this to be a good approximation, yielding a mean axial ratio of 0.92 ± 0.01 (see for example White and Shawl 1987).

1.3.2.2 Dynamical properties

The dynamics of GCs has been largely studied in the years (see for example Meylan and Heggie 1997; Spitzer 1987; Djorgovski and Meylan 1993). In this section we refer to the internal dynamical processes in GCs, which are mostly independent of the external tidal field due to the host galaxy.

For many Milky Way GCs, the only available mass estimates are obtained by combining an observed cluster luminosity with an assumed mean mass-to-light ratio for the cluster stars. However, in some cases, the central line of sight velocity dispersion, σ_0, has been determined, through the measurement of the individual velocities of a number of stars in the cluster. A dynamical mass estimate can be obtained by combining σ_0 with I_0 and $r_{1/2}$, defined in the previous Subsection. The mass-to-light ratio is related to these quantities through the expression:

$$\frac{M}{L} = \eta \frac{9\sigma_0^2}{2\pi G I_0 r_{1/2}} \tag{1.4}$$

where η is a dimensionless constant. Obtaining a mass-to-light ratio in this manner is often referred as “core fitting” and was for the first time described in detail by Rood *et al.* (1972a).

For the King (1966) model, numerical studies have shown that η has a slight dependence on W_0, but is close to unity for all reasonable models (Richstone and Tremaine, 1986). The mass-to-light ratio along with the integrated luminosity of a cluster, gives an estimate of the cluster mass. This technique has the advantage to employ readily accessible observational quantities. However there are issues raising from the usage of the central velocity dispersion. Indeed, it assumes isotropic orbits and a mass-to-light ratio independent of radius. These assumption are not strictly true. The many two body encounters between stars in GCs tend to produce energy equipartition between stars (each star has the same kinetic energy). As a result, lower mass stars acquire higher velocities and preferentially occupy the outer regions of GCs. Since low mass stars have high mass-to-light ratios, the mass to light ratio of a cluster probably increases with growing radius.

One attempt to overcome these problems is the use of King-Michie dynamical models (Michie, 1963). These models involve lowered Maxwellian energy distributions like the King (1966) ones but include the possibility of velocity anisotropy. To account for the different velocity distributions of stars with different masses, multi-component models, with different mass populations, are usually taken into account. Instead of the King (1966) distribution, one has the energy angular momentum distribution of the form:

$$f_i(E, J) \propto \left(e^{-A_i E} - 1\right) e^{-\beta J^2}, \tag{1.5}$$

where the subscript i identifies the individual populations and A_i is proportional to the mean mass of stars in the i^{th} population. The relative number of stars in each mass bin is determined by the mass function index.

In order to obtain the mass to light ratio, reasonable models are necessary. Such models must fit both the observed surface brightness profile and the radial velocities of stars in the GC.

Some observed GCs are characterized by a power-law cusp, instead of a central core, in the surface brightness profile. These clusters are believed to have suffered core collapse. This dynamical process involves the migration of stars from the GC core to the outer regions of the cluster, leading to a loss of energy from the core and subsequent core contraction. The process is sometimes referred as gravothermal instability. While this process will occur for an isolated cluster, studies have shown that it is enhanced by the presence of an external field (see Chapter 6). Thus the position of the cluster in the host galaxy is important in determining whether core collapse has occurred at present epoch.

1.4 Nuclear Star Clusters

During the last decade, the analysis of the images obtained by the Hubble Space Telescope (HST) has revealed the presence of compact and sometimes resolved sources at the center of many galaxies. Basing on their structural properties and on their spectra was possible to demonstrate the stellar nature of these sources. This kind of objects, similar to GCs, are known as “Nuclear Star Clusters” (NSCs).

NSC will be the object of study in Chapter 5, so it is now worth introducing their properties. They are the most massive and dense clusters found in the Universe and they constitute the last level in the hierarchy of bound systems we want to describe.

NSCs are intriguing objects that are linked to a number of research areas: i) they are a promising environments for the formation of massive black holes because of their extreme stellar density, ii) they may also constitute the progenitors of at least some halo globular clusters via NSC capture following the tidal disruption of a satellite galaxy, and iii) their formation process is influenced by (and important for) the central potential, which in turn governs the secular evolution of their host galaxies.

NSCs have been found in galaxies of all Hubble types, suggesting a close link between their formation history and the evolution of the mother galaxy. In the following Subsection some of their main features are highlighted.

1.4.1 Nuclear star clusters along the Hubble sequence

NSCs are characterized by peculiar conditions due to their position in the bottom of the potential well of the host galaxy.

This position is connected to various phenomena, like the presence of Active Galactic Nuclei (AGN), the occurrence of central starbursts and central very high densities. Scale relations between the galaxy and nucleus global structures have been discovered; these suggest a strong correlation of the evolution of the NSCs with the history of their host galaxy. As an example, left panel of Figure 1.3 shows the nearby Sd

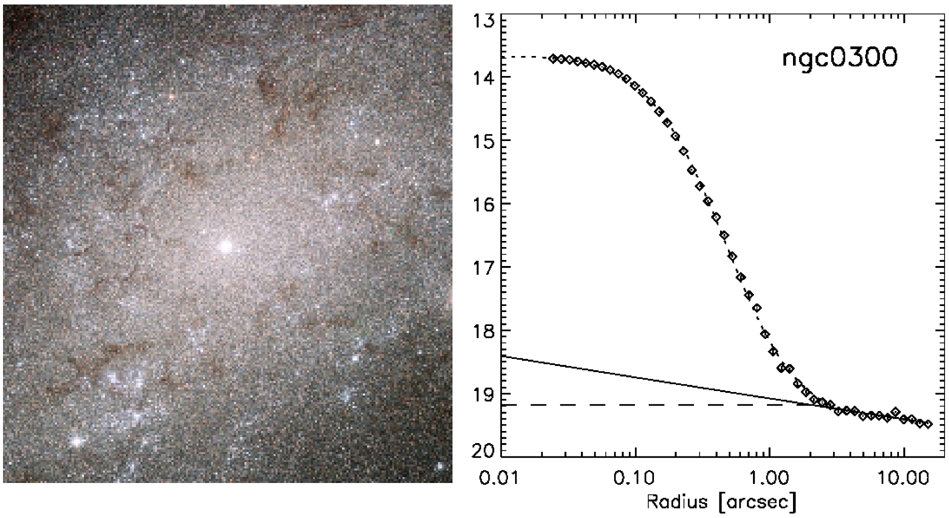

Figure 1.3. Left panel: Color composite image of the central region of the Sd galaxy NGC 300. A NSC resides at the galactic center. Right panel: Radial surface brightness profile in the I band measured in mag/arcsec^2. The NC is evident as a marked overluminosity in the brightness profile, as compared to inward extrapolations (solid, dashed lines) of the the brightness profile at large radii. [van der Marel *et al.* 2007]

galaxy NGC 300 as an example (van der Marel *et al.*, 2007). This galaxy has a NSC, which is easily identified as a separate component because of the marked upturn in the surface brightness profile at small radii (right panel of Figure 1.3). King model fits (see Section 1.3) to the two-dimensional images yield the effective radius and luminosity of the NSC of NGC 300, which result to be $r_{eff} = 2.9$ pc and $L_I = 10^{6.2} L_\odot$.
Observations in the last years lead to to the following picture of NSCs (Böker, 2010a):

1. NSCs are common: the fraction of galaxies with an unambiguous NSC detection is 75% in late-type (Scd-Sm) spirals (Böker *et al.*, 2002a), 50% in earlier-type (Sa-Sc) spirals (Carollo *et al.*, 1997), and 70% in spheroidal (E & S0) galaxies (Côté *et al.*, 2006). All these numbers are likely lower limits, although for different reasons. In the latest-type disks, it is sometimes not trivial to locate the galaxy center unambiguously so that no particular source can be identified with it. In contrast, many early-type galaxies have very steep surface brightness profiles (SBPs) that make it difficult to detect even luminous clusters against this bright background.

2. NSCs are much more luminous than “normal” globular clusters (GCs). With typical absolute I-band magnitudes between −14 and −10 (Böker *et al.* (2002a); Côté *et al.* (2006)), they are roughly 40 times more luminous than the average MW globular cluster (Harris, 1996a).

3. However, NSCs are as compact as MW GCs. Their half-light radius typically

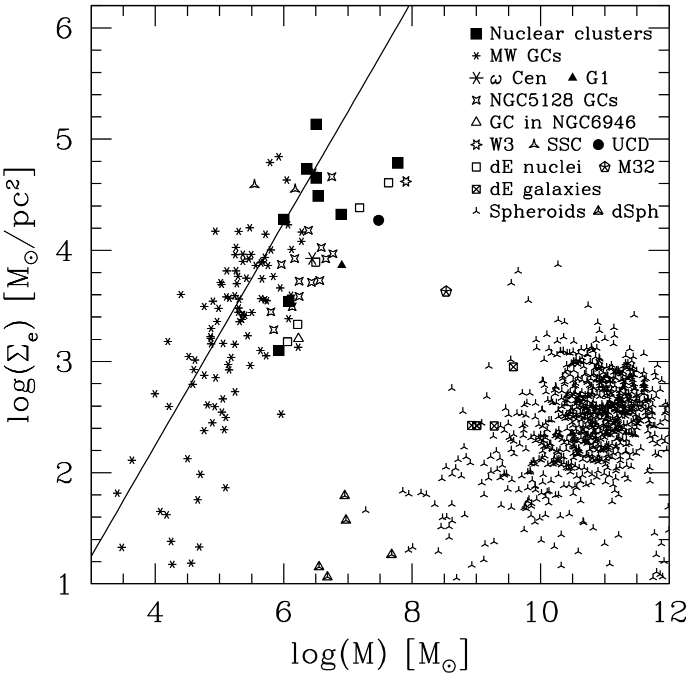

Figure 1.4. Mean projected mass density of various stellar systems inside their effective radius r_e, plotted against their total mass. This is similar to a face-on view of the fundamental plane. NCs occupy the high end a region populated by other types of massive stellar clusters, and are well separated from elliptical galaxies and spiral bulges. The solid line represents a constant cluster size, i.e. $r_e = 3$ pc. [Böker 2007]

is $2 - 5$ pc, independent of galaxy type (Böker *et al.*, 2004; Geha *et al.*, 2002; Côté *et al.*, 2006).

4. Despite their compactness, NSCs are very massive: their typical dynamical mass is $10^6 - 10^7$ $M_\odot$ (Walcher *et al.*, 2005) i.e. at the extreme high end of the GC mass function.

5. Their mass density clearly separates NSCs from compact galaxy bulges. This is demonstrated in Figure 1.4 which compares the mass and mass density of NSCs to that of other spheroidal stellar systems. The clear gap between bulges/ellipticals on the one hand, and NCs on the other hand makes a direct evolutionary connection between the two classes of objects unlikely.

6. The star formation history of NSCs is complex, as evidenced by the fact that most NSCs have stellar populations characterized by multiple generations of stars (Wehner and Harris 2006a; Rossa *et al.* 2006). While all NSCs show evidence for an underlying old ($\gtrsim 1$ Gyr) population of stars, most also have a young generation with ages below 100 Myr. This strongly suggests that NSCs experience frequent and repetitive star formation episodes (see Wehner and Harris 2006a and Section 5.21).

7. NSCs follow similar scaling relations with host galaxy properties as do Supermassive Black Holes (SMBHs). SMBHs are a particular class of black holes with masses $10^6\ M_\odot \leq M_\bullet \leq 10^{10}\ M_\odot$. These objects are formed in the center of spheroidal galaxies, and they have been proven to exist in almost all galaxies. This finding has triggered a very active research area, but its implications are still to be understood fully.

8. NSCs have been found to coexist with SMBHs in a small but steadily increasing (due to improved observations) number of cases (e.g., Filippenko and Ho, 2003; González Delgado *et al.*, 2008; Seth *et al.*, 2008a; Kormendy and Bender, 2009). Based on a compilation of the cases of coexisting NSCs and SMBHs with reliably estimated masses, Graham and Spitler (2009a) show that the masses of the nuclei of the most massive ellipticals appear to be dominated by SMBHs, with NSCs not detected in many cases. The nuclear masses of the least massive spheroids appear to be dominated, however, by the masses of their respective NSCs. There is a transitional zone between these two regimes, where SMBHs and NSCs clearly coexist (see Figure 1 in Graham and Spitler, 2009a).

The formation and evolution of NSCs, with particular attention to the Milky Way case, will be explored in Chapter 5.

Chapter 2

Globular cluster system erosion in elliptical galaxies

Since GCs are neither intermingled with nor closely surrounded by other stars they can be considered as isolated laboratories where it is possible to investigate many aspects of stellar dynamics and of the evolution of stellar systems. Obviously they are subjected to the general potential of the host galaxy, which influence decreases with increasing galactocentric distances.
Since GCs are the oldest objects found in the Galaxy (see Section 1.3), the Globular Cluster System (GCS), as a whole, is actually a witness of the formation epoch of its host galaxy. Thus, investigating its structure, we can derive some information about the dynamical and chemical features at that epoch. Observational data about GCSs can contribute to build up reliable models of formation and evolution of galaxies; moreover estimating the age of GCs we can obtain a minimum age of the galaxy to which they belong, and, therefore, for the whole Universe.

We start our work dealing with a large scale problem, i.e. the the study of the dynamical evolution of GCs due to the interaction with the potential of their host galaxy. This problem is addressed by mean of data analysis and will be also faced using numerical tools in Chapter 6. The work of this Chapter, much of which has been published in an article by Capuzzo-Dolcetta and Mastrobuono-Battisti (2009), is devoted to the analysis of the comparison of GCS and star distribution in galaxies, dealing with 8 galaxies for which good photometric data are available in literature such to draw reliable radial profiles. In all galaxies studied, the GCS density profile is significantly flatter towards the galactic centre than that of the stars. A quantitative comparative analysis of the profiles may provide insight into both galaxy and globular cluster formation and evolution. If the observed difference is caused by erosion of the GCS, the missing GCs in the galactic central region may have merged around the galactic centre and formed, or at least increased in mass, the galactic nucleus (see Chapter 5). Observational support to this are the correlations between the galaxy integrated absolute magnitude and the number of globular clusters lost and that between the central massive black hole mass and the total mass of globular clusters lost. The Chapter is organized as follows. In Section 2.1 the formation and evolutionary mechanisms of GCSs are resumed; in Section 2.2 we show the general method generally used to obtain the number and mass of GCs lost. We also resume some results found in literature. In Section 2.3 we present the improvements that we developed for the data analysis method; here we discuss the observational data, as well as the analytical fit expressions to the density profiles. In Section 2.4 we present the extension, to the data of this work, of the correlation found by Capuzzo-Dolcetta and Donnarumma (2001) between the mass lost by the GCS, the host galaxy luminosity and the mass of the galactic central massive black hole. Finally, in Section 2.5 we summarize results. An error analysis of the methods used is presented in Appendix A.

2.1 The formation and the evolutionary mechanisms of GCSs

Many elliptical galaxies contain more or less populous GCSs, that are, usually, less concentrated towards the galactic centre than the bulge-halo stars.

A huge amount of literature has been dedicated to GCSs identification in external galaxies and study of their properties, since the seminal review by Harris and Racine (1979) up to Harris *et al.* (2009).

One of the main results of such analysis is that the halo stars have a greater central density respect to the respective GCS. Moreover, there is a general agreement that the difference between the two radial distributions is real and not caused by a selective bias. Different hypotheses have been advanced with the purpose of explaining this feature. Among these, two seem the most probable:

- the first one claims for different formation ages for the systems (**Scenario 1**);
- in the second one the GCS and the halo stars born at the same time with the same radial distribution and differentiate later (**Scenario 2**).

2.1.1 Scenario 1: different formation ages

- *Model and authors*
  As stated above, the first hypothesis adopted to explain the difference between the two distributions is that it reflects different formation ages of the two systems, as suggested by Harris and Racine (1979) and Racine (1991); in the opinion of these authors, globular clusters originated earlier, when the density distribution was less peaked. Also Forbes *et al.* (1996), and Ashman and Zepf (1998), on an observational basis, and Bekki and Forbes (2006), on a theoretical basis, suggest that the halo-bulge and the globular cluster components may have been formed differently and thus their profiles should not be, initially, identical. Recent hydrodynamical simulations by Hopkins *et al.* (2009) suggest, for cuspy ellipticals, that the center of these objects have

been constructed by gaseous dissipation in mergers of gas-rich progenitors. The pre-existing stars (and clusters) would not participate in this dissipation, and would thus be relegated to larger radii. In this scheme, the merged system would not have identical cluster and stellar distributions.

- *Model failure*
  However, these hypotheses hardly explain why the stellar and GCS distributions are usually very similar in the outer galactic regions. Of course, there are few exceptions like the two giant ellipticals NGC 4472 (M 49) and NGC 4486 (M 87) and the lenticular NGC 4374 in the Virgo cluster, which seems to have a more radially extended distribution of GCs than that of the stellar component, while the lenticular NGC 4406, also in Virgo and close to NGC 4374, has a steeper declining slope of the GCS radial profile than that of the galactic stellar component. These two substantially different behaviours can be, without contradiction, both attributed to tidal effects, in the sense that in some galaxies an external perturber may cause a tidal stripping of outskirt GCs causing depletion of the outer radial population with a corresponding enrichment of the GCS of the perturbing (likely massive) galaxy. This scheme is sketched in Elmegreen (1999) and have a support by numerical simulations of Forte *et al.* (1982), and Muzzio (1987). In any case, all these bright galaxies lie in the cluster central potential well, and their outskirts are noticeably distorted, because of gravitational interactions with other Virgo Cluster galaxies and because of material acquired during cannibalistic encounters, so they cannot be considered as representative of the “average” elliptical.

2.1.2 Scenario 2: The coeval birth hypothesis

- *Model and authors*
  Another explanation of the difference between the inner GCS and galactic stellar component radial profiles is based on the, simpler, assumption of a coeval birth of globular clusters and halo stars, with a further evolution of the GCS radial distribution, while the collisionless halo stands almost unchanged.

  The GCS evolution is caused mainly by dynamical friction, which brings massive clusters very close to galactic centre, where they are tidally disrupted by interactions with the growing nucleus, as suggested first by Tremaine *et al.* (1975) for M 31 (see Chapter 5).

- *Tests and applications*
  This view for the galaxy nuclei formation was, later, abandoned because it seemed that the dynamical friction time for braking GCs to be confined around the galactic center were too long to account for a quick accretion in mass of the central galactic regions (see for instance Fall and Rees 1977 and Lauer and Kormendy 1986, this latter work dealing with M 87). This view has

been shown to be erroneous, because it is based on the oversimplified assumption that GCs are moving on quasi circular orbits at large distances from the galactic center, where star density is low as, consequently, is their dynamical friction braking on massive satellites. A more likely quite radial biased orbital distribution for GCs shortens significantly the dynamical friction time scales; additionally, the efficiency of dynamical friction is enhanced in triaxial galaxies, where box orbits are maximizing the effect of dynamical friction, as suggested first by Ostriker (1988). Note that box orbits constitute a significant fraction of orbits in stable triaxial galaxies; actually, the prototype of self consistent triaxial models, that studied by Schwarzschild (1979) by mean of his orbital superposition technique, having axial ratios 1:0.625:0.5, contains a large fraction of box orbits, and is stable, as shown by Smith and Miller (1982). It is the major family of box orbits which provides the density concentration on and near the long axis of a triaxial figure and thus support its deviation from axial symmetry (Vietri and Schwarzschild 1983). Also the tidal interaction with a compact nucleus is enhanced in a triaxial potential (Ostriker *et al.*, 1989; Capuzzo-Dolcetta and Tesseri, 1997, 1999; Capuzzo-Dolcetta and Vicari, 2005). The combined effect of these dynamical mechanisms acts to deplete the GCSs in the central, denser, galactic regions, leaving the outer profile unaltered, then remaining similar to the profile of the halo stars, or, when the galaxy interacts significantly with others in a environment, shows an expansion towards outer regions. Under the hypothesis that the initial GCS and halo-bulge radial distributions were the same, an accurate analysis of the observations would allow an estimate of the number of “missing clusters” and therefore of the mass removed from the GCSs. Actually, McLaughlin (1995), Capuzzo-Dolcetta and Vignola (1997), Capuzzo-Dolcetta and Tesseri (1999) and Capuzzo-Dolcetta and Donnarumma (2001), scaling the radial surface profiles of the halo stars of a galaxy to that of its GCS, estimated the number of missing globular clusters as the integral of the difference between the two radial profiles (see Section 2.2). Capuzzo-Dolcetta and Vignola (1997) and Capuzzo-Dolcetta and Tesseri (1999) suggested that the compact nuclei in our galaxy, M 31 and M 87, as well as those in many other galaxies, could have reasonably sucked in a lot of decayed globular clusters in the first few Gyrs of life.

- *Model failure*
  Two objections are often done against the evolutionary scheme. One is that in the hypothesis of efficient dynamical friction braking, acting differentially on clusters of different mass, one would expect a radial dependence of the GC luminosity function, thing usually not seen. The radial dependence is not necessarily expected because the two main external effects acting on the GCSs, dynamical friction and tidal disruption, acts on the opposite sides of the mass

(luminosity) function leaving the average value almost unaltered (Capuzzo-Dolcetta and Tesseri, 1997). Another objection claims the incompatibility about the observed, usually high, metallicities of the central galactic regions and the, usually low, metal content of GCs. This objection relies on that the presently observed GC population is representative of the initial one, which in its massive ($M > 10^6$ $M_\odot$) tail should be lost to the inner galactic zone by strong braking. If the common mass-metallicity relation yields down to very massive globular cluster scale, no surprise in that massive, decayed GCs were also metal rich.

2.2 Scenario 2: the estimate of the number and mass of globular clusters lost. Previous results

As shown in the previous Section, under the hypothesis that the flattening of the GCS distribution in the central region, compared to the distribution of the stars in the galactic bulge, is due to an evolution of the GCS, the number of GCs lost to the centre of the galaxy is obtained by the simple difference of the (normalized) density profiles integrated over the whole radial range (see McLaughlin 1995). Obviously, the limitations in the magnitude range of observations of globular clusters in the different galaxies, the difficulty in the reconstruction of both the high- and low- luminosity tails of the actual GCLF that requires an assumption on its shape and other sources of incompleteness or observational uncertainties negatively affect the evaluation of the number and mass of missing clusters (see Capuzzo-Dolcetta and Vignola 1997, Capuzzo-Dolcetta and Tesseri 1999 and Capuzzo-Dolcetta and Donnarumma 2001). It is clear that the relevant region of number incompleteness should be the low-mass one. As stated in McLaughlin (1995) it is seen that the correction for number incompleteness is significant only in the low-mass tail and slightly overestimated because it is obtained by integrating the hypothetical mass function from zero up, while it is clear that just systems over a certain mass can be considered globular clusters.

Incompleteness is of course a less serious problem for the mass evaluation. Indeed, the contribution to the total mass comes mainly from high-mass clusters, which are now observable unless they have disappeared into unobservable regions.

It's important to stress that, throughout this Chapter, we are mainly interested in the evaluation of the possible relative cluster population impoverishment and mass contribution to the central region, quantities that are both fairly robust against incompleteness corrections that will not taken into account (Capuzzo-Dolcetta and Donnarumma, 2001).

Throughout this Chapter, the "initial" distribution of GCs, $\Sigma_{GC,0}(r)$ is assumed to be equal in shape to the present stellar profile; consequently, it can be obtained by a vertical translation of the stellar profile, $\Sigma_s(r)$, to match the present GCS distribution, $\Sigma_{GC}(r)$, in the outer zone. The number of GCs lost is given by the surface

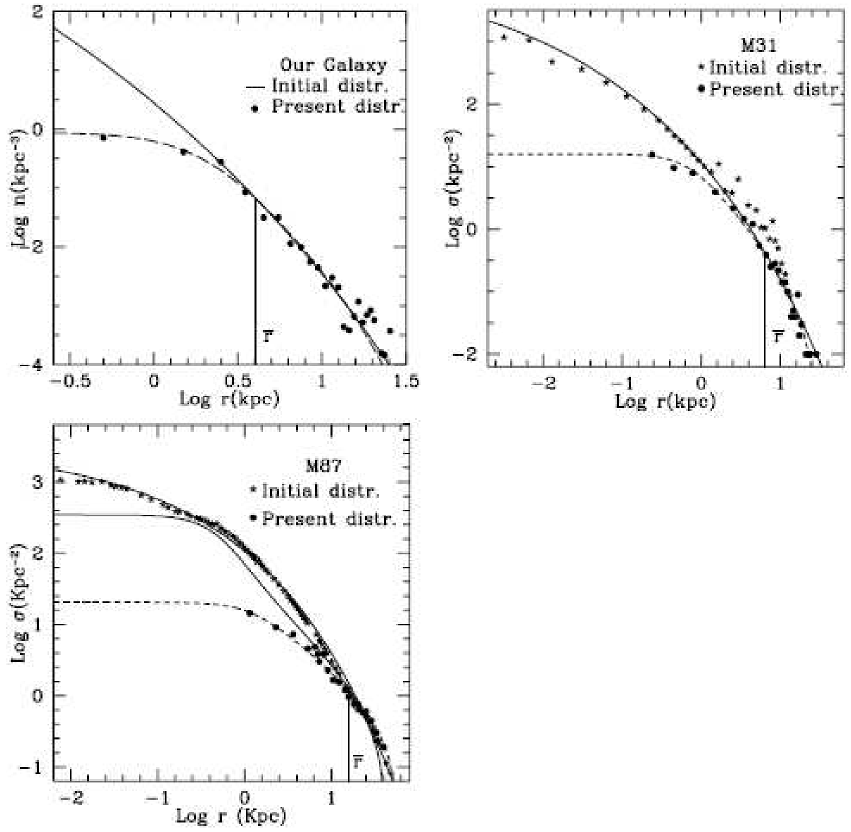

Figure 2.1. Upper left panel: The globular cluster initial distribution (solid curve) and the present one (dashed curve) for our Galaxy. The vertical line refers to the point $\bar{r}$ where the bulge and GCS profiles start to overlap. Upper right panel: Initial and present globular cluster distributions in M 31. Lower panel: The initial and the present globular cluster distributions in M 87; for comparison, the McLaughlin (1995) initial cluster distribution is shown as thick solid line. [Capuzzo-Dolcetta and Vignola 1997]

integral of the difference between the initial and present GCs radial distributions. An estimate of the mass removed from the GCS (M_l) can be obtained through the number of GCs lost, N_l, and the estimate of the mean mass of the missing globular clusters, $\langle m_l \rangle$. A priori, the determination of $\langle m_l \rangle$ needs the knowledge of the initial mass spectrum of the GCS, which has suffered of an evolutionary erosion. However, the most relevant evolutionary phenomena (tidal shocking and dynamical friction) act on opposite sides of the initial mass function, and so we expect that the mean value of the globular cluster mass has not changed very much in time (see Capuzzo-Dolcetta and Tesseri 1997 and Capuzzo-Dolcetta and Donnarumma 2001). Hence, we can assume the present mean value of the mass of globular clusters, $\langle m \rangle$, as a good reference value for $\langle m_l \rangle$.

In the following Subsections we will list the main results found in literature.

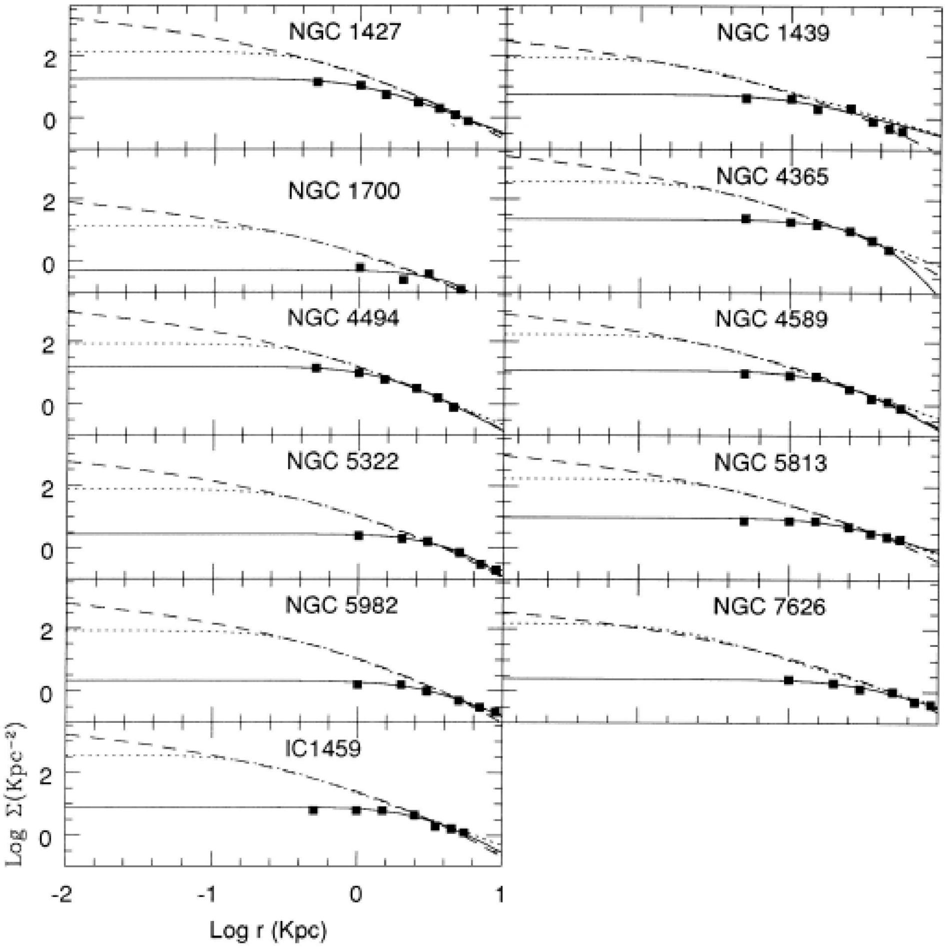

Figure 2.2. Surface number densities for the galaxies of the selected sample analysed by Capuzzo-Dolcetta and Tesseri (1999). Black squares represent the observed globular cluster distribution; the solid line is its modified core model fit. Dashed and dotted lines are de Vaucouleurs and modified core model fits to the normalized galaxy profile respectively. [Capuzzo-Dolcetta and Tesseri 1999]

2.2.1 The Milky Way, M 31 and M 87

This method has been used to analyse several galaxies and, in particular, the Milky Way, M 31 and M 87 (Capuzzo-Dolcetta and Vignola 1997). In these galaxies the radial distribution of GCs, in the central region, is apparently flatter than that of the stellar bulge of the respective host galaxy, as shown in Figure 2.1 (Capuzzo-Dolcetta and Vignola, 1997).

- *The Milky Way*
  Capuzzo-Dolcetta and Vignola (1997) estimated that the Milky Way lost a number $N_l = 56$ of GCs, i.e. the 36% of the current number of GCs ($N = 154$). The mean mass of globulars in our Galaxy is $\langle m \rangle = 3.3 \times 10^5$ $M_\odot$; as described

Galaxy	N	N_i	Δ	M_l ($M_\odot$)
Milky way	155	211	0.26	1.80×10^7
M 31	283	368	0.23	2.30×10^7
M 87	4456	8021	0.44	2.33×10^9
NGC 1379	132	512	0.74	1.50×10^8
NGC 1399	5168	9680	0.63	1.44×10^8
NGC 1404	508	1061	0.53	1.75×10^8
NGC 1427	248	487	0.49	8.86×10^7
NGC 1439	130	141	0.08	4.79×10^6 :
NGC 1700	25	39	0.36	3.66×10^6 :
NGC 4365	517	849	0.39	7.48×10^7
NGC 4494	200	297	0.33	2.98×10^7
NGC 4589	241	371	0.35	7.58×10^7
NGC 5322	175	266	0.34	6.51×10^7
NGC 5813	382	596	0.36	1.03×10^8
NGC 5982	135	260	0.48	8.86×10^7
NGC 7626	215	365	0.41	3.59×10^8
IC 1459	271	516	0.47	1.57×10^8

Table 2.1. The presently observed number of clusters (N), its initial value (N_i), its fractional variation (Δ), the mass lost in form of disappeared globulars (M_l) in the set of galaxies analysed by Capuzzo-Dolcetta and Tesseri (1999) and Capuzzo-Dolcetta and Tesseri (1999). [Capuzzo-Dolcetta 2002]

in Section 2.2 this value can be taken as an estimate of the mean mass of the lost GCs, thus the total mass lost by the Milky Way GCS is $M_l = 1.8 \times 10^7$ M$_\odot$.

- *M 31*
  In the case of M 31 the integral of the difference between the initial and present GCs radial distribution profile gives $N_l = 85$, i.e. the 30% of the present number of globular clusters. Assuming $\langle m \rangle = 3.2 \times 10^5$ M$_\odot$, Capuzzo-Dolcetta and Vignola (1997) found that total mass lost by the GCS of M 31 is $M_l = 2.3 \times 10^7$ M$_\odot$.

- *M 87*
  The number of GCs lost by M 87 seems to be $N_l = 3565$, which is only slightly smaller than the number of cluster currently observed in the same galaxy. The mean mass of the GCs in M 87 is $\langle m \rangle = 6.6 \times 10^5$ M$_\odot$, and so this galaxy has lost a mass equal to $M_l = 2.35 \times 10^9$ M$_\odot$. In Figure 2.1 the best fit to the present and initial GCs distribution for the three galaxies is shown.

2.2.2 Other 11 elliptical galaxies

There are many other galaxies whose GCS is centrally less concentrated than the halo stars. Capuzzo-Dolcetta and Tesseri (1999) evaluated the number of clusters lost by 11 galaxies observed by mean of the WFPC2 of the Hubble Space Telescope (NGC 1427, NGC 1439, NGC 1700, NGC 4365, NGC 4494, NGC 4589, NGC 5322, NGC 5813, NGC 5982, NGC 7626, IC 1459). In Figure 2.2 the dashed and dotted lines represent respectively the de Vaucouleurs model and the core model fits to each galaxy profile. The solid lines show the best fit to the density profiles of the GCSs, obtained through a "modified core model"

$$\Sigma(r) = \frac{\Sigma_0}{\left[1 + \left(\frac{r}{r_c}\right)^2\right]^\gamma} \tag{2.1}$$

where γ is a free parameter. Table 2.1 lists the results of the analysis of these galaxies.

2.2.3 The Fornax cluster: NGC 1379, NGC 1399, NGC 1404

Another contribution to the study of the GCs evolution is due to Capuzzo-Dolcetta and Donnarumma (2001), who analysed the GCSs of three of the Fornax Cluster galaxies, observed by mean of the WFPC2. Also for these galaxies the halo stars results to be more concentrated in the central region respect to the GCs (see Figure 2.3).

- NGC 1379
  NGC 1379 is a galaxy of type E0 and the number of clusters that disappeared from this galaxy, obtained, as usual, assuming that the stellar profile represents the initial distribution of the GCs, is $N_l = 380$. Thus, NGC 1379 lost about the 74% of the initial population of GCs. This great number of globulars sunk toward the internal galactic region corresponds to a big quantity of mass, $M_l = 1.5 \times 10^8 \mathrm{M}_\odot$, probably fallen toward the center of the galaxy.

- NGC 1399
  NGC 1399 is a giant elliptical galaxy located at the center of the Fornax Cluster, and among the galaxies studied by Capuzzo-Dolcetta and Donnarumma (2001) is the one which has the bigger number of GCs. In this case the number of GCs lost results to be equal to 4515, i.e. to the 47% of the initial number of clusters ($N = 9680$). The mass lost by the GCS of NGC 1399 is $M_l = 1.44 \times 10^9 \mathrm{M}_\odot$.

- NGC 1404
  NGC 1404 is a galaxy of type E1, which is located at 10 arcmin from NGC 1399. This proximity make the evaluation of the number of lost GCs quite

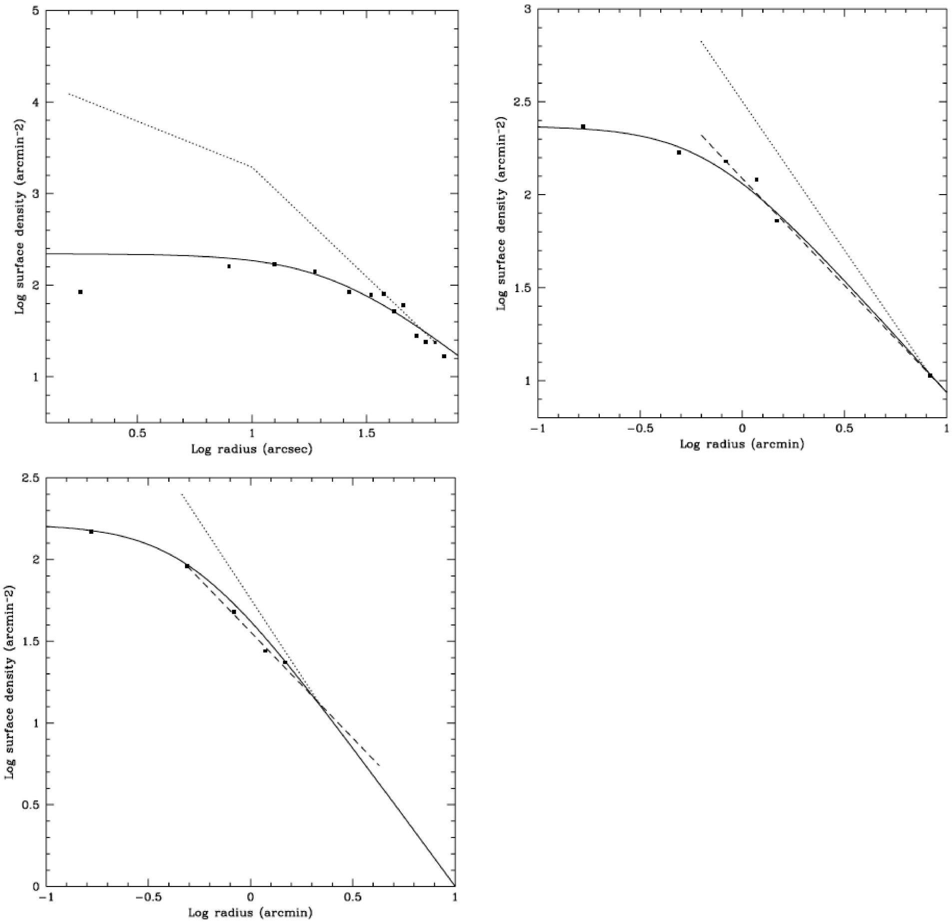

Figure 2.3. Upper left panel: Surface density profile for the globular cluster system in NGC 1379 (black dots). The solid line is the modified core-model fit for GCS. The dotted curve is the surface brightness profile of the underlying galaxy, vertically normalized to match the radial profile of cluster system in the outer regions. Upper right panel: the same but for NGC 1399. Lower panel: the same for NGC 1404. [Capuzzo-Dolcetta and Donnarumma 2001]

difficult, but this issue as been solved by Forbes *et al.* (1998). Initially the galaxy was populated by 1061 GCs; at present the observed clusters are 508. Thus NGC 1404 lost $N_l = 553$ GCs, i.e. the 52% of the initial sample. The mass lost by the GCS is $M_l = 1.75 \times 10^9 \mathrm{M}_\odot$.

2.3 Method for Scenario 2: improvements and new results

In this Section we analyse data of 8 elliptical galaxies to obtain the number of GCs lost in their GCS systems (see Capuzzo-Dolcetta and Mastrobuono-Battisti 2009). The galaxies are: NGC 1400, NGC 1407, NGC 4472 (M 49), NGC 3268, NGC 3258, NGC 4374, NGC 4406, and NGC 4636. In all these galaxies, the GCS density profile is significantly flatter towards the galactic centre than that of the stars. Here we assume, in all cases but for NGC 4472, as fitting function for the GCS projected radial distribution, $\Sigma_{GC}(r)$, a "modified core model". The general expression of this model is given by Equation (2.1) where Σ_0, r_c and γ are free parameters. The choice of this function to fit the GCS profiles is motivated by the good agreement found with almost all the data used for the purposes of this work, as confirmed by, both, the local maximum deviation of the fitting formula from the observed data and the computed χ^2.

For the galaxy stellar profile, $\Sigma_s(r)$, we rely on the fitting formulas provided by the authors of the various papers where we got the data from, that may change case by case, checking how good are the approximations to observed data. The choice of taking outer radial galaxy stellar profiles from the same source paper where we got the data for the GCS profile was done for the sake of homogeneity with GCS profiles because the galaxy photometry was usually taken with the same instrument, in the same photometric band and, probably, in comparable observation conditions). Note that this was possible for the external radial profiles of NGC 1400, NGC 1407, NGC 4374, NGC 4636, while for NGC 3258 and NGC 3268 a single law (modified Hubble's) was adopted over the whole radial extension. In the two remaining cases, NGC 4406 and NGC 4472, we selected the most reliable and recent among the various photometric profiles found in literature.

A check of the sensitivity to a different choice in galactic photometry is found in the discussion of NGC 4636 data (Subsection 2.3.8). In order to obtain the initial distribution of GCs, as said above, we vertically shifted the stellar distribution toward the current GCS radial profile, in order to match both profiles in the external region. The magnitude of the shift, d, has been determined minimizing the square of the difference between the logarithmic values of the data in the tails of the two distributions

$$\sum_i \left[\log \Sigma_s(r_i) - \log \Sigma_{GC}(r_i)\right]^2 \tag{2.2}$$

where r_i is the galactocentric radius of the ith bin in the data. Thus the initial distribution of the GCs is given by

$$\log \Sigma_0(r) = \log \Sigma_s(r) + d. \tag{2.3}$$

We calculate the number of missing (lost) clusters as the surface integral of the difference between $\Sigma_{GC,0}(r)$ and $\Sigma_{GC}(r)$ over the radial range $[0, r_{max}]$ of difference of these two profiles, where r_{max} is defined as the radial coordinate of the intersection of the GCS and stellar radial profiles, that minimizes, upon vertical shift of the stellar radial profile, the squared deviation of the GCS and stellar density distributions over the range $[0, r_{max}]$. Consequently, the number of lost clusters is

$$N_l = 2\pi \int_0^{r_{max}} \left[\Sigma_{GC,0}(r) - \Sigma_{GC}(r)\right] r dr. \tag{2.4}$$

Galaxy	Σ_0	r_c	γ	r_{max}	R
NGC 1400	14.1	0.7	0.88	2.3	2.8
NGC 1407	17.8	1.02	0.85	2.34	7.3
NGC 3258	16.9	3.1	2.4	2.51	7.94
NGC 3268	24.4	2.6	1.9	2.51	7.94
NGC 4374	58.4	0.31	0.278	3.84	11.8
NGC 4406	26.76	3.52	1.19	5.36	24
NGC 4472	107	8.47	0	7	22
NGC 4636	77.66	0.823	0.691	4.75	6.6

Table 2.2. Col. 1: galaxy name; col. 2, 3 and 4: parameters of the modified core model fit for all the galaxies studied; col. 5: upper limit in the integral giving the number of the lost GCs (r_{max}); col. 6: upper limit of the integral performed to estimate the present number of GCs (R). Σ_0 is in arcmin^{-2}; r_c, r_{max} and R are in arcmin.

The present number of GCs, N, is obtained integrating $\Sigma_{GC}(r)$ over the radial range, $[0, R]$, covered by the observations (for the value of R we rely on the papers where we got the GCs distribution data from). The values of N obtained with this method are usually different from those given by the authors of the papers, but for the purposes of this work what is important is the difference between N and N_l and, so, it is crucial a homogeneous way to determine them.
The initial number of GCs in a galaxy is, indeed, estimated as $N_i = N_l + N$.
The numerical values of N_l, N_i and N are functions of the fitting parameters and of the integration limits. These dependences and their contribution to the errors on the final results are discussed in Appendix A.
For NGC 4374, NGC 4406 and NGC 4636 we calculated $\langle m \rangle$ using their GC luminosity functions (GCLFs) and assuming the same typical mass-to-light ratio of GCs in our Galaxy, i.e. $(M/L)_{V,\odot} = 1.5$ for NGC 4406 and NGC 4636 or $(M/L)_{B,\odot} = 1.9$ Illingworth (1976) in the case of NGC 4374. For NGC 4636 we used also the mass function that represents its present distribution of GCs (see Section 2.3.8). For the remaining galaxies (NGC 1400, NGC 1407, NGC 4472, NGC 3258 and NGC 3268) there is no better way to estimate the total mass of 'lost' GCs than adopting as a 'fiducial' reference value for their mean mass, $\langle m_l \rangle$, a value, $\langle m_{MW} \rangle = 3.3 \times 10^5 M_\odot$, which is a reliable estimate of the present mean GC mass in our Galaxy, as obtainable form their LF (Abraham and van den Bergh 1995).

In the following subsections the data and results for the 8 analysed galaxies are shown.

2.3.1 NGC 1400

The surface density profile of this galaxy is given by Forbes *et al.* (2006) (hereafter F06) who fitted it by mean of a power law $\Sigma_s(r) \propto r^{-1.88}$. This fitting law is reliable outside the galactic core, i.e. for $r > r_b = 0.0055$ arcmin (Spolaor *et al.* 2008). The

Galaxy	Model	η	r_b	r_e	b_n	n	α	β	γ
NGC 1400	lc	7.76	0.0055	-	-	-	1.88	-	-
NGC 1407	lc	12.6	0.045	-	-	-	1.42	-	-
NGC 3258	cM	4365	0.036	-	-	-	-	-	0.796
NGC 3268	cM	13490	0.044	-	-	-	-	-	0.936
NGC 4374	lc	135	0.0398	-	-	-	1.67	-	-
NGC 4406	cS	13490	0.012	6.86	13.649	7.02	-	-	0.021
NGC 4472	cS	10471	0.0323	3.47	10.635	5.503	-	-	0.086
NGC 4636	lc	70.8	0.0573	-	-	-	1.5	-	-

Table 2.3. Galactic luminosity fitting parameters. Col. 1: galaxy name; col. (2) key identifying the galaxy light profile model (lc=linear with a flat core in the inner region, cS=core-Sérsic, cM= modified core model); col. 3-10: parameters of the various profile models (see Section 2.2 for details). η is in arcmin^{-2}; r_b and r_e are in arcmin.

luminosity profile of the galaxy for $r \leq r_b$ is almost flat, and linked to the external power law. We fitted the GCS distribution by a modified core model with $\Sigma_0 = 14.1$ arcmin^{-2}, $r_c = 0.7$ arcmin and $\gamma = 0.88$. Integrating $\Sigma_{GC}(r)$ in the radial range where GCs are observed, i.e. from $r_{min} = 0\,$arcmin to $R = 2.8\,$arcmin, we obtain $N = 73$ as the present number of GC in NGC 1400. The initial GCS distribution results to be approximated by:

$$\Sigma_{GC,0}(r) = \begin{cases} 1.37 \times 10^5 \text{ arcmin}^{-2} & r \leq r_b \\ 7.76 r^{-1.88} & r > r_b \end{cases} \tag{2.5}$$

(see Figure 2.4).

Using the general method described in Section 2.2 and the estimated value $r_{max} = 2.3\,$arcmin we have that the number of missing clusters in this galaxy is $N_l = 183$, i.e. about 71% of the initial population of globular clusters, $N_i = N_l + N = 256$. An estimate of the mass lost by the GCS is $M_l = N_l \langle m_{MW} \rangle = 6.04 \times 10^7 M_\odot$.

2.3.2 NGC 1407

As for NGC 1400, data for this galaxy and its GCS are taken from F06. The luminosity profile of the galaxy stars is fitted by a power law, $\Sigma_s(r) \propto r^{-1.42}$. This power law fit fails in the inner region where luminosity shows a core of radius $r_b \simeq 0.045\,$arcmin (Spolaor *et al.* 2008). As for NGC 1400 we thus assume, for $r \leq r_b$, a flat distribution matched to the external power law. The GCS modified core model has, in this case, $\Sigma_0 = 17.8\,$arcmin^{-2}, $r_c = 1.02\,$arcmin and $\gamma = 0.85$ as better fitting parameters. The normalizing vertical translation of the stellar profile leads to

$$\Sigma_{GC,0}(r) = \begin{cases} 1.04 \times 10^3 \text{ arcmin}^{-2} & r \leq r_b \\ 12.6 r^{-1.42} & r > r_b \end{cases} \tag{2.6}$$

(see Figure 2.4).

Integrating the difference of the GCS “initial” and present radial profiles in the

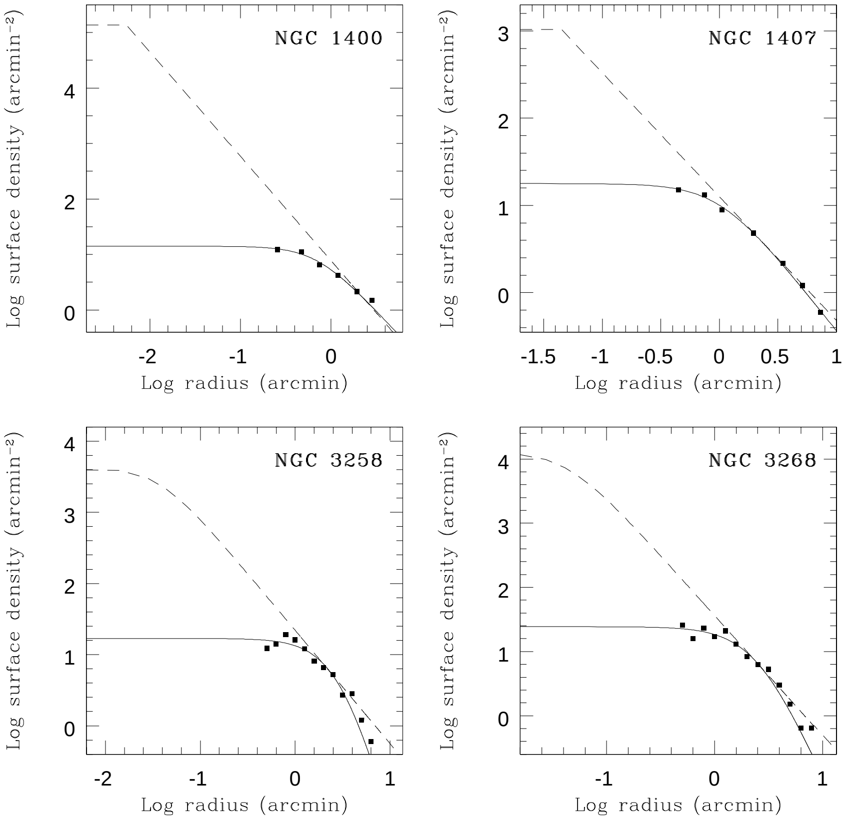

Figure 2.4. Surface number density for NGC 1400, NGC 1407, NGC 4472 (M 49) and NGC 3268. Black squares represent the observed GC distribution; the solid line is its modified core model fit. The dashed curve is the surface brightness profile of the underlying galaxy (a power law and a central flat core for NGC 1400 and NGC 1407, a Sérsic core model for NGC 4472 and a modified Hubble's law for NGC 3268), vertically normalized to match the radial profile of the GCS in the outer regions.

galactic region where these differ, i.e. up to $r_{max} = 2.34\,\mathrm{arcmin}$ (see Equation 2.4), we obtain $N_l = 84$. The present number of GC obtained integrating $\Sigma_{GC}(r)$ in the radial range covered by the observations (i.e. from 0 to $R = 7.3\,\mathrm{arcmin}$) is $N = 314$. The GCS has therefore lost 21% of its initial population, $N_i = 398$.
In this case, we can evaluate the mass lost by the system as $M_l = N_l \langle m_{MW} \rangle = 2.77 \times 10^7 M_\odot$.

2.3.3 NGC 3258

The GCS density profile data for this galaxy are discussed by Dirsch *et al.* (2003). The best modified core model fit is given by the values $\Sigma_0 = 16.9\,\mathrm{arcmin}^{-2}$, $r_c = 3.1\,\mathrm{arcmin}$ and $\gamma = 2.4$. The stellar luminosity profile, within 5 arcmin, following Dirsch *et al.* (2003), is well represented by another modified core model fitting law.

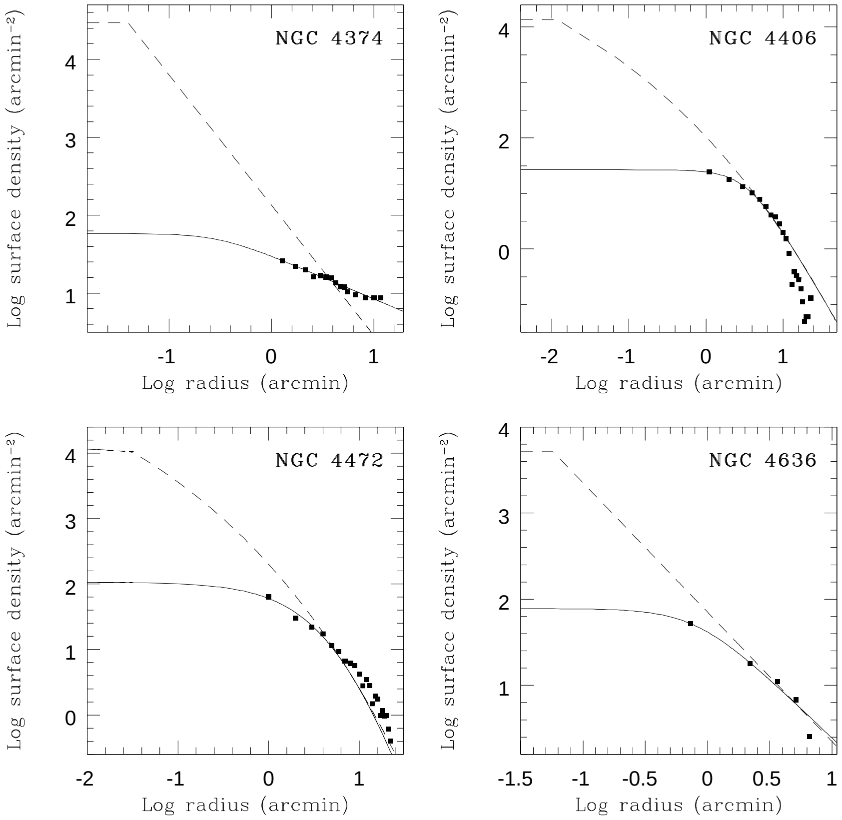

Figure 2.5. Surface number density for NGC 3258, NGC 4374, NGC 4406 and NGC 4636. Black squares represent the observed GC distributions; the solid lines are their modified core model fit. The dashed curves are the surface brightness profile of the underlying galaxy (a modified Hubble's law for NGC 3268, a power law and a central flat core for NGC 4374 and NGC 4636 and a Sérsic core model for NGC 4406), vertically normalized to match the radial profile of the cluster system in the outer regions.

By mean of the usual procedure, the initial GCS profile is obtained:

$$\Sigma_{GC,0}(r) = \frac{4365}{\left[1+\left(\frac{r}{0.036}\right)^2\right]^{0.796}}\,\mathrm{arcmin}^{-2}. \tag{2.7}$$

The present number of GCs is $N = 343$ (with $R = 7.94\,\mathrm{arcmin}$). Performing the surface integral of the difference of the initial and present distribution in the radial range up to $r_{max} = 2.51\,\mathrm{arcmin}$ (see Equation 2.4) we have $N_l = 220$, corresponding to 39% of the initial GCS population, $N_i = 563$.
For this galaxy, we obtained $M_l = N_l\,\langle m_{MW}\rangle = 7.26 \times 10^7 M_\odot$.

Galaxy	N	N_i	N_l	δN	ϵ_l	M_i	M_l
NGC 1400	73	256	183	0.71	0.40	8.45×10^7	6.04×10^7
NGC 1407	314	398	84	0.21	0.12	1.31×10^8	2.77×10^7
NGC 3258	343	563	220	0.39	0.16	2.47×10^8	7.26×10^7
NGC 3268	505	1117	612	0.55	0.12	3.69×10^8	2.02×10^8
NGC 4374	4655	7016	2361	0.34	0.050	2.34×10^9	7.86×10^8
NGC 4406	2850	4209	1359	0.32	0.23	1.25×10^9	4.04×10^8
NGC 4472	6514	14752	4792	0.44	0.14	4.87×10^9	1.58×10^9
NGC 4636	1411	2157	746	0.35	0.11	6.41×10^8	2.22×10^8

Table 2.4. col. (1): galaxy name; col. 2-8: the present number of GCs (N), its initial value (N_i), the number of GCs lost (N_l), the percentage of GCs lost and the estimated relative error on N_l (ϵ_l, see Appendix A), the estimate of the initial mass of the whole GCS (M_i) and of the mass lost by each GCS (M_l). M_i and M_l are in solar masses.

2.3.4 NGC 3268

As for NGC 3268 the GC distribution of NGC 3258 is taken from Dirsch *et al.* (2003).

The resulting core model fit parameters have the values: $\Sigma_0 = 24.4$ arcmin^{-2}, $r_c = 2.6\,$arcmin and $\gamma = 1.9$. The analytical fit to the luminosity profile (within 5 arcmin) of the galaxy is, again, obtained with the same law (modified core model) as used for the cluster density distribution (Dirsch *et al.* 2003). After the vertical translation we have

$$\Sigma_{GC,0}(r) = \frac{13490}{\left[1 + \left(\frac{r}{0.044}\right)^2\right]^{0.936}} \text{arcmin}^{-2}. \tag{2.8}$$

Integrating $\Sigma_{GC}(r)$ from $r_{min} = 0\,$arcmin to $R = 7.94\,$arcmin we have $N = 505$ as present GC number.

The number of globular clusters lost is found to be $N_l = 612$ (from 0 to $r_{max} = 2.51\,$arcmin), that means about 55% of the initial abundance, $N_i = 1117$.

Also in this case, to evaluate the mean mass of lost GC in NCG 3268 we have to assume $\langle m_l \rangle = \langle m_{MW} \rangle$, obtaining $M_l = N_l \langle m_{MW} \rangle = 2.02 \times 10^8 M_\odot$.

2.3.5 NGC 4374 (M 84)

Gómez and Richtler (2004) studied the GCS of this giant elliptical galaxy, using photometry in the B and R bands, to draw its radial surface distribution.

In this case, contrarily to all the other galaxies discussed here, the profile of the GC number density is flatter than the galaxy light (see Figure 2.5). This may be due to tidal interaction with the nearby NGC 4406 galaxy, which shows, indeed, a sort of depletion of the outer GC population. The best modified core model fit to the GC data is given by $\Sigma_0 = 58.4\,$arcmin^{-2}, $r_c = 0.31\,$arcmin and $\gamma = 0.278$.

The galaxy light is characterized by a central core of radius $r_b \simeq 0.0398\,$arcmin

(Lauer *et al.* 2007); for $r > r_b$, it is well fitted by the power law $\Sigma_s(r) \propto r^{-1.67}$ (Gómez and Richtler 2004). Figure 2.5 shows a clear departure of the GCS from the stellar profile in the galactic outskirts; this is not a surprise because it occurs out of the galactic apparent radius (~ 3.1 arcmin, as from NASA/IPAC Extragalactic Data base) i.e. in a region profoundly contaminated by interaction with the tidal field of the inner, crowded Virgo cluster region.
The usual normalization leads to

$$\Sigma_{GC,0}(r) = \begin{cases} 2.94 \times 10^4 \text{ arcmin}^{-2} & r \leq r_b \\ 135 r^{-1.67} & r > r_b, \end{cases} \tag{2.9}$$

as GCS initial radial profile. Integrating our core model up to $R = 11.8$ arcmin we get $N = 4655$ as present number of GCs. The usual integration of the difference of the initial and present GC distribution (Equation 2.4 with $r_{max} = 3.84$ arcmin) leads to $N_l = 2361$. Hence NGC 4374 has lost 34% of its initial population of globular clusters, $N_i = 7016$.
In the case of NGC 4374 the value of the mean mass of a GC has been evaluated using the GCLF in the R band given by Gómez and Richtler (2004). The mean color $\langle (B-R)_0 \rangle = 1.18$ of GCs in this galaxy (Gómez and Richtler 2004) allows us to estimate the mean B absolute magnitude and the mean luminosity of GCs in the B band, $\langle (L/L_B)_\odot \rangle$ assuming $m - M = 31.61$ (Gómez and Richtler 2004). It results $\langle (L/L_B)_\odot \rangle = 1.75 \times 10^5$ (with $M_{B,\odot} = 5.47$, Cox 2000).
Adopting the mass to light ratio $(M/L)_{B,\odot} = 1.9$ obtained by Illingworth (1976) for 10 galactic globular clusters, we get $\langle m_l \rangle = 3.33 \times 10^5 M_\odot$ and $M_l = N_l \langle m_l \rangle = 7.86 \times 10^8 M_\odot$.

2.3.6 NGC 4406 (VCC 881)

NGC 4406 is another giant elliptical in Virgo; its GCS has been studied by mean of the Mosaic Imager on the 4m Mayall telescope at the KPNO (Rhode and Zepf 2004) in the B, V and R bands. The resulting best fit core model is characterized by $\Sigma_0 = 26.76$ arcmin^{-2}, $r_c = 3.52$ arcmin and $\gamma = 1.19$. The core model fit is not satisfactorily reproducing the outer ($r > 50$ kpc) GCS distribution (see Figure 2.5). Due to that NGC 4406 has a massive close companion (NGC 4374) it is possible that its GCS is showing signs of tidal truncation either due to interaction with the companion or the tidal field of the Virgo cluster (see Rhode and Zepf 2004).

The galaxy star luminosity distribution, according to Ferrarese *et al.* (2006b), is well reproduced by a Sérsic core model (Trujillo *et al.* 2004), i.e. by

$$\Sigma_s(r) = \Sigma_b \left[\left(\frac{r_b}{r} \right)^\gamma \theta(r_b - r) + \mathrm{e}^{b_n \left(\frac{r_b}{r_e} \right)^{\frac{1}{n}}} \theta(r - r_b) \mathrm{e}^{-b_n \left(\frac{r}{r_e} \right)^{\frac{1}{n}}} \right], \tag{2.10}$$

where $\Sigma_s(r_b) = \Sigma_b$, $\theta(x)$ is the usual Heaviside function, r_b (*break* radius) divides the profile into an inner ($r \leq r_b$) power-law region and an outer ($r \geq r_b$) exponential region; r_e is the 'effective' radius and $b_n = 1.992n - 0.3271$, with n free fitting

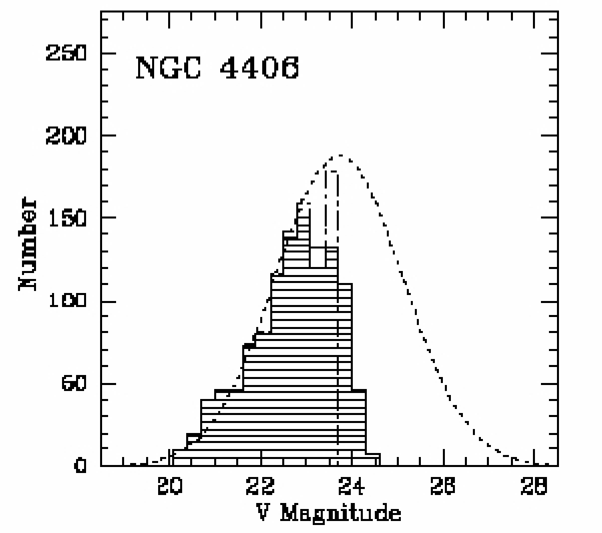

Figure 2.6. GCLF for NGC 4406. The shaded histogram is the GCLF for the observed GCs, used to evaluate the average mass of the same clusters. [Rhode and Zepf 2004]

parameter.
For NGC 4406 the parameter values are (Ferrarese *et al.* 2006b): $\gamma = 0.021$, $n = 7.016$, $b_n = 13.649$, $r_e = 411.84$ arcsec (= 6.864 arcmin), $r_b = 0.72$ arcsec (= 0.0127 arcmin). Its vertical translation gives the initial GCS radial profile

$$\begin{aligned}\Sigma_{GC,0}(r) = 13490 \Bigg[\left(\frac{0.012}{r}\right)^{0.021} \theta(0.012 - r) + \\ + 250\theta(r - 0.012)\mathrm{e}^{-13.649\left(\frac{r}{6.864}\right)^{0.142}} \Bigg] .\end{aligned} \tag{2.11}$$

We note that in this case, unique in the sample of 8 galaxies examined in this work, the stellar profile in the external zone is more slowly decreasing than that of the GCS, because, probably, of GC stripping from the companion NGC 4374 and from the external field in the dense central Virgo cluster region where NGC 4406 is.
Integrating the present distribution of GCs, from $r_{min} = 0\,\text{arcmin}$ to $R = 24\,\text{arcmin}$, we have $N = 2850$. The surface integral given in Equation 2.4, with $r_{max} = 5.36\,\text{arcmin}$, gives the number of globular clusters lost, $N_l = 1359$, i.e. about 32% of the initial GC population ($N_i = 4209s$).
Using the GCLF of this galaxy (see Figure 2.6) and its distance modulus $m - M = 31.12$ (Rhode and Zepf 2004), we evaluated the mean value of the absolute GC V magnitude, $\langle M_V \rangle = -8.42$ which corresponds to the mean luminosity $\langle L/L_\odot \rangle_V = 1.98 \times 10^5$ ($M_{V,\odot} = 4.82$ from Cox 2000).
Assuming $(M/L)_{V,\odot} = 1.5$, we obtain $\langle m_l \rangle = 2.97 \times 10^5 M_\odot$. This estimate leads to the value of the mass lost by the GCS, $M_l = N_l \langle m_l \rangle = 4.04 \times 10^8 M_\odot$.

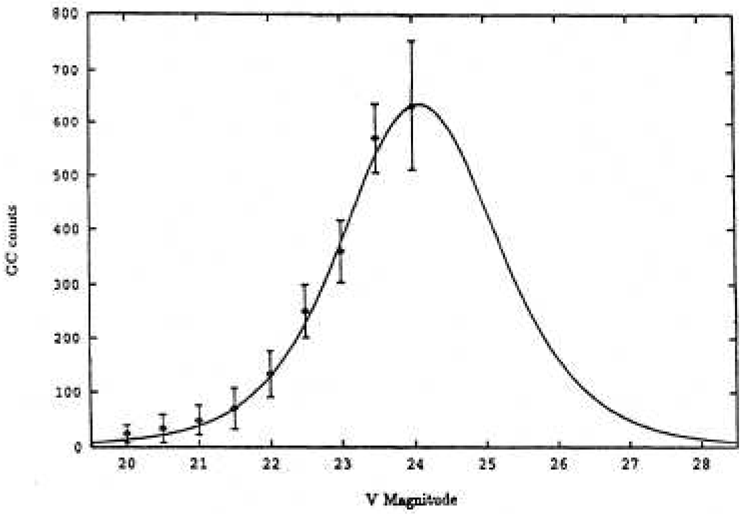

Figure 2.7. GCLF for NGC 4636. The diamond symbols are the number of GCs in each magnitude bin. [Kissler *et al.* 1994]

2.3.7 NGC 4472 (M 49)

Data for the GC distribution in this giant elliptical galaxy in Virgo are taken from Rhode and Zepf (2001). The galaxy light is well fitted by a Sérsic core model (Equation 2.10), whose parameters, determined by Ferrarese *et al.* (2006b), are: $\gamma = 0.086$, $n = 5.503$, $b_n = 10.635$, $r_e = 208.01$ arcsec (= 3.47 arcmin), $r_b = 1.94$ arcsec (= 3.47 arcmin).

In this case the core model profile does not give a good approximation to the observed GCS distribution. A better fit is given by one of the family of galaxy models developed by Dehnen (1993): $\Sigma_{GC} = \Sigma_0 (r/r_c)^{-\gamma}(1 + r/r_c)^{\gamma-4}$. Here we assume $\gamma = 0$, has suggested by Côté *et al.* (2003). Using this law we obtained

$$\Sigma_{GC}(r) = 107.0 \left(1 + \frac{r}{8.465}\right)^{-4} \tag{2.12}$$

The usual vertical translation leads to

$$\begin{aligned} \Sigma_{GC,0}(r) = 10471 \Bigg[& \left(\frac{0.0323}{r}\right)^{0.086} \theta(0.0323 - r) + \\ & +94.7\theta(r - 0.0323) \mathrm{e}^{-10.635\left(\frac{r}{3.47}\right)^{0.18}} \Bigg] . \end{aligned} \tag{2.13}$$

The surface integral (Equation 2.4), performed with $r_{max} = 7\,\text{arcmin}$, gives $N_l = 4792$. Integrating $\Sigma_{GC}(r)$ up to $R = 22\,\text{arcmin}$ we have that $N = 6514$. Hence, M 49 has lost 44% of the initial population of its GCs, $N_i = 14752$.

As for NGC 1400 and NGC 1407, no better estimate of $\langle m_l \rangle$ is available, so we evaluate M_l as $M_l = N_l \langle m_{MW} \rangle = 1.58 \times 10^9 M_\odot$.

2.3.8 NGC 4636

The GC content of this galaxy has been studied by Kissler *et al.* (1994). The modified core model fit has $\Sigma_0 = 77.66$ arcmin^{-2}, $r_c = 0.823$ arcmin and $\gamma = 0.691$ as optimal parameter values.

The galactic light profile shows an inner flat distribution (a core with radius $r_b \simeq 0.0573$ arcmin (Lauer *et al.* 2007), while for $r > r_b$ the light distribution is well fitted by the power law fit $\Sigma_s(r) \propto r^{-1.5}$ (Kissler *et al.* 1994).

The vertical translation of the stellar profile gives the initial GCS profile:

$$\Sigma_{GC,0}(r) = \begin{cases} 5.16 \times 10^3 \text{ arcmin}^{-2} & r \leq r_b \\ 70.8 r^{-1.5} & r > r_b. \end{cases} \tag{2.14}$$

Integrating the present surface density profile of the GCS up to $R = 6.6$ arcmin, we obtain $N = 1411$. Performing the surface integral given in Equation 2.4 (with $r_{max} = 4.75$ arcmin), we estimate that the number of GCs disappeared is $N_l = 746$, i.e. 35% of the initial population, $N_i = 2157$. In the case of this galaxy we obtained two different estimates of the mass lost by the GCS, starting from data taken from Kissler *et al.* (1994). The first estimate has been obtained using the GCLF (Kissler *et al.* 1994, see Figure 2.7). As for NGC 4406 we calculated the mean absolute V magnitude of GCs, $\langle M_V \rangle = -8.07$, (given $m - M = 31.2$ by Kissler *et al.* 1994. Assuming for GCs in NGC 4636 the same M/L_V ratio of galactic GCs, $(M/L_V)_\odot = 1.5$, the deduced mean luminosity of GCs, $\langle L/L_\odot \rangle_V = 1.43 \times 10^5$, gives $\langle m_{l,1} \rangle = 2.15 \times 10^5 M_\odot$, and so $M_{l,1} = N_l \langle m_{l,1} \rangle = 1.29 \times 10^8 M_\odot$.

Another estimate is found using the mass distribution of GCs obtained in Kissler *et al.* (1994) transforming the magnitude bins of the GCLF candidates into masses using the relation given by Mandushev *et al.* (1991): $\log(M/M_\odot) = -0.46 M_V + 1.6$ (corresponding to a mean mass to light ratio $(M/L)_{V,\odot} \simeq 2.0$). Knowing the mass distribution we can directly calculate the mean mass of GCs, $\langle m_{l,2} \rangle = 3.79 \times 10^5 M_\odot$, and thus $M_{l,2} = N_l \langle m_{l,2} \rangle = 2.97 \times 10^8 M_\odot$.

The averages of our two estimates gives $M_l = 2.22 \times 10^8 M_\odot$.

To give some insight into the role of taking a different photometry for the galaxy stellar profile, we adopted for the whole radial extension of NGC 4636 the “Nuker" stellar profile given in Lauer *et al.* (2007) and evaluated again the N_l value. In this way we obtained $N_l = 748$ (versus the previous value of 645) with $r_m ax = 2.2$ arcmin (previously 4.75 arcmin), with a 14.8% relative variation.

Tables 2.2 and 2.3 resume the parameters of the radial profile fitting functions for the studied galaxies, while Table 2.4 resume the results in terms of the estimated number and mass of GC lost.

Regarding the error estimates of Table 2.4 (see Appendix A), it may be worth noting that a 1% error in r_{max} contributes from 1.4% (NGC 1400) up to 26% (NGC 1407) to the total error. In the case of the greatest difference in the slope of the external GCS and stellar profiles (NGC 4374) the contribution of a 1% indeterminacy in r_{max} is for 22% of the total error.

Galaxy	M_V	M_{bh}	M_l	Sources
MW	-20.60	3.61×10^6	1.80×10^7	E05, VV00, CDV97
M 31	-19.82	6.19×10^7	2.30×10^7	M98, CDV97
"	”	4.50×10^7	”	TR02
M 87	-22.38	3.61×10^9	2.33×10^9	M98, CDV97
"	-22.95	3.67×10^9	”	KB09
NGC 1427	-20.43	1.17×10^8	8.86×10^7	VM99, CDT99
NGC 4365	-22.06	7.08×10^8	7.48×10^7	VM99, CDT99
"	-23.63	3.94×10^8	"	KB09
NGC 4494	-20.94	4.79×10^8	2.98×10^7	VM99, CDT99
NGC 4589	-21.14	3.09×10^8	7.58×10^7	VM99, CDT99
NGC 5322	-21.90	9.77×10^8	6.51×10^7	VM99, CDT99
NGC 5813	-21.81	2.82×10^8	1.03×10^8	VM99, CDT99
NGC 5982	-21.83	7.94×10^8	8.86×10^7	VM99, CDT99
NGC 7626	-22.34	1.95×10^9	3.59×10^8	VM99, CDT99
IC 1459	-21.68	2.60×10^9	1.57×10^8	Fe05, VM99, CDT99
"	"	2.50×10^9	"	TR02
NGC 1399	-21.71	5.22×10^9	1.44×10^8	M98, CDD01
"	"	5.10×10^8	"	GE07
NGC 1400	-20.63	3.71×10^8	6.04×10^7	VM99, F06, CDM
NGC 1407	-21.86	5.55×10^8	2.77×10^7	Z07, F06, CDM
NGC 3258	-21.40	2.14×10^8	7.26×10^7	BC06, D03, CDM
NGC 3268	-22.07	4.68×10^8	2.02×10^8	BC06, D03, CDM
NGC 4374	-22.62	1.41×10^9	7.86×10^8	R98, GR04, CDM
"	-23.63	8.87×10^8	"	KB09
NGC 4406	-22.30	1.40×10^8	4.04×10^8	CJ93, RZ04, CDM
"	-22.69	2.29×10^8	"	KB09
NGC 4472	-23.10	2.63×10^9	1.58×10^9	M98, RZ04, CDM
"	-23.24	6.10×10^8	"	KB09
NGC 4636	-21.70	3.63×10^8	2.22×10^8	VM99, KR94, CDM
"	-22.10	2.06×10^9	"	KB09

Table 2.5. col. (1) galaxy name; col. (2), (3) and (4): the V absolute magnitudes, the galactic central black hole masses and the mass lost by GCSs (both in solar masses), respectively; col. (5): bibliographic reference sources for entries in col. (2), (3) and (4); the acronyms are defined in the Bibliography. For 9 galaxies, double entries for M_V and/or M_{bh} are available and given in the second row. When the entry was not modified a " symbol is present.

2.4 A new result: the correlation between M_l, M_V and M_{bh}

At present, although the explanation of the difference between the GCS and stellar bulge radial distributions as a result of dynamical evolution well fits with observational data and theoretical arguments, we cannot state it firmly. However, this theory implies a correlation between the (supposed) mass lost by GCS with the

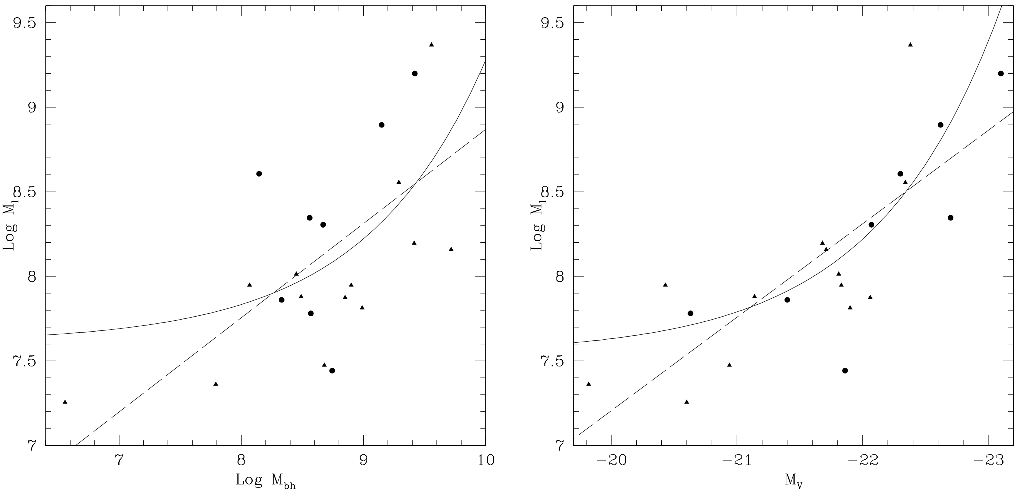

Figure 2.8. The correlation between the GCS (logarithmic) mass lost and the central galactic black hole mass (left panel) and integrated V magnitude of the host galaxy (right panel) for the set of galaxies in Table 2.5. Masses are in solar masses. Black circles represent the eight galaxies whose GCS data are discussed in this Chapter, black triangles refer to the others. The straight lines and curves are the approximation fits discussed in Section 2.4.

mass of the galactic central Supermassive Black Hole (M_{bh}) and, likely, with the host galaxy luminosity (M_V). We verified the existence of these correlations in order to support this interpretation. Tab. 2.5 reports the whole set of galaxies for which we have the estimate of M_V, M_{bh} and M_l and the corresponding references. Figure 2.8 shows a plot of Tab. 2.5 data. For some galaxies, two estimates of M_V and/or M_{bh} were available. In these cases, we took from Tab. 2.5 the entries in the first to plot in Figure 2.8. The figure clearly indicates an increasing trend of M_l as function of M_{bh} (left panel) and of M_V (right panel).

In particular, the linear fit of data in the left panel is given by $\log M_l = a \log M_{bh} + b$ with $a \pm \sigma(a) = 0.56 \pm 0.14$ and $b \pm \sigma(b) = 3.3 \pm 1.2$, giving $\chi^2 = 3.8$. The, alternative, exponential fit gives $\log M_l = \alpha \exp(\log M_{bh}) + \beta$ where $\alpha \pm \sigma(\alpha) = (7.6 \pm 2.7) \times 10^{-5}$ and $\beta \pm \sigma(\beta) = 7.61 \pm 0.22$ and $\chi^2 = 4.6$.
For the 9 galaxies for which alternative data are available we re-evaluated the linear and exponential fit to data using the second row values in Tab. 2.5, getting $a \pm \sigma(a) = 0.51 \pm 0.16$ and $b \pm \sigma(b) = 3.7 \pm 1.3$, with $\chi^2 = 4.1$ for the linear fit and $\alpha \pm \sigma(\alpha) = (1.04 \pm 0.30) \times 10^{-4}$ and $\beta \pm \sigma(\beta) = 7.44 \pm 0.22$, with $\chi^2 = 4.0$. The difference in the fit coefficients are not significant.

The least square, straight-line, fit to the whole set of data shown in the right panel of Figure 2.8 is given by $\log M_l = aM_V + b$ with $a \pm \sigma(a) = -0.55 \pm 0.10$ and $b \pm \sigma(b) = -3.8 \pm 2.2$, giving $\chi^2 = 2.6$. The exponential fit on the same data gives $\log M_l = \alpha \exp(-M_V) + \beta$ where $\alpha \pm \sigma(\alpha) = (1.90 \pm 0.40) \times 10^{-10}$ and $\beta \pm \sigma(\beta) = 7.54 \pm 0.16$ and $\chi^2 = 3.4$. As before, we evaluated again the linear

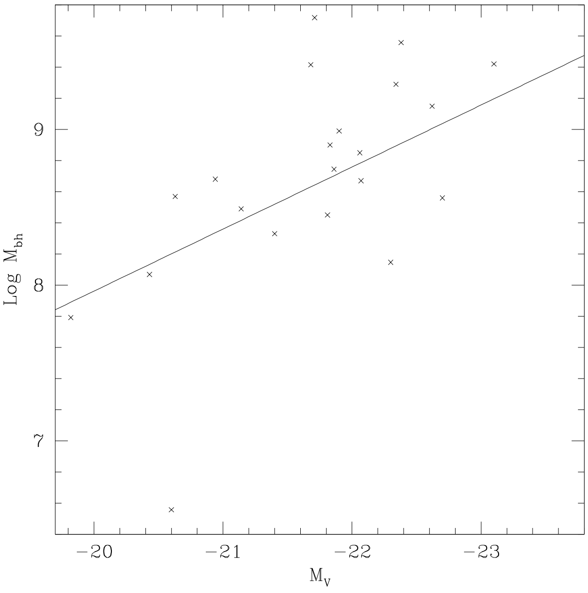

Figure 2.9. The correlation between the logarithm of the central galactic black hole mass (in solar masses) and the integrated V galactic magnitude (see Table 2.5).

and exponential fits using the entries in the second row of the galaxies having two evaluations in Tab. 2.5 and get $a \pm \sigma(a) = -0.48 \pm 0.08$ and $b \pm \sigma(b) = -2.30 \pm 1.70$, giving $\chi^2 = 2.30$, for the linear fit and $\alpha \pm \sigma(\alpha) = (1.01 \pm 0.19) \times 10^{-10}$ and $\beta \pm \sigma(\beta) = 7.67 \pm 0.11$ and $\chi^2 = 2.6$, for the exponential fit.

The correlation seen in the right panel of Figure 2.8 between M_l and M_V reflects, both, an expected physical dependence on the total galactic mass of evolutionary processes acting on GCSs and, simply, the positive correlation between M_{bh} and M_V for the same set of galaxies. Actually, the M_{bh}-M_V correlation for the set of galaxies in Tab. 2.5 has a clearly positive slope, as shown also by the least square fit in Figure 2.9. The least square fit is $\log M_{bh} = aM_V + b$ with $a \pm \sigma(a) = -0.52 \pm 0.15$ and $b \pm \sigma(b) = -2.6 \pm 3.2$, giving $\chi^2 = 5.2$. When using the alternative entries in Tab. 2.5 the fit coefficients transform into $a \pm \sigma(a) = -0.41 \pm 0.12$ and $b \pm \sigma(b) = -0.40 \pm 2.70$, giving $\chi^2 = 5.5$.

On the astrophysical side, Capuzzo-Dolcetta and Vignola (1997) have pointed out how a correlation between GCS radial profiles and the parent galaxy luminosity is expected on the basis of larger tidal disturbance when a more massive compact central nucleus is present in the galaxy, which erodes the GC distribution peaked to the center due to frictionally decayed massive clusters.

2.5 Summary

After a brief review about results found in literature we presented a comparative discussion of radial distribution of the globular cluster systems and of the stars in a sample of eight elliptical galaxies observed by various authors. The main results we found are listed in the following:

- GCS distributions flatten towards the centre, showing a broad core in the profile, contrarily to the surrounding star field.
- This result agrees with many previous findings, indicating, indeed, that GCs are usually less centrally concentrated than stars of the bulge-halo. A debate is still open on the interpretation of this observational issue.
- The "evolutionary" interpretation is particularly appealing; it claims that, initially, the GCS and stellar profiles were similar and, later, GCS evolved to the presently flatter distribution due to dynamical friction and tidal interactions (Capuzzo-Dolcetta 1993).
- In this picture, the flatter central profile is due to the erosion of the inner GCS radial profile. Many GCs are, consequently, packed in the inner galactic region, where they influence the physics of the host galaxy.
- Many of the galaxies studied so far have massive black holes at their centers, whose mass positively correlates with our estimates of number and mass of GC lost. This is a strong hint to the validity of the mentioned evolutionary scenario, together with the other evident correlation between number and mass of GC lost and their parent galaxy luminosity.
- The evolutionary hypothesis is also supported by the positive (although statistically uncertain) correlation between the (rough) estimate of the galactic central phase-space density and integrated magnitude.

At the light of these encouraging findings, we think that much effort should be spent into deepening the observational tests of this astrophysical scenario.

Chapter 3

The N-body problem and the dynamical evolution of stellar systems

In the second part of this Thesis we will keep on dealing with the study of dynamical evolution of stellar systems on different scales, but now using numerical tools. Thus, at this point, it is worth introducing some concepts about stellar dynamics. The study of systems where each particle interacts with each other is a common topic of a large number of scientific fields (e.g. nuclear physics, molecular dynamics, stellar dynamics, etc.). Since many astrophysical systems can be considered as systems of point mass particles, the so called classical N-body problem is of great relevance. In this Chapter a brief review on this subject is presented. In particular, in Section 3.1 and in Section 3.2 the N-body problem is described from an analytical point of view. In Section 3.3 we introduce the numerical approach to the the N-body problem, its computational issues and the possible techniques adopted in its solution. In Section 3.5 some modern hardware solutions adopted to face the problem are described.

3.1 The N-body problem

Unlike the other kinds of objects, astronomical systems are self-gravitating. This means that, while generally mutual gravitational interactions between the components of a system are negligible with respect to the external field, this is not the case for the stars in a stellar system.

Thus self-gravity cannot be neglected respect to the external field, when dealing with physics of astronomical objects. To study stellar dynamics we need to consider the mutual gravitational interactions between the components of a given stellar system and not only the effect of the external, analytically approximated, gravitational field. As we will describe in this Chapter, this is what makes theoretical astrophysics a hard field to be investigated.

Much of the present understanding of the dynamics of stellar clusters and galaxies has emerged from numerical models of these systems. The simplest type of model is one in which a number of particles move under the influence of their mutual gravitational attraction. In these N-body models, bodies are represented by point masses. In a system of N gravitating point-masses, the force acting on the i^{th} body of mass m_i and position $\mathbf{r}_i$ in a cartesian reference frame is the sum of the individual forces, $\mathbf{F}_{ij}$, due to all the other $j = 1, 2, ..., N,\ j \neq i$ bodies

$$\mathbf{F}_{ij} = G\frac{m_i m_j}{|\mathbf{r}_j - \mathbf{r}_i|^3}(\mathbf{r}_j - \mathbf{r}_i), \tag{3.1}$$

such that the total force acting on i, $\mathbf{F}_i$, is

$$\mathbf{F}_i = \sum_{j=1, j\neq i}^{N} \mathbf{F}_{ij} = G m_i \sum_{j=1, j\neq i}^{N} \frac{m_j}{|\mathbf{r}_{ij}|^3}\mathbf{r}_{ij}, \tag{3.2}$$

where

$$r_{ij} = |\mathbf{r}_j - \mathbf{r}_i| = \sqrt{(x_j - x_i)^2 + (y_j - y_i)^2 + (z_j - z_i)^2}, \tag{3.3}$$

is the module of the distance between the particles i and j. The potential function is defined as

$$U(\mathbf{r}_1, \mathbf{r}_2, ..., \mathbf{r}_N) \equiv \frac{1}{2}\sum_{i=1}^{N}\sum_{\substack{j=1\\ j\neq i}}^{N} G\frac{m_i m_j}{r_{ij}}\ . \tag{3.4}$$

The gravitational force field is conservative, and so $\nabla_{x_k} U = \mathbf{F}_{x_k}$ (∇ is the usual gradient operator acting on the potential), and in fact

$$\frac{\partial U}{\partial x_k} = \frac{\partial}{\partial x_k}\left[\frac{1}{2}\sum_{\substack{i=1\\ i\neq k}}^{N} G\frac{m_i m_k}{r_{ik}} + \frac{1}{2}\sum_{\substack{j=1\\ j\neq k}}^{N} G\frac{m_k m_j}{r_{kj}}\right] = \frac{\partial}{\partial x_k}\left[\sum_{\substack{l=1\\ l\neq k}}^{N} G\frac{m_l m_k}{r_{lk}}\right] =$$
$$= -\sum_{\substack{l=1\\ l\neq k}}^{N} G\frac{m_l m_k}{r_{lk}^2}\frac{\partial r_{lk}}{\partial x_k} = \sum_{\substack{l=1\\ l\neq k}}^{N} G\frac{m_l m_k}{r_{lk}^3}(x_l - x_k) = \sum_{\substack{l=1\\ l\neq k}}^{N} G\frac{m_l m_k}{r_{lk}^3}(x_l - x_k) = F_{x_k};$$

similar expressions can be easily obtained for the other components.

Clearly, the anti-symmetry condition $\mathbf{F}_{ij} = -\mathbf{F}_{ji}$ holds, implying the linear and angular momentum conservation laws for the isolated case (see Section 3.1.1). The resulting system of equations of motion, subjected to given initial conditions, is

$$\begin{cases} m_i\ddot{\mathbf{r}}_i &= \mathbf{F}_i + \mathbf{F}_{ext}(\mathbf{r}_i) \\ \mathbf{r}_i(0) &= \mathbf{r}_{i0} \\ \dot{\mathbf{r}}_i(0) &= \dot{\mathbf{r}}_{i0}, \end{cases} \tag{3.5}$$

where $\mathbf{F}_{ext}$ accounts for an external force, expressed by $\mathbf{F}_{ext}(\mathbf{r}_i) = \nabla U_{ext}(\mathbf{r}_i)$ if conservative.

The system given by Equations (3.5) can be transformed into a system of $6N$ first-order scalar equations putting $\dot{\mathbf{r}}_i = \mathbf{v}_i$ and remembering that $\dot{\mathbf{v}}_i = \frac{1}{m_i}\frac{\partial U}{\partial \mathbf{r}_i}$. Although the theoretical formulation of the problem is very simple, its numerical resolution presents significant difficulties.

3.1.1 The integrals of motion

A strategy to simplify the problem is to reduce the order of the system of Equations (3.5) by mean of conserved quantities. In particular, an *integral of motion* is a function I of the positions and velocities $(\mathbf{x}, \mathbf{v})$ of all the particles that is constant along solution trajectories; thus at two generic different times we have

$$I\left[\mathbf{x}(t_1), \mathbf{v}(t_1)\right] = I\left[\mathbf{x}(t_2), \mathbf{v}(t_2)\right].$$

The integrals which restricts the phase space available to a dynamical system are known as *isolating integrals.* For an N-body system, up to 12 isolating integrals can be found: 10 of them can be determined thanks to the Newtonian formalism and, the others 2 were found, for the first time, by Jacobi using the so called procedure of *eliminating nodes.*

- *Total energy*

  The total energy of the system is

  $$E = T - U = \frac{1}{2}\sum_{i=1}^{N} m_i \dot{r}_i^2 - \frac{1}{2}\sum_{i=1}^{N}\sum_{\substack{j=1 \\ j\neq i}}^{N} G\frac{m_i m_j}{r_{ij}}, \tag{3.6}$$

  Where T is the total kinetic energy and $-U$ is the potential energy, as given by Equation (3.4). If

  $$\dot{E} = \dot{T} - \dot{U} = 0\ . \tag{3.7}$$

  then the total energy of the system is constant with time and this means that it is an integral of motion. For the kinetic energy time derivative we have that

  $$\dot{T} = \frac{1}{2}\sum_{i=1}^{N} 2m_i \dot{\mathbf{r}}_i \cdot \ddot{\mathbf{r}}_i = \sum_{i=1}^{N} m_i \dot{\mathbf{r}}_i \cdot \ddot{\mathbf{r}}_i.$$

  Since the potential function depends on time through the positions, we may write

  $$\dot{U}(x_1, y_1, z_1, ..., x_N, y_N, z_N) = \sum_{i=1}^{N}\left(\frac{\partial U}{\partial x_i}\frac{\partial x_i}{\partial t} + \frac{\partial U}{\partial y_i}\frac{\partial y_i}{\partial t} + \frac{\partial U}{\partial z_i}\frac{\partial z_i}{\partial t}\right) = \sum_{i=1}^{N} \nabla_{\mathbf{r}_i} U \cdot \dot{\mathbf{r}}_i \tag{3.8}$$

  The force can be written as $\mathbf{F}_i = m_i\ddot{\mathbf{r}}_i = \nabla_i U$; substituting this expression into Equation (3.8) we obtain

  $$\dot{U} = \sum_{i=1}^{N} m_i \dot{\mathbf{r}}_i \cdot \ddot{\mathbf{r}}_i = \dot{T}\ .$$

Thus, the condition given by Equation (3.7) is fulfilled, and this means that the total energy is actually an integral of motion; its existence allows to reduce the order of the system given by Equations (3.5) to $6N - 1$.

- *The total angular momentum*
  The total angular momentum of an N-body system is
  $$\mathbf{L} = \sum_{i=1}^{N} m_i \mathbf{r}_i \wedge \dot{\mathbf{r}}_i .$$
  As we will show, for an isolated system, $\dot{\mathbf{L}} = \mathbf{0}$ and so, the total angular momentum is an integral of motion. For the second cardinal equation of dynamics the time derivative of angular momentum of a system is equal to the sum of the momenta due to both the external and internal forces
  $$\dot{\mathbf{L}} = \mathbf{M}^{(\text{ext})} + \mathbf{M}^{(\text{int})} = \sum_{i=1}^{N} \mathbf{r}_i \wedge \mathbf{F}_i^{(\text{ext})} + \sum_{i=1}^{N} \mathbf{r}_i \wedge \mathbf{F}_i^{(\text{int})} .$$
  For an isolated system $\mathbf{M}^{(\text{ext})} = \mathbf{0}$, so we have
  $$\dot{\mathbf{L}} = \sum_{i=1}^{N} \mathbf{r}_i \wedge \mathbf{F}_i . \tag{3.9}$$
  Thanks to the equality given by Equation (3.2), we obtain
  $$\dot{\mathbf{L}} = \sum_{i=1}^{N} \mathbf{r}_i \wedge \sum_{\substack{j=1 \\ j\neq i}}^{N} \mathbf{F}_{ij} = \sum_{i=1}^{N} \sum_{\substack{j=1 \\ j\neq i}}^{N} \mathbf{r}_i \wedge \mathbf{F}_{ij} . \tag{3.10}$$
  Here we have a sum of terms $\mathbf{r}_i \wedge \mathbf{F}_{ij}$ and $\mathbf{r}_j \wedge \mathbf{F}_{ji}$ so, we can write
  $$\dot{\mathbf{L}} = \sum_{\substack{(i,j)=1 \\ j\neq i}}^{N} \left(\mathbf{r}_i \wedge \mathbf{F}_{ij} + \mathbf{r}_j \wedge \mathbf{F}_{ji}\right) \tag{3.11}$$
  obtaining a single summation on the couple of values $(i,\ j)$. Taking into account the anti-symmetry relation, we have
  $$\dot{\mathbf{L}} = \sum_{\substack{(i,j)=1 \\ j\neq i}}^{N} \left(\mathbf{r}_i \wedge \mathbf{F}_{ij} - \mathbf{r}_j \wedge \mathbf{F}_{ij}\right) = \sum_{\substack{(i,j)=1 \\ j\neq i}}^{N} G\frac{m_i m_j}{r_{ij}^3} \left(\mathbf{r}_i - \mathbf{r}_j\right) \wedge \left(\mathbf{r}_j - \mathbf{r}_i\right) = \mathbf{0} ,$$
  where we have used the expression of the force given by Equation (3.2). Therefore the 3 components of angular momentum $\mathbf{L}$ is an integral of motion and this allows to reduce the order of the system of Equations (3.5) to $6N - 4$.

- *The total momentum and the center of mass*
  To derive another integral, let us begin to consider the equation of motion
  $$m_i \ddot{\mathbf{r}}_i = \sum_{\substack{j=1 \\ j\neq i}}^{N} G\frac{m_i m_j}{r_{ij}^3} \left(\mathbf{r}_j - \mathbf{r}_i\right) ;$$

summing the right-end sides over i, we obtain

$$\sum_{i=1}^{N}\sum_{\substack{j=1\\ j\neq i}}^{N} G\frac{m_i m_j}{r_{ij}^3}\left(\mathbf{r}_j-\mathbf{r}_i\right)=\mathbf{0};$$

this summation is, indeed, a sum of terms $\mathbf{r}_j-\mathbf{r}_i$ and $\mathbf{r}_i-\mathbf{r}_j$ which cancel each other. At this point it is apparent that

$$\sum_{i=1}^{N} m_i\ddot{\mathbf{r}}_i=\mathbf{0}\ . \tag{3.12}$$

Introducing the position of the center of mass of the system we have

$$\mathbf{r}_{c.m.}=\frac{\sum_{i=1}^{N} m_i\mathbf{r}_i}{\sum_{i=1}^{N} m_i}=\frac{1}{M}\sum_{i=1}^{N} m_i\mathbf{r}_i$$

where M is the total mass of the system. Therefore, the relation (3.12) is equivalent to

$$\ddot{\mathbf{r}}_{c.m.}=\mathbf{0}$$

and, integrating, we have

$$\dot{\mathbf{r}}_{c.m.}=\frac{1}{M}\sum_{i=1}^{N} m_i\dot{\mathbf{r}}_i=\frac{\mathbf{Q}}{\mathrm{M}}=\text{constant}\,. \tag{3.13}$$

Thus, the total momentum $\mathbf{Q}$ is an integral of motion and it allows to reduce the order of the system of Equations (3.5) of other 3 units (one for each component). If we choose a new reference frame whose origin is in the center of mass of the system, then Equation (3.13) can be written as

$$\dot{\mathbf{r}}_{c.m.}=\frac{\mathbf{Q}}{M}=\mathbf{0}$$

and, integrating again, we obtain

$$\mathbf{r}_{c.m.}=\text{constant}=\mathbf{0}$$

which is another integral of motion and so its existence allows to reduce the order of the main system to $6N-10$.

3.1.2 The Virial Theorem

Another useful property of dynamical system is the one known as *virial theorem.* The virial theorem was formulated by Clausius in 1870 in order to study the mechanical origin of heat (his work had the title *"On a mechanical theorem applicable to heat"*) and, then, it was employed in other fields, including stellar dynamics. To derive the compact expression of this theorem, we may start from the equation of motion of a generic particle k, belonging to an N-body system, written in terms of the derivative of the potential

$$m_k \ddot{\mathbf{r}}_k = \frac{\partial U}{\partial \mathbf{r}_k} \ . \tag{3.14}$$

Remembering that

$$\frac{1}{2}\frac{\mathrm{d}^2}{\mathrm{d}t^2}\left(\mathbf{r}_k \cdot \mathbf{r}_k\right) = \frac{\mathrm{d}}{\mathrm{d}t}\left(\mathbf{r}_k \cdot \dot{\mathbf{r}}_k\right) = \left|\dot{\mathbf{r}}_k\right|^2 + \mathbf{r}_k \cdot \ddot{\mathbf{r}}_k$$

and using Equation (3.14) we get

$$\frac{1}{2}\frac{\mathrm{d}^2}{\mathrm{d}t^2}\left(m_k r_k^2\right) = m_k \left|\dot{\mathbf{r}}_k\right|^2 + \mathbf{r}_k \cdot \frac{\partial U}{\partial \mathbf{r}_k} \ .$$

Summing over k and multiplying by $\frac{1}{2}$, we have

$$\frac{1}{4}\frac{\mathrm{d}^2}{\mathrm{d}t^2}\sum_{k=1}^{N} m_k r_k^2 = \sum_{k=1}^{N}\frac{1}{2}m_k \left|\dot{\mathbf{r}}_k\right|^2 + \frac{1}{2}\sum_{k=1}^{N}\mathbf{r}_k \cdot \frac{\partial U}{\partial \mathbf{r}_k} \ . \tag{3.15}$$

The *polar moment of inertia* is defined as

$$I \equiv \sum_{k=1}^{N} m_k r_k^2. \tag{3.16}$$

Using this equation and the definition of the total kinetic energy of the system we have that Equation (3.15) can be rewritten as

$$\frac{1}{4}\frac{\mathrm{d}^2 I}{\mathrm{d}t^2} = T + \frac{1}{2}\sum_{k=1}^{N}\mathbf{r}_k \cdot \frac{\partial U}{\partial \mathbf{r}_k} \ . \tag{3.17}$$

The so called *Clausius' virial*, i.e. the last term on the right side of Equation (3.17), can be shown in a more common form. A real function $f(\mathbf{r})$, of m real variables, is *homogeneous* of degree n if

$$f(\alpha\mathbf{r}) = \alpha^n f(\mathbf{r}) \tag{3.18}$$

$\forall\alpha \in \mathbb{R}$ ($\alpha \neq 0$) and $\forall\mathbf{r} \in \mathbb{R}^m$. From Equation (3.18) it can be readily shown that the potential function $U(\mathbf{r}_1, \mathbf{r}_2, ..., \mathbf{r}_N)$ is homogeneous of degree $n = -1$. In light of this property, we can write

$$\frac{\partial U(\alpha\mathbf{r})}{\partial\alpha} = \frac{\partial(\alpha^n U)}{\partial\alpha} = n\alpha^{n-1}U \ . \tag{3.19}$$

Thus, we have

$$\frac{\partial U(\alpha\mathbf{r})}{\partial\alpha} = \sum_{i=1}^{N}\left(\frac{\partial U}{\partial\alpha x_i}\frac{\partial\alpha x_i}{\partial\alpha} + \frac{\partial U}{\partial\alpha y_i}\frac{\partial\alpha y_i}{\partial\alpha} + \frac{\partial U}{\partial\alpha z_i}\frac{\partial\alpha z_i}{\partial\alpha}\right) = \sum_{i=1}^{N}\left(\nabla_{\alpha\mathbf{r}_i}U\right)\cdot\mathbf{r}_i \ . \tag{3.20}$$

Since α is arbitrary, we can choose $\alpha = 1$ and, using the equalities (3.19) and (3.20), we obtain

$$\sum_{i=1}^{N}\nabla_{\mathbf{r}_i}U \cdot \mathbf{r}_i = -U \, . \tag{3.21}$$

Substituting Equation (3.21) into Equation (3.15) we get

$$\frac{1}{2}\ddot{I} = 2T - U \tag{3.22}$$

which represents the final form of the virial theorem. If the potential energy $\Omega = -U$ is introduced, Equation (3.22) becomes

$$2T + \Omega = \frac{1}{2}\ddot{I}$$

that, since $E = T - U = T + \Omega$, can also be expressed as

$$E + T = \frac{1}{2}\ddot{I}\ . \tag{3.23}$$

3.1.3 Stability and some consequences of the virial theorem

Generally, an N-body system is said to be *stable*, in the sense that it remains confined to a limited region of space, only if both the following conditions are verified:

1. $|\mathbf{r}_{ij}(t)| \neq 0$ for every $i \neq j$ and any t;
2. $|\mathbf{r}_{ij}(t)| < A$ for any t, where A is a positive constant.

This is only possible if the total energy of the system is $E < 0$. In fact, if $E > 0$, through Equation (3.23) we have

$$\frac{1}{2}\ddot{I} \geq E$$

and integrating two times, we get

$$I(t) \geq Et^2 + \dot{I}(t_0)t + I(t_0)$$

i.e. the moment of inertia grows quadratically with t yielding to $I \rightarrow \infty$ when $t \rightarrow \infty$. Thus the second condition is not fulfilled and $r_k \rightarrow \infty$ at least for one value of k. Since, in an N-body system, the energy of a single particle is not a conserved quantity, $E < 0$ is a necessary, but not sufficient, condition. Thus, although the energy of the system is negative, a particle, locally, can reach (and maintain), at position $\mathbf{r}_p$, an energy E_p such that

$$E_p = \frac{1}{2}m_p v_p^2(\mathbf{r}_p) - U(\mathbf{r}_p) > 0,$$

this implies that

$$v_p(\mathbf{r}_p) > \sqrt{\frac{2U(\mathbf{r}_p)}{m_p}} = v_e^{(\mathrm{p})}(\mathbf{r}_p)$$

where $v_e^{(\mathrm{p})}(\mathbf{r}_p)$ is the *escape velocity* of the particle p at position $\mathbf{r}_p$. In this case, the particle p escapes from the system and the condition number 2 is no longer verified.

The virial theorem provides some information about the global behaviour of the system. Given a quantity $A(t)$, its average over the time interval $(0, t)$ is given by

$$\langle A \rangle_t \equiv \frac{1}{t} \int_0^t A(\tau) d\tau \ . \tag{3.24}$$

Applying this definition to Equation (3.22) we obtain

$$\frac{\dot{I}(t) - \dot{I}(0)}{2t} = 2 \langle T \rangle_t - \langle U \rangle_t \ .$$

If the system is limited in the phase space, we have that $\dot{I}(t) - \dot{I}(0)$ is a limited quantity and, if $t \rightarrow \infty$, we have

$$2 \langle T \rangle_\infty - \langle U \rangle_\infty = \lim_{t \rightarrow \infty} \frac{\dot{I}(t) - \dot{I}(0)}{2t} = 0 \ .$$

Therefore, a limited system, after a long time, is said to be *virialized* if it has an average *virial ratio* $\langle Q \rangle_\infty$ such that

$$\langle Q \rangle_\infty = \frac{2 \langle T \rangle_\infty}{\langle U \rangle_\infty} = 1 \, .$$

Generally, when $\ddot{I} > 0$ it is clear that $T > -E$ and the system, globally, tends to expand. On the contrary, when $\ddot{I} < 0$ we have $T < -E$ and the system tends to contract. However, even if a system is initially characterized by a value $\ddot{I} \neq 0$, it tends to a virialized condition, which corresponds to gravitational equilibrium, on a time comparable to the relaxation time (see the next Section).

3.2 Time scales in N-body systems

To study properly the evolution of a stellar system it's fundamental to know the time scales over which it changes it's properties. The *crossing time* is undoubtedly the most intuitive time-scale relating to self-gravitational systems and is usually defined as the time that a particle needs to cross the typical dimension (R) of the system to which it belongs. Remembering that

$$v^2 \sim \frac{GM}{R} \sim \frac{G\bar{m}N}{R}$$

with $\bar{m}$ the mean mass of the N particles in the system, we have

$$t_{cr} = \frac{R}{v} = \frac{R^{\frac{3}{2}}}{\sqrt{G\bar{m}N}} \, . \tag{3.25}$$

For a system in approximate dynamical equilibrium the crossing time is alternatively defined as

$$t_{cr} = \frac{2R_V}{\sigma}, \tag{3.26}$$

where R_V is the virial radius, obtained from the potential energy by $R_V = N^2\bar{m}^2/2|U|$, and σ is the root mean square velocity dispersion (Aarseth, 2003). In a state of approximate equilibrium, $\sigma^2 \simeq GN\bar{m}/2R_V$, which gives

$$t_{cr} \simeq 2\sqrt{2}\left(\frac{R_V^3}{GN\bar{m}}\right)^{1/2}, \tag{3.27}$$

or alternatively $t_{cr} = G(N\bar{m})^{5/2}/(2|E|)^{3/2}$ from $E = \frac{1}{2}U$. Unless the total energy is positive, any significant deviation from an overall equilibrium causes a stellar system to adjust globally on this time-scale which is also comparable to the free-fall time[1]. The close encounter distance is a useful concept in collisional dynamics. It may be defined by the expression (Aarseth and Lecar, 1975)

$$R_{cl} = 2G\bar{m}/\sigma^2, \tag{3.28}$$

which takes the simple form $R_{cl} \simeq 4R_V/N$ at equilibrium.
A rich open star cluster may be characterized by $N \simeq 10^4$, $\bar{m} \simeq 0.5\ \mathrm{M}_\odot$ and $R_V \simeq 4$ pc, which yields $t_{cr} \simeq 5 \times 10^6$ yr. Many such clusters have ages exceeding several Gyr, hence a typical star may traverse or orbit the central region many times, depending on its angular momentum.

Another important time scale is the *relaxation time*; it is, indeed, one of the most important parameters used to describe exhaustively the evolution of a generic stellar system. It is defined as the time over which, as a result of collisions between particles, a stellar system completely loses memory of its initial state. After this time a system is said to be *relaxed.* A simplified evaluation of the relaxation time, which leads to the expression

$$t_r \simeq n_R t_c = \frac{1}{8}\frac{N}{\ln\Lambda}t_{cr} = \frac{1}{8}\frac{N}{\ln\Lambda}\frac{R^{3/2}}{\sqrt{GM}} \tag{3.29}$$

where $\ln\Lambda$ is the Coulomb logarithm, can be found in Appendix B. Going beyond this simplified derivation a more detailed analysis of the subject of relaxation time was mainly formulated by Rosseland (1928), Ambartsumian (1985), Spitzer (1940) and Chandrasekhar (1942). The classical expression of the relaxation time is given by

$$t_E = \frac{1}{16}\left(\frac{3\pi}{2}\right)^{1/2}\left(\frac{NR^3}{GM}\right)^{1/2}\frac{1}{\ln(0.4N)}, \tag{3.30}$$

(Chandrasekhar, 1942). For the purposes of star cluster dynamics, another definition, known as the half-mass relaxation time is perhaps more useful since it is not sensitive to the density profile.
Following Spitzer (1987) the relaxation time at the half mass radius it is

$$t_{rh} = 0.138\left(\frac{Nr_h^2}{Gm}\right)^{1/2}\frac{1}{\ln(\gamma N)}, \tag{3.31}$$

---

[1] The free-fall time is the characteristic time that would take a body to collapse under its own gravitational attraction, if no other forces existed to oppose the collapse.

where r_h is the half mass radius and $\Lambda = \gamma N$ is the argument of the Coulomb logarithm. Formally this latter factor is obtained by integrating over all impact parameters in two-body encounters (see Appendix B), and, commonly, γ is set equal to 0.4. From the numerical example above we then have $t_{rh} \simeq 3 \times 10^8$ yr for $r_h \simeq 4$ pc and an equal-mass system with $N = 1 \times 10^4$ stars of half a solar mass. In comparison, $t_{rh} \simeq 3 \times 10^{10}$ yr for a globular cluster with $N \simeq 10^6$ and $r_h \simeq 25$ pc.

Equation (3.31) gives an estimate of the time for the root mean square velocity change arising from small angle deflections at the half-mass radius to become comparable to the initial velocity dispersion. It serves as a useful reference time for significant dynamical changes affecting the whole cluster even though there is no corresponding numerically well-defined quantity. The assumption of approximate equilibrium with the above definition of the crossing time leads to the relation (Spitzer, 1987)

$$\frac{t_{rh}}{t_{cr}} \simeq \frac{N}{22\ln(\gamma N)}, \tag{3.32}$$

which shows that close encounters become less important for increasing particle number since the potential is smoother. Hence if the relaxation time for an equal-mass system exceeds the time interval of interest by a significant factor, the use of the collisionless approximation which neglects close encounters may be justified. However, the approach to the collisionless regime is slow and in any case the central relaxation time may be much shorter.

3.3 The numerical approach

After discussing the general properties of the N-body problem we shift to the study of its solution. As well known there is no general analytic solution of the N-body problem for $N \geq 3$, so that numerical methods must be used to evaluate the mutual forces and to solve the equations of motion.

In relatively recent times, the numerical approach to the star cluster dynamics has greatly benefited from the huge development of computational hardware and software tools. The study of the dynamics of a real cluster in a galaxy implies the numerical solution of an N-body problem with N up to 10^6, for a time extension up to ~ 10 Gyr. It can be easily shown that the computational effort grows as N^3, two powers of N due to the pair-wise force interaction and another power because larger N values slow down two-body relaxation effect and, so, slow down the "heat" flow time. Since the sixties of last century to present, direct N-body simulations gained a factor greater than 10^4: from simulations of systems with tens of stars to simulation with few hundred thousand stars. This progress may seem not very fast, but the explanation for this is the told $\propto N^3$ dependence of the computational time on N. Note that, when dealing with high-precision simulations of N-body systems, aimed at studying the evolution of collisional systems, algorithmic and software developments are of difficult achievement. The most relevant technical improvements to numerical algorithms are due, mainly, to Aarseth's work (for an

overview see Aarseth 2003).
In the following Subsections we will explain why the N-body problem is so difficult to solve numerically.

3.3.1 Computational issues and possible solutions

Implementation of numerical methods is challenging due to the co-existence of problems on both small scales (i.e. close gravitational encounters) and large ones (the newtonian pair-wise gravitational force never vanishes, so that every component of the system, however distant, contributes to the force calculation). This “double divergence” of the classic newtonian interaction potential has two different consequences: i) close encounters correspond to an unbound force between colliding bodies ($|\mathbf{F}_{ji}| \rightarrow \infty$ when $|\mathbf{r}_{ij}| \rightarrow 0$) yielding to an unbound error in the relative acceleration (ultraviolet divergence); ii) the need of the force summation over the whole set of distinct $N(N-1)/2$ pairs in the system implies an overwhelming CPU challenge for values of N of astrophysical interest over a sufficient number of time steps (infrared divergence), practically unaffordable even with most modern, fast CPUs (see Section 3.3).

- *A possible solution to ultraviolet divergence*

The ultraviolet divergence is often cured by mean of the introduction of a “softening” parameter, ϵ, in the interaction potential, which assumes the smoothed form

$$U_{ij} = G\frac{m_j}{\sqrt{|\mathbf{r}_{ij}|^2 + \epsilon^2}}. \tag{3.33}$$

The corresponding total force acting on the i^{th} particle is

$$\mathbf{F}_i \simeq Gm_i \sum_{j=1}^{N} \frac{m_j \mathbf{r}_{ij}}{(|\mathbf{r}_{ij}|^2 + \epsilon^2)^{3/2}}. \tag{3.34}$$

In the latter sum the condition $j \neq i$ is no longer needed, because, in its smoothed form, $\mathbf{F}_{ii} = 0$ if $\epsilon \neq 0$. Note that the introduction of the softening parameter corresponds to substitute point masses with Plummer’s spheres (Plummer, 1911), where the mass m_i is distributed around the centre according to the density law

$$\rho_i(r) = \frac{3m_i}{4\pi\epsilon^3}\frac{1}{(\epsilon^2 + r^2)^{5/2}}. \tag{3.35}$$

It is relevant recalling that, in any case, the chance of close encounters is larger for small values of N, when the “granularity”[2] of the system is more significant.

- *Possible solutions to infrared divergence*

---

[2] Granularity is the extent to which a system is broken down into small parts, either the system itself or its description or observation. It is the “extent” to which a larger entity is subdivided.

The infrared divergence is faced in many different ways (simplifying the interaction force calculation, reducing the number of times that the forces have to be evaluated, using a more powerful computer, if available, see Section 3.4). Force computation is a very expensive process because of the evaluation of the distance r_{ij} between the generic i and j particle. It requires the computation of a square root which, even on modern computers, is based on dated algorithms. The Newton-Raphson's method is one of the most famous among them and it is used to find the solutions of the quadratic equation $f(x) = x^2 - r_{ij}^2 = 0$. Given a starting value x_0 (the closer to the root, the better), a better approximation of the square root is given by $x_1 = x_0 - \frac{f(x_0)}{f'(x_0)}$. The process can be iterated until a sufficiently accurate value is reached:

$$x_{n+1} = x_n - \frac{f(x_n)}{f'(x_n)} = \frac{1}{2}\left(x_n + \frac{r_{ij}^2}{x_n}\right) .$$

The Newton-Raphson's method converges quadratically and so, near a root, the number of significant digits approximately doubles with each step. As a result, to calculate a square root, at least 20 flops are needed. Thus, as will be better shown in Subsection 4.2.1, the single pair force evaluation requires about 30 flops. This means that, if we call n_{flops} the number of flops performed in calculating the acceleration of each particle per time step in an N-body system, we have

$$n_{flops} = \frac{30}{2} N(N-1) .$$

One of the fastest CPU which can be found on the market nowadays is the Intel Core i7-980X Processor Extreme Edition which can reach a speed of nearly 100 GFLOPs[3]. A globular cluster, composed of $N = 10^6$ stars, needs at least 1000 steps per crossing time to be simulated. If we wanted a full view of system evolution, we should integrate over, at least, 5000 crossing times, so $k = 5 \times 10^6$ is the total number of the steps which will be performed and $f = k \times n_{flops}$ is the corresponding total number of flops. Thus, assuming a complete parallelization of the mutual forces evaluation and neglecting additional $O(N)$ computations, we can say, optimistically, that this processor could complete this simulation in

$$\Delta t \simeq \frac{f}{S \cdot 10^9} \simeq 7.5 \cdot 10^8 s \simeq 23.8\,\text{years} .$$

Clearly the task of following numerically the long term evolution of a large N-body system, using a program based on direct summation of pair forces, is very far out for the capability even of the most powerful computer.

The common line is introducing averaging (mean-field) methods, dividing the force acting on a particle (and due to the rest of the system) into a "large" scale, slowly varying, coarse-grain, contribution ($\mathbf{F}_{ls}$) and into a "small" scale, rapidly varying,

---

[3] In computing, FLOPs (or flops or flop/s, for floating-point operations per second) is a measure of a computer's performance, especially in fields of scientific calculations that make heavy use of floating-point calculations.

fine-grain, contribution, which is represented as a summation limited to a set of $n < N$ neighbouring particles, to give

$$\mathbf{F}_i \simeq G m_i \sum_{j=1}^{n} \frac{m_j \mathbf{r}_{ij}}{(|\mathbf{r}_{ij}|^2 + \epsilon^2)^{3/2}} + \mathbf{F}_{ls}(\mathbf{r}_i). \tag{3.36}$$

Usually, the direct summation is performed considering an individual value of n as that given by the number of “neighbour” stars, as those contained in a sphere of radius such to guarantee a sufficient resolution of the granular component of the field, while farther stars give the large scale force $\mathbf{F}_{ls}$ which can be evaluated in different ways. Most classical methods to evaluate $\mathbf{F}_{ls}$ include solution of Poisson’s equation on a grid (Hockney and Eastwood, 1988) or multipole expansion of the potential generated by stars outside the neighbouring sphere (Barnes and Hut, 1986). Section 3.4 will give more information about this methods. Of course, setting $n = N$ (which means that the neighbouring sphere contains all the system particles) makes the approximated expression above equal to the correct direct summation; in this case $\mathbf{F}_{ls}$ is contributed by an external force, only, and thus corresponds to $\mathbf{F}_{ext}$ in Equation (3.5).

Another way to reduce the computing time is to minimize the number of times that the forces have to be evaluated. Stellar systems are characterized by different time-scales, so, with this method, particles are advanced with just a time step proper to the individual acceleration felt, allowing a substantial speed up without introducing approximations. Thanks to this strategy, it is possible to take enormous advantages in simulating systems with some binary stars which must be followed by a time step smaller than the one required by the overall dynamics. Nevertheless, implementing an individual time step requires caution because a synchronous integration must be guaranteed and, often, this implies a reduction of precision of the integration method.

Moreover it’s possible to use faster machines (see Section 3.5). The use of a more powerful, parallel workstation is not so obvious as it seems. In fact, the parallelization of gravitational codes is a difficult task because gravity is such that the force on every particle depends on the position of all the others.

3.4 Numerical methods

In the following we present a small summary of the algorithms used in the numerical solution of the N-body problem.

3.4.1 Tree methods

Tree code method (Barnes and Hut, 1986) provides a fast, general integrator for collisionless systems, when close encounters are not important and where the force contributions from very distant particles does not need to be computed at very high accuracy. In a tree code, in fact, small scale and strong interaction are typically softened (McMillan and Aarseth, 1993), while the potential due to groups of distant particles is approximated by multipole expansions about the group centers of mass. The computation time for this kind of codes scales as $O(N \log N)$ but the approximation causes errors in the force evaluation. The error on the long-range force evaluation is controlled by only one parameter, the opening angle, which tells whether a group of particles is distant enough to apply the approximation. In this way it is possible to control and keep low the average error on the force, however unbound errors can arise for rare, but astrophysically reasonable configurations, such as that of the classic "exploding galaxy". Moreover the momentum conservation can be violated due to force errors in a tree code. Typical implementations of the tree code expand the potentials to quadrupole order and construct a tree hierarchy of particles using a recursive binary splitting algorithm. The tree does not need to be recomputed from scratch at every time-step, saving significant CPU time. Systems with several hundred thousands of collisionless particles can be easily simulated on a GFLOPs workstation for a Hubble time using this method.

3.4.2 Fast Multipole methods

A standard tree code implementation does not take into account the fact that a group of particles causes almost the same acceleration over close and distant particles. The Fast Multipole Method (FMM, Cheng *et al.* 1999) uses this observation and a multipole expansion to compute the force from a distant source cell within a sink cell. In such a way the computational weight decreases scaling as $O(N)$. This scaling is not exactly correct, and a wide debate on this result is present in literature (Dehnen, 2000). Fast multipole methods are characterized by symmetry in treatment of sink and source cells with respect to the multipole expansion can guarantee an exact conservation of the momentum.

3.4.3 Particle-mesh methods

Another way to speed up the force evaluation is given by the particle mesh method. Here we have a grid over which the gravitational potential of the system is built, starting from the density field and by solving the associated Poisson's equation. Particles do not interact directly between each other but only through a mean field. Essentially, in this method, the small scale interactions are softened if they are below the cell length. The density field is constructed using a kernel to split the mass of the particles to the grid cells around the particle position. The simplest choice is to assign all the mass to a single cell, but this leads to significant force fluctuations, which can be reduced using a cloud in cell (8 points) or a triangular shaped cloud (27 points) kernel. The Poisson equation is typically solved using a Fast Fourier Transform, but other grid methods such as successive over-relaxation can also be used (e.g. see Bodenheimer *et al.* 2007). The deriving force, defined on the grid, is then assigned back to the particles using the same kernel employed for the density field construction, in order to avoid spurious self forces. The complexity of the method is linear in the number of particles and scales as $O(N_g \log(N_g))$ in the number of grid cells (this latter scaling is that of the FFT method). The price to pay is in terms of short range accuracy as the force is a poor approximation of Newton's law up to several grid spacing of distance.

3.4.4 Adaptive Mesh Refinement method

The dynamic range of particle-mesh codes can be increased by using an adaptive rather than a static grid to solve the Poisson Equation. In the Adaptive Mesh Refinement (AMR) method the grid elements are concentrated where a higher resolution is needed, for example around the highest density regions. One possibility to obtain an adaptive resolution is to first construct a low-resolution solution of the Poisson Equation and then to progressively refine regions where the local truncation error (estimated through the Richardson extrapolation) is highest. A multigrid structure needs to take into account issues such as matching the solution at the grid interfaces. AMR codes are well suited for cosmological simulations (e.g. see the ENZO code, Bryan and Norman 1998).

3.4.5 Self consistent field methods

A variant over the Particle Mesh code is the expansion of the density and potential of the system in terms of a basis of orthogonal eigenfunctions. Clutton-Brock (1972) as one of the first to apply this idea in stellar dynamics, while a modern implementation is that of Hernquist and Ostriker (1992). This method guarantees at fixed computational resources a higher accuracy than the tree code and the particle mesh algorithms, provided that the set of basis function is appropriately selected. This limits in practice a general application of the method, which remains however very competitive for the study of the dynamical stability of collisionless systems constructed from distributions functions models.

3.4.6 P3M and PM-Tree methods

In order to increase the force resolution of particle mesh codes it has been proposed to couple a mean field description on large scales with a direct, softened, treatment of the gravitational interactions on distances of the order of or below a few grid spacing (Springel, 2005). This method is called P^3M: Particle-Particle-Particle-Mesh and efficiently increases the dynamic range of the parent PM algorithm. However in presence of strong clustering a large number of particles will interact directly between each other, slowing down significantly the computation to $O(N^2)$. This problem can be resolved by using adaptive meshes, so that the spatial resolution is refined in regions of high density. Adaptive P^3M codes have a computational cost which scales as $O(N \log N)$, like in a tree code. Finally another possibility is to resort to a tree code for the short range force evaluation leading to a hybrid PM-Tree scheme. These methods are generally extremely well suited for cosmological simulations, and one of the most used codes, Gadget2 (Springel, 2005), is based on it.

3.4.6.1 Direct N-body calculations and time integration

The last class of methods we introduce are the ones we will use in our work: the direct methods. Direct methods do not introduce approximations in the solution of the equations of motion and thus deliver the highest accuracy at the price of the longest computation time, of order $O(N^2)$ per timestep. The only choice is possible to make is the one regarding the time integration. If we choose a "standard" integration method (like, for example, an high order Runge-Kutta method, or the simple and fast, but not so accurate, Euler's explicit method, etc.) we will obtain, for long time integrations, a slower or faster growth of the energy error. This error is produced almost exclusively in close encounters where the problem becomes *stiff*. A problem is said to be stiff when some of the involved quantities (like, in our case, positions, velocities and accelerations) change their values too fast, making the numerical solution stable only when the time integration steps are extremely small. Introducing the softening parameter, we avoid this behavior caused by ultra-violet divergence but this is not enough to solve the main problem. The real issue is the integration method, in fact, standard integrators become dissipative and exhibit incorrect long term behavior because these "classical" schemes perform, step by step, non-canonical transformations (from (x_n, y_n) to (x_{n+1}, y_{n+1})) yielding to a conserved quantity different from the known expression, for example, of the total system energy. This issue can be partially removed using symplectic integrators which will be described in the next Section.

3.4.7 From Hamiltonian dynamics to symplectic integrators

A *canonical transformation* is a transformation which preserves the Hamiltonian form of dynamics. This means that, performing a coordinate change from (u, v) to (x, y), we will have

$$H(u,v) = K(x,y) = K[x(u,v), y(u,v)]$$

where H and K are, respectively, the old and the new expression of the Hamiltonian function of the system. We have to underline that an *Hamiltonian system* is a dynamic system, having n degrees of freedom, defined by an *Hamiltonian function* (H) which satisfies the so called *canonical equations*

$$\begin{aligned} \dot{p}_k &= - \frac{\partial H}{\partial q_k} \\ \dot{q}_k &= \frac{\partial H}{\partial p_k} \end{aligned} \tag{3.37}$$

where q_k is the k^{th} generalized coordinate and p_k is its momentum conjugate. This system, of $2n$ first-order differential equations, can be written in a form, known as *symplectic*, through the matrix formalism, defining the column vectors $\mathbf{z}$ and $\partial H/\partial \mathbf{z}$, both of them having $2n$ components, and a $2n \times 2n$ square matrix $\mathbf{J}$ such that

$$z_i = q_i, \qquad z_{i+n} = p_i$$

$$\left(\frac{\partial H}{\partial \mathbf{z}}\right)_i = \frac{\partial H}{\partial q_i}, \qquad \left(\frac{\partial H}{\partial \mathbf{z}}\right)_{i+n} = \frac{\partial H}{\partial p_i}$$

$$\mathbf{J} = \begin{pmatrix} \mathbf{0} & \mathbf{1} \\ -\mathbf{1} & \mathbf{0} \end{pmatrix}$$

where $i = (1, 2, ..., n)$, $\mathbf{0}$ is the $n \times n$ matrix composed of vanishing elements and $\mathbf{1}$ is the $n \times n$ identity matrix. Using these new entries, we can write the system of Equations (3.37) in a more compact form

$$\dot{\mathbf{z}} = \mathbf{J}\frac{\partial H}{\partial \mathbf{z}} \ .$$

It can be shown that *the necessary and sufficient condition for a transformation* $(q, p) \rightarrow (Q, P)$ *to be canonical is that the Jacobian matrix of the transformation* $(\mathbf{\Lambda})$ *is symplectic*

$$\mathbf{\Lambda}^T \mathbf{J} \mathbf{\Lambda} = \mathbf{J} \tag{3.38}$$

where

$$\mathbf{\Lambda} \equiv \frac{\partial\,(Q, P)}{\partial\,(q, p)} \ .$$

Consider, for example, the simplest and very fast integration method, known as Euler's explicit method. For simplicity we will refer to a one-degree-of-freedom system and so we may write

$$\begin{aligned} q_{n+1} &= q_n + p_n \mathrm{d}t \\ p_{n+1} &= p_n + f(q_n; t_n)\mathrm{d}t \end{aligned} \tag{3.39}$$

where n indicates the n^{th} integration step and $f(q_n; t_n) = \dot{p}_n = -\partial H/\partial q_n$. From Equation (3.39) we have

$$\Lambda = \begin{pmatrix} \frac{\partial q_{n+1}}{\partial q_n} & \frac{\partial q_{n+1}}{\partial p_n} \\ \frac{\partial p_{n+1}}{\partial q_n} & \frac{\partial p_{n+1}}{\partial p_n} \end{pmatrix} = \begin{pmatrix} 1 & \mathrm{d}t \\ \frac{\partial f}{\partial q_n}\mathrm{d}t & 1 \end{pmatrix} = \begin{pmatrix} 1 & \mathrm{d}t \\ \nabla_q f(q_n)\mathrm{d}t & 1 \end{pmatrix}$$

where it has been set $\partial/\partial q_n = \nabla_q$. Since this is a one dimensional problem, from Equation (3.38) we argue that the necessary and sufficient condition for the matrix Λ to be symplectic is that $\det(\Lambda) = 1$. In our case we have

$$\det(\Lambda) = 1 - \nabla_q f(q_n)\mathrm{d}t^2 = 1 \Rightarrow f(q_n) = \text{constant}$$

but, obviously, this does not happen for a generic N-body system, where $f(q_n; t_n)$ is the gravitational acceleration. So, Euler's explicit method is not symplectic.

It is well known that ordinary numerical methods for integrating Newtonian equations of motions become dissipative and exhibit incorrect long term behaviour (see, e.g., Menyuk 1984, MacKay 1990, Cartwright and Piro 1992). This is a serious problem particularly when studying the evolution of systems over long time periods. Here we show how this issue can be partially solved introducing symplectic methods. Symplectic integrators can be constructed thanks to Hamiltonian splitting. It can be verified that, if $H = H_1 + H_2 + ... + H_k$, then we may construct, at least, a first-order symplectic method by mean of the composition of k coordinate changes. For example, if we consider a typical Hamiltonian function given by

$$H(\mathbf{q}, \mathbf{p}) = K(\mathbf{p}) + U(\mathbf{q}) \ ,$$

where K can be considered the kinetic part of H and U is the potential part, the canonical Equations (3.37) corresponding to $H_1 = K$ are

$$\begin{aligned} \dot{\mathbf{q}} &= \nabla_{\mathbf{p}} K(\mathbf{p}) \\ \dot{\mathbf{p}} &= \mathbf{0} \end{aligned} \qquad (3.40)$$

while, the others are

$$\begin{aligned} \dot{\mathbf{q}} &= \mathbf{0} \\ \dot{\mathbf{p}} &= -\nabla_{\mathbf{q}} U(\mathbf{q}) \, . \end{aligned} \qquad (3.41)$$

Integrating Equations (3.41) and applying the resultant transformation to a generic point of phase space $(\mathbf{q}_n, \mathbf{p}_n)$ we obtain another point $(\widehat{\mathbf{q}}, \widehat{\mathbf{p}})$ such that

$$\begin{aligned} \widehat{\mathbf{q}} &= \mathbf{q}_n \\ \widehat{\mathbf{p}} &= \mathbf{p}_n - \nabla_{\mathbf{q}} U(\mathbf{q}_n) \Delta t \, . \end{aligned} \qquad (3.42)$$

Now, integrating Equations (3.40) and applying the transformation to the point $(\widehat{\mathbf{q}}, \widehat{\mathbf{p}})$ we obtain

$$\begin{aligned} \mathbf{q}_{n+1} &= \widehat{\mathbf{q}} + \nabla_{\mathbf{p}} K(\mathbf{p}_{n+1}) \Delta t \\ \mathbf{p}_{n+1} &= \widehat{\mathbf{p}} \, . \end{aligned} \qquad (3.43)$$

Thus, eliminating $(\widehat{\mathbf{q}}, \widehat{\mathbf{p}})$ from Equation (3.42) and Equation (3.43) we may write

$$\begin{aligned} \mathbf{q}_{n+1} &= \mathbf{q}_n + \nabla_{\mathbf{p}} K(\mathbf{p}_{n+1}) \Delta t \\ \mathbf{p}_{n+1} &= \mathbf{p}_n - \nabla_{\mathbf{q}} U(\mathbf{q}_n) \Delta t \, . \end{aligned} \qquad (3.44)$$

This is a first-order symplectic method known as Euler's symplectic method. The construction of higher order symplectic methods is a hard task. Standard numerical integration schemes neglect relevant features of the dynamics of Hamiltonian systems, like that the time-Δt map of phase space is symplectic, i.e. the evolution of points in the phase space from 0 to t preserves the Poincaré invariants (Abraham and Mardsen 1978). It is possible to see that a consequence is the Liouville's theorem: phase-space volume is preserved. Moreover, symplecticity places much stronger conditions on the global geometry of the dynamics in the phase space than Liouville's theorem; standard numerical integration schemes do not respect these restrictions even if energy conservation is a priori implied. Consequently, reliability of numerical integration schemes is limited to a narrow time extension above which there is no guarantee they keep global properties implied by the Hamiltonian nature of the dynamical system. Standard integration techniques are worthily used in the analysis of short-time quantitative phenomena but not suited to investigate properties on a long-time scale. In other words, secular variations of Hamiltonian dynamical system parameters cannot be reliably foreseen by non-symplectic integrators. In particular, the local truncation error grows secularly in non-symplectic integrations, while it is kept bound by symplectic schemes provided the use of a small time step (Yoshida 1990). Symplectic algorithms suffer much less indeed of the numerical dissipation induced by round off error in standard numerical integrators, even if also symplectic schemes are not exactly time-reversible as exact Hamiltonian systems are. This is due to that symplectic integrators do not conserve the original Hamiltonian but just a numerical, discrete variation of the original Hamiltonian. This means that also symplectic integrations may have problems in following the evolution of chaotic systems, although these problems are much smaller than with non symplectic methods.

3.5 Hardware solutions for the direct summation method

Due to the unavoidable, hard, step of direct summation of the gravitational force to keep the error to round-off level alone, one cannot expect order of magnitude earning in computational time just by algorithm and software improvements. As stated above, the fundamental bottleneck is, indeed, the evaluation of the euclidean distance between the generic pair of stars of the system, which is an irrational operation, intrinsically slow for any standard CPU. Another, time related, bottleneck is the possible presence of binaries which must be followed by a time step order of magnitudes less than the one required by the overall dynamics. A good analysis of these, and others, bottlenecks in simulations of dense stellar systems is found in Makino and Hut (1990). In this frame, it is not obvious to decide what is the best choice between a general purpose large computational main frame and a dedicated, special purpose, machine. The advantages of a parallel main frame are quite evident: power, large storage capacity, specialized staff dedicated to maintenance. The disadvantages are clear, too: low flexibility, difficulty in the access to a, usually, remote site with connected complications in large data transfer. To avoid part of these problems, and having in mind that the main bottleneck is, as said before, the pair-wise force computation by mean of the mutual distance evaluation, at the end of years 80's Sugimoto, Hut and Makino started a project at Tokyo University to build specialized hardware for stellar dynamics calculations, the well known GRAPE project. GRAPE boards were characterized by an efficient hardware implementation of Newtonian forces between particles in an N-body system which are computed at a speed greatly in excess of a general purpose computer. The board can, thus, be used as a computational booster, a gravity accelerator indeed, in conjunction with a normal host workstation. GRAPE-1 was the first in a series of such specialized boards working at low precision, while GRAPE-2, GRAPE-4 and GRAPE-6 use floating point arithmetics for more accurate calculation. The most recent in these series of boards is GRAPE-6, with a peak performance of 1 TFlops. At the beginning of years 2000 the cost of a single GRAPE-6 board allowed a 1 TFlops peak performance for a cost one or two order of magnitude lower than commercial products working at same speed. The use of these boards allowed direct simulations of systems of the size of 10^5 bodies, i.e. a factor of ten less than the real number of stars in a globular cluster. The "one million body problem", discussed in the Heggie and Hut (2003) book was, so, very near to be numerically approached without excessive simplifications. We will not speak here much about the introduction and use of the Field Programmable Gate Arrays (FPGAs) accelerators (see, anyway, an interesting discussion of its application to the N-body problem in Lienhart and Männer 2002), which have the advantage to be highly customizable, but do not have the same massive parallel execution resources and high memory bandwidth of the last generation Graphic Processing Units (GPUs). Another, cheaper approach to high speed computing is that through the modern GPUs, formally dedicated to the acceleration of graphic tasks on personal computers but which are actual "supercomputers" when inserted in a host governed by a certain number of standard processors. Graphics chips started as fixed function graphics pipelines. Over the years, these graphics chips became increasingly programmable, which led NVIDIA to introduce the first Graphics Processing Unit. In the 1999-2000 timeframe, computer scientists in particular, along with researchers in fields such as medical imaging and electromagnetics started using GPUs for running general purpose computational applications. They found the excellent floating point performance in GPUs led to a huge performance boost for a range of scientific applications. This was the advent of the movement called GPGPU or General Purpose computing on GPUs. The problem was that GPGPU required using graphics programming languages like OpenGL and C to program the GPU. Developers had to make their scientific applications look like graphics applications and map them into problems that drew triangles and polygons. This limited the accessibility of tremendous performance of GPUs for science. NVIDIA realized the potential to bring this performance to the larger scientific community and decided to invest in modifying the GPU to make it fully programmable for scientific applications and added support for high-level languages like C and C++. This led to the CUDA general purpose parallel computing architecture for the GPU. CUDA is a computing architecture developed by NVIDIA that extends C by allowing the programmer to define C functions, called kernels, that, when called, are executed n times in parallel by n different CUDA threads. CUDA programming language is basically a C programming language extended with a number of keywords. CUDA threads

System	Open cluster	Glob. clus., gal. nucleus	Galaxy, clus. of gal.
N	$< 10,000$	$10^5 \div 10^9$	$> 10^{10}$
Gravity	Newtonian	Newtonian, gen. rel.	Newtonian,gen. rel.
Time scale ord.	$t_{rel} < t_{cr} < t$	$t_{cr} << t_{rel} < t$	$t_{cr} << t < t_{rel}$
Regime	Collisional	Secularly collisional	Collisionless
Technique	gas+direct N-body	F-P,direct N-body,tree-c.	tree-c.,PM,P3M

Table 3.1. Stellar systems time scales and other relevant characteristics to the types of simulations needed.The age of the system is t. In the last row F-P means Fokker-Planck method, tree-c. means tree-based codes, PM and P3M stand for Particle-Particle and Particle-Particle-Particle-Mesh algorithms, respectively.

may execute on a physically separate device that operates as a coprocessor to the host running the C program.

Regarding to specific applications for physics, it is worth cited what done by Ageia technologies that in early 2006 launched the PhysX "physics processing unit" (PPU), a PCI card with a custom parallel-processing chip tweaked for physics computations. Game developers could use Ageia's matching application programming interface to offload physics simulations to the PPU, enabling not only lower CPU utilization, but also more intensive physics simulations with many more objects. The PhysX card itself looked like a video card, having the same structure, but was actually thought for number crunching and for driving a display. The PhysX custom designed physics processor packed 125 million transistors into a 14 mm by 14 mm space. For various reasons, PhysX did not meet great success. In spite of this Ageia was purchased by NVIDIA corp. in 2008 with the idea to add PhysX support to GeForce 8-series graphics.

The scheme of GPU computing is similar to that of GRAPE: a heterogenous computing model where the CPUs exploit a part of the application in a sequential, or parallel, mode while the computationally-intensive part of the code runs on the GPU. A code previously working on a multicore CPU just needs to extract its most computationally expensive kernels and map them to the GPU. Mapping a function to the GPU requires rewriting the function exposing its parallelisms and adding "C" keywords to move data to and from the GPU. As primary examples of applications of GPU computing we mention (see Owens *et al.* 2008) game physics, computational biophysics, large-scale molecular dynamics, as well as astrophysics.

In the next chapter we will see more in detail how it is possible to exploit the GPUs, describing different versions a new code apt to run on such devices and that exploit the high reliability of direct methods coupled to symplectic integration algorithms (see Section 3.4.7).

As a conclusion of this chapter a summary of the information on various gravitating aggregates are resumed in Table 3.1 (Capuzzo-Dolcetta, 2005) along with the numerical technique apt to their numerical study.

Chapter 4

NBSymple, a double parallel, symplectic N-body code running on Graphic Processing Units

To face the N-body problem and to study the dynamics of stellar systems in a more direct and efficient way we developed an innovative, fast and reliable code. Here, we present and discuss its characteristics and performances, both in term of computational speed and precision. This code which integrates the equation of motions of N "particles" interacting via Newtonian gravitation and moving in an external galactic smooth field. The force evaluation on every particle is done by mean of direct summation of the contribution of all the other system's particles, avoiding truncation errors (see Section 3.3). The time integration is done with second-order and sixth-order symplectic schemes. The code, NBSymple, has been parallelized twice, by mean of the Compute Unified Device Architecture (CUDA, see Section 3.5) to make the all-pair force evaluation as fast as possible on high-performance Graphic Processing Units NVIDIA TESLA C1060, while the $O(N)$ computations are distributed on various CPUs by mean of OpenMP Application Program. The code works both in single-precision floating point arithmetics or in double precision. The use of single-precision allows the use of the GPU performance at best but, of course, limits the precision of a simulation in some critical situations. We find a good compromise in using a software reconstruction of double-precision for those variables that are most critical for the overall precision of the code. The code is available on the web site `astrowww.phys.uniroma1.it/dolcetta/nbsymple.html` and it is widely described in Capuzzo-Dolcetta, Mastrobuono-Battisti, and Maschietti (2011a).

4.1 The N-body code

As described in the previous Chapter, the study of the dynamical evolution of stellar systems in an external field, is a topic of great interest. As we have already explained, the external field is relevant in the evolution of a self-gravitating system, inducing tidal effects which are effective, for instance, in accelerating the two-body processes within the system. A reliable interpretation of the structure and phenomenology of stellar clusters cannot, thus, be done as if they were in isolation. Our aim is to study the evolution of star clusters in our Galaxy as N-body systems where an external galactic gravitational field, represented as an analytical expression, is summed to the mutual interaction among all the stars of the cluster. The code that we wrote and that is going to be described is characterized by high precision and speed and it is able to study the evolution of gravitational N-body systems, and can be applied to the study of systems composed by a number of objects up to few millions, covering the astrophysical range from planetary systems ($N \leq 10$) to stellar systems of the size of open clusters and globular clusters ($N \simeq 10^6$).

For what regards precision, we approached the problem resorting to (i) direct summation (to avoid truncation error in force evaluation), that is setting $n = N$ in Equation (3.36), and to (ii) the use of high order, symplectic time integration methods (see Section 3.4.7). Speed, at a reduced cost, has been attained implementing direct summation codes on a hybrid architecture where multi core CPUs are linked to GPUs acting as computational accelerators (see Section 3.5). The reliability is due to the choice of simplicity in the implementation technique, like, for instance, the use of a constant time step, δt, instead of more sophisticated techniques. It should not be forget, indeed, that a formally correct estimate of the time integration truncation error requires constant time stepping.

In the following we resume how our code works. It generates, first, the initial conditions for the N particles of the system, whose individual masses are chosen by a given mass spectrum. For the scope of this work, which aims, mainly, at investigating the code quality and performances in different hardware and software environments, we gave, for the sake of simplicity, all the particles the same mass $m_i = m$ ($i = 1, 2, .., N$) (as mass unit we use the total mass, M, of the system, i.e. $M = Nm$). For the same purpose of simplicity we give particles an initial spatially uniform distribution within a sphere of given radius, R, that is assumed as length unit, with velocities, also, uniformly distributed in direction and absolute values and rescaled, in their magnitude, to reproduce a given value of the virial ratio (we remind that the virial ratio is defined as $Q = 2K/|\Omega|$, where K and Ω are, respectively, the system kinetic and potential energies; for a stationary system, $Q = 1$). Note that the further assumption $G = 1$ in the equations of motion implies that the crossing time $T = (GM)^{-1/2}R^{3/2}$ is the unit of time. The forces due to the mutual interaction among stars in the cluster (internal forces) are given by Equation (3.34) and the external force is then added. In our tests we used a softening parameter $\epsilon = 0.005(R/N^{1/3})$, where $R/N^{1/3}$ is a measure of the average distance of a particle of the N-body system to its closest neighbour. For the external force, we use the analytic expression for the Galactic potential as given by Allen and Santillan (1991). In this paper the authors consider the Galactic potential as given by three components: a bulge, a disk, and a halo. The bulge and the halo have a spherical symmetry, while the disk is axisymmetric (see Section 6.2.2 for more details). As seen in Section 3.4.7 symplectic method are a good choice if we want to perform high precision simulations, so we directed our attention towards these methods to introduce theme in the code. The choice of symplectic methods is wide, for it is possible the construction of high order integrators (Yoshida, 1991). Our code allows the choice of two different symplectic methods. One is the simple, classic, "leapfrog" method, which is 2^{nd}-order accurate; the other is a more accurate 6^{th}-order explicit scheme whose coefficients are taken from the first column of the Table 1 (SI6A) of Kinoshita *et al.* (1991), which leads to a conservation of energy for a factor fifty better than that with the other two possible sets of coefficients. Of course, the 6^{th}-order symplectic integrator is much slower than the leapfrog, requiring 7 evaluations of force functions per time step, like, for instance, in a 6^{th}-order Runge Kutta method.

Its important to stress that any kind of generalization to different sets of initial conditions and external potentials is easy done by mean of appropriate external subroutines provided by the user.

4.2 Implementation of the code

4.2.1 Hardware and software

As we have already described and discussed, the direct evaluation of the pair-wise forces in an N-body system is a computationally challenging task, mainly because of the computation of the $N(N-1)/2$ distinct elements of the $|\mathbf{r}_{ij}|$ (Euclidean distance) array. Each computation requires the evaluation of a square root, which is an expensive task (see Section 3.3). Actually, every pair force vector, $\mathbf{F}_{ij}$, requires between 20 and 30 floating point operations. The calculation of the three components of the acceleration induced on the generic i particle by another generic j particle requires the $|\mathbf{r}_{ij}|$ calculation, that means 3 differences, 2 sums, 4 products and 1, heavy, square root evaluation, which implies, normally, one Newton-Raphson iteration (in single precision) rising to two or three in double precision, see Section 3.3. The total number of operations required for the complete evaluation of the vector acceleration of the two particles in a pair is so: 2 sums, 3 differences, 11 products plus the square root evaluation and 3 changes of sign which correspond to the $\mathbf{F}_{ij} = -\mathbf{F}_{ji}$ relation. To this computational load, various memory storing and transfer are necessarily added, which do not constitute, however, a significant fraction of the total time spent. All this must be done $N(N-1)/2$ times at every time step. Consequently, the time integrations of N-body systems, when extended over a time interval large enough to have a scientific relevance, overwhelm the power

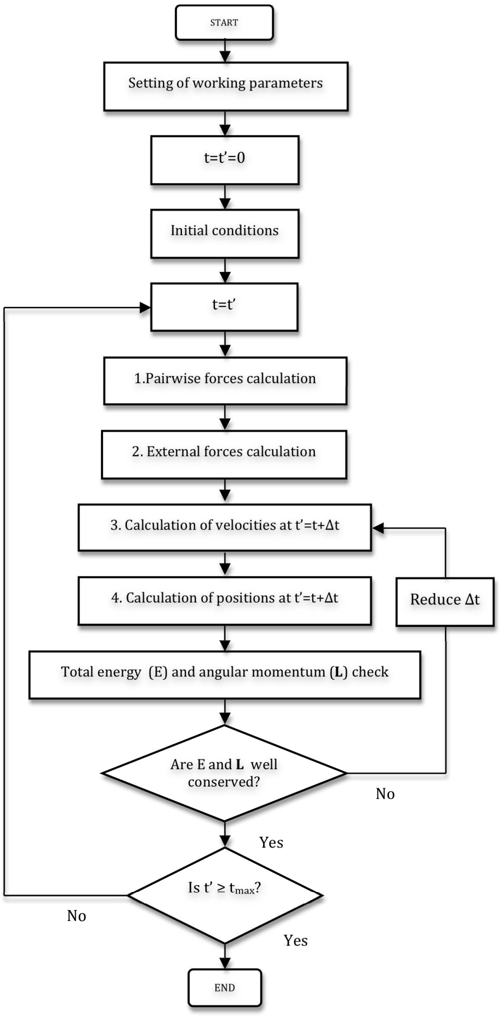

Figure 4.1. Flowchart of our basic code

of every single CPU platform for N above few thousands (see Section 3.3.1). If one wants to keep direct summation, without relying on approximations like, for instance, mean-field techniques, the only possibility is resorting on parallel computing and/or dedicated machines (like GRAPE, for instance, as explained in Section 3.4).

It is out of the purposes of this work the discussion of parallelization of N-body codes on large main frames, which is not a trivial task, due to the slow decay with distance of the gravitational interaction. Here we deal with the problem of implementing an efficient N-body integrator on a hybrid CPU+GPU platform. A typical architecture of such machines consists of a multicore CPU based server, usually under LINUX, connected through PCI express ports to one or more multithread (hundreds) GPU boards acting as computational accelerators.

Some authors have already faced the problem of implementing gravitational N-body integrations on GPUs with different approaches (Barsdell *et al.*, 2010; Belleman *et al.*, 2008; Elsen *et al.*, 2006; Hamada and Iitaka, 2007; Portegies Zwart *et al.*, 2007). Some of these earlier works were limited by the lack of double precision support in GPU hardware, while now DP is supported in NVIDIA TESLA C1060, and will be much faster in TESLA based on the Fermi technology.

Here we explain how we get our own implementation, leading to a code, which we call NBSymple (acronym for NBody Symplectic integrator). Various versions of the same basic code have been realized.
The first is fully serial (NBSympleA), i.e. it runs on a single processor. This serial version of the code constitutes the basic structure for all our other versions; this required its optimization, by minimizing the number of floating point operations needed to evaluate the pair interaction force and exploiting the anti-symmetry of the force array. This code constitutes a “unit of measure” of the performances of the various parallel versions.

In a second version of the code (NBSympleB) we implemented parallelization with Open Multi-Processing (OpenMP, in the following also referred to as OMP) directives of both the $O(N^2)$ pair-wise interactions and the $O(N)$ calculations (i.e. the time integration and evaluation of the Galactic component of the force on the system stars) over the multicore CPU host.

OpenMP (see `http://openmp.org/wp/about-openmp/`) is a portable, scalable model that allows easy C/C++ and Fortran programming on shared-memory parallel platforms from various vendors and from the portable computer to the large main frame. As already said in Chapter 4, it consists of a set of compiler directives, library routines, and environment variables that influence run-time behavior.
In the third version (NBSympleC) the all-pairs interactions ($O(N^2)$ calculations) are demanded to the GPU (here an NVIDIA TESLA C1060), using Compute Unified Device Architecture (CUDA, see `http://www.nvidia.com/object/cuda_home.html` and Section 3.5) while all the remaining tasks are done by a single CPU.
In another (fourth) version of the program (NBSympleD) we again use CUDA to evaluate the $O(N^2)$ portion of the code (like in NBSympleC), while the $O(N)$ computations (time integration and evaluation of the acceleration due to the Galaxy) are parallelized sharing work between all the cores of the host (8 in our hybrid platform), using OpenMP in the same way done in NBSympleB.
The last (fifth) implementation (NBSympleEk, k=1,2) uses CUDA on one or two GPUs to evaluate the total force over the system stars, i.e. both the all-pairs component and that due to the Galaxy. In NBSympleEk, the O(N) computations were shared into an OMP part (time integration) and into a GPU part (smooth galactic force contribution) to maximize the efficiency.
Table 4.1 summarizes the above (main) characteristics of the various versions of the code.

The platform we used is made by a 2 Quad Core Intel Xeon 2.00GHz workstation

Version	**Time integ., O(N)**	**Pair-wise, O(N^2)**	**External, O(N)**
NBSympleA	1 CPU	1 CPU	1 CPU
NBSympleB	8 CPUs (OMP)	8 CPUs (OMP)	8 CPUs (OMP)
NBSympleC	1 CPU	1 GPU	1 CPU
NBSympleD	8 CPUs (OMP)	1 GPU	8 CPUs (OMP)
NBSympleE1	8 CPUs (OMP)	1 GPU	1 GPU
NBSympleE2	8 CPUs (OMP)	2 GPUs	2 GPUs

Table 4.1. Synoptic table summarizing the distribution of the main tasks (time integration, pair-wise force evaluation, external force evaluation) of the various versions of the NBSymple code to the CPUs and GPUs of the hybrid machine.

and two GPUs NVIDIA TESLA C1060, connected to the host via slots PCI-E 16x. NVIDIA TESLA C1060 supports both single-precision (SP, 32-bit) and double-precision (DP, 64-bit) floating point arithmetic. At present, each of the processing units in the TESLA C1060 contains one DP processor alongside the 8 SP processors; the TESLA C1060 GPU has 240 threads, meaning that 30 threads are at work when fully exploiting DP calculations.
A basic version of the NBSymple code, along with instructions on how to use it, is available at `http://astrowww.phys.uniroma1.it/dolcetta/nbsymple.html`.

4.2.2 The code structure

The N-body integration scheme consists of two main parts. In the first one, given positions and velocities of all the N bodies, the forces between stars and those due to the overall, smooth, Galaxy distribution are evaluated. Consequently, in the second part, the code predicts the velocities and positions of the particles by mean of the previously calculated accelerations (see flow-chart in Figure 4.1).
In all of the five implementations of the code the advancing in time of velocities and positions of stars of the system is performed by the CPUs. This choice is motivated by that time advancing is more sensitive to round-off errors and the time needed for its computation grows only linearly with N making convenient using the double precision representation available on the CPUs. Actually, TESLA C1060 supports double-precision floating point arithmetics, but in this case performances decay significantly with respect to using single precision. Another problem is due to the bandwidth available for the data exchange between GPUs and CPUs. Performing time integration on GPUs would require sending and receiving a huge amount of data from GPUs to CPUs, thing that could imply a significant decay of performance.

We verified that the time required to transfer data from the CPU to the GPU and viceversa is never negligible, even in the case of bigger N. We found this by comparing the time required by NBSympleE1 to evaluate the acceleration of the whole system of N bodies, by mean of data transfer from CPU to GPU, GPU

N	t_1	t_2
480	0.019	0.016
960	0.021	0.017
1920	0.028	0.018
3840	0.030	0.025
7680	0.036	0.027
15,360	0.055	0.023

Table 4.2. Time (in sec) spent by the original NBSympleE1 code (t_1) and by the same code performing only the data exchange to and from the GPU (t_2).

computation and data transfer back to the CPU, with the time required by the same code when the force calculation section is switched off, leaving, in this case, only the bidirectional data transfer between the host and the device. The results are shown in Table 4.2.

Before we invoke the kernel we copy the positions of the N particles on the GPU's global memory; the accelerations are calculated on the GPU device and then sent to the CPU memory. The kernel and device functions used to evaluate the forces are very similar to those described in Nyland *et al.* (2007), with some important modifications, as indicated later in this Subsection. In this latter paper the authors introduced the notion of a "computation tile", as a squared $p \times p$ sub-array of the $|\mathbf{F}_{ij}|$, $N \times N$, force array. To calculate p^2 interactions we need the knowledge of the positions of $2p$ bodies (for details see Nyland *et al.* 2007). These "body descriptions" are stored in the shared memory, which has little reading latency (4 clock cycles) respect to global memory (400-600 clock cycles). To achieve optimal reuse of data, the computation of a tile is arranged in a way that the interactions in each row are evaluated in sequential order (updating the acceleration vector), whilst the various rows are evaluated in parallel.

The interaction between a pair of bodies is implemented as an entirely serial computation. A tile is evaluated by p threads performing the same sequence of operations on different data. Each thread updates the acceleration on one body as a result of its interaction with p other bodies. They load p body descriptions from the GPU device memory into the shared memory provided to each thread block in the CUDA model. Each thread in the block evaluates p successive interactions. The results of the tile calculation are the p updated accelerations.

A thread block is defined as a collection of p threads that execute some number of tiles in sequence. In a thread block, there are N/p tiles, with p threads computing the forces on p bodies (one thread per body). Each thread computes all the N interactions for one body.

The kernel is invoked on a grid of thread blocks to compute the acceleration of all the N bodies. Because there are p threads per block and one thread per body, the number of thread blocks needed to complete all N bodies is N/p, so we have a $1D$ grid of size N/p. The result is a total of N threads that perform N force calculations each, for a total of N^2 interactions.

The number of calculations performed by the device is N^2, which is redundant respect to the actual number of distinct pairs in the system, $N(N-1)/2$. By the way, the limitation to $N(N-1)/2$ of the number of force evaluations would require a heavier load of internal communication and synchronizations (Belleman *et al.* 2008), with a resulting net performance decrease.

The dimension of the tile and the number of thread blocks depend on the number of particles involved in the simulation. There are 30 multiprocessors on the NVIDIA TESLA C1060, so the block dimension (p) must be such that N/p is 30 or larger to use all the multiprocessors available. We stress that we used the general scheme proposed by Nyland *et al.* (2007), adapting it to our double-parallel environment, scaling the dimension of the block and of the grid in order to exploit the power of GPUs as much as possible. Moreover, we introduced a new device function that allows the calculation of the external forces directly on the GPUs and we modified the kernel in order to use double precision arithmetics. Memory usage was optimized as inNyland *et al.* (2007), trying to use at most shared memory, which has low latency and so allows highest efficiency in calculations. We underline that the code is such that it is sufficient to resize the block dimension to exploit at best the characteristics of the specific GPUs available, according to the number of "particles" used in the computation. In Section 4.5, we will show some benchmarks of the code, displaying its almost perfect scalability, on a different kind of GPUs.

The entire part of the program that performs the time integration of the system is enclosed in a parallel section, through OpenMP directives. We shared work among all the CPUs available declaring variables in an appropriate way, and using properly the OpenMP directives to parallelize the various 'for-cycles ' that perform the time integration and the computation of the galactic contribution to the accelerations (both scaling as N). The copy of the data from and to the GPU and the kernel are invoked by the master thread.

As we said above, our GPUs allow us the use of DP floating point representation. To reduce the bandwidth needed to transfer data between CPUs and GPUs we constructed C structures of four DP variables, emulating CUDA's float4. As we see in the next Section the performances of the program decrease a lot. On the other side, using the 6^{th} order integrator we reach a precision 7 or 8 orders of magnitude better than that reached with single-precision arithmetics.

Finally, we say how the computation load is shared over GPUs, when more than one is available (NBSympleEk).

Through OpenMP directives we created k threads. Each thread communicates with one of the device and copies the positions of all the particles on its global memory. Moreover each of the k threads, launches a kernel on one of the k available devices. So we have k kernels, each of which calculates the accelerations for N/k particles (in our case $k = 1$ or 2). After this calculation, the instanced thread copies the results on the host and the number of threads is reset to 8 to continue the time integration.

t	$\langle\lvert\frac{\Delta E}{E_0}\rvert\rangle$	$\langle\lvert\frac{\Delta L_x}{L_0}\rvert\rangle$	$\langle\lvert\frac{\Delta L_y}{L_0}\rvert\rangle$	$\langle\lvert\frac{\Delta L_z}{L_0}\rvert\rangle$
0.5	2.63×10^{-15}	2.27×10^{-9}	2.32×10^{-9}	1.41×10^{-16}
1.0	6.26×10^{-15}	4.43×10^{-9}	3.00×10^{-9}	9.90×10^{-16}
1.5	2.42×10^{-14}	4.91×10^{-9}	2.42×10^{-9}	1.27×10^{-15}
2.0	2.87×10^{-14}	6.74×10^{-9}	1.87×10^{-9}	1.70×10^{-15}
2.5	2.67×10^{-14}	1.26×10^{-8}	5.42×10^{-10}	1.41×10^{-15}
3.0	2.67×10^{-14}	2.36×10^{-8}	2.44×10^{-9}	1.41×10^{-16}
3.5	2.48×10^{-14}	3.94×10^{-8}	7.70×10^{-9}	2.55×10^{-15}
4.0	3.13×10^{-14}	5.78×10^{-8}	1.78×10^{-8}	7.07×10^{-16}
4.5	2.12×10^{-14}	7.52×10^{-8}	3.34×10^{-8}	1.27×10^{-15}
5.0	2.77×10^{-14}	8.86×10^{-8}	5.45×10^{-8}	5.37×10^{-15}

Table 4.3. Relative variations in energy and angular momentum as function of time in the time interval [0,5], which corresponds to about 1/10 orbital revolution around the galactic center. The symplectic 6^{th} order method is used in double-precision mode.

N	480	30,720	1,536,000	
NBSympleC	5.97	409	423	SP
”	3.36	21.9	22.0	DP
NBSympleE2	11.29	797	846	SP
”	3.37	43.8	44.0	DP

Table 4.4. Performances in GFLOPs of two versions of the NBSymple code (C and E2) with the leapfrog time integrator, using the single (SP) and double (DP) precision (last column). Remember that NBSympleE2 exploits the power of two TESLA C1060 GPUs.

4.3 Results

4.3.1 Performances and accuracy of the codes

We tested the performances in terms of both precision and speed of our code in its various versions. As outlined in Section 4.1, the initial conditions for the N-body system are picked from a uniform phase-space distribution of equal mass particles, with an initial virial ratio $Q = 0.3$. The particle-particle interaction potential is softened (see Equation 3.33 and 3.34) and the system moves in the Galaxy, represented with the Allen and Santillan (1991) model, on a quasi circular, planar orbit at about the same galactocentric distance of the Sun.

To evaluate the quality of integration we checked the time behaviour of 4 quantities: the total energy (E) and the three components of the angular momentum ($\mathbf{L}$) vector. The energy is a true constant of motion, while $\mathbf{L}$ should vary in time due to the external field torque, $\dot{\mathbf{L}} = \mathbf{M}_{ext}$, being a constant only in case of either isolated system or system embedded in an external spherically symmetric (respect to the

	Leapfrog		Sixth Order	
N	$\|\Delta E/E_0\|_{DP}$	$\|\Delta E/E_0\|_{DSP}$	$\|\Delta E/E_0\|_{DP}$	$\|\Delta E/E_0\|_{DSP}$
480	3.39×10^{-13}	6.68×10^{-10}	3.09×10^{-15}	1.15×10^{-10}
960	1.57×10^{-10}	5.93×10^{-11}	3.20×10^{-15}	5.10×10^{-11}
1920	6.75×10^{-13}	1.90×10^{-11}	3.04×10^{-15}	2.11×10^{-11}
3840	8.60×10^{-13}	1.18×10^{-11}	8.10×10^{-15}	1.19×10^{-11}
7680	1.12×10^{-12}	7.32×10^{-12}	1.01×10^{-15}	4.64×10^{-12}
15360	1.18×10^{-12}	2.73×10^{-13}	2.83×10^{-15}	5.12×10^{-12}

Table 4.5. Relative errors in energy evaluated over 1000 time steps as $\Delta E/E_0 = [E(1000\Delta t) - E(0)]/E(0)$. The code used is NBSympleE2.

system barycenter) potential.

In our case, the MW potential being axisymmetric, only the z-component of **L** should be conserved, while L_x and L_y vary. In any case, the external torque is expected to be little due to the small cluster size, as we checked by the computation of the total torque via direct summation,

$$\mathbf{M}_{ext} = \sum_{i=1}^{N} \mathbf{r}_i \times \mathbf{F}_{ext}(\mathbf{r}_i) \tag{4.1}$$

The energy conservation and angular momentum variation are evaluated by computation of

$$\frac{\Delta E}{|E(0)|} = \frac{E(t) - E(0)}{|E(0)|}, \tag{4.2}$$

and

$$\frac{\Delta \mathbf{L}}{|\mathbf{L}(0)|} = \frac{\mathbf{L}(t) - \mathbf{L}(0)}{|\mathbf{L}(0)|}. \tag{4.3}$$

Of course the quality of both energy and angular momentum conservation depends on the code version, the best conservation performances being achieved with the use of double-precision and 6^{th} order symplectic integration. Table 4.3 gives the run with time of the relative errors in the case of the symplectic 6^{th} order time integration with DP arithmetics, for $N = 7680$. In the explored time interval $[0, 5]$, the energy is conserved at a $\sim 3 \times 10^{-14}$ level, while the z component of the angular momentum is conserved up to $\sim 5 \times 10^{-15}$. On the other side, the x and y components of the angular momentum (which should not be conserved) vary in the range $[5.42 \times 10^{-10}$,$8.86 \times 10^{-8}]$.

To have a reliable evaluation of the computing times, we ran the codes up to $0.5T$ using a (constant) time step $\Delta t = 5 \times 10^{-4}T$, this means the code was run for 1000 cycles. This way, we have a robust average value of the time spent per cycle by the various code versions in each task by the simple ratio of the total time to the number (1000) of cycles.

Table 4.4 gives the computing speed in GFLOPs of the slowest and fastest versions

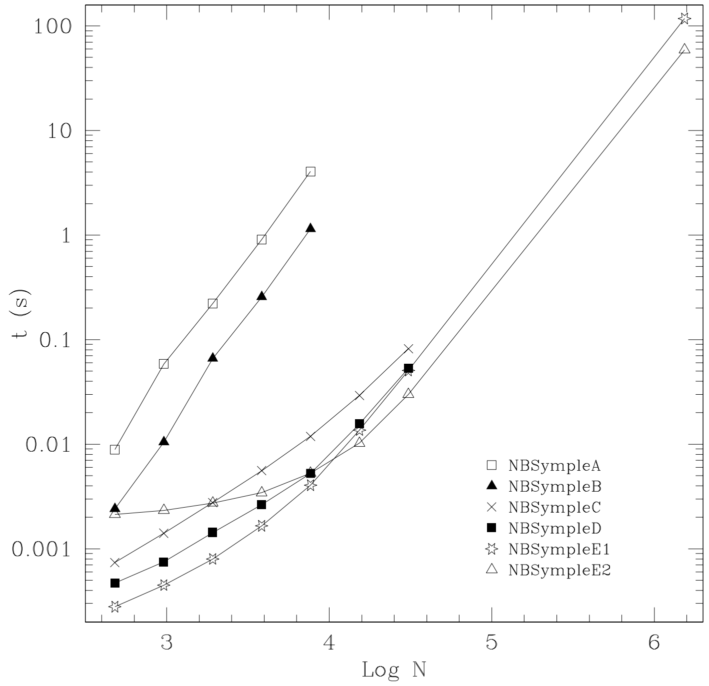

Figure 4.2. The (averaged over 1000 cycles) solar time (in seconds) spent for one leap-frog integration step in single precision mode, as a function of N. Line with empty squares: NBSympleA code. Line with filled triangles: NBSympleB. Line with crosses: NBSympleC. Line with filled squares: NBSympleD. Line with stars: NBSympleE with a single GPU. Line with empty triangles: NBSympleE with two GPUs.

of NBSymple making use of GPUs (C and E2 versions, see Table 4.1). The speed scaling from 1 to 2 GPUs is almost perfect for the largest value of N in the table.

Figure 2.5 shows the (average) time required by the various versions of NBSymple for a single time step integration with the leapfrog method. For a system of $480 \leq N \leq 1,536,000$ particles (the largest value of N used is quite representative of the number of stars in a real, populous, globular cluster). In the case of the fully serial code on a single PE (NBSympleA) and of the OpenMP parallel code on the double quadcore host (NBSympleB), the test is limited to a maximum value of $N = 7680$ because larger values require too long CPU times. Their computing times show clearly the expected N^2 behaviour. The ratio (version A to version B) of their computational times indicates a speed-up about ~ 3.6 (the best obtainable being 8, as the number of PEs). This is about 50% of maximum speed obtainable, not too bad if considering that we implemented our code on the Xeon multithread system using straightforwardly standard OpenMP directives, without looking for sophisticated implementations which were not in the scopes of this work. Using standard OpenMP directives, indeed, is not possible to parallelize the whole integration loop but rather, it is only possible to open a parallel section at each time

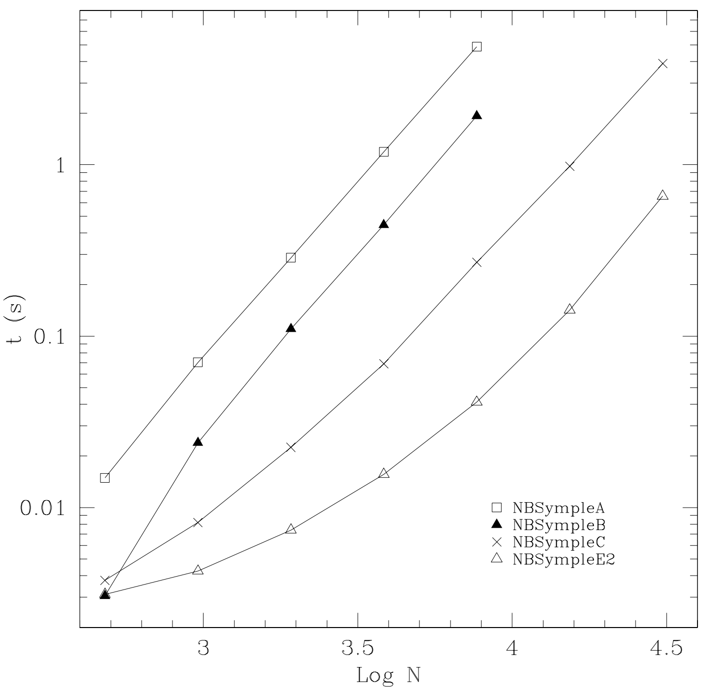

Figure 4.3. As in Figure 4.2, but for the double-precision codes. The line with filled squares is not reported because it is almost identical to that with crosses.

step and parallelize the internal loops.

The most immediate sketch of the advantage in using the GPU is by comparing the curve with empty squares to that with crosses, this latter referring to NBSympleC, that is the version of the code where the $O(N^2)$ part of the code is performed by a single TESLA C1060 GPU. The speed-up given by the GPU ranges between ~ 15 (for $N = 480$) and ~ 330 (for $N = 7680$). The NBSympleE code which exploits two TESLA GPUs becomes two times faster than when using a single GPU, showing an almost perfect efficiency when N is large enough to overcome the overhead, as evident in Figure 4.2 for $N \lesssim 10^4$. The fastest version available (the one which uses two TESLA GPUs and the leapfrog time integration in SP) requires one minute to accomplish a full integration time step for $N = 1,536,000$; taking into account the need of at least 2×10^3 cycles in a crossing time to have an acceptable precision, this means about 33 hours (1.4 days) to simulate by direct summation the evolution over one internal crossing time of a globular cluster moving in the galactic potential, and about 211 hours (8.8 days) to follow a complete revolution of the system around the galactic center, if the cluster is moving quasi-circularly at the Sun distance from the centre.

Figure 4.3 reports compared performances of the versions of NBSymple in double-precision mode. The basic, single PE, version decays in performances of a factor

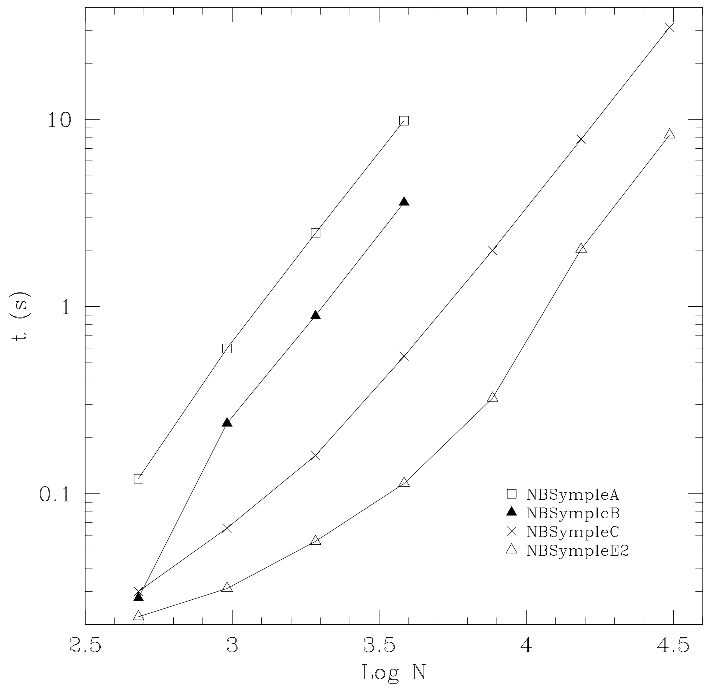

Figure 4.4. As in Figure 4.2, but for the sixth-order, double-precision codes. The line with filled squares is not reported because it is almost identical to that with crosses.

$\sim$ 1.5 respect to the SP mode. The ratio between time spent by the single PE version and the OpenMP version remains similar to the SP case in Figure 2.5. Of course, the best performances are achieved by the full GPU NBSympleE code, although the performance degradation respect to the SP version is of a factor $\sim$ 18, as expected due to the characteristics of the TESLA C1060 architecture.

The symplectic 6^{th} order, double precision performances are shown in Figure 4.4. We decided to investigate the 6^{th} order method performances in its DP mode, only, because the use of high order symplectic integration is done to keep high precision, which would be lost if using SP arithmetics. The gain in precision is, of course, paid by a significant loss in speed. At this regard, a useful indication comes from comparing Figure 4.3 and Figure 4.4 with Figure 4.1. Considering the, fastest, NBsympleE2, version (the one exploiting 2 GPUs) we see that the ratios between computing times per cycle, in the most significant range covered by all the figures ($4 \leq \log N \leq 4.5$) scales by 2 factors of 10 for $\log N = 4$ (the time required for a time cycle by the 6^{th} order DP code is about 10 times longer than by the 2^{nd} order DP code, which, in its turn, is about 10 times longer than the 2^{nd} order SP code) and by a factor of 20 and a factor of 12 for $\mathrm{Log}N = 4.5$. The performance degrading when using the DP instead of SP with the 2^{nd} order leap-frog integrator is mainly explained by the specific architecture of the TESLA C1060 GPU (1 DP

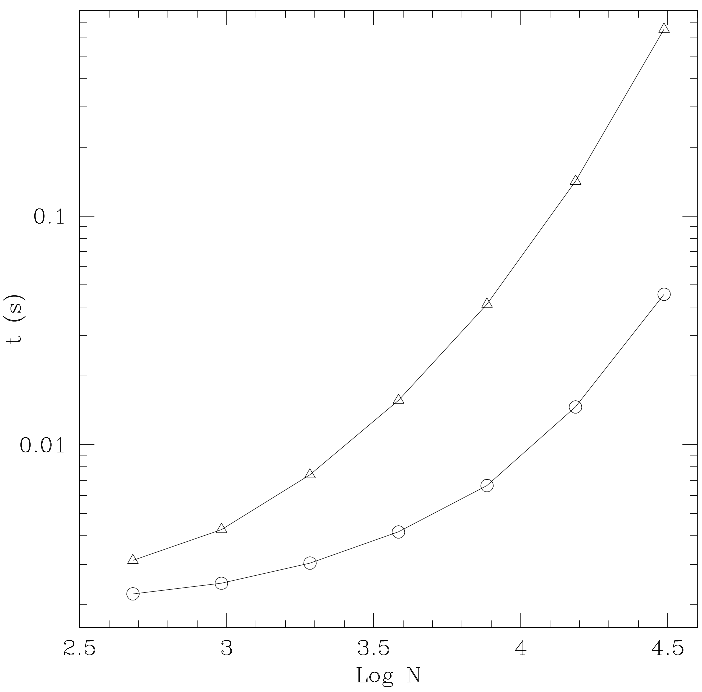

Figure 4.5. The (averaged over 1000 cycles) solar time (in seconds) spent for a single integration step as a function of N by the NBSympleE codes in the leapfrog, hardware double precision mode (line with triangles) and in the leapfrog, software double precision mode (line with circles).

processor per 8 SP processors), while the further degrading when using the 6^{th} order integrator is explained by both the 7 force evaluations per cycle needed and the repeated transfers from the host to the GPU device memory and back (a total of 16 per particle).

4.3.2 Hardware and software double precision arithmetics

The study of N-body system evolution is, in many cases, characterized by the requirement of high precision in the computations. This for two main reasons, that are different for small and large values of N.

For small values of N (celestial mechanics) the high precision in the acceleration calculation is required to avoid secular growth of the error over the huge time extension (thousands of orbital periods) of the integration; for large values of N, when time integration is not too extended, precision is mainly required to reduce the so called problem of cancellation of terms, i.e. the error due to difference between numbers that are very similar. This happens when evaluating the distances of bodies in the system in an inertial reference frame, usually centered at the center of symmetry of the external potential where the system is orbiting, in the case when

	480			30,720			1,536,000		
task	C	D	E1	C	D	E1	C	D	E1
1	23.5	36.4	81.4	58.4	89.6	94.2	98.56	99.74	99.87
2	70.3	36.0	-	38.0	9.0	-	1.31	0.18	-
3	4.5	16.8	13.8	2.7	0.9	4.4	0.10	0.06	0.10
4	1.7	10.8	4.8	0.9	0.5	1.4	0.03	0.02	0.03

Table 4.6. Time profiling (in percentage) of NBSymple in 3 of its versions (as labeled by the capital letter) for the 4 main tasks, labeled as in Figure 4.1, for the three values of N given in the table heading. The codes work in their 2nd order, SP modes.

$R << d$, where R and d are the sizes of the system and its distance to the origin of the reference frame, respectively. The correct approach to the problem of error reduction is via coupling a symplectic, high order, integration scheme to double or quadruple (in the case of celestial mechanics applications) precision arithmetics. At present, the NVIDIA TESLA C1060 GPU supports double-precision 64bit floating point arithmetics in a limited way, because each of the processing units contains one DP processor alongside the 8 SP processors. This means that there are only 30 DP units available if doing DP only calculations. The relevant performance degradation convinced us to seek for a possible solution to join precision and speed. A straightforward way to emulate DP with single precision arithmetic is done transferring the DP representation of every particle space coordinate to the GPU memory where it is shared into two SP allocations, one where the most significant digits are stored and and another for the lesser significant digits. When forces have to be computed by the GPU, it joins the two SP memory allocations to give a good DP emulation (14 digits instead of 16) yielding to a satisfactory round-off error in the, delicate, evaluation of coordinate difference. Such a representation of DP is known as 'double-single' precision (DSP[1]).

The loss in performance has been checked to be acceptable, and the implementation is not dependent on the particular hardware used. The practical implementation of DSP in our code was done by mean of the SAPPORO library (Gaburov *et al.*, 2009).

Figure 4.5 shows a performance comparison between the DP and DSP codes using the leapfrog integrator. It shows the (average) time spent for integrating the system for a single time step, as function of the number of bodies. It is evident that the DSP precision allows to integrate a system much faster than the DP precision. Finally, Tab. 4.5 shows the total energy conservation for the leapfrog and 6^{th} order methods in both DP and DSP after 1000 time steps, performed by NBSympleE2.

---

[1] http://crd.lbl.gov/ dhbailey/mpdist/

task	order	N_1	N_2	N_3
1	2nd	94.0	99.03	99.98
1	6th	85.5	99.14	99.98
2	2nd	5.3	0.90	1.65×10^{-2}
2	6th	13.1	0.80	1.63×10^{-2}
3	2nd	0.5	0.06	1.80×10^{-3}
3	6th	0.9	0.04	1.20×10^{-3}
4	2nd	0.2	0.02	7.00×10^{-4}
4	6th	0.5	0.02	6.00×10^{-4}

Table 4.7. Profiling for NBSympleC in its leapfrog, second order (2nd) and in its sixth order (6th), double precision, modes. The entries are the time fractions (in percentage) spent by the code in performing the 4 main tasks (numbered as in Figure 1 and Tab. 4.6) for three values of the number of particles: $N_1 = 480$, $N_2 = 30,720$, and $N_3 = 1,536,000$.

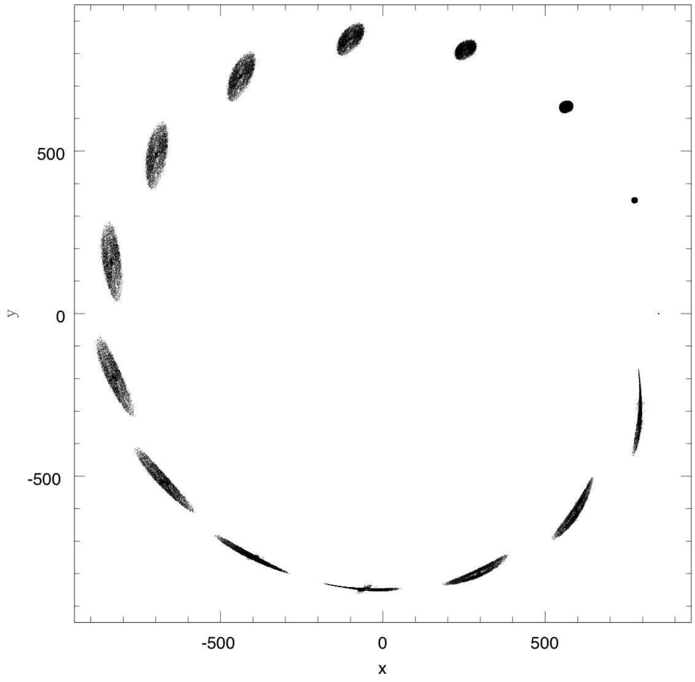

Figure 4.6. Configurations of the $N = 15,360$ simulated cluster moving on the Milky Way symmetry plane, at various times, from t=0 to t=60. The cluster motion is counterclockwise.

4.3.3 Code time profiling

In order to see whether and where it is possible to work to improve code performances, we checked the time spent by the versions of the codes that actually run on GPUs (versions C, D and E) in their different main tasks, which are essentially

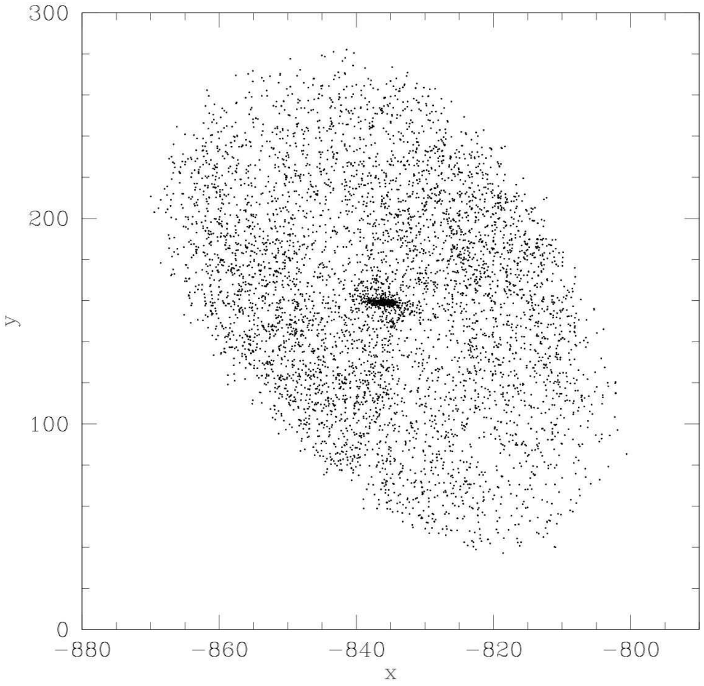

Figure 4.7. Snapshot of the cluster on quasi-circular orbit at the time $t = 29.4$ (i.e. at about half of its first revolution around the galactic centre).

defined by the flow-chart in Figure 4.1 and numbered from 1 to 4. Regarding code optimization, we remind what said in Section 4.2.1. In the time integration, we optimized our codes minimizing the number of floating point operations and we took care of avoiding the use of mathematical functions and use only fundamental operations (sums, subtractions, products).

The profiling is resumed in Tabs. 4.6 and 4.7. As expected, the pair-wise force calculation (task 1) requires a longer time at increasing N, rising to more than 99.8% for the largest N. Only the version C of the code (the one which gives to a single CPU the O(N) computational load) spends a relatively significant fraction of time in other tasks than 1. Due to that version E performs both pair-wise and external force calculations on the GPU, no distinction is possible between tasks 1 and 2, and this explains the absence of values in the task 2 row for this code version.

4.4 Some simulation tests

4.4.1 Quasi circular cluster orbits in the Milky Way

In Figs. 4.6, 4.7 and 4.8 we display some snapshots of the projections onto the $x - y$ coordinate plane of a cluster composed by $N = 15,360$ equal mass stars moving

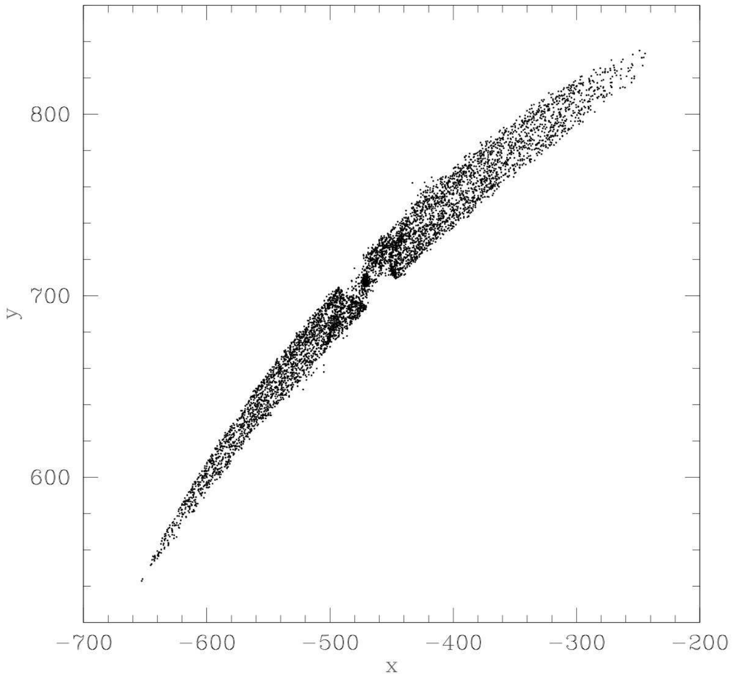

Figure 4.8. Snapshot of the cluster on quasi-circular orbit at $t = 84$ (i.e. at about 1.4 revolutions around the galactic centre).

very close to the Milky Way plane of symmetry on a quasi circular orbit with radius $\sim$ 8 kpc, simulated with NBSymplE using two TESLA C1060 GPUs. Figure 4.6 shows a clear, quick development of a tidal tail in less than one orbital period (here, one orbital period is about $60T$, where T is the internal crossing time, we adopted as time unit). Figure 4.7 is a zoom of the cluster configuration at about half revolution around the galactic centre: note the evident barlike structure in the inner zone. After about 1.5 revolutions around the galactic centre, the cluster shows two extended tails along its orbit, with two clumps, one in the leading and one in the trailing tail. These clumps have already been noted in previous high precision N-body simulations of globular clusters moving in an external field and their explanation is attempted by Capuzzo Dolcetta *et al.* (2005) and Di Matteo *et al.* (2005). These authors describe the overdensities as due to a local deceleration of the stellar motion, causing an effect similar to a “motorway traffic jam” (essentially, if we compare the stellar motion to a fluid stream, for which the continuity equation holds, along the tail an overdensity occurs whenever $\nabla \cdot \mathbf{v} < 0$, where $\mathbf{v}$ is the collective stellar velocity). It is relevant noting that similar clumps have actually actually been observed in real globular clusters, the most know example being Pal 5 (see Odenkirchen *et al.* 2003). A more quantitative analysis of their origin can be found in Chapter 5.

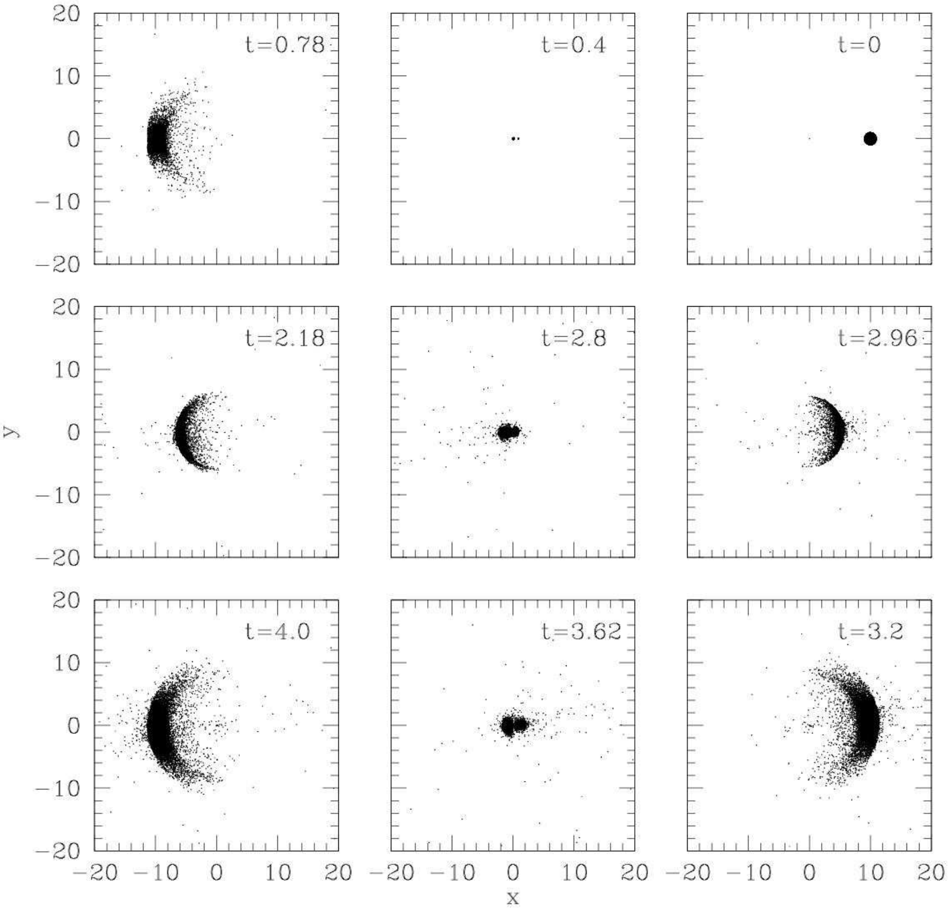

Figure 4.9. Snapshots of the $N = 15,360$ cluster plunging on quasi-radial orbit through the massive central object ($M_{bh}/M = 10$) at the times labeled in the various panels.

4.4.2 Quasi radial cluster-massive black hole collisions

For the sake of testing the capabilities of our code we ran some "stiff" simulations, i.e. those of the face-on collision of a star cluster with a massive black hole located in the Galaxy center, during its quasi radial motion in the central part of the Galaxy. These simulations, at varying the mass ratio between the black hole (represented as a further massive point) and the star cluster and at varying the number of stars in the cluster have a great astrophysical interest because they deal with the process of strong interaction with a massive central object that orbitally decayed globular clusters may have actually suffered in their motion in the parent galaxy. Apart from this scientific relevance, these simulations represent a serious and difficult test for an N body code. Actually, the close interaction of a star system composed by N point masses with a single body (the "black hole") much heavier than the individual

M_{bh}/M	$\Delta E/E_0$	$\Delta L/L_0$
0.1	3.06×10^{-7}	5.90×10^{-4}
1	7.75×10^{-6}	1.06×10^{-2}
50	9.23×10^{-5}	2.65
100	5.63×10^{-3}	3.91

Table 4.8. Relative variations in energy and angular momentum over the time interval [0,4], which corresponds to about 6.4 complete radial oscillation through the galactic center of an $N = 15,360$ star cluster. The ratio between the black hole mass and the cluster mass is M_{bh}/M. The motion starts with cluster barycenter at $(x_0, y_0, z_0) = (10, 0, 0)$ with initial velocity $(\dot{x}_0, \dot{y}_0, \dot{z}_0) = (0, 0.001v_c, 0)$, where v_c is the local circular velocity. The number of time steps is 4×10^4; the total CPU time $\simeq 9.1 \times 10^4$ sec.

cluster objects is hard to be followed by a numerical code because the very large acceleration induced by the massive black hole on passing-by cluster stars may cause an exceedingly large energy error. The energy error can, partially, be controlled by a proper reduction of the time step which cannot be, however, reduced below a threshold under which cumulation round-off error and CPU time get exceedingly large. The difficulty of such simulation grows at reducing the "collision" impact parameter b, i.e. the minimum distance between the cluster barycenter and the black hole during the cluster oscillatory motion around the massive object. To maximize the sharpness of collision we chose almost radial trajectories ($b \simeq 0$) for the cluster moving in the inner part of the Galaxy. A summary of results of our simulations at varying the black hole to cluster mass ratio is given in Table 4.8. Figure 4.9 shows the motion of the cluster on the x, y plane at various times, showing the very fast development of the cluster "arc"-like shape around the apocenter.

4.5 FERMI architecture: benchmarks and comparisons

Our code is built in order to be scalable on different GPU architectures, and to test this scalability we run the code on a different kind of graphic cards. One of the most recent NVIDIA cards, based on so called FERMI architecture, have 14 SMs (up to 16) each of them containing 32 *Streaming (or Scalar) Processors* (SPs), for a total of 448 *CUDA cores* in single precision (and 224 in double precision). After using TESLA C1060, we tested NBSymple on our workstation previously used now equipped with two TESLA Fermi C2050 (Spera 2010).

Since the CPUs on the machine are the same, NBSympleA and NBSympleB should give us the same results in terms of performance, so we only tested some of the versions of the code, and in particular NBSympleD, NBSympleE1, NBSympleE2. Figure 4.10 and Figure 4.11 show the average time required by the different versions of NBSymple to perform a single integration step, as a function of the number of particles of the N-body system. Both single and double precision are explored. In single precision, as it is apparent from Figure 4.10, there are no net

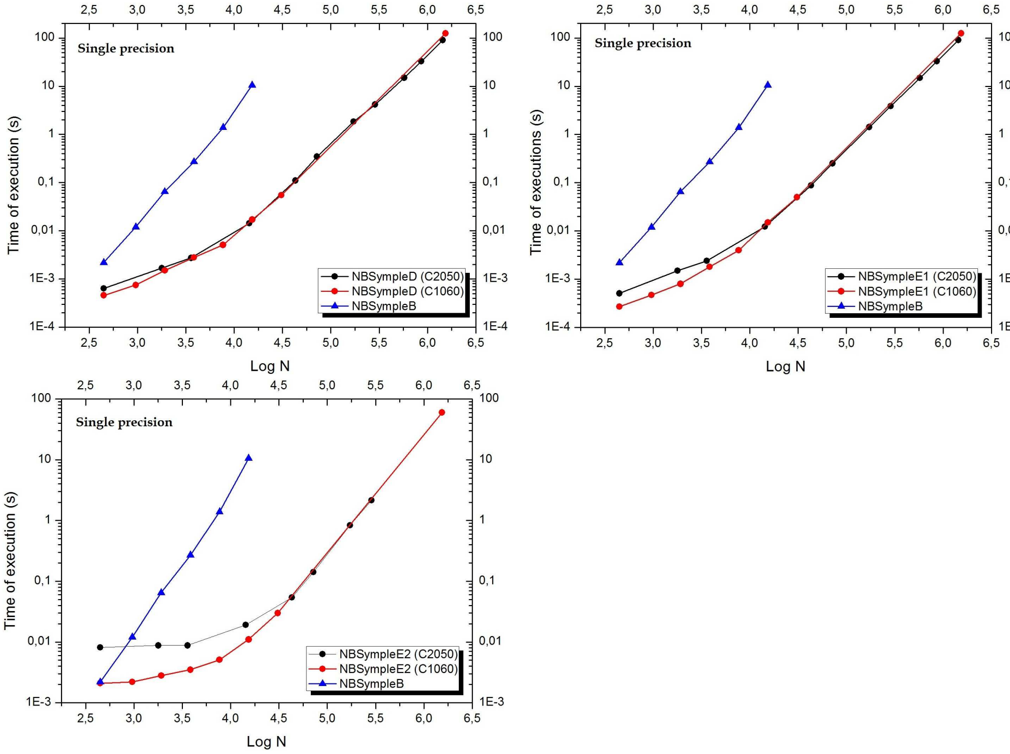

Figure 4.10. Top left panel: Time spent by NBSympleD (running on one TESLA C1060), NBSympleD (running on one TESLA C2050) and NBSympleB (running on two Intel Xeon E5405) to execute one integration step as a function of the number of particles of the system, in SP. Top right panel: The same for NBSympleE1 (running on one TESLA C1060 and one TESLA C2050) and NBSympleB (running on two Intel Xeon E5405). Bottom left panel: The same for NBSympleE2 (running on 2 TESLA C1060 and 2 TESLA C2050) and NBSympleB (running on two Intel Xeon E5405).

benefits in using a TESLA C2050 rather than a TESLA C1060. This latter can indeed reach a maximum performance $\sim$ 933 GFLOPs while the C2050 has a peak around 1030 GFLOPs. The small difference between the two cards is reflected by a slight relative speed-up, $\sim$ 1.1, for large enough values of N. When N is large NBSympleD and NBSympleE1 codes are indeed almost equal in terms of performances (see top left and top right panels of Figure 4.10), while, for small numbers of particles, NBSympleD offers a slight speed-up. When N is small, the time spent to compute the accelerations due to the external field becomes indeed comparable to that demanded to the evaluation of the mutual forces. If we assign this $O(N)$ computation to the GPU we lose in efficiency because these operations are not very complex and so the slow memory access times causes a disadvantage in terms of performances. Thus, in this case, it is better to demand the $O(N)$ calculations to CPUs rather than using GPUs. In Figure 4.10, if N is big enough, we can again appreciate, the net advantages in using two GPUs coupled with a leapfrog integration in single precision. As shown in Subsection 4.3.1 for the Tesla C1060 GPUs,

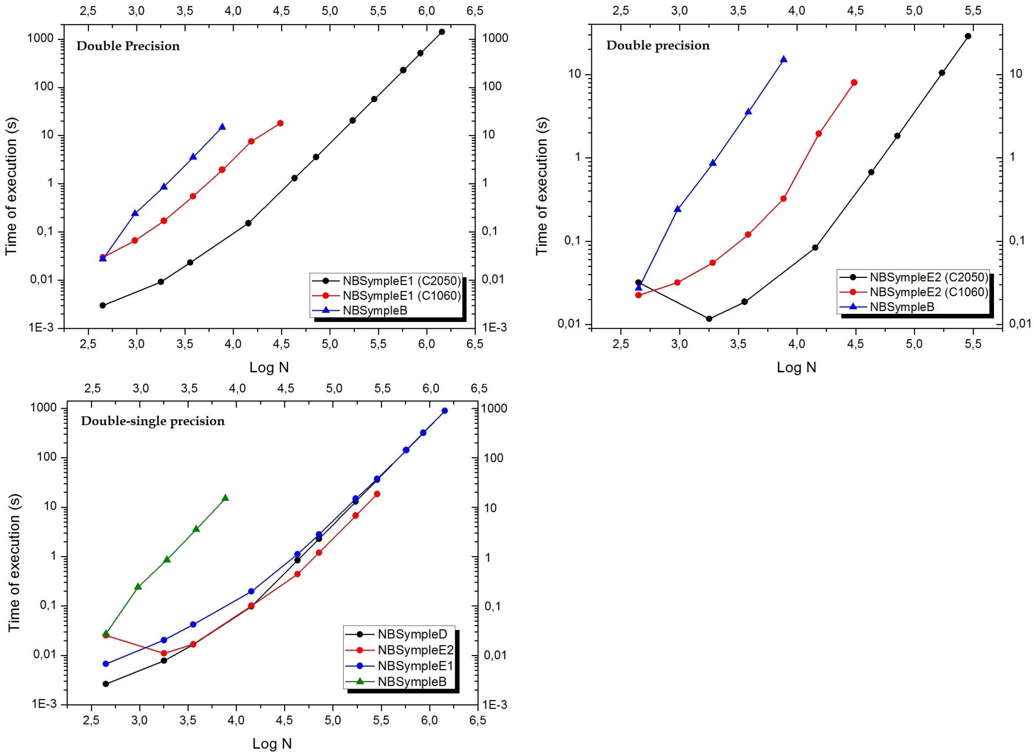

Figure 4.11. Top left panel: The same as Figure 4.10 for NBSympleE1 (running on a TESLA C1060 and a TESLA C2050) and NBSympleB (running on two Intel Xeon E5405) but in DP. Top right panel: The same for NBSympleE2 (running on 2 TESLA C1060 and 2 TESLA C2050) and NBSympleB (running on two Intel Xeon E5405), in DP. Bottom panel: The same for NBSympleD, NBSympleE1, NBSympleE2 (each of them running on one or two TESLA C2050) and NBSympleB (running on two Intel Xeon E5405) but employing DSP.

the speed-up is $\simeq 2$ times respect to the one obtained using only one TESLA (see Figure 4.10 and Figure 4.11). Nevertheless, as for TESLA C1060, when N is small, the performance decreases significantly. We must point out another problem that is relevant when N is very small. The section of the code which performs the time integration of the system is enclosed in a parallel section using the OpenMP directives. When N is small, although its lower efficiency, the kernel execution (and other CUDA operations), is much faster than the sequential opening and closing operations of the parallel sections. Its execution time becomes negligible only when N is large enough to ensure that the time spent to compute the kernel, and to update the positions and the velocities (CPU), is greater than that required to manage the parallel sections. This can explain the flat trend of the black curve shown in the bottom panel of Figure 4.10 (and also in Figure 4.4). In the top right panel of Figure 4.11 the anomalous trend for small N is even much clear. Nevertheless, in this case, the parallelization begins to be efficient already for $\log N = 3.25$ because the compute capability of the CPU in double precision is greatly reduced and the

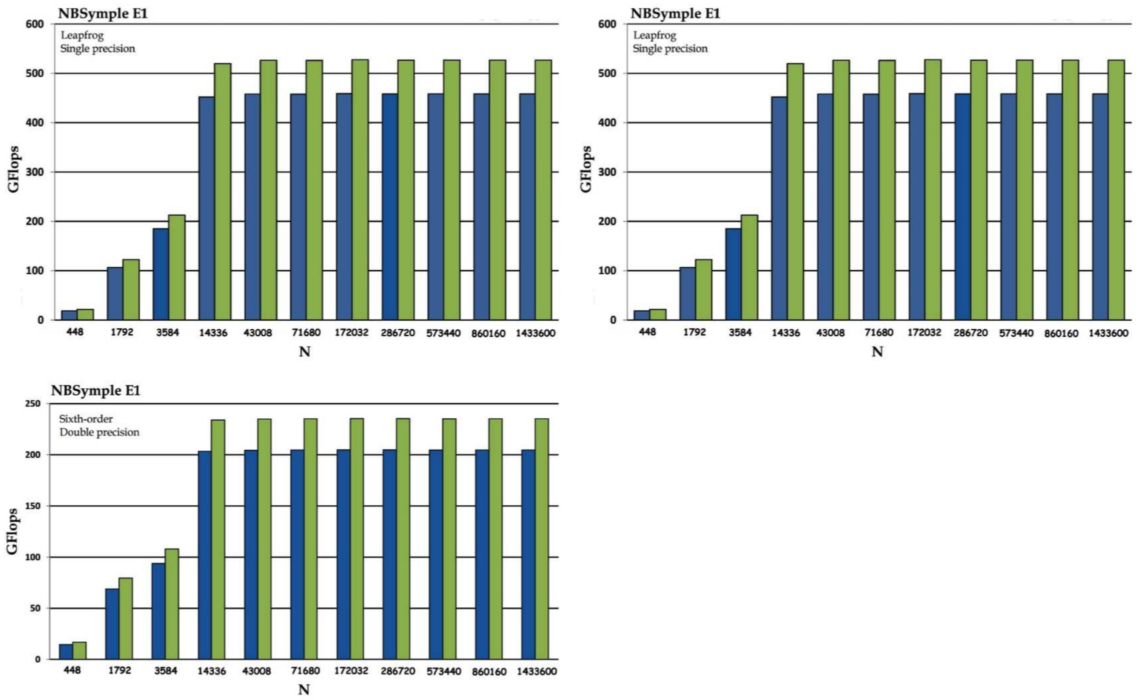

Figure 4.12. Top left panel: Effective performance (in GFLOPs), for different values of N, reached by NBSympleE1 in single precision. The blue bars show the results obtained with our estimate of the number of floating point operations while the green bars represent the results obtained using the estimate given by the CUDA programming guide. Top right panel: The same for NBSympleE1 in double-single precision. Bottom panel: The same for NBSympleE1 in double precision.

time spent to execute the update of positions and velocities becomes, soon, relevant, allowing a more efficient parallelization. In the bottom panel of Figure 4.11, where the performances of NBSymple running on one or two TESLA C2050 in DSP are shown, there is the same anomalous trend, (red curve, NBSympleE2). Obviously, the first red point (corresponding to $N = 448$) is slightly lower than the first black point in the top right panel of Figure 4.11 and this is due to a faster memory allocation and data transfer between the GPU and CPU. In double precision we have indeed to manipulate accelerations of type double4 while in double-single precision they are float4 variables. The same anomalous trend is negligible in the black curve shown in the top left panel of Figure 4.11 because, in this case, with only a GPU, some parallel regions are not opened and this allows a more efficient parallelization. From the upper panels of Figure 4.11 the greater efficiency of Tesla C2050 in DP respect to the Tesla C1060 is apparent. The first kind of GPUs has indeed much more cores (224) able to work in DP than Tesla C1060 (which has only 30 cores which work in DP). It is interesting to evaluate the performances in GFLOPs obtained using TESLA C2050 instead of TESLA C1060. We refer to NBSympleE1 and NBSympleE2, in single, double-single and double precision. The number of

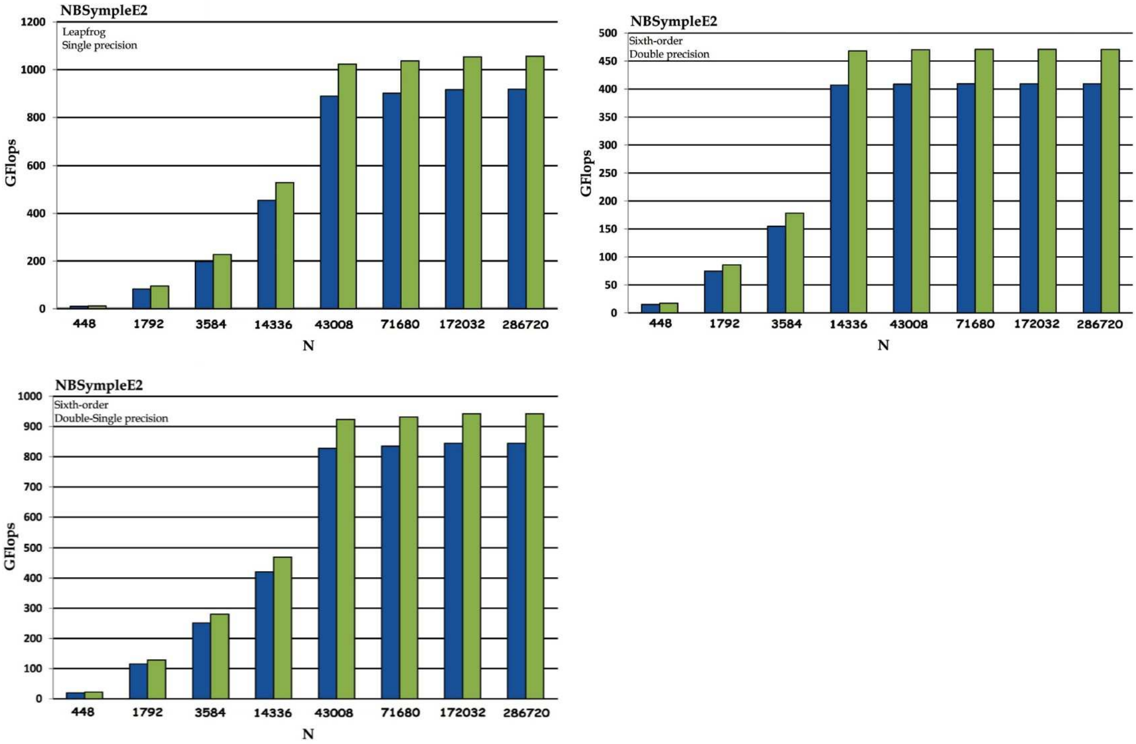

Figure 4.13. Top left panel: The same as Figure 4.12 for NBSympleE2 in single precision. Top right panel: The same for NBSympleE2 in double precision. Bottom panel: The same for NBSympleE2 in double-single precision.

floating point operations for every mutual force calculation is the same as in the case of the code running on TESLA C1060 and the results are shown by the blue bars in the the histograms in Figure 4.12 and Figure 4.13. As comparison we show the same results, but using the number of floating point operations given by the CUDA programming guide (green bars in the same histograms). The performances obtained running the code in single precision, using the second-order method on a single GPU are $\sim 50\%$ of the peak performance (both in single and double precision) of the a single TESLA C2050, as already found using TESLA C1060 (see Section 4.3.1 and Table 4.4). This confirms the good scalability of our code and also means that the code is well suit to exploit the computational resources of GPUs. We must point out that the performance obtained using two TESLA C2050 (or 2 TESLA C1060) are almost doubled both in single and double precision compared to the ones obtained with a single GPU. Due to the fact that, on a Tesla C2050, the cores which work in DP are 224 while the one that work in SP are 448, the performances reached in DP are approximately half of those in SP. As the value of N increases, every thread must execute more and more operations and all the latencies are adequately covered, allowing better performances. Thus, each thread must read the global memory $\frac{N}{p}$ times and it must compute N iterations (p indicates the number of threads per block). The time difference between these two process

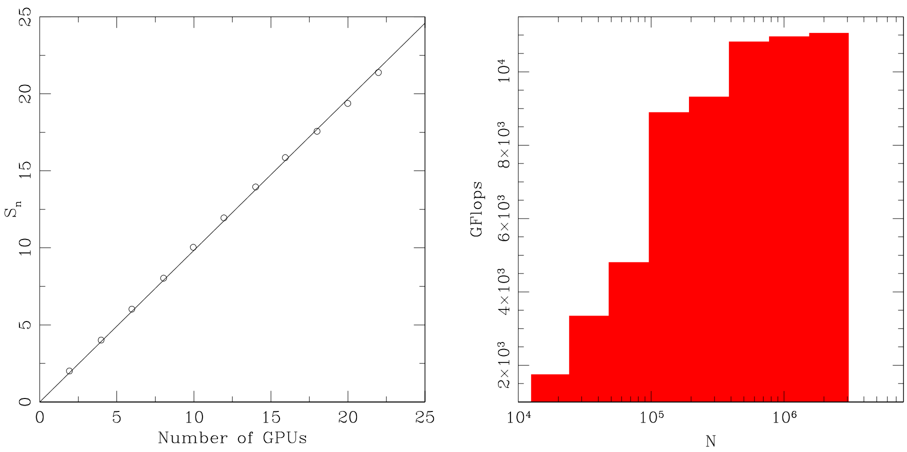

Figure 4.14. Left panel: The empty circles show the speedup as a function of the number of GPUs. The solid line is the best fit to the data. The number of particles used is $N = 1966080$. Right panel: NBSymple performance in double-single precision, for different values of N, using 11 nodes.

can be expressed as

$$D = Nt_{int} - \frac{N}{p}t_{mem} = \frac{N}{p}\left(pt_{int} - t_{mem}\right) \tag{4.4}$$

where t_{int} represents the time needed to complete the computation of a single iteration and t_{mem} is the time spent to execute a single global memory access. Although it is not a rigorous treatment, from Equation (4.4) we can deduce that, if p is constant, the latencies become negligible compared to the work executed by a generic thread, when this latter increases.

This is reflected in an increase in GFLOPs performances.

4.6 MPI implementation and benchmarks

Given the parallelizzation based on OpenMP, NBSymple can only work on hardwares based on shared memory architectures. This is a serious limitation if we think to the potential of the resources made available by hybrid GPUs+CPUs clusters. A GPU cluster is a computer cluster in which each node is equipped with one or more GPUs, allowing very fast calculations.
To use these systems, which are based on distributed memory architectures is necessary to parallelize the code by mean of MPI. The Message Passing Interface or MPI, is a standardized and portable message-passing system for computers and it actually constitutes the standard for the communication between different nodes of a cluster of computers on which a parallel code, suitable for a distributed memory system, is run. MPI is portable (being implemented for different parallel architectures) and fast (MPI is optimized for every architectures).

Thus we implemented a new version of NBSymple where the intercommunication between different CPUs is no more demanded to OpenMP but to MPI (see Capuzzo Dolcetta, Arca Sedda, Mastrobuono Battisti, Montuori, Punzo, and Spera 2011).
This new code was tested on JAZZ, a hybrid CPU+GPU cluster managed by CASPUR (Consorzio i nteruniversitario per le applicazioni di supercalcolo per università e ricerca). We tested our code with a high number of stars (up to $N = 1966080$), to obtain the relative speed up, defined as

$$S_n = \frac{T_p(1)}{T_p(n)}, \tag{4.5}$$

where p is the number of processors, $T_p(1)$ is the execution time of the sequential algorithm and $T_p(n)$ is the execution time of the parallel algorithm on p processors, obtained testing the code on different numbers of nodes of the cluster. The speed up is approximately linear; the best linear fit slope is equal to 0.98, value close to the ideal one, i.e. 1 (see left panel of Figure 4.14). We also estimated the code performances in GFLOPs, when using all the 11 nodes of the cluster. The results of this benchmark is given in the right panel of Figure 4.14. It is worth to underline that the larger is the number of stars, the better is the computational capacity of this kind of architectures. As expected, for a small number of bodies, the performances of GPUs decrease significantly, since the time spent in performing memory transfers becomes comparable to that spent in calculating accelerations between particles. As we said above, the result is that GPU-computing is worth only for a sufficiently large number of particles.The sustained performance is more than 11 TFlops. This is a very high value, although reached using a hybrid cluster which is small if compared to the top supercomputers in the world.

4.7 A new code, benchmarks and tests

The fixed time step guarantees a very good conservation of energy provided the introduction of an appropriate softening parameter in the forces expression, but it is not actually the best choice in terms of speed performances. To accelerate the calculation maintaining an high degree of accuracy we modified the NBSymple code introducing different integration methods coupled with variable time steps. The varying time step algorithm is more complicated than the constant time step alternative (see Section 3.3). However, we developed a new direct N-body code which supports both a Hermite 4^{th} order and a Hermite 6^{th} order time integrators implemented by mean of a hierarchical block time stepping. As for NBSymple, the external galactic potential is considered analytically and the code is again implemented using MPI, OpenMP and CUDA to fully exploit the available computational power of hybrid architectures. This version of the code allows a much better treatment of the close interactions between particles of extremely different mass ratios (for example a star and a black hole) than possible with constant time stepping, by

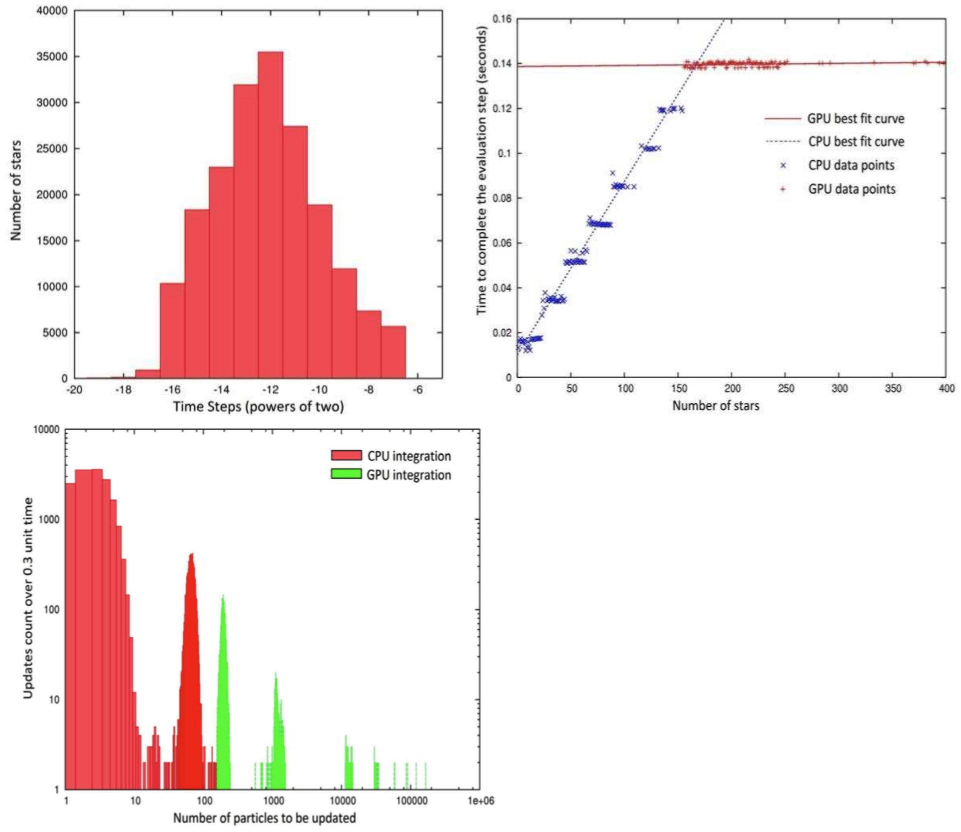

Figure 4.15. Top left panel: the initial distribution of time steps, obtained by using the generalized Aarseth's criterion (Nitadori and Makino, 2008). Top right panel: The CPU (blue data) and the GPU (red data) time spent in executing the evaluation step as a function of the number of stars to be integrated. Bottom panel: It is shown the update frequency of a specific number of stars over 0.3 time units. The red bars are for the particles integrated by the CPU while the green one are referred to the GPU integration.

means of the the generalized Aarseth's criterion (Nitadori and Makino, 2008). The code has been tested on a machine composed by 2 NVIDIA TESLA C2050 GPUs and 2 Intel Xeon X5650 CPUs. The MPI parallelization was done so that there is a one to one correspondence between MPI processes and computational nodes while the resources per node are fully exploited opening OpenMP forks. Specifically, the predictor and corrector parts of the code (less expensive in terms of computational time) are performed using the CPU while the force evaluation is performed on the available GPUs.

4.7.1 Some tests of the code

The code has been tested running some simulations involving a star cluster located at the center of the Galaxy where a SMBH of mass 4×10^6 M$_\odot$ is located (see

Chapter 5 for ore details about such kind of simulations). The star cluster has a mass $M_{cl} = 1.32 \times 10^7$ $\mathrm{M}_\odot$ and its N-body representation counts a number of particles $N \simeq 270000$. The adopted softening parameter is $\varepsilon = 0.01$ pc and the accuracy parameter for the 6^{th} order Hermite integrator was set equal to $\eta = 0.5$. As shown by the top left panel of Figure 4.15, the majority of stars share a time step between 10^{-4} and 5×10^{-4}. Stars with much smaller time steps ($\sim 10^{-6}$) are candidates for encounters with the SMBH. One of the relevant features of this new code is the splitting of the calculation of the pair-wise forces on the CPUs when the particles-per-block to be updated are small in number. The top right panel of Figure 4.15 shows the CPU and the GPU time spent executing the evaluation step as a function of the number of stars to be integrated. It is apparent that it is crucial to improve the performances for small number of bodies because, in this situation, the GPU computational capability tends to saturate. This results in an almost flat GPU best fit curve. The importance of the split-strategy is better understood if we look at the bottom panel of Figure 4.15 which shows the time that a certain number of particles needs to be updated over an integration time equal to 0.3 time units. We must point out that, as the Hermite scheme requires, the update frequency is much higher for small number of bodies even if the integration time is obviously smaller. This constitutes a real bottleneck for such kind of simulations and the split method contributes significantly to reduce it.

4.8 Young clusters primordial evolution with NBSymple

Here we present an application of NBSymple to an open astrophysical topic: the formation and primordial evolution of star clusters. It is widely accepted that stars form in aggregates (Lada and Lada, 2003), at least in a wide mass range. Giant molecular clouds (GMCs) fragment and origin a clumpy structure, where stars form (see Chapter 1). In some cases, the protocluster may dissolve due to tidal interaction with massive external objects (other molecular clouds) on a small spatial scale or with the general galactic field, over a larger spatial scale. Stars coming from dissolved clusters go to enrich the general field stellar population. Star clusters are, thus, among the basic building blocks of galaxies. As a consequence, studying the formation of clusters means approaching a better knowledge of both star and galaxy formation. Unfortunately, the problem of cluster formation is not an easy task to face. This because of the presence of a multiplicity of space-time scales, from the microscales of the gas thermodynamics to the macro-scales of gravitational and magnetic instabilities. The role of turbulence has also been ascertained in its importance. Thus, even with the modern computing systems, it is still impossible to follow the evolution of a cluster forming region over the whole dynamic range. A theoretical insight to cluster evolution thus requires an approach which is different when dealing with the formation itself than with the following, embedded,

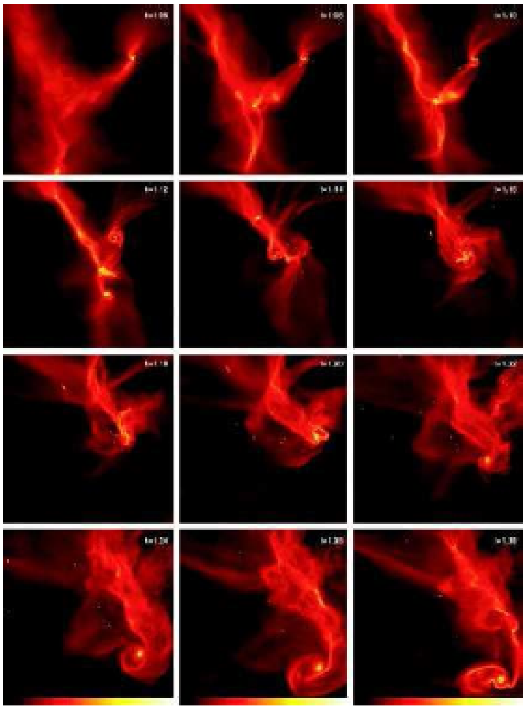

Figure 4.16. Evolutionary sequence for cluster formation. [Bate *et al.* 2003]

phase and, later in time, with the “quasi-dry” system evolution, after gas removal. The approach to cluster formation relies on self-gravitating calculations (Clarke, 2010). They are a step further the previous no-gravity, grid-based models (Lemaster and Stone, 2008; Kitsionas *et al.*, 2009) that supported the interpretation of star formation as a cascade of energy from some large scale where it is being continuously injected. Fluid-dynamics simulations of self gravitating clouds are more easily treated with Lagrangian (particle) codes, mainly smoothed-particle-hydrodynamics (SPH; Lucy 1977; Gingold and Monaghan 1977) than with eulerian (grid) methods, these latter difficult to implement in absence of geometrical symmetries. We cite Monaghan (2005) for an excellent review of SPH properties which makes it particularly effective in the study of unstable gaseous systems. The main problem of SPH is resolution, which is limited by the number of particles in the simulation, although it can be partly cured by a variable kernel size. Low resolution makes impossible dealing with shock fronts as well as with, e.g., Riemann solvers. Anyway, SPH is capable of producing the pre- and post-shock values correct to any degree of accuracy. In SPH, artificial viscosity is needed for handling shocks, but it must be taken under control to avoid an excessive injection of energy on microscopic scales altering the global dynamics. In star formation, this has the consequence that the Reynolds number is artificially increased implying the Kelvin-Helmoltz shear instabilities are heavily diffused. In spite of these problems, various authors faced the study of star cluster formation by mean of SPH calculations. First works are Chapman *et al.* (1992) and Klessen *et al.* (1998). Usually, models are not fully self-consistent, because the velocity field, relevant in determining the characteristics of turbulence, is just assumed (Schmeja and Klessen, 2004; Padoan *et al.*, 1997; Bonnell *et al.*, 2001). In the assumption that a "star" is forming when enough gravitationally bound gas is accumulated within "sink particles" of specified radius (Bate *et al.*, 1995), the main result of hydro calculations is that stars typically form in the dense gas at the intersection of collapsing filaments (see Figure 4.16).

There is less agreement among authors about the cluster initial mass function (IMF). Anyway, the high mass tail of the IMF seems to be a power law with exponent -2 at 10% level of accuracy. A notable result is a flatter slope within individual clusters than for the whole (cluster+field) population (Bonnell *et al.*, 2008, 2003). The paper by Bonnell *et al.* (2008) shows that the upper IMF in the simulated clusters is best fit by truncated power laws for which the truncation mass depends on the cluster mass. Another result worth mentioning is the mass segregation of massive stars in very young (0.5 Myr) clusters. This segregation has been observed in some embedded clusters (Hillenbrand and Hartmann, 1998; Lada *et al.*, 1991) and is difficult to explain (Bonnell and Davies, 1998) as a two-body relaxation, because the relaxation time is about 10 times longer than the age of these clusters. According to Bonnell *et al.* (2001) and Beuther *et al.* (2007) competitive accretion preferentially forms massive stars in the deepest part of the cluster potential well, near the center. On another side, many young clusters have subvirial ("cold") initial conditions and clumpy substructure (McMillan *et al.*, 2007; Allison *et al.*, 2009; Moeckel and Bonnell, 2009; Walsh *et al.*, 2004; André, 2002; Peretto *et al.*, 2006; Kirk *et al.*, 2006). Although the most massive stars are not formed within the cluster core, they are the first to form and the first to start accretion process and to get involved in merging process, which could be responsible of dynamical dragging of massive stars in the cluster core (de Grijs, 2010). Hydrodynamical results give an interesting snapshot of the cluster embedded in filamentary gas structure. On the observational side, Lada (2010) claims that in the Milky Way the primary mode of cluster formation is Jeans instability (triggered by environmental effect) of massive dense cores in GMCs. Important reference data are those indicating that in a typical GMC the star forming cores occupy only 1% of its volume and from 1% to 10% of its mass. Both observations and theory indicate that just a fraction of clusters resist upon emersion from the embedded phase: the "infant mortality" is high (Kirk *et al.*, 2006). Chandra X ray observations (Preibisch and Feigelson, 2005) confirm that 10 Myr is a relevant time scale. There is surely a relation between X ray with the established absence of gas clouds surrounding clusters older than 5 Myr (Leisawitz *et al.*, 1989). According to Clarke (2010) this means a duration of the embedded phase between 3 and 5 Myr, giving a typical age of embedded clusters between 1 and 2 Myr. It results a birthrate from 2 to 4 $\mathrm{Myr}^{-1}\mathrm{kpc}^{-2}$, much greater than the birthrate of classical open clusters in the vicinity of the Sun, estimated by Battinelli and Capuzzo-Dolcetta (1991) 0.45 Myr^{-1} kpc^{-2}. This large difference between the

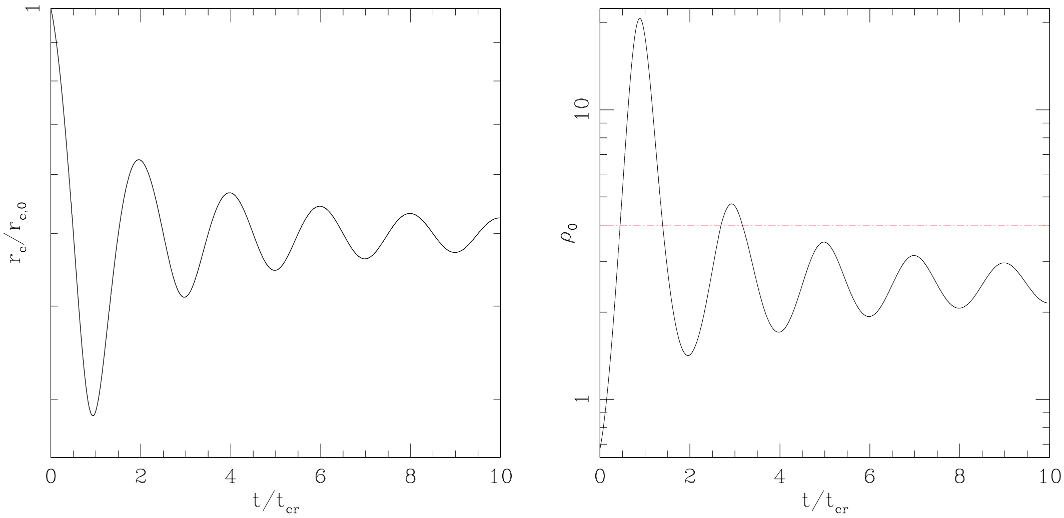

Figure 4.17. Left: time evolution of the GMC core radius. Right: time evolution of the GMC central density; the horizontal dot-dashed red line marks the threshold for star formation.

two birthrates is crucial in the interpretation of the post-embedded phase.
Clearly, the possibility for a cluster of emerging from the embedded state as a bound system depends not only on the initial binding energy but also on many variables, like star formation efficiency, the IMF, the external galactic effect and the initial virial or subvirial state of the born cluster, as shown by Lada *et al.* (1984) and Capuzzo Dolcetta and di Lisio (1994), Goodwin (2009).
With our work we tried to begin the study the cluster evolution just after the embedded phase testing NBSymple in a rapidly varying situation.

4.8.1 The model

In our simulations, we modeled the gas environment as a Plummer's spherical cloud (Plummer, 1911)

$$\rho(r;t) = \frac{\rho_0(t)}{\left[1+\left(\frac{r}{r_c(t)}\right)^2\right]^{\frac{5}{2}}}, \tag{4.6}$$

where the central density, ρ_0, and the core radius, r_c are assumed to vary with time as an oscillatory, damped, function mimicking the approach to the virial state of a gravitationally unstable cloud on few free-fall times.

The core radius varies as

$$r_c(t) = \frac{\alpha}{2}\frac{cos\,(\pi)}{(1+t)^{\frac{5}{4}}} + \frac{\alpha}{2} + \beta\ . \tag{4.7}$$

In our case we assumed $\alpha = 1$ and $\beta = 0$ in such a way that $r_c(0) = r_{c,0} = 1$ (see Figure 4.17). Thus, we took the initial value of the core radius, $r_{c,0}$, of the cloud as

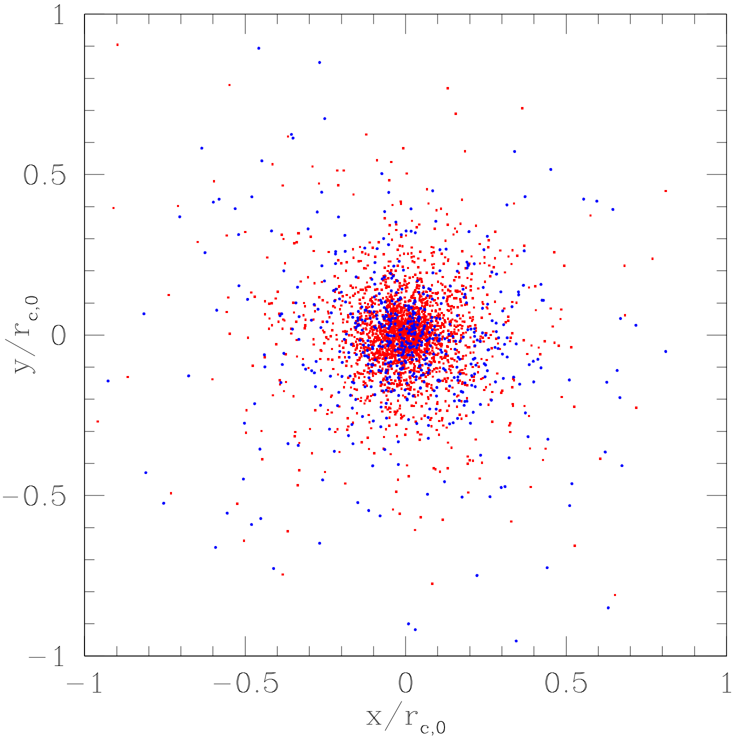

Figure 4.18. Snapshot of the simulated cluster after 10 crossing times. Red dots are stars with mass equal to 2 M$_\odot$; blue squares refer to 1 M$_\odot$.

the length unit; the mass unit is given by the mass of gas initially contained within $r_{c,0}$, $M_{gas}(0) = M_{gas,0}$. G is assumed equal to 1. In such a way the unit of time is the "initial" crossing time of the system

$$t_{cr} = \sqrt{\frac{r_{c,0}^3}{GM_{gas,0}}}. \tag{4.8}$$

Substituting Equation (4.7) into Equation (4.6) we obtain the density as a function of time (see Figure 4.17). The quantity $\rho_0(t)$ has to be evaluated at each time normalizing to the total mass of gas within a certain fixed radius $R > r_c(t)$. In this simplified approach, given this "large" scale gas dynamics, the phase transition from gas to stars is governed by a time differential equation

$$\dot{\Sigma}_* = c\Sigma_g^n, \tag{4.9}$$

saying that the time rate of conversion of gas mass into stars is proportional to a given power n (usually $n = 2$, Schmidt's Schmidt 1959) of the gas mass density, whenever the gas density exceeds a certain threshold, defined by observations. The oscillating and damping density evolution has a behavior such that the star formation governed by the Schmidt's like law occurs on different episodes, corresponding

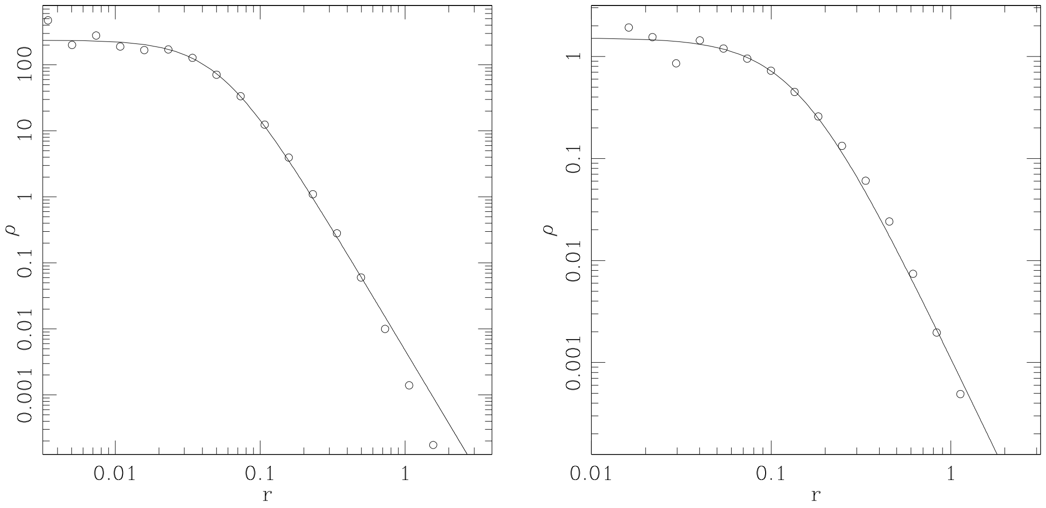

Figure 4.19. Left panel: Spatial density profile (empty circles) for the more massive stars that forms during the first episode taken after 25 t_{cr}. Right panel: The same for the less massive stars, formed during the second episode. The solid line, in both cases, is the best fitting low to the data. Radius are in units of $r_{c,0}$ and densities are in units of $M_{gas,0}/r^3_{c,0}$.

to the phases when gas density grows over the threshold. In every episode stars are assumed to form with the same mass (which is changing from episode to episode) and with initial conditions inherited by the cloud: initial positions are randomly sampled within the core radius of the Plummer's sphere at the formation time and the velocities are randomly taken (both in absolute value and direction) sampling the instantaneous collapse speed of the cloud. This preliminary approach does not account for a radiative and/or ram pressure star-gas feedback and just consider the feedback of gas and stars through the inclusion of the gas gravitational contribution to the force acting on stars. This modeling is, of course, of limited astrophysical relevance but it is useful because allows an easy testing of how the N-body code reacts to the quasi-sudden "injection" of stars in the system.
We found that in these conditions NBSymple code keeps almost unchanged its conservation characteristics with respect to the "dry" case. As a first application we simulated an isolated cloud of the type described above with star formation occurring in two episodes. Thus, we chose an arbitrary threshold in such a way the oscillating density is bigger than its value in two different time intervals (see the right panel of Figure 4.17 where the red line with dots and dashes represents the limiting density). During these intervals the gaseous material is converted in stars (see Figure 4.18 for a snapshot of the simulation). We gave to stars formed earlier a mass twice larger than the stars formed in the second episode. This corresponds to a slight mass segregation, for the first episode of star formation occurred at a first, deeper, bounce of the gaseous cloud (smaller core radius). We evaluated the density profile of the more massive star population (left panel of Figure 4.19) and

of the less massive population (right panel of Figure 4.19) after 25 t_{cr}. We fitted the profiles using a modified core model as given by Equation (2.1). For the first population of stars that forms we have that the best fitting law is

$$\rho(r, t = 25t_{cr}) = \frac{2.38 \times 10^2}{\left[1 + (\frac{r}{0.0528})^2\right]^{1.84}} \frac{M_{gas,0}}{r_{c,0}^3} \tag{4.10}$$

while for the less massive group of stars that forms during the second episode we have

$$\rho(r, t = 25t_{cr}) = \frac{1.52}{\left[1 + (\frac{r}{0.151})^2\right]^{1.84}} \frac{M_{gas,0}}{r_{c,0}^3} \tag{4.11}$$

in units of the simulation. Being the core radius in Equation (4.10), $r_{c,1}(t = 25t_{cr}) = 0.0528$, smaller than the one in Equation (4.11), $r_{c,2}(t = 25t_{cr}) = 0.151$, and the exponent γ the same in both cases we found that the more massive stars are more concentrated to the center than the less massive ones; thus the "primordial " mass segregation (due to the initial conditions) is enhanced by 2-body encounters during a 25 crossing times evolution. Even in this simplified scheme, this result has itself an astrophysical interest because it constitutes a possible answer to the observed (Hillenbrand and Hartmann, 1998; Lada *et al.*, 1991) mass segregation in very young clusters, younger than their 2-body relaxation time.

4.9 Tidal tails around Palomar 14

Here we present an application of NBSymple to the study of a large scale dynamical problem: the formation of tidal tails around one of the furthest Galactic GCs, Palomar 14. The Palomar GCs were discovered in the 1950s on the survey plates of the first Palomar Observatory Sky Survey (POSS). Several of the Palomar GCs, including Palomar 6, Palomar 7, Palomar 9, Palomar 10 and Palomar 11, are nearby clusters of average size that just happen to be heavily obscured by dust in our line of sight. Others, including Palomar 3, Palomar 4, and Palomar 14, are giant globulars that are very far away in the extreme outer halo of the Milky Way.

In particular, Palomar 14 is characterized by a very low density and mass, and by its remote position ($\sim$ 71 kpc from the Galactic center, see Jordi *et al.* 2009). Even if theoretical predictions tell us that the external potential is not enough strong to significantly change the shape of a clusters at that distances Sollima *et al.* (2011b) found a power-law departure from a King profile at large distances to the center of Palomar 14 which, together with the observed elongated distribution of stars on both sides of the cluster, forming an S-shape characteristic of mass loss, is an signature of tidal stripping in action (see Chapter 6).

Thus these recent observations have revealed the presence of tidal tails around this cluster. Our goal was to reproduce these tails by mean of numerical simulations performed using NBSymple. We used the observed position and the predicted proper motion by (Lynden-Bell and Lynden-Bell, 1995) of Palomar 14 to start

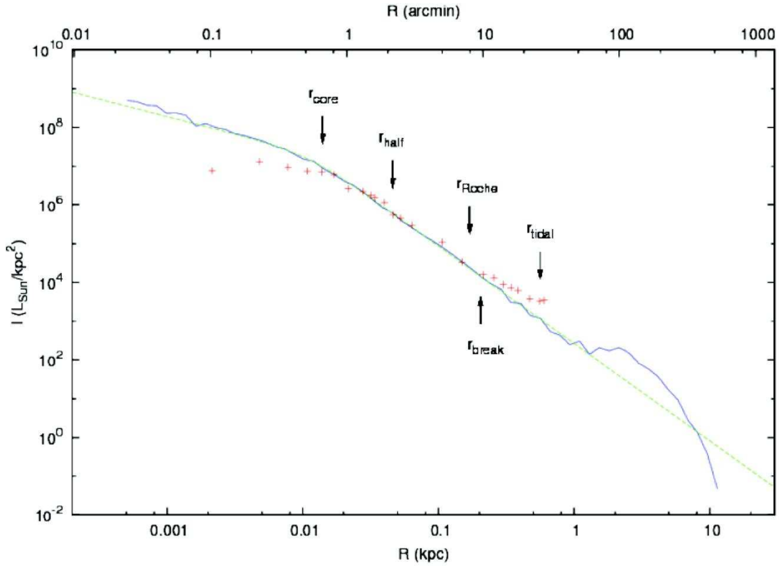

Figure 4.20. Comparison between the observed luminosity profile (red crosses) and characteristic radii (Sollima *et al.*, 2011b) with the simulated projected density profile from an N-body simulation of the cluster (blue solid line). The green dashed line, a Nuker profile with a radius of 11 pc, to guide the eye, reinforces the predicted excess of stars in the tidal tail, beyond the tidal radius.

a (single particle) backwards simulation. In such a way we obtained the initial conditions for the center of mass of the cluster 6.5 Gyr ago. We built a GC using typical parameters (Harris, 1996a) and sampling the N-body model by mean of the package *mkking* of NEMO toolkit (see Teuben 1995). The cluster core radius is $r_c = 1$ pc, the tidal radius is $r_t = 31$ pc, the central velocity dispersion is $\sigma = 5$ km/s and $W_0 = 7$. For the preliminary simulation we used a number of particles $N = 7680$; all these particles have the same mass. This conditions can be definitely improved.

We integrated the cluster forwards for 6.5 Gyr, using NBSymple and we analysed the final model. Although the simulation we performed is only an initial trial the results obtained are interesting. As we can see from Figure 4.20 the line-of-sight projected surface density of the final model (blue solid line) is well fitted by a Nuker law (green dashed line) with break radius ~ 11 pc, value close to the observed core radius of the cluster (12 pc, see Sollima *et al.* 2011b). We vertically shifted the observed profile (red crosses in Figure 4.20, see Sollima *et al.* 2011b) in order to match the simulated model profile. The slope of the profile external to the central core is exactly the same in the two cases, but our profile has not a core. In the most external region of the profile we can see an over-density; this is clearly the signature of the presence of the tails. Such structures are evident in Figure 4.21 that shows the isodensity contours of the cluster at the end of the simulation. Even if the cluster is very far from the Galactic center and so it is subjected to a low tidal effect, after 6.5 Gyr it seems to be very extended and so, future observations,

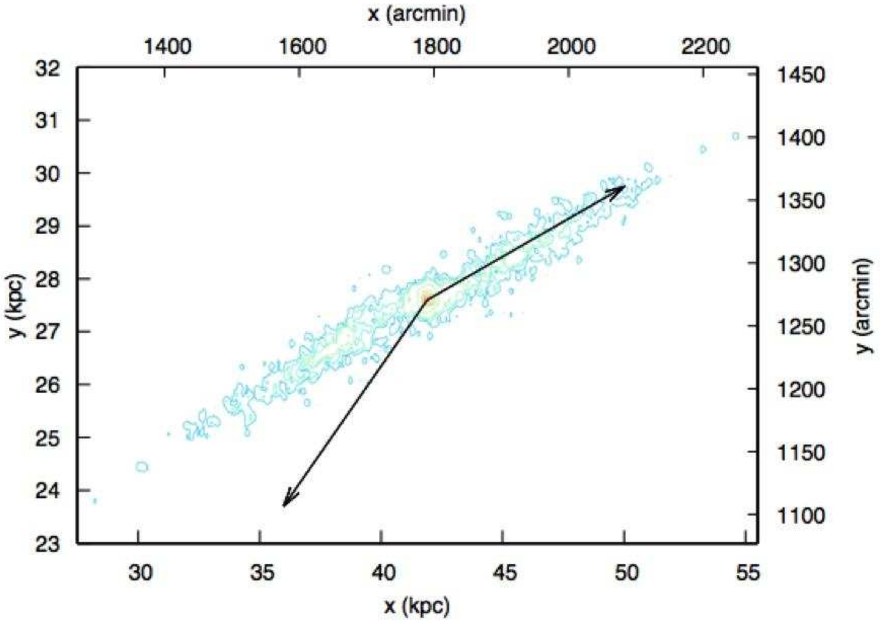

Figure 4.21. Predicted extension of the stellar stream associated with Palomar 14. The map has been stretched to show the extension in the direction perpendicular to the proper motion (arrow).

could detect the tails improving our knowledge about Galactic potential which is the main responsible for the formation of such structures.

NBSymple has been also used to simulate Palomar 14 with N=61440 particles for a shorter time interval (4 Gyr) in order to estimate its velocity dispersion in the Newtonian case and compare this result with the one obtained with simulation performed using the MOND code NMODY (Londrillo and Nipoti, 2009). From the results obtained it seems that observational data well match with the Newtonian simulated case while they are consistent with the results obtained considering MOND only assuming very low values of the mass-to-luminosity ratio for the cluster (Sollima, Nipoti, Mastrobuono-Battisti, Montuori, and Capuzzo-Dolcetta, 2011).

4.10 Summary

Hybrid computational architectures composed by a standard multicore CPU host connected to some dedicated (or specialized) hardware apt to perform specific applications at a much higher speed than the host constitute viable ways to high performance computing in those scientific fields where it is sufficiently easy to enucleate a kernel of heavy computation. Graphic Processing Units (GPUs) represent a modern approach to the problem of providing the CPU based host of a “number cruncher” coupling the advantages of a general purpose, quite easily programmable, hardware to that of a high computational speed, reached mainly via its massively parallel structure. Moreover, the purchase expenditure and the modest power consumption make CPU+GPU hybrid architecture particularly attractive at least when dealing with problem up to a certain scale. The initial difficulties in using GPUs for scientific applications were mainly due to the obvious necessity to make them apt to an efficient data exchange with the hosting system and to exploit efficiently their huge number of threads to perform numerical computations on these data. The development of CUDA (Compute Unified Device Architecture) allowed a relatively easy use of GPUs, whose computing performances have been recently particularly enhanced. This framework well fits with the astrophysical topic of the evolution of stellar systems as classic gravitational N-body systems, where the $\mathrm{O}(N^2)$ pair-wise interactions constitute a clear bottleneck over the $\mathrm{O}(N)$ time integration and evaluation of the external force assumed given by a smooth mass distribution.

In this Chapter we attacked the problem of studying the evolution of an N body system in presence of an external field aiming at both high precision and good performances at least up to N of the order of few millions, like in populous globular clusters. The main results we obtained are listed and resumed in the following.

- We chose to implement symplectic time integration up to sixth order, to exploit also the machine double precision made available by NVIDIA GPUs of the TESLA series.

- Our code, called NBSymple, has a fast version which implements a second order in time, single precision arithmetics; when using two TESLA C1060 GPUs, this code allows the simulation of an $N = 1,536,000$ star globular cluster over the few internal crossing times (each crossing time requiring about 1.4 days) corresponding to an orbital period in the external field.

- The use of sixth order time integration implies a factor ~ 8 of performance decay, which couples with the contemporary worsening of TESLA C1060 performance when exploiting its double precision. This because TESLA C 1060 has 1 DP thread over 8, so that the speed performance decays substantially when using DP.

- A good compromise between computational velocity and precision is obtained resorting to the 'software' double precision, which works at a speed ~ 15 times higher than DP keeping a very good energy and momentum conservation.

- The time gain in using 2 GPUs instead of 1 begins at $\log N \simeq 4.1$, over which the N^2 scaling is clearly shown up. In the N^2 regime the speed ratio between the 2 GPUs and the 1 GPU codes is exactly 2. This suggests that having a shared-memory system with n GPUs yields a speed n times higher than a single GPU, provided an N large enough to overcome the overhead threshold.

- We also tested NBSymple with one or two boards of the last generation NVIDIA Fermi technology (TESLA C2050) showed easiness of porting. (i)

Regarding performances, they are about the same of TESLA C1060 when using SP, (ii) while they are much higher in DP, with a speed ratio about 20 when using sixth order time integration.

- The performance scaling when using two TESLA C2050 is linear, as in the case of TESLA C1060.
- We presented new versions of the code using MPI parallelization and variable time step. We also introduced 4^{th} and 6^{th} order Hermit integrators and we benchmarked the codes obtaining significant speed-up values.
- Moreover we run the MPI-version of NBSymple on Jazz hybrid cluster, equipped with 22 GPUs on 11 different nodes, verifying that the code performances scale linearly with the number of GPU provided that the number of particle in the system is big enough to exploit all the resources of each GPU.
- Given this, the aim of following the evolution of a GC over few hundred relaxation times in an external galactic field, as well as its interaction with a massive black hole in the inner galactic region is a reasonable aim by a hybrid architecture with a sufficient number of Fermi TESLA GPUs.
- In the last part of the Chapter we presented some applications of NBSymple where the code is used (i) to study the primordial evolution of young star cluster and (ii) to study the formation of tidal tails around Pal 14, one of the farthest Galactic GCs.
- We definitely found that NBSymple is able to handle such problems giving reliable results, even if run on only two GPUs.

Chapter 5

Dissipationless Formation and Evolution of the Milky Way Nuclear Star Cluster

As stated in Chapter 2 the dynamical evolution of GCSs could have influenced the properties of the central region of its host galaxy. In particular, in one widely discussed model for the formation of nuclear star clusters (NSCs), massive globular clusters spiral into the center of a galaxy and merge to form the nucleus. It is now known that at least some NSCs coexist with supermassive black holes (SMBHs, see Chapter 1); this is the case, for instance, in the Milky Way. In this Chapter, mainly collected in Antonini, Capuzzo-Dolcetta, Mastrobuono-Battisti, and Merritt (2011), Mastrobuono-Battisti and Capuzzo-Dolcetta (2011) and Capuzzo-Dolcetta, Antonini, and Mastrobuono-Battisti (2011), we keep on studying the stellar dynamics and star cluster evolution investigating how the presence of a SMBH at the center of the Milky Way impacts the merger hypothesis for the formation of its NSC. After general tests of the model we will focus our attention on the Milky Way NSC. Starting from a model consisting of a low-density nuclear stellar disk and the SMBH, we use large-scale N-body simulations to follow the successive inspiral and merger of globular clusters. The clusters are started on circular orbits of radius 20 pc, and their initial masses and radii are set up in such a way as to be consistent with the galactic tidal field at that radius. A total of 12 inspiral events are followed; the total accumulated mass is about $1.5 \times 10^7 M_\odot$. Each cluster is disrupted by the SMBH at a distance of roughly 1 pc. The density profile that results after the final inspiral event is characterized by a core of roughly this radius, and an envelope with density that falls off $\rho \sim r^{-2}$. These properties are similar to those of the Milky Way NSC, with the exception of the core size, which in the Milky Way is a little smaller. But by continuing the evolution of the model after the final inspiral event, we find that the core shrinks substantially via gravitational encounters in a time (when scaled to the Milky Way) of 10 Gyr as the stellar distribution evolves toward a Bahcall-Wolf cusp. We also show that the luminosity function of the Milky Way

NSC is consistent with the hypothesis that 1/2 of the mass comes from old (~ 10 Gyr) stars, brought in by globular clusters, with the other half due to continuous star formation. We conclude that a model in which a large fraction of the mass of the Milky Way NSC arose from infalling globular clusters is consistent with existing observational constraints.

This Chapter is organized as follows. Section 5.1 gives a general introduction to the faced problem and of the models involved. In Section 5.2 some general test of the merger model are described. The details of the initial models adopted in the Milky Way specific case are given in Section 5.4. Section 5.5 describes our simulations and results. Section 5.6 is devoted to the study of the collisional evolution of the NSC following its formation. The implications of our results in the contest of NSCs and Galactic center dynamics are discussed in Section 5.7. Section 5.8 sums up.

5.1 NSCs formation models

As shown in Section 1.4, the centers of low-luminosity spheroids, $M_B \gtrsim -18$, are often marked by the presence of compact stellar nuclei with half-light radii of a few parsecs and luminosities that are ~ 20 times that of a typical globular cluster (Carollo *et al.*, 1998; Böker *et al.*, 2002b; Côté *et al.*, 2006). The nearest such system is at the center of our Galaxy (Schödel, 2011). The Milky Way NSC is close enough that its radial and kinematical structure can be resolved (Schödel *et al.*, 2007, 2009; Oh *et al.*, 2009). Its total mass is estimated at $\sim 10^7 M_\odot$ (Launhardt *et al.*, 2002; Schödel *et al.*, 2008) and its half-light radius is roughly 3-5 pc (Graham and Spitler, 2009b; Schödel *et al.*, 2009; Schödel, 2011). There is a central core of radius ~ 0.5 pc (Buchholz *et al.*, 2009), beyond which the density falls off roughly as $r^{-1.8}$ (Oh *et al.*, 2009).

NSCs with properties similar to those of the Milky Way have now been detected in galaxies of all Hubble types (see Section 1.4). NSCs exhibit complex star formation histories; while the bulk of the stars appear to always be old, the fraction of young stars increases toward late-type galaxies. In galaxies beyond the Local Group, NSCs are typically unresolved, and the only structural properties that can be derived are half-light radii and total luminosities.

The study of NSCs has raised considerable interest because of the fairly strong correlations between their masses and the properties (mass, velocity dispersion) of their host galaxies (Ferrarese *et al.*, 2006a; Wehner and Harris, 2006b). These correlations suggest that the formation of NSCs and their host galaxies are linked in important ways (see also Section 1.4).

Two models for the formation of NSCs have been widely discussed. In the *insitu formation model*, buildup of molecular gas near the center of a galaxy leads to episodic star formation events. In this model, a NSC consists mostly of stars that formed locally (Schinnerer *et al.*, 2006, 2008). A number of mechanisms have been discussed for bringing the gas to the center, including the magneto-rotational instability in a differentially rotating gas disk (Milosavljević, 2004), tidal compression in shallow density profiles (Emsellem and van de Ven, 2008) or dynamical instabilities (Shlosman and Begelman, 1989; Bekki, 2007).

Alternatively, in the *merger model*, GCs sink to the center of a galaxy via dynamical friction and merge to form a compact stellar system (Tremaine *et al.*, 1975; Capuzzo-Dolcetta, 1993; Agarwal and Milosavljević, 2011). Observations of NSCs in dwarf elliptical galaxies suggest that the majority of such nuclei might have formed in this way (Lotz *et al.*, 2004). Numerical simulations have also shown that the basic properties of NSCs are consistent with a merger origin (Bekki *et al.*, 2004; Capuzzo-Dolcetta and Miocchi, 2008a,b; Hartmann *et al.*, 2011).

In addition to a NSC, the Milky Way also contains a massive black hole (SMBH) whose mass, $M_\bullet \approx 4 \times 10^6 M_\odot$ (Ghez *et al.*, 2008; Gillessen *et al.*, 2009), is comparable with that of the NSC. A handful of other galaxies are also known to contain both a NSC and a SMBH (Seth *et al.*, 2008b; Graham and Spitler, 2009b), and the ratio of SMBH to NSC mass in these galaxies is of order unity.

A simple argument leads to a 1 pc scale as the relevant one for the merger model for the formation of NSCs. The beginning of the disruption process of a globular cluster due to tidal stresses from a SMBH is expected when it passes within a certain distance of the galaxy center, limiting the density within that radius. Disruption occurs at a distance $r = r_{\rm disr}$ from the SMBH, where

$$\frac{M_\bullet}{\frac{4}{3}\pi r_{\rm disr}^3} \approx \rho(0) \approx \frac{9}{4\pi G}\frac{\sigma_K^2}{r_K^2}. \tag{5.1}$$

Here $\rho(0)$ is the central (core) density of the globular cluster, σ_K its central, one-dimensional velocity dispersion, and r_K its core radius; the second relation is the "core-fitting formula" (King, 1966). Writing

$$r_{\rm infl} \equiv \frac{GM_\bullet}{\sigma_{\rm NSC}^2} \approx 1.3{\rm pc}\left(\frac{M_\bullet}{4\times 10^6 M_\odot}\right)\left(\frac{\sigma_{\rm NSC}}{100{\rm km\ s}^{-1}}\right)^{-2} \tag{5.2}$$

for the gravitational influence radius of the SMBH, where $\sigma_{\rm NSC}$ is the stellar velocity dispersion in the NSC, Equation (5.1) becomes

$$r_{\rm disr} \approx 2\left(\frac{\sigma_{\rm NSC}}{5\sigma_K}\right)^{2/3}\left(\frac{r_{\rm infl}}{r_K}\right)^{1/3} r_c. \tag{5.3}$$

Setting $r_K = 0.5$ pc and $\sigma_K = 20$ km s^{-1}, values characteristic of the most massive globular clusters, we find $r_{\rm disr} \approx 1$ pc for the Milky Way. This is roughly equal to the radius of the core (~ 0.5 pc) that is observed in the distribution of late-type stars (Buchholz *et al.*, 2009).

5.2 General tests

Before studying the Milky Way we performed some self-consistent simulations referred to a generic galaxy where a GC decays toward its center and settle there reaching a steady state around the SMBH of mass 5×10^6 M$_\odot$ located at the center of the same galaxy. Our aim is to test the merger model in a generic background, before adopting it to explain the Milky Way NSC formation.

5.2.1 The code

All the simulations presented in this Chapter were performed by using NBSymple (for basic tests) and ϕGRAPE (Harfst *et al.*, 2007), a direct-summation code optimized for computer clusters incorporating the GRAPE special-purpose accelerators (Makino and Taiji, 1998). ϕGRAPE implements a fourth-order Hermite integrator with a predictor-corrector scheme and hierarchical time stepping. The accuracy and performance of the code are set by the time-step parameter η and the smoothing length ϵ. In what follows, we set $\eta = 0.01$ and $\epsilon = 0.02 r_K$ (10^{-2} pc in our case), With this choices, energy conservation was typically $\lesssim 0.01\%$ during a single merging event. The simulations were carried out using the 32-node GRAPE cluster at the Rochester Institute of Technology, and also on our workstations containing TESLA C2050 graphics processing units (see Chapter 4). In the latter integrations, ϕGRAPE was used with SAPPORO, a CUDA library that emulates double-precision force calculations on single precision hardware (Gaburov *et al.*, 2009).

5.2.2 The models

In order to test the model the galaxy was modeled as a truncated Dehnen law (Dehnen, 1993)

$$\rho(r) = \frac{(3-\gamma)M_{gal}}{4\pi} \frac{a}{r^\gamma (r+a)^{4-\gamma}} \text{sech}\left(\frac{r}{r_{cut}}\right), \tag{5.4}$$

where $\gamma = 0.5$, $M_{gal} = 2.0 \times 10^9$ M$_\odot$, $a = 420$ pc, $r_{cut} = 150$ pc. The value of γ corresponds to the shallowest power law density profile consistent with an isotropic velocity distribution around a dominating point mass potential (Merritt, 2006) Only compact and very massive GCs can spiral to the center of their host galaxy in a time interval significantly smaller than the Hubble time (Capuzzo-Dolcetta, 1993). Thus, for the GC, we chose a King model (King, 1966) with $W_0 = 8$, total mass $M_{tot} = 5 \times 10^6$ M$_\odot$, core radius $r_c = 0.5$ pc, tidal radius $r_t = 36$ pc, and a central velocity dispersion $\sigma_K = 37.7$ km/s.
Therefore, the SMBH and the GC has the same mass.

We sampled the N-body representation of the galaxy given by Equation (5.4), using single mass particle, with $m_* = 400$ M$_\odot$; the total number of particles in the galaxy is $N_{gal} = 359238$. The King model was also sampled using particles of mass, m_*, and obtaining a GC N-body representation composed by $N_{GC} = 12500$ particles.
In the following subsections the results of two different simulations performed using these initial conditions are presented.

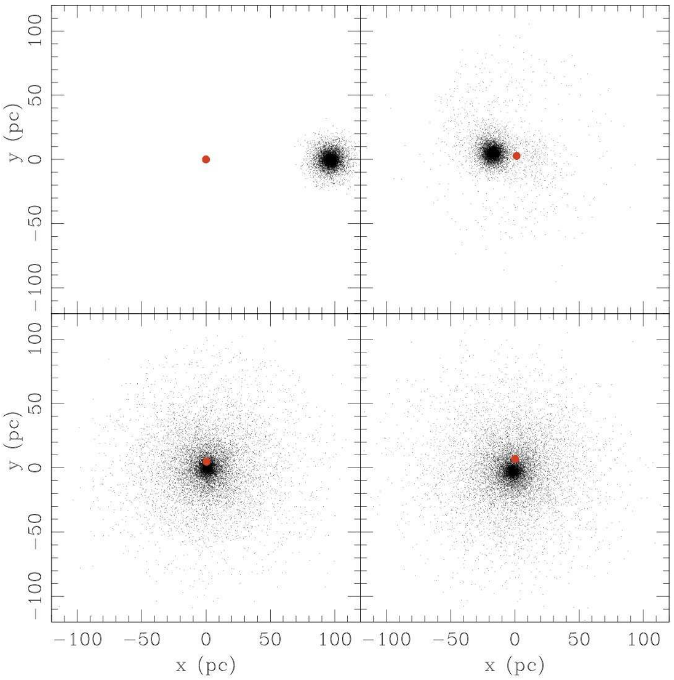

Figure 5.1. Some snapshots, taken at regular interval of time, of the simulation where the GC is initially on a circular orbit. The red dot represents the central SMBH.

5.2.3 GC on a circular orbit

We initially put the GC at a distance of 100 pc from the galactic center on its circular orbit. Due to dynamical friction, the cluster spirals and reaches the inner region of the galaxy where it merges around the central SMBH (see Figure 5.1 for some snapshots of the simulation) settling on a quasi stable condition. The decay and the merger happen in a relatively short time (~ 52 Myr$\simeq 36\ t_{cr}$, where t_{cr} is the internal crossing time of the GC) and at the end of the simulation we obtain a central cluster which shows the same features of the observed NSCs. Its spatial density is indeed well distinguishable from the one of the underlying galaxy. Moreover it is well fitted by a a modified Hubble law[1] (Rood *et al.*, 1972a):

$$\rho_{cl}(r) = \frac{\rho_{0,cl}}{\left[1 + \left(\frac{r}{r_{0,cl}}\right)^2\right]^{\frac{3}{2}}}, \tag{5.5}$$

---

[1] The core radius of the modified Hubble law is almost identical to the "core" radius of a King profile, the King radius being the radius at which the projected density of an isothermal sphere drops to almost half (0.5013) as oppose to half (0.5) for the core radius of the modified Hubble law (Kissler-Patig *et al.*, 1999; Rood *et al.*, 1972a).

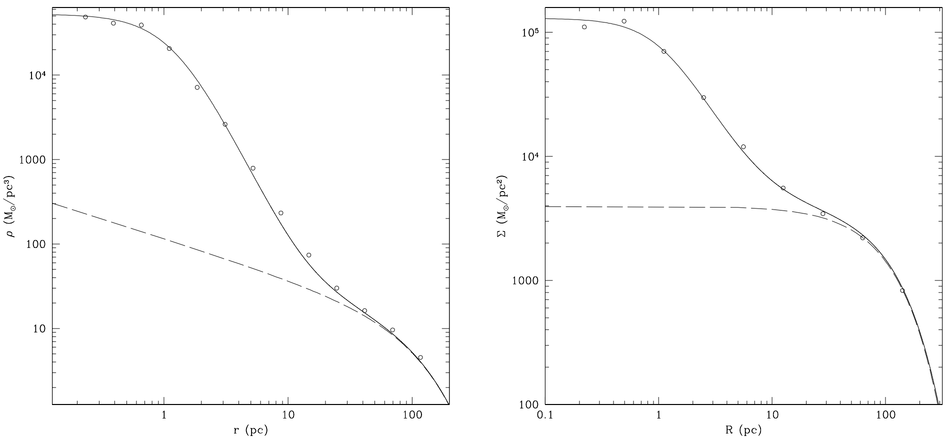

Figure 5.2. Left panel: spatial density profile (empty circles) of the total system at the end of the decay and of the following merger with the central SMBH in the case of an initially circular orbit. The dashed line is the Dehnen model that best fits the density profile of the galaxy, the solid line is the best fit on the total (NSC and galaxy) system. Right panel: Projected density profile of the same total system. The dashed line is the best Sérsic fitting law to the galaxy projected density profile while the solid line is the best fitting law to the total system (see text for the details).

where $\rho_{0,cl} = 4.2 \times 10^4$ M$_\odot$/pc^3 and $r_{0,cl} = 1.2$ pc. The spatial density profile of the galaxy is well fitted by a Dehnen model (see Equation (5.4))

$$\rho_{gal}(r) = \frac{1.7 \times 10^{11}\ \mathrm{M_\odot pc}}{r^{0.47}(r + 420\mathrm{pc})^{3.53}} \mathrm{sech}\left(\frac{r}{150\mathrm{pc}}\right) \tag{5.6}$$

and is represented by the dashed line in the left panel of Figure 5.2; the solid line, in the same plots, gives the sum of the fits on the NSC and on the galaxy density profiles, thus it represents the best fit to the spatial profile of the total system composed by the galaxy and the central super cluster. The projected profile of the same total system is well modeled by the sum of a modified core model (see Equation (2.1))

$$\Sigma_{tot}(R) = \frac{1.0 \times 10^5}{\left[1 + \left(\frac{R}{1.1\mathrm{pc}}\right)^2\right]^{0.86}}\ \mathrm{M_\odot/pc^2}, \tag{5.7}$$

and of a Sérsic law (Sérsic, 1963)

$$\Sigma(R) = \Sigma_0 \mathrm{e}^{\left[-b\left(\frac{R}{R_e}\right)^{\frac{1}{n}} + b\right]}, \tag{5.8}$$

with

$$b = 2n - \frac{1}{3} + \frac{0.009876}{n}. \tag{5.9}$$

The best fitting parameter of this law are: $\Sigma_0 = 8.4 \times 10^2$ M$_\odot$/pc^2, $b = 1.33$, $R_e = 124.4$ pc and $n = 0.83$ (see dashed line in right panel of Figure 5.2). As we

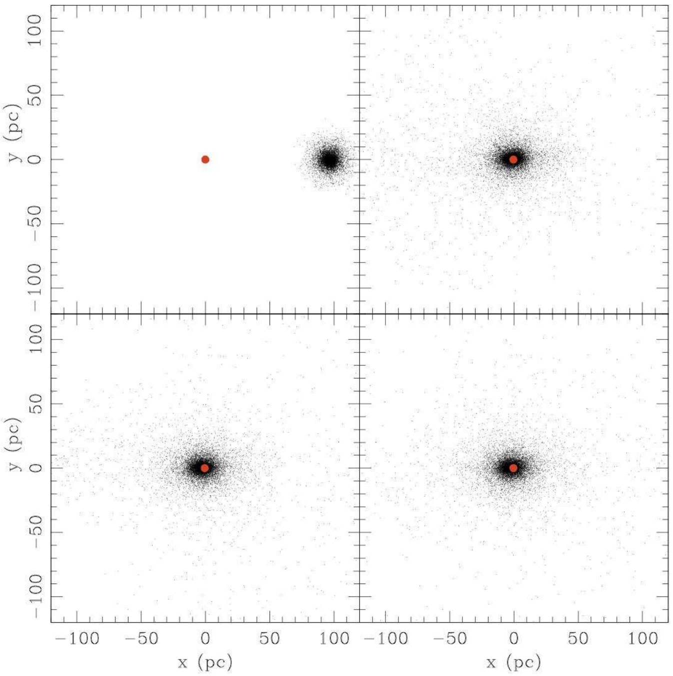

Figure 5.3. Some snapshots, taken at regular interval of time, of the simulation where the GC is initially on a radial orbit. The red dot represents the SMBH. Only the particles in the GC are shown.

will see in the following Sections, this results corroborate the hypothesis that NSC could have originate from the decay of globular clusters toward the center of their host galaxy where a SMBH is located. Obviously in this scenario, more than one GC may arrive in the central galactic center, and we will investigate this hypothesis in Section 5.3.

5.2.4 GC on a radial orbit

In the second simulation we run, the GC is initially put on a radial orbit at an initial distance of 100 pc. Some snapshots of the simulation are shown in Figure 5.3. We waited for the complete decay of the GC and then we took the spatial and projected density profiles, and using the same laws adopted in the "circular" case we obtained that for the total system the best fitting law to the spatial density profile is given by

$$\rho_{tot}(r) = \left\{ \frac{8.84\times 10^3}{\left[1+\left(\frac{r}{2.6\mathrm{pc}}\right)^2\right]^{\frac{3}{2}}} + \frac{2.0\times 10^{11}}{r^{0.54}(r+415\mathrm{pc})^{3.46}}\mathrm{sech}\left(\frac{r}{150\mathrm{pc}}\right)\right\}\frac{\mathrm{M}_\odot}{\mathrm{pc}^3} \qquad (5.10)$$

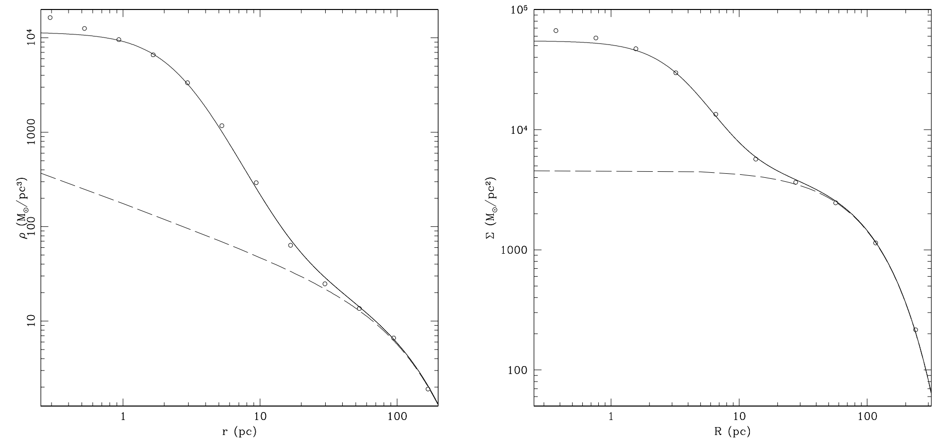

Figure 5.4. Left panel: spatial density profile (empty circles) of the total system at the end of the decay and of the following merger with the central SMBH in the case of an initially radial orbit. The dashed line is the Dehnen model that best fits the density profile of the galaxy, the solid line is the best fit on the total (NSC and galaxy) system. Right panel: Projected density profile of the same total system. The dashed line is the best Sérsic fitting law to the galaxy projected density profile while the solid line is the best fitting law to the total system (see text for the details).

(see left panel of Figure 5.4), while for the projected density profile we have

$$\Sigma_{tot}(R) = \left\{ \frac{4.2 \times 10^4}{\left[1 + \left(\frac{R}{3.8\mathrm{pc}}\right)^2\right]^{1.26}} + 2.2 \times 10^3 \left[\mathrm{e}^{-1.58\left(\frac{R}{121\mathrm{pc}}\right)^{1.12} + 1.58}\right] \right\} \frac{\mathrm{M}_\odot}{\mathrm{pc}^2} \tag{5.11}$$

as the best fitting law (see right panel of Figure 5.4). Also in this case we obtained a system that resembles the observed NSCs (see Section 1.4); this system shows the same properties of the one obtained in the case of the circular orbit except for the fact that the value of the central density is slightly smaller than in this case.

5.3 The Milky Way NSC

In the following Sections we will focus on the Milky Way case. Our initial conditions consist of a SMBH and a diffuse stellar component that models the inner parts of the nuclear stellar disk (Launhardt *et al.*, 2002). The NSC is built up by the successive inspiral of globular clusters, which we inject into the system at a radius of 20 pc. The clusters are assigned masses and radii consistent with those of globular clusters that were initially very massive ($\sim 4 \times 10^6 M_\odot$) but which were tidally limited by the Galaxy's tidal field. As the clusters spiral is due to dynamical friction against the stars in the disk component, they eventually come within the radius of tidal disruption of the SMBH. We follow 12 such inspirals, resulting in the accumulation of $\sim 10^7 M_\odot$. The NSC that results has properties that are consistent with the observed properties of the Milky Way NSC, including a $\rho \sim r^{-2}$ density profile and a parsec-scale core.

At the Galactic center, the relaxation time at SgrA*'s influence radius is roughly $20 - 30$ Gyr, assuming Solar-mass stars (Merritt, 2010). This is too long for a Bahcall and Wolf (1976) cusp to have formed over the Galaxy's lifetime, consistent with the observed lack of a cusp (Buchholz *et al.*, 2009; Do *et al.*, 2009; Bartko *et al.*, 2010). But a pre-existing core with radius smaller than the SMBH influence radius would have shrunk appreciably over a time of 10 Gyr due to gravitational encounters (Merritt, 2010). We investigate the effect of such evolution on our NSC model by continuing the N-body integrations after the final infall event, for a time that corresponds to roughly 10 Gyr after scaling to the Milky Way. The core radius decreases by roughly a factor of two in this time, bringing it to a size that is more consistent with the observed core size. The density profile beyond the core remains nearly unchanged.

In the merger model the bulk of the nuclear population is predicted to be as old ($\sim$ 10 Gyr) as the oldest globular clusters. Accordingly, using *Hubble Space Telescope* Near-Infrared Camera and Multiobject spectrometer (NICMOS) imaging of the inner 30 pc of the Galaxy, we show that the luminosity function of the Milky Way NSC is consistent with the hypothesis that a large fraction of its mass is in ancient stars.

5.4 The Milky Way case: Initial conditions

In the following, we perform full N-body simulations to study the consecutive infall and merging of a set of 12 globular clusters each starting from a galactocentric distance of 20 pc. After the first globular cluster is disrupted, we wait for the NSC to reach a steady state and we add to the system a second globular cluster. This procedure was iterated until 12 clusters accumulated and merged in the inner regions of the galaxy where we initially placed a central SMBH. Snapshots from the simulations are given in Figure 5.5.

We begin in this section by outlining the details of the initial conditions adopted in the simulations.

5.4.1 The Galactic Model

The nuclear bulge is distinguished from the larger Galactic bulge (effective radius $\sim$ 1 kpc) by its flat disk-like morphology, high stellar densities, and a history of continuous star formation. The nuclear bulge dominates the inner 300 pc of the Milky Way and it appears as a, distinct, massive disk-like complex of stars and molecular clouds which is, on a large scale, symmetric with respect to the Galactic center. It consists of an r^{-2} nuclear stellar cluster within the inner $\sim$ 30 pc, a larger nuclear stellar disk and a nuclear molecular disk of same size (radius $\sim$ 200 pc and

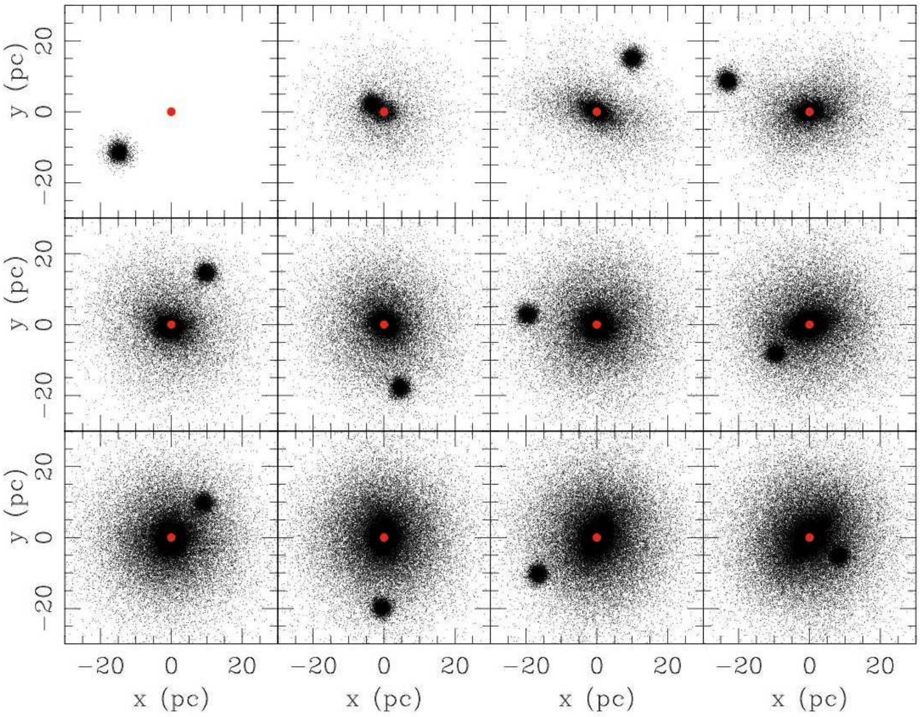

Figure 5.5. Snapshots from the N-body integrations, projected onto a fixed $(x-y)$ plane at the start of each infall event. Only particles coming originally from the infalling clusters are displayed. The SMBH is shown as the red circle.

scale height ~ 45 pc). The total stellar mass and luminosity of the nuclear bulge are 1.5×10^9 $\mathrm{M}_\odot$ and $\sim 2.5\times10^9$ $\mathrm{L}_\odot$, respectively (Launhardt *et al.*, 2002). The r^{-2} density distribution holds only within the NSC in the central ~ 30 pc, while, at larger radii, the mass distribution is dominated by the nuclear stellar disk which has essentially a flat density profile (Schödel, 2011). The initial conditions for the galaxy in our simulations model the nuclear stellar disk and they omit the central NSC. Accordingly, they correspond to a shallow density cusp around a SMBH, which is included as a massive particle, $M_\bullet = 4\times10^6\mathrm{M}_\odot$, located at the origin.

We adopted a truncated power-law model for this component:

$$\rho_{gx}(r) = \tilde{\rho}\left(\frac{r}{\tilde{r}}\right)^{-\gamma} \mathrm{sech}\left(\frac{r}{r_{\mathrm{cut}}}\right). \tag{5.12}$$

where $\tilde{\rho} = 400\mathrm{M}_\odot/\mathrm{pc}^3$ is the density at $r=\tilde{r}=10$pc, and the truncation function is the same used by McMillan and Dehnen (2005), see left panel of Figure 5.6. Since $\mathrm{sech}(x)\approx 1-\frac{x^2}{2}$ for $x\ll1$, the model is essentially a power law at $r\ll r_{\mathrm{cut}}$, but it tends exponentially to zero for $r\gg r_{\mathrm{cut}}$. As done in the previous tests, we chose $\gamma=0.5$. The resulting model implies a mass density at 10 pc similar to what is found in the Galaxy outside the NSC ($\sim 400\ M_\odot/\mathrm{pc}^3$). We chose $r_{\mathrm{cut}}=22$ pc which gives a total mass of the (truncated) galactic model equal to $9.1\times10^7\mathrm{M}_\odot$. In order

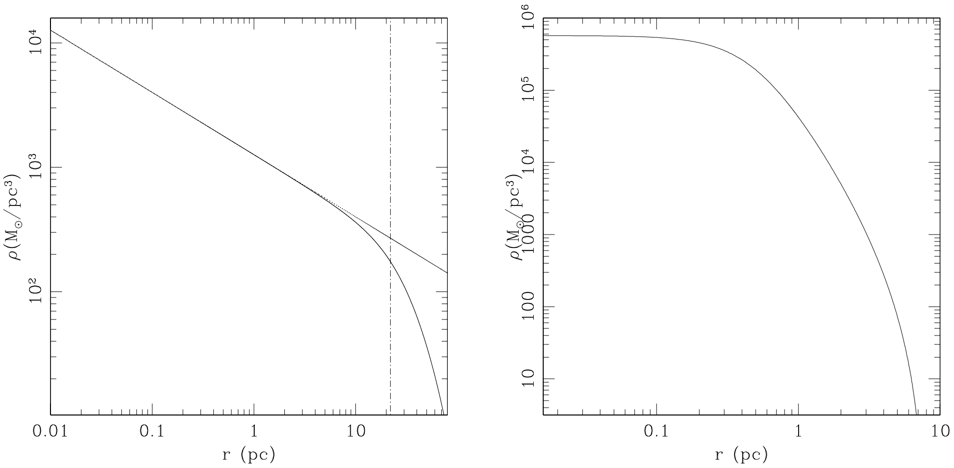

Figure 5.6. Left panel: untruncated (dashed line) and truncated (solid line) initial Galaxy density profile. Right panel: Initial GC profile.

to generate a Monte-Carlo realization of the distribution function corresponding to the truncated density profile of Equation (5.12) we followed the method described in Szell *et al.* (2005). Using Eddington's formula, it can be shown that the cumulative fraction of stars at radius r with velocities less than v is:

$$\begin{aligned} F(<v,r) &= 1-\frac{1}{\rho}\int_0^E d\phi' \frac{d\rho}{d\phi'} \times \\ & \left\{1+\frac{2}{\pi}\left[\frac{v/\sqrt{2}}{\sqrt{\phi'-E}}-\tan^{-1}\left(\frac{v/\sqrt{2}}{\sqrt{\phi'-E}}\right)\right]\right\}, \end{aligned} \tag{5.13}$$

where $E=\frac{1}{2}v^2+\phi(r)$ and $\phi(r)$ is the total gravitational potential produced by the stars and the SMBH. Once the positions are assigned, Equation (5.13) can be numerically solved to distribute the particles in velocity space.

A good compromise between reliability of the results and computational effort was found by setting $N = 240,000$ for the galaxy, which implies a mass of $380\mathrm{M}_\odot$ for each particle in the system.

5.4.2 The Globular Cluster Model

The globular clusters were initially placed on circular orbits with orbital radii $r_0 =$ 20 pc. In order not to favor any particular direction for the inspiral, the orbital angular momenta were selected in the following way (e.g., Gualandris and Merritt, 2009). The surface of a sphere can be tessellated by means of 12 regular pentagons, the centers of which form a regular dodecahedron inscribed in the sphere. The coordinates of the centers of these pentagons were identified with the tips of the 12 orbital angular momentum vectors. In this way, the inclination and longitude of ascending node of each initial orbit were determined. The choice of circular orbits was motivated by the well-known effect of orbital circularization due to dynamical friction (Casertano *et al.*, 1987; Ibata and Lewis, 1998; Hashimoto *et al.*, 2003).

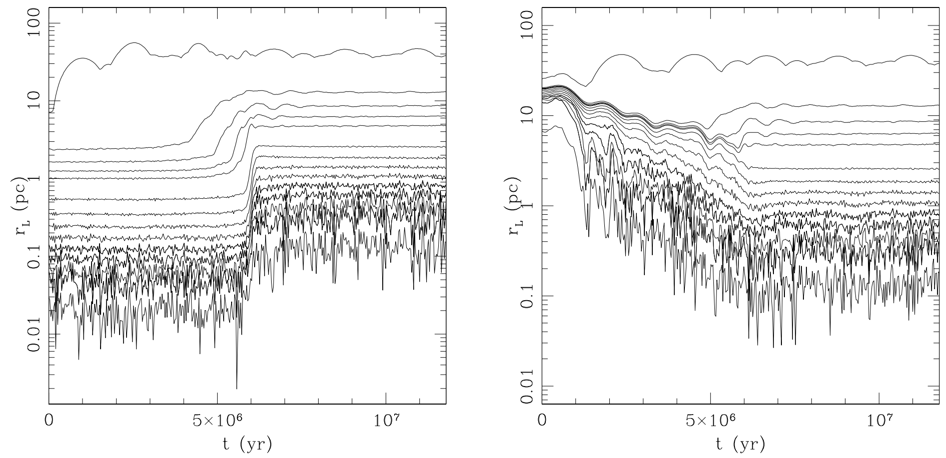

Figure 5.7. Lagrange radii of the first cluster that arrives at the center of the galaxy. In the left panel the Lagrangian radii are computed with respect to the center of density of the globular cluster, while in the right panel with respect to the central SMBH. The time for each cluster to settle in a steady state after its disruption is only few Myrs.

At a distance of 20 pc from the Galactic center, a globular cluster would already have been subject to tidal forces from the galaxy and the SMBH, and its total mass and radius would be less than their original values when the globular cluster was far from the center. We assumed that the *central* properties of the globular clusters were unaffected by tidal forces during the inspiral to 20 pc, and adopted values characteristic of massive clusters: central velocity dispersion $\sigma_K = 35$ km s^{-1} and core radius $r_K = 0.5$ pc. If the dimensionless central (King) potential is $W_0 = 8$, the total mass works out to be $m \approx 4 \times 10^6$ M$_\odot$. This value of σ_K is roughly two times the maximum value of $\sim$ 18km s^{-1} listed in Harris (1996b)'s compilation of Galactic globular clusters properties, while the core radius is roughly equal to the median value in that compilation. Our choice of such a large value for σ_K is justified by the fact that only massive clusters, if they are compact enough, could have arrived in the central regions of the Galaxy in a reasonable time without being destroyed by Galactic tidal forces in the process (Miocchi *et al.* 2006 and Section 5.7.1).

We then needed to generate equilibrium models for globular clusters with these same central properties, but with total masses and limiting (tidal) radii consistent with the known tidal forces from the Galaxy model at 20 pc. This is not a completely straightforward exercise, since the gravitational force from the globular cluster acting on a star at the cluster's limiting radius, r_T, depends both on r_T and on the cluster mass m_T within r_T, and m_T is a function of r_T.

We proceeded in the following way. We first assumed $r_T \gg r_K$. In this case, a King-like model satisfies the following relation between m_T and r_T:

$$Gm_T \approx \frac{1}{2}\sigma_K^2 r_T. \tag{5.14}$$

Given this relation, the tidal radius can then be related to the Galactic potential ϕ

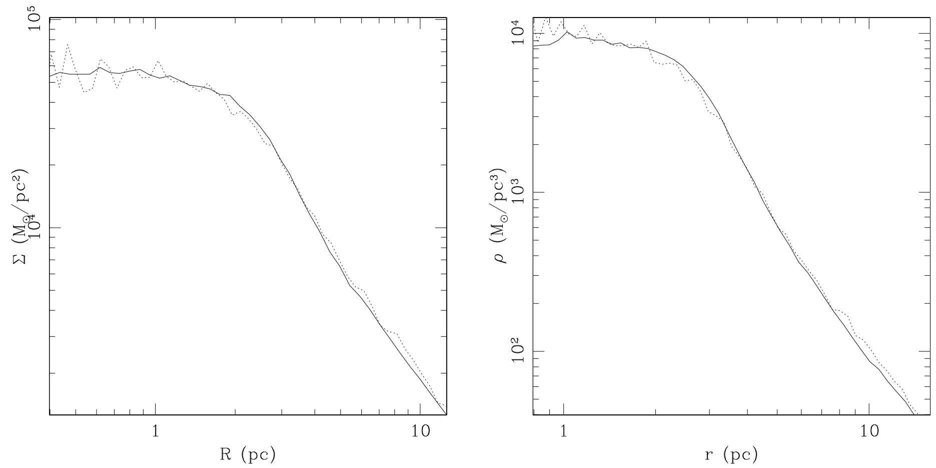

Figure 5.8. Comparison between the projected (left panel) and spatial (right panel) density profiles obtained with $N_{GC} = 5715$ (solid line) and $N_{GC} = 57150$ (dotted line).

and density ρ by (e.g., King, 1962)

$$r_T = \frac{1}{\sqrt{2}}\sigma_K \left[\frac{3}{r_0}\left(\frac{d\phi}{dr}\right) - 4\pi G\rho\right]^{-1/2}. \tag{5.15}$$

Using the galaxy mass distribution of Equation (5.12) and considering the presence of the SMBH, but ignoring the truncation function, we find

$$\frac{d\phi}{dr} = \frac{8\pi}{5}G\tilde{\rho}\tilde{r}\left(\frac{r}{\tilde{r}}\right)^{\frac{1}{2}} + \frac{GM_\bullet}{r^2}\ , \tag{5.16}$$

giving a limiting radius of

$$r_T = \frac{1}{\sqrt{2}}\sigma_K \left[\frac{4\pi}{5}G\tilde{\rho}\left(\frac{r_0}{\tilde{r}}\right)^{-1/2} + \frac{3GM_\bullet}{r_0^3}\right]^{-1/2} \tag{5.17}$$

and a tidally-truncated mass from Equation (5.14). Adopting a distance $r_0 = 20$ pc we find $r_T \approx 8$ pc and $m_T \approx 1.1 \times 10^6$ M$_\odot$; in other words, roughly 3/4 of the globular cluster mass would have been removed in the process of inspiralling to 20 pc.

We then equated this m_T with the mass of a new King model having the same core properties:

$$m_T = m_K \equiv \rho(0)r_K^3\mu(W_0) \approx \frac{9}{4\pi G}\sigma_K^2 r_K \mu(W_0). \tag{5.18}$$

Here $\mu(W_0)$ is a function of the dimensionless central potential that is tabulated by King (1966). Since all the quantities in Equation (5.18) are known except for W_0, we can solve for this variable, and find $W_0 = 5.8$. The three parameters (W_0, r_K, σ_K) then uniquely define the King model that was used to generate the initial conditions of the globular clusters (see right panel of Figure 5.6).

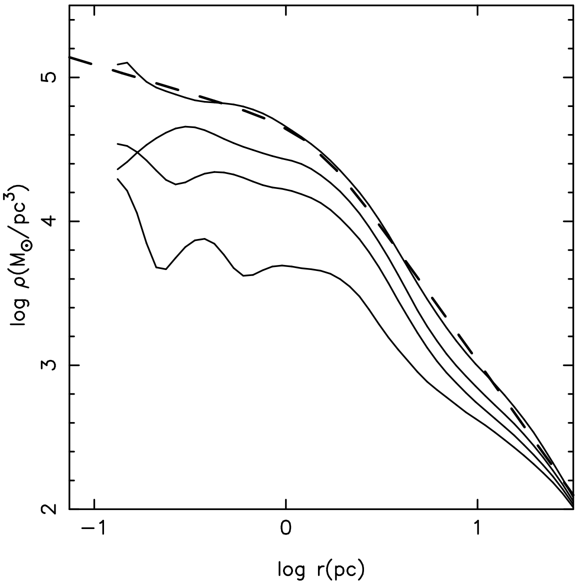

Figure 5.9. Spatial profile of the central NSC after 3, 6, 9 and 12 mergers. The central density grows with time. The dashed line is the fit to the NSC profile obtained at the end of the entire simulation using the broken power law model of Equation 5.19.

As previously stated, the mass of the single particle in the galaxy was 380 $M_\odot$. For the particles in the clusters we choose $200M_\odot$, approximately one half of that value. With this choice, the total number of particles in each globular cluster was $5,715$ with 740 particles contained within the cluster core.

5.5 N-body simulations

During each infall event, we followed the evolution of the system until the globular cluster had reached the center of the galaxy and established an approximately steady state. This condition was verified by studying the time evolution of the globular cluster Lagrange radii, constructed both with respect to the center of density of the cluster (as defined by the algorithm in Casertano and Hut (1985)), and with respect to the central SMBH. When the Lagrange radii had reached nearly constant values, the next globular cluster was introduced. Figure 5.7 plots the time evolution of Lagrange radii for the first infall event. The figure shows that each merging episode lasts approximately 10^7yr and that the time scale for a globular cluster to reach a steady state following its disruption is indeed very short, of the order of Myr.

We evaluated the N-dependence of our results by simulating the first three infalls using the same orbital initial conditions but with ten times more particles to represent the clusters. Comparing the density profile of the NSC after the three infalls with that obtained in the original integrations did not reveal any significant differences between the two cases (see Figure 5.8).

In addition, we tested the alternative scenario where the 12 clusters, initially

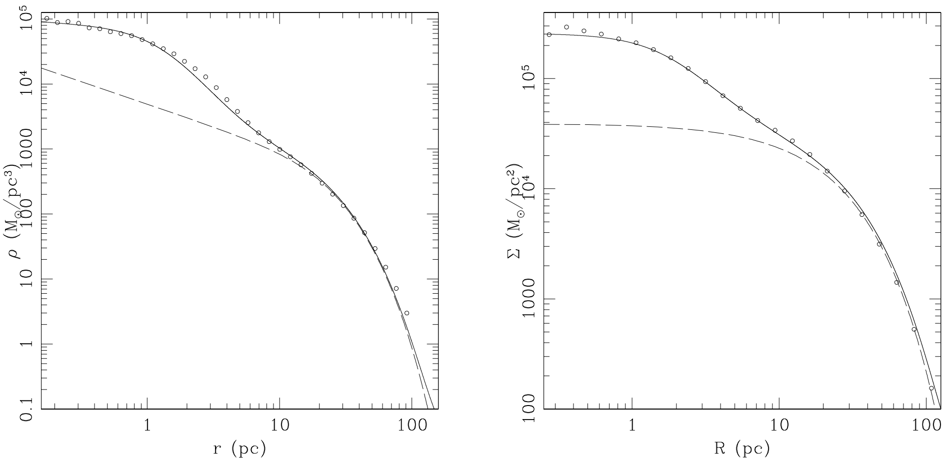

Figure 5.10. Spatial (right panel) and projected (left panel) density profiles at the end of the simulation. In each panel, the empty circles give the density profile of the N-body model, the solid lines give the best fitting model to the entire system (galaxy+NSC) and the dashed curves give the fit to the density profile of the galaxy, see text for explanation.

located on their respective orbit, start to decay all at the same time. We stress that this "contemporary" infall scenario, adopted in most previously published works, would require a quite special initial state in which all the clusters start their infall at the same radius at a given time. In reality, globular clusters will arrive at the center at essentially random times, and the interval between these events, which is fixed by dynamical friction time-scale (of the order Gyr), will almost certainly be long compared with the time required for a single globular cluster to reach a steady state following its disruption (∼Myr in Figure 5.7). We also notice that, as long as the simulations respect this separation of timescales, the exact interval between the infall events is essentially irrelevant. In this sense, the "repeated" initial conditions are more generic. For this reason, in what follows, we will focus on this latter scenario, but we will also briefly discuss the results from a "contemporary" infalls simulation.

5.5.1 Results: density profiles

Figure 5.9 shows the density profile of the system after the complete merging of 3, 6, 9 and 12 clusters. We fitted the spatial density of the final system, within 10 pc around the SMBH, using the broken power law model (e.g., Saha, 1992; Zhao, 1996):

$$\rho(r) = \rho_b \left(\frac{r}{r_b}\right)^{-\gamma_i} \left[1 + \left(\frac{r}{r_b}\right)^{\alpha}\right]^{(\gamma_i-\beta)/\alpha}, \tag{5.19}$$

where γ_i is the slope of the inner density profile, β the external slope and α is a parameter that defines the transition strength between inner and outer power laws. The best-fit parameters were $\rho_b = 4.1 \times 10^4 \mathrm{M}_{\odot}/\mathrm{pc}^3$, $r_b = 1.5$pc, $\gamma_i = 0.45$, $\beta = 1.90$

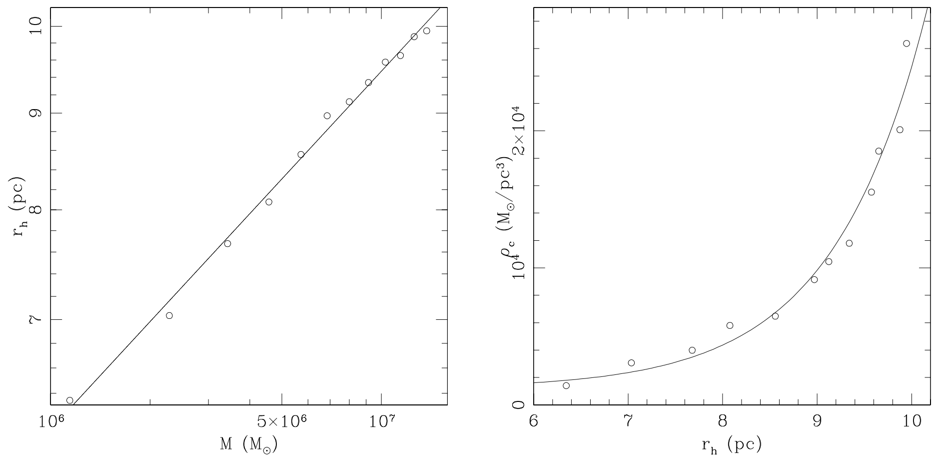

Figure 5.11. Left panel: empty circles represent the half mass radius of the central NSC as a function of the total mass of the same system. The solid line represents the scaling relation given in Equation (5.24). Right panel: the core density of the cluster versus its half mass radius (empty circles). The solid line shows the $\rho_c - r_h$ relation given by Equation (5.25).

and $\alpha = 3.73$. The model corresponding to this set of parameters is given by the dashed line in Figure 5.9.

Figure 5.10 (right panel) plots the spatial density at the end of the simulation over a wider radial range than in Figure 5.9. We fitted the total density as a superposition of two parametric models, one intended to represent the NSC and the other the galaxy. For the NSC we adopted the modified Hubble law (Rood *et al.*, 1972b):

$$\rho_{cl}(r) = \rho_{0,cl}\left[1+\left(\frac{r}{r_{0,cl}}\right)^2\right]^{-\frac{3}{2}}, \tag{5.20}$$

with best fitting parameters $\rho_{0,cl} = 7.46 \times 10^4$ M$_\odot$/ pc^3 and $r_{0,cl} = 1.4$ pc. The galaxy remained well-fit by the initial “truncated” power law of Equation (5.12), when $\tilde{\rho} = 9.91 \times 10^2$ M$_\odot$/ pc^3, $\tilde{r} = 10$ pc, $\gamma = 0.69$, and $r_{\rm cut} = 16.3$ pc. The right panel of Figure 5.10 shows the projected density of the N-body model at the end of the simulation. We again fit this profile with a two-component model. For the NSC we used

$$\Sigma_{cl}(R) = \Sigma_{0,cl}\left[1+\left(\frac{R}{R_{0,cl}}\right)^2\right]^{-\zeta}, \tag{5.21}$$

while the projected density profile of the galaxy was represented by a Sérsic law:

$$\Sigma_{gx}(R) = \Sigma_{0,gx}\text{exp}\left[-b\left(\frac{R}{R_{0,gx}}\right)^{\frac{1}{n}}+b\right], \tag{5.22}$$

with

$$b = 2n - \frac{1}{3} + \frac{0.009876}{n}. \tag{5.23}$$

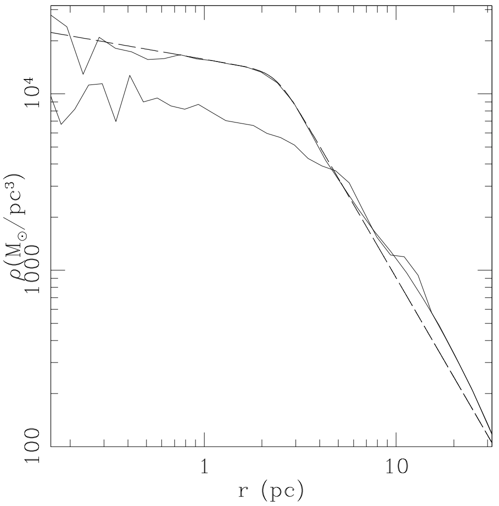

Figure 5.12. Spatial profile of the central super cluster at two different times. The long dashed line represents the Nuker best fit on.

The best-fit parameters were $\Sigma_{0,cl} = 2.18{\times}10^5$ M$_\odot$/pc^2, $R_{0,cl} = 1.99$ pc and $\zeta = 1.03$ for the NSC; $\Sigma_{0,gx} = 7.31 \times 10^3$ M$_\odot$/ pc^2, $b = 1.68$, $R_{0,gx} = 32.3$ pc and $n = 1.003$ for the bulge.

Remarkably, our simulations result in a final density profile having nearly the same power-law index beyond $\sim$ 0.5 pc as observed ($\Sigma(r) \sim r^{-1}$; Becklin and Neugebauer, 1968; Haller *et al.*, 1996). In addition, the central region ($r < r_b$) of our model exhibits a shallow density profile (or core) near the SMBH, also in agreement with observations (Buchholz *et al.*, 2009). The core radius in our model ($\sim$ 2 pc) is somewhat larger than the observed core, of radius $\sim$ 0.5 pc. In Section 5.6 we show that two-body relaxation would cause such a core to shrink over Gyr time scales, as the density evolves toward, but does not fully reach, a collisional steady state.

In the right panel of Figure 5.11 the half-mass radius (r_h) of the NSC component is plotted as a function of the NSC mass (M_{cl}) at the end of each infall. At any time, the NSC mass is given by the sum of the accumulated globular cluster masses. A good fit to the data is obtained by

$$r_h = 0.45 \left(\frac{M_{cl}}{M_\odot}\right)^{0.19} \text{ pc} , \tag{5.24}$$

represented by the solid line. The dependence of r_h on M_{cl} is weak, due to the fact that the size of the NSC is determined essentially by the fixed tidal field from the SMBH.

Assuming for the growing NSC the density law of Equation (5.20), the core density can be defined as $\rho_c = \rho_{0,cl}/2^{\frac{3}{2}}$ and the values of ρ_c, obtained after the end of each infall, can be plotted as a function of the half mass radius of the same

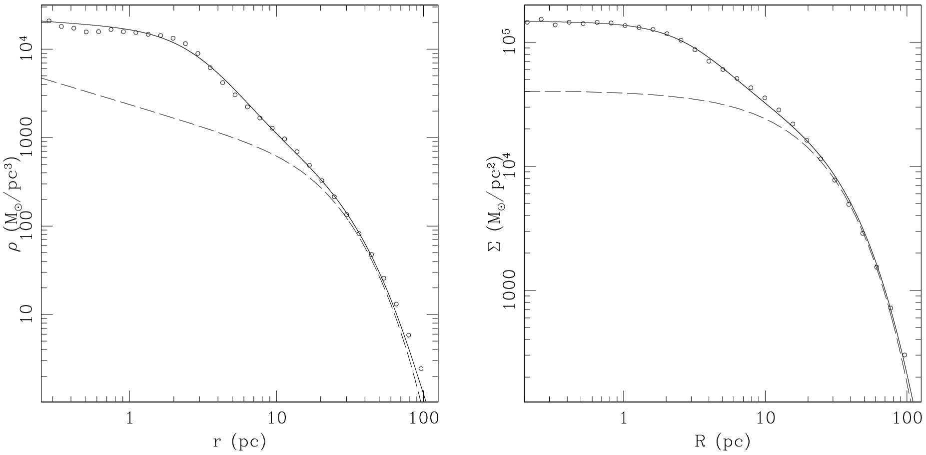

Figure 5.13. Spatial (right panel) and projected (left panel) density profiles at the end of the contemporary merging of the 12 GCs. In each panel the dashed line is the fit to the Nuclear Bulge profile, see text for explanation.

system (bottom panel of Figure 5.11). These data are well fit by

$$\rho_c = \left[1.2 \times 10^3 + 1.1 \exp\left(\frac{r_h}{1 \text{ pc}}\right)\right] \frac{\mathrm{M}_\odot}{\mathrm{pc}^3} \;, \tag{5.25}$$

shown as solid curve in the figure.

We also carried out a separate simulation in which all 12 clusters were placed at the same time on their initial orbits. We analysed the spatial and projected density profile of the system obtained at the end of this simultaneous decay and merging. We used the same functions adopted in the previous case to fit the spatial and projected profiles of galaxy and NSC.

In particular, in Figure 5.12 the central region of the Galaxy is shown at two different times: the lower solid curve is the inner region spatial density profile before the complete merging of the GCs, the upper one is the density profile at the end of the merging process. The long dashed line represents the broken power law fit (see Equation (5.19)) on the final profile.

The best fit parameters are $\rho_b = 1.3 \times 10^4 \mathrm{M}_\odot/\mathrm{pc}^3$, $r_b = 2.4$ pc, $\gamma_i = 0.19$, $\gamma = 1.85$ and $\alpha = 9.3$. Also in this case we have a central super cluster with an external slope ~ 1.8 and a central core, but in this case the break radius is larger than in the previous one. This is due to the fact that between a merger event and the consecutive one the central cluster partially relaxes decreasing the core size. On the contrary, the contemporary decay is very fast and, at the end of merger, the central cluster shows a bigger central core.

We used the same functions adopted in the previous case to fit the spatial and projected profiles of the Galaxy and of the super cluster.

In the left panel of Figure 5.13 the spatial profile of the total system is shown. We fit the cluster density profile using a modified Hubble law given by Equation (refeq:mhl) with parameters $\rho_{0,cl} = 1.62 \times 10^4$ $\mathrm{M}_\odot$/ pc^3 and $r_{0,cl} = 3.4$ pc. For the galaxy we used the power law density profile of Equation (5.12) with $\tilde{\rho} = 7.48 \times 10^2$ M$_\odot$/ pc^3 and $\gamma = 0.50$, $\tilde{r} = 10$ pc and $r_{cut} = 15.6$ pc.

For the total system projected density profile, we summed the modified core model of Equation (5.21) with $\Sigma_{0,cl} = 1.07 \times 10^5$ M$_\odot$/pc^2, $R_c = 3.7$ pc and $\zeta = 1.23$, to a Sérsic law (Equation [5.22]) with $\Sigma_0 = 7.84 \times 10^3$ M$_\odot$/ pc^2, $b = 1.65$, $R_e = 30.8$ pc and $n = 0.99$. This profile is given in the right panel of Figure 5.13.

In the following we will focus on the repeated infall simulation, that, as previously pointed out, is believed to be more generic. However, it is worth noting the similarity of the NSC in the two different cases of repeated and simultaneous decay, both characterized by an external steep ($d\ln\rho/d\ln r \sim -2$) power law density profile and a flat core within the SMBH influence radius ($r_{\rm infl} \sim 6$ pc in our model). This homogeneity reinforces the idea that our results are robust and not very sensitive to the particular choice made for the initial conditions. We conclude that the basic properties of the Galactic NSC, including its mass and density profile, are the natural product of a model in which this is formed via inspiral of massive clusters into the Galactic center and that such properties can be reproduced under a variety of initial conditions.

5.5.2 Results: morphology of the NSC

Observationally constraining the morphology of galactic nuclei is a fundamental step toward understanding their origin.

Unfortunately, as a consequence of the strong interstellar extinction along the Sun-Galactic center line of sight, our knowledge of the Galactic NSC morphology and size is very limited. Some indications are derived using kinematic modeling of the dominant population of old (few Gyr) stars that can be well described by a uniform, spherical model cluster exhibiting slow solid body rotation (amplitude ~ 1.4(km s^{-1})/arcsec; Trippe *et al.* 2008; Schödel *et al.* 2009).

Aspherical NSCs are commonly observed in external galaxies. For instance, in a sample of 9 edge-on nucleated late-type galaxies, Seth *et al.* (2006) reported that three of these galaxies (IC 5052, NGC 4206, and NGC 4244) have NSCs with significantly flattened isophotes and evidence for multiple structural components. In addition, one of these galaxies (NGC 4206) showed possible indication of AGN activity, suggesting the presence of a black hole within the core of the central cluster. The NSC of the face-one galaxy M33, for which a SMBH is instead not detected, is also known to be elongated along an axis parallel to the major axis of the galaxy (Lauer *et al.*, 1998; Matthews *et al.*, 1999). Accordingly, nuclei in the case of formation via clusters inspiral, are expected to be not spherical since mergers tend to destroy spherical symmetry (e.g. Moore *et al.*, 2004).

We quantified the model shape in our simulation by constructing isodensity contours and also by the moment-of-inertia tensor (e.g., Katz, 1991; Poon and Merritt, 2004; Antonini *et al.*, 2009), as described in what follows: the symmetry axes are

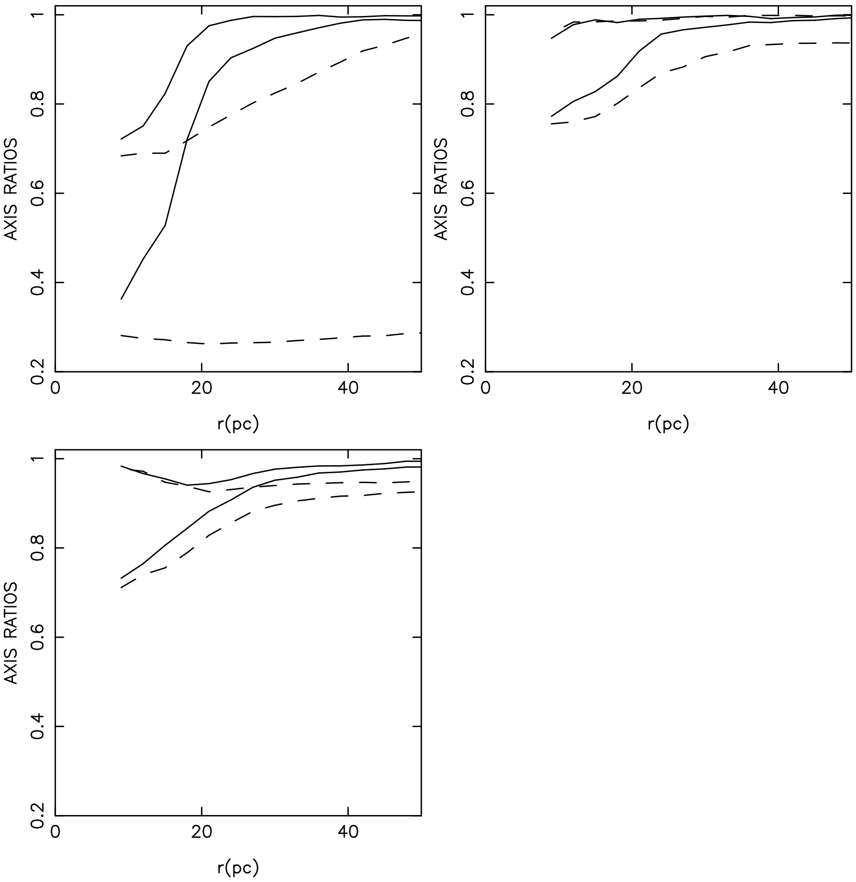

Figure 5.14. Axial ratios of the N-body system as a function of galactocentric radius computed after 1 (top left panel), 6 (top right panel) and 12 (bottom panel) infalls. Solid curves correspond to the entire model (i.e., galaxy plus the NSC), while dashed curves gives the axis ratios of NSC only. After the first infall the NSC is strongly triaxial in the inner regions, but appears nearly oblate at the end of the simulation.

calculated as

$$\tau_1 = \sqrt{I_{11}/I_{max}}\ ,\ \tau_2 = \sqrt{I_{22}/I_{max}}\ ,\ \tau_3 = \sqrt{I_{33}/I_{max}}\ , \tag{5.26}$$

where I_{ii} are the principal moments of the inertia tensor and $I_{max} = \max\{I_{11}, I_{22}, I_{33}\}$; particles are then enclosed within the ellipsoid $x^2/{\tau_1}^2 + y^2/{\tau_2}^2 + z^2/{\tau_3}^2 = r^2$. These previous two steps were iterated until the values of the axial ratios had a percentage change of less than 10^{-3}. Finally, we define $a > b > c$ letting $c/a = min\{\tau_1, \tau_2, \tau_3\}$ and b/a the intermediate value. We also define the triaxiality via the parameter $T \equiv \left(a^2 - b^2\right) / \left(a^2 - c^2\right)$. Oblate and prolate galaxies have $T = 0$ and 1, respectively. The value $T = 0.5$ corresponds to the maximally "triaxiality" case.

The results are summarized in Figure 5.14 which displays the axial ratios of the NSC as a function of radius and at different times. The model morphology evolves from an initially strong triaxiality (after the first infall) into a more oblate quasi-axisymmetric shape. In particular, notice that the morphological structure of the

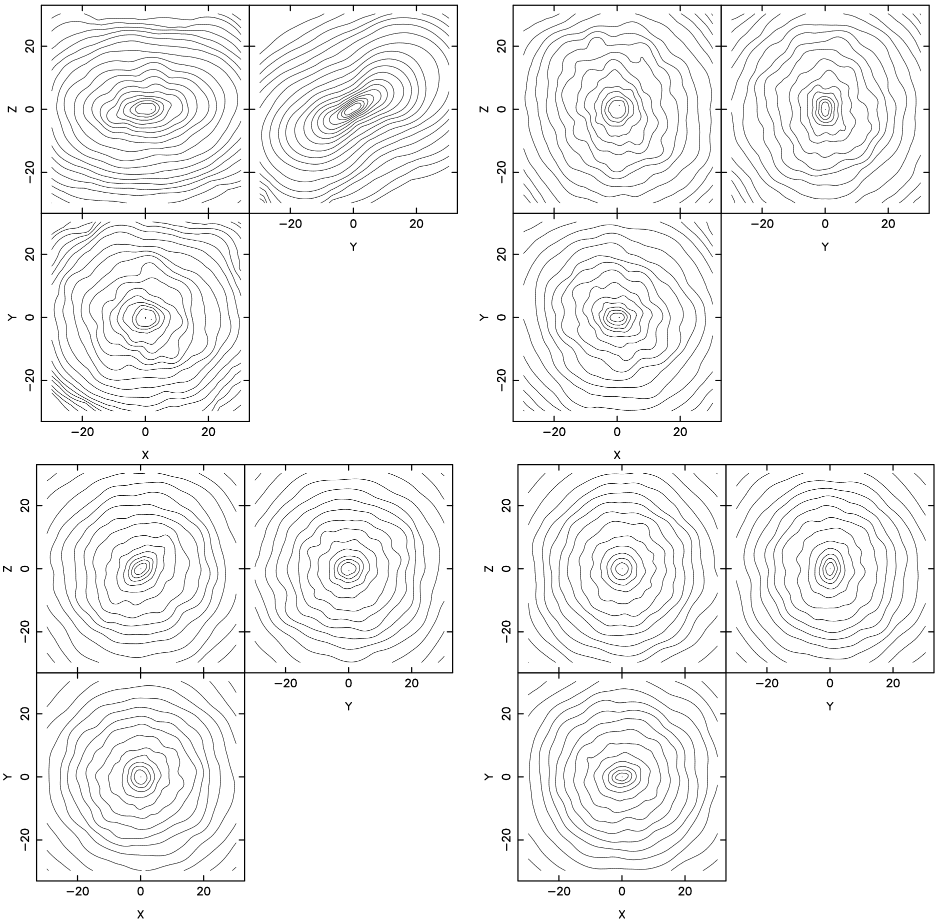

Figure 5.15. Contours of the projected density of the NSC after 1 (upper-left panel), 4 (upper-right panel), 8 (lower-left panel) and 12 (lower-right panel) infalls. As more stellar clusters accumulate to the center, the NSC becomes rounder. However, Its shape, at the end of the simulation (lower-right panel), is still very aspherical, especially in the innermost regions.

final product (right panel) is very similar to that after the 6th infall event (middle panel). This shows that the NSC is transformed into a nearly oblate system ($T \lesssim 0.2$ at $r < 20$ pc) after few infalls (~ 4), but its shape remains essentially unchanged from that point on. In the outer regions ($\gtrsim 20$ pc), the system remained instead nearly spherical for the entire course of the simulation.

The shape evolution of the model is more qualitatively illustrated in Figure 5.15 where the contours of the projected density of the NSC are displayed at different times. The morphological transition from a triaxial configuration into a rounder (nearly-oblate) shape can be clearly seen in the figure.

Based on this analysis, a NSC that forms via repeated cluster inspiral will most likely exhibit a nearly oblate shape with $T \sim 0.3$. We note, however, that this result must somewhat depend on the orbital parameters of the progenitor globular

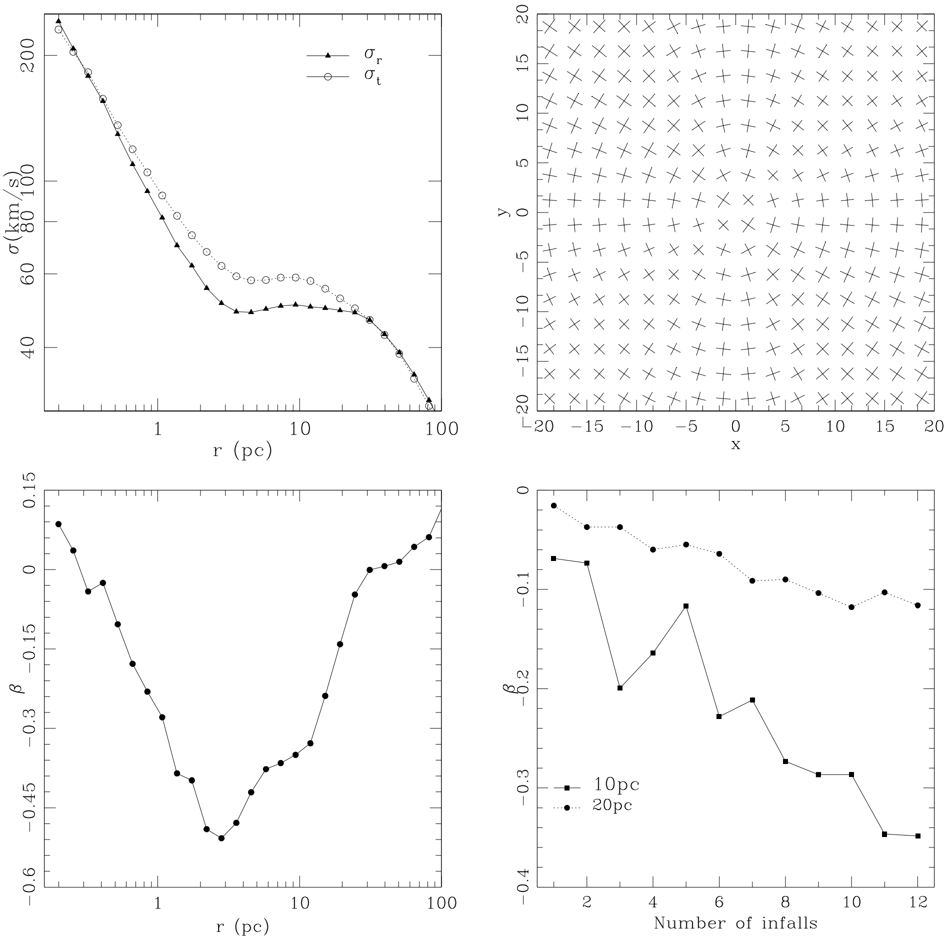

Figure 5.16. Radial (σ_r) and tangential (σ_t) velocity dispersion profiles as a function of distance from the central SMBH (upper-left panel). Map of the principal axes of the 2D velocity ellipses of stars in the NSC on the x-y plane(upper-right panel). Anisotropy parameter β of the merging product plotted as a function of radius (lower-left panel). The anisotropy parameter evaluated at 10 and 20 pc versus time (lower-right panel). All profiles refer to the end of the 12th globular cluster inspiral.

clusters, as a more prolate shape is expected to occur for almost radial mergers (Preto *et al.*, 2011). In addition, two-body relaxation by particle-particle interaction will produce a secular drift of our model towards spherical symmetry (Section 5.6, Theis and Spurzem 1999).

5.5.3 Results: kinematics

The formation mechanism of a NSC strongly influences its kinematical properties.

Studying the dynamics of the Galactic center evolved late-type CO absorption line star cluster, Trippe *et al.* (2008) showed that the 3D stellar velocity distribution is approximately Maxwellian, suggesting relaxation of the old stellar component of the NSC. Fitting the observed velocity dispersion and the rotation curve of the NSC, these authors found that the NSC is well modeled by a spherical density profile.

Schödel *et al.* (2009) investigated the proper motion of more than 6000 old-type stars within 1 pc of SgrA*. Moreover, they analysed the radial and tangential mean velocity of their star sample in circular shells around SgrA*. Schödel *et al.* (2009) found evidence for rotation of the NSC parallel to the Galactic plane. This could suggest that the formation mechanism of the NSC may include the accretion of gas and/or star clusters from the Galactic disk (see Seth *et al.*, 2008c). In particular, it is relevant for our results to mention their Figure 6 where radial and tangential velocity dispersion in circular radial bins are plotted versus the distance from the central SMBH. The result is that the NSC is nearly isotropic with only a small bias toward tangential motion within the radial range 1 arcsec − 10 arcsec. However, global rotation could mimic isotropy for an anisotropic NSC. Future observations are needed to solve this issue.

In Figure 5.16 we study the velocity dispersion of the stars in the NSC at the end of the 12th merger (for the same analysis repeated after about a relaxation time see Section 5.6). The upper-left panel of the figure shows the radial (solid line with empty circles) and tangential (dotted line with filled triangles) velocity dispersion as a function of galactocentric radius. We find that:

- for $r < 0.3$ pc the system is quite isotropic;
- for $0.3 < r < 20$ pc the tangential velocity profile is systematically above the radial velocity dispersion curve;
- for $r \gtrsim 20$ pc the system is isotropic. A small degree of radial anisotropy characterizes the model outside ~ 60 pc.

In the upper right panel of Figure 5.16 we show a local measure of the velocity dispersion along radial and tangential directions. We partitioned the $x - y$ plane in boxes and evaluated the aforementioned dispersions in each of them. The length of the plotted axes is proportional to the corresponding value of dispersion. As apparent, the system shows a tangential anisotropy whose value decreases with radius.

The lower panels of Figure 5.16 show the anisotropy parameter

$$\beta = 1 - \frac{\sigma_t^2(r)}{2\sigma_r^2(r)} \ , \tag{5.27}$$

as a function of the radial distance from the SMBH (lower left panel) and as a function of time at two different distances, 10 pc and 20 pc, from the center (lower right panel). In the radial range between 0.3 − 40 pc, β is negative and the system is tangentially anisotropic. The anisotropy grows with the number of infalls and, as just said, is bigger in the inner region (see bottom right panel of Figure 5.16). This is consistent with the results obtained studying the shape an the axial ratios of the system (see Section 5.5.2).

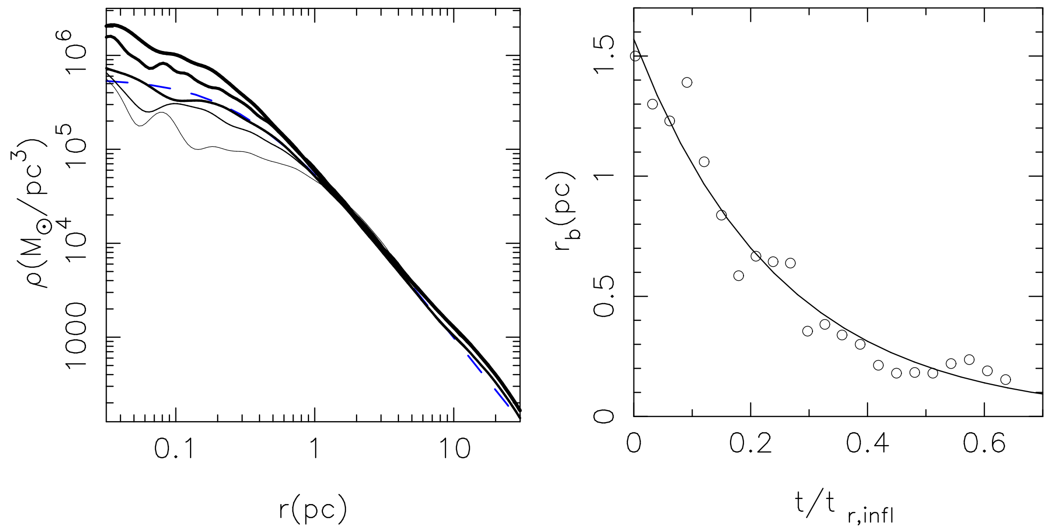

Figure 5.17. Post-merger evolution of the N-body model. Left panel shows the density profile at four times: $t = (0.12, 0.24, 0.36, 0.48, 0.6)$ in units of the relaxation time at the influence radius; line thickness increases with time. The dashed (blue) curve shows a fit of the density to the broken power-law model of Equation (5.19) at $t \approx 0.36\ t_{\mathrm{r,infl}}$, i.e., $\sim$ 10 Gyr when scaled to the Milky Way. Right panel plots the break (core) radius as a function of time. The solid line is the best-fit exponential, Equation (5.29).

5.6 Collisional evolution of the Nuclear Star Cluster

The simulations of globular cluster inspiral described above took place in a short enough span of time that two-body relaxation effects could be ignored. The local relaxation time (see Section 3.2) can be defined as (Spitzer, 1987)

$$t_{\mathrm{r}} = \frac{0.33\sigma^3}{G^2 \rho m_\star \ln\Lambda} \tag{5.28}$$

where $m_\star$ is the stellar mass, ρ is the mass density and σ is the one-dimensional velocity dispersion. Near the influence radius of a SMBH, the Coulomb logarithm can be approximated as $\ln\Lambda = \ln(r_{\mathrm{infl}}\sigma^2/2Gm_*)$. The relaxation time at the influence radius of Sgr A*, $r_{\mathrm{infl}} = 2 - 3\,\mathrm{pc}$, is $t_{\mathrm{r,infl}} \sim 20 - 30\,\mathrm{Gyr}$, assuming a stellar mass of $1 M_\odot$ (Merritt, 2010). This is roughly 2×10^5 times the period of a circular orbit at r_{infl}. In our N-body simulations, the relaxation time is shorter (compared with the crossing time) by a factor of approximately 200, the mass of a single cluster particle in solar masses; in other words, it is roughly 10^3 times the crossing time at r_{infl}.

In the absence of large-scale changes to the gravitational potential, an N-body model like ours continues to evolve due to gravitational encounters. The evolution that occurs should mimic the evolution that would take place in the real system, of much larger N, if the unit of time is taken to be the relaxation time (e.g. Aarseth and Heggie, 1998).

In the Milky Way, the relaxation time is short enough that significant evolution of the stellar distribution near the SMBH would take place over the age of the galaxy.

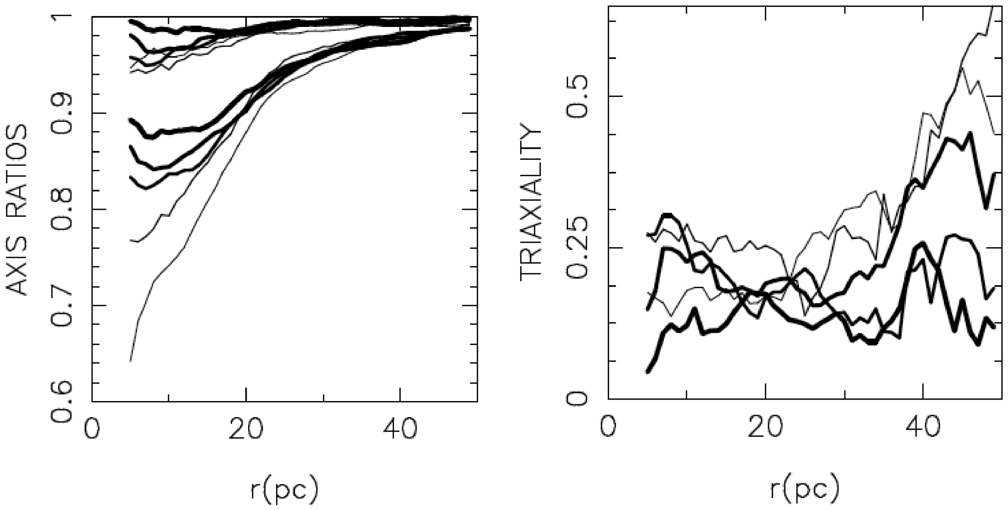

Figure 5.18. Evolution of the model axis ratios (left panel) and triaxiality parameter (right panel), as functions of radius, in the post-merger phase. Times are the same as in Figure 5.17; line thickness increases with time.

The distribution of late-type stars in the Milky Way NSC exhibits a nearly flat core of radius ~ 0.5 pc (Buchholz *et al.*, 2009). In a time of 10 Gyr, such a core would shrink, as the stellar density evolved toward the Bahcall-Wolf (1976) $\rho \sim r^{-7/4}$ form inside $\sim 0.2 r_{\mathrm{infl}}$. Since the density profile beyond the core is observed to have roughly this slope (Oh *et al.*, 2009), such evolution would tend to preserve the outer slope while gradually reducing the size of the core. A core of initial radius $1-2$ pc is expected to reach a size of $\sim$ 0.5 pc, the size of the observed core, after $\sim$ 10 Gyr (Merritt, 2010). These arguments motivated us to continue the integration of our N-body models after the final inspiral event. Figure 5.17 shows the density profile of the NSC at different times during its post-merger evolution. At the end of this integration, i.e. after $\sim 0.6\, t_{\mathrm{r,infl}}$, the distribution shows an inner core of size $\sim$ 0.2 pc, substantially reduced from its initial value of $\sim$ 1.5 pc. The right panel of Figure 5.17 plots the evolution of the break radius, r_b, of the best fitting broken power law profile as a function of time. The value of the break radius can be used as an approximate estimate of the model core radius. The time dependence of the core radius is well described by an exponential:

$$r_b(t) = 1.57 e^{\frac{-t}{0.25 t_{\mathrm{r,infl}}}}\ \mathrm{pc}. \tag{5.29}$$

As expected, the slope of the density profile outside the core remains nearly unchanged during this evolution, $\rho \simeq r^{-1.8}$.

A core radius of $\sim$ 0.5 pc is reached after a time of $\sim 0.25 t_{\mathrm{r,infl}}$. Scaled to the Milky Way, this time would be $5-8$ Gyr.

Of course, in the real galaxy, it is likely that cluster inspiral would occur more or less continuously over the lifetime of the galaxy. Our separation of the evolution into an inspiral phase, followed by a relaxation phase, is artificial in this sense.

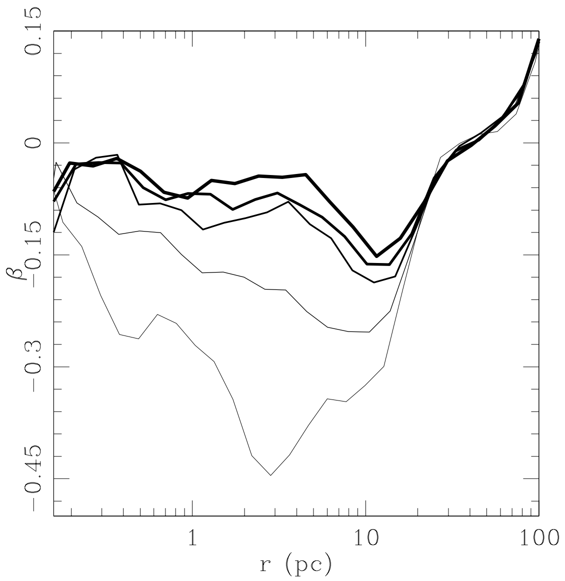

Figure 5.19. Evolution of the anisotropy parameter β during the post-merger phase. Times shown are the same as in Figure 5.17.

Nevertheless it is reasonable to draw the conclusion that the size of the core resulting from the combined effects of cluster inspiral and relaxation would be somewhat smaller than the ~ 1.5 pc that we found above, and therefore, closer to the observed core size of ~ 0.5 pc.

Figure 5.18 shows the morphological evolution of the NSC during the relaxation phase: the radial dependence of the axis ratios (left panel) and the triaxiality parameter (right panel). There is essentially no evolution in the intermediate axis ratio. However, in the innermost regions of the model, the shortest axis length significantly increases with time. Two-body relaxation results in an evolution toward quasi-spherical symmetry, but at the end of the simulation the model has not yet reached this final state, still exhibiting some non-negligible triaxiality. The final model is nearly oblate with $0.3 \lesssim T \lesssim 0.1$.

Figure 5.19 illustrates the evolution of the velocity anisotropy profile, $\beta(r)$, during the post-merger phase. Relaxation tends to drive the velocity distribution toward isotropy, causing β to increase toward zero. After $0.4t_{\mathrm{r,infl}}$, i.e., ~ 10 Gyr, there remains only a small bias toward tangential motions, $\beta \sim -0.1$, $r \lesssim 10$ pc. The final anisotropy profile is consistent with measurements of the Galactic center (Schödel *et al.*, 2009; Merritt, 2010). In the radial range 1 arcsec − 10 arcsec, the late-type stars are observed to have a mean projected anisotropy of $1-\langle\sigma_T^2/\sigma_R^2\rangle = -0.124^{0.098}_{-1.05}$ with σ_R and σ_T the radial and tangential velocity dispersions in the plane of the sky.

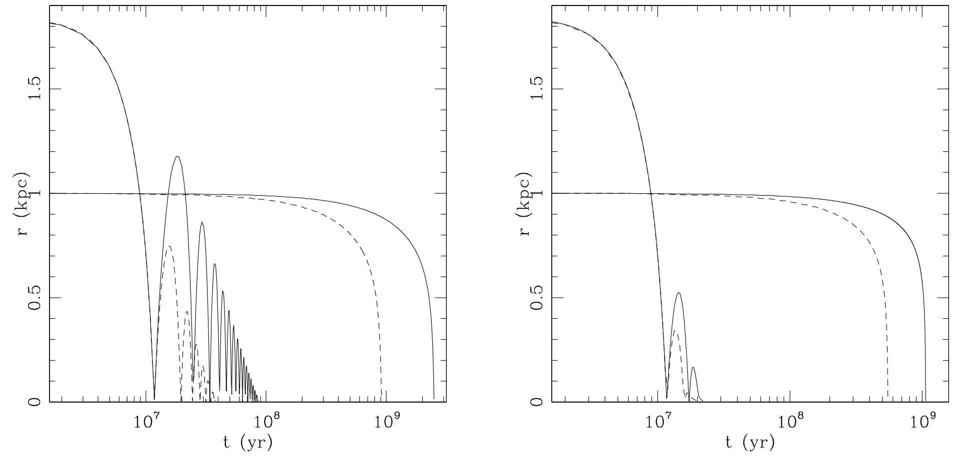

Figure 5.20. The time evolution of the distance to the galactic center of a massive (solid lines for $10^6 M_\odot$, dashed lines for 4×10^6 $M_\odot$) test object in the case of radial orbits and initially circular orbits, for $\gamma = 1/2$ (left panel) and $\gamma = 1$(right panel).

5.7 Discussion

5.7.1 Massive Globular Cluster Orbital Decay in the Milky Way

The study of dynamical friction decay of massive globular clusters in galaxies has been extensively investigated by many authors in different schemes and approximations (as one body problem with Chandrasekhar's like frictional term or, more recently, with N-body simulations) and in different galactic environments (spherical, axisymmetric and triaxial galaxies). The general conclusion is that dynamical friction is actually a relevant orbital decay mechanism, not only for most massive clusters but also for intermediate mass GCs, provided their orbit are radially biased. This decay effect is enhanced in triaxial galaxies, where box orbits are common and allow GCs on such orbits to approach closely the galactic center where dynamical friction is maximized in its effect (see Section 2.1). Another indication of the importance of dynamical friction is that it may influence (Capuzzo-Dolcetta and Tesseri 1997, 1999; Capuzzo-Dolcetta and Mastrobuono-Battisti 2009 and Chapter 2) the large scale distribution of the GC system in elliptical galaxies which, as shown by many authors (e.g. Lauer and Kormendy 1986; Capuzzo-Dolcetta and Tesseri 1997, 1999; Capuzzo-Dolcetta and Mastrobuono-Battisti 2009 and Chapter 2), is flatter than that of galaxy stars (Lauer and Kormendy, 1986; Harris, 1986).

In order to give a quantitative indication of the time required for a massive body to fall to the Milky Way center we numerically integrated the equations of motion of a test particle in a fixed potential including the contribution of dynamical friction:

$$\ddot{\mathbf{r}} = -\nabla\phi + \mathbf{a}_{\rm df}, \tag{5.30}$$

where the frictional deceleration is usually expressed by mean of the so called *local* approximation form of the classic (Chandrasekhar, 1943) impact integral:

$$\boldsymbol{a}_{\mathbf{df,loc}} \approx -4\pi G^2 M\rho(r)F(<v,r)\ \ln\Lambda\frac{\boldsymbol{v}}{v^3}. \tag{5.31}$$

Here $\rho(r)$ is the mass density of background stars, $F(<v,r)$ is the fraction of stars that, locally, are slower than the infalling cluster and $\ln\Lambda$ is the usual Coulomb's logarithm.

Clearly, the local approximation fails in central, cuspy regions of galaxies, because the role of collision at intermediate and large impact parameters is weighted with the local (about central) density which is unbound, implying a substantial overestimate of the actual dynamical friction. Actually, the real dynamical friction during the passage of a massive objects through the galactic center is given, in spherical symmetry, by the integral

$$\mathbf{a}_{df} = -\frac{8\pi m}{M+m}\int_{b_{min}}^{b_{max}}\int_{\mathbf{v}_m} f(b,\mathbf{v}_m)\times\frac{\mathbf{v}_M-\mathbf{v}_m}{1+\frac{b^2|\mathbf{v}_m-\mathbf{v}_M|^4}{G^2(M+m)^2}}\,|\mathbf{v}_M-\mathbf{v}_m|\,bd^3\mathbf{v_m}db, \tag{5.32}$$

where $f(b,\mathbf{v}_m)$ is the distribution function of background stars of mass m and b is the impact parameter. The integral in Equation (5.32) is reasonably easily performed numerically, although with the care due to its double singularity in phase space. Arca-Sedda and Capuzzo-Dolcetta (2011) show that a good expression for the dynamical friction deceleration, valid in cases of cuspy galaxies on a large scale around singularity is obtainable as an averaged interpolation between the *central* value of Equation 5.32 impact integral and the local approximation:

$$\mathbf{a}_{df} = p(r)\mathbf{a}_{df,cen} + [1-p(r)]\mathbf{a}_{df,loc}, \tag{5.33}$$

where the interpolation function $0 \le p(r) \le 1$ is such that $p(0)=1$. It has been shown that a good interpolation is $p(r)=e^{-r/r_C}$ where r_C is the distance over that local dynamical friction tends to diverge ($r_C \sim 0.1$).

For the background stellar distribution we adopted a density model given by the sum of three components, nuclear bulge (NB), bulge (B) and halo (H):

$$\begin{aligned}\rho(r) = \rho_{\rm NB}(r)+\rho_{\rm B}(r)+\rho_{\rm H}(r) &= \frac{(3-\gamma)M_{NB}b_{NB}}{4\pi r^\gamma(r+b_{NB})^{4-\gamma}}\\ &+\frac{3b_B^2M_B}{4\pi\left(r^2+b_B^2\right)^{5/2}}+\frac{b_H^3\rho_H}{r(r+b_H)^2}\ ,\end{aligned} \tag{5.34}$$

where $M_{NB} = 2.40\times10^9$ M$_\odot$, $b_{NB} = 0.5$ kpc, $M_B = 1.32\times10^{10}$ M$_\odot$, $b_B = 0.39$ kpc are the mass and length scales of the Dehnen's $\gamma = 1/2$ model (Dehnen, 1993) for the nuclear bulge and of the Plummer's model for the bulge (Plummer, 1911), while ρ_H and b_H are the central density and length scales of the halo, modeled as a Navarro, Frenk and White profile (Navarro *et al.*, 1996). These values are giving a good fit to the observed properties of the Milky Way at intermediate-large scales

(Allen and Santillan, 1991; Dehnen, 1993). Figure 5.20 plots the orbital evolution of the distance to the Galactic center of GCs with two different values of the mass (assumed constant along the evolution) and starting on initially circular orbits of radius 1 kpc as well as on radial orbits of same energy. These plots show that all GCs more massive than 10^6 $M_\odot$ decay in the innermost galactic region in less than 3 Gyr, the dynamical friction decay time ranging between the shortest (most massive GC on radial orbit in the $\gamma = 1$ model) time $\simeq 3 \times 10^7$ yr and the longest (less massive GC on circular orbit in the $\gamma = 1/2$ model) time $\simeq 2.1 \times 10^9$ yr, in any case much shorter than the Hubble time. Clearly, all other orbits of same energy but eccentricity different from 0 (circular orbits) or ∞ (radial orbits) have sinking times within the range defined by radial and circular orbits.

We stress that the calculations presented in Figure 5.20 give likely a conservative upper limit to the decay times for various reasons. Some of these are: i) the presence of gas in the central regions could dramatically decrease the sinking time of a stellar cluster; ii) the background stellar distribution is assumed to be spherical, while in a, more realistic, triaxial distribution the decay time could be significantly reduced (Pesce *et al.*, 1992).

This basic calculation suggests therefore that a significant fraction of the most massive globular clusters in the Galactic bulge population would have had enough time to spiral in by now.

5.7.2 Star Formation History of the Milky Way Nuclear Cluster

The NSC at the center of the Milky Way appears to have undergone continuous star formation over the last 10 Gyr (e.g., Serabyn and Morris, 1996). The evidence that a large fraction of the Galactic center mass was formed in situ at an approximately constant rate over the last 10 Gyr has been extensively used in the past to argue against the merger model for the Milky Way NSC.

In this section, we compare the observed luminosity function (LF) of the stellar populations at the Galactic center with synthetic LFs obtained for different star formation scenarios. Our analysis suggests the possibility that about 1/2 of the Milky Way nuclear population consists of $\sim$ 10 Gyr old stars brought in by infalling globular clusters, while the remaining mass is due to continuous star formation.

Dereddened LFs of the observed populations were generated by *Hubble Space Telescope* NICMOS data taken from Figer *et al.* (2004). The fields are all within the central 30 pc of the Galactic center; their exact locations are given in Table 1 and shown in Figure 1 of that paper. Data are complete at the 50% level at $m_{\rm F205W} = 19.3$, averaged over all fields. The details of the technique used to generate both model and observed LFs are also described in Figer *et al.* (2004) and are summarized in what follows.

The LFs of the Galactic center populations are constructed under the assumption that each star has the intrinsic colors of a red giant and by subtracting reddening values for each star corresponding to its color in $H - K$ or $m_{\rm F160W} - m_{\rm F205W}$.

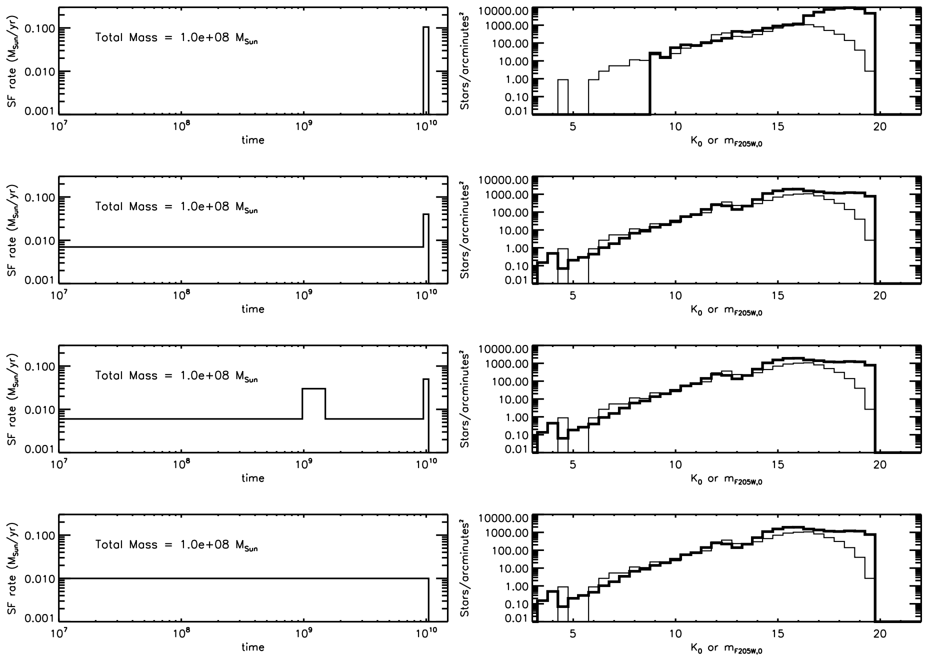

Figure 5.21. Left panels display different star formation scenarios in which, from top to bottom: the entire mass is build up by ancient ($\sim$ 10 Gyr old) stars, that we assume to be brought into the Galactic center by infalling globular clusters; half of the mass is contributed by ($\sim$ 10 Gyr) old stars and half due to continuous star formation; at the mass contributed by continuous star formation and globular clusters we add stars formed during a starburst episode occurred at $\sim$ 1 Gyr; all the mass is contributed by continuous star formation. Right panels compare the observed LF of the Galactic center (light lines) with the LFs (heavy lines) resulting from the different star formation scenarios assuming Solar metallicity and canonical mass loss-rates in the Geneva models. Note that the data are much more than 50% incomplete for the faintest few bins. The models have not been scaled for mass, but rather have been rescaled along the vertical axis to mach the number counts in the $K = 11.0$ bin. The star formation histories corresponding to the three bottom set of panels are essentially indistinguishable from each other and they all reproduce quite well the observed LF.

Geneva isochrones are used to model the LFs corresponding to different star formation histories. The Geneva stellar evolutionary models are described in Schaller *et al.* (1992), Schaerer *et al.* (1993a,b), Charbonnel *et al.* (1993) and Meynet *et al.* (1994). We adopted a mass spectrum of stars with a Salpeter (Salpeter, 1955) power law index (i.e., $dN/dm = m^{-1.35}$) and upper and lower mass cutoff of 120 $M_{\odot}$ and 0.1 $M_{\odot}$ respectively. The Geneva models are used to convert theses masses to the absolute magnitudes in the V band that are subsequently transformed in the K band through a lookup table that relates color index to magnitude. We then sum over the histogram to produce the LF of each star formation event and sum the individual LFs to derive the LF for a given star formation scenario.

Figure 5.21 displays the results of this study for various star formation histories, with the model counts modified by the observed completeness fractions from Figer *et al.* (1999). From the top to the bottom panels, the plots correspond to star formation models in which: i) the entire mass is build up by ancient ($\sim$ 10 Gyr old) stars, possibly brought into the Galactic center by infalling globular clusters; ii) the mass model is composed by ancient globular clusters stars plus stars formed via continuous star formation; iii) some ($\sim$ 1/3) of the mass is formed during a starburst at $\sim$ 1 Gyr (e.g., Sjouwerman *et al.*, 1999), while the remainder is due to continuous star formation and to an ancient burst at 10 Gyr; iv) the entire mass is formed through continuous star formation over the last 10 Gyr.

The counts at faint magnitudes ($K_0 > 15$) are controlled by ancient star formation, while the counts at the bright end ($K_0 < 8$) are controlled by the extent of recent star formation activity. The brightness of the red clump (at $K_0 \sim 12$) is related instead to the extent of intermediate age star formation activity.

The figure shows that the ancient burst model, corresponding to a NSC composed of only ancient stars, fails at reproducing the observed LF. This model overestimates the counts at faint magnitudes and it does not reproduce the number of counts seen in the bright end. Our analysis rules out the possibility that the nuclear population consists entirely of ancient stars. On the other hand, star formation models in which ancient bursts are accompanied by continuous star formation at other times, produce a LF essentially indistinguishable from that obtained when the mass is entirely due to continuous star formation. All these latter models fit quite well number counts and shape of the observed LF. We conclude that the observed Galactic center LF is consistent with a star formation history in which a large fraction of the mass consists of ancient ($\sim$ 10 Gyr) stars.

5.7.3 Mass-radius relation

In Figure 5.22 the mean half-mass radius is plotted against total mass for nuclei (filled circles) globular clusters (open circles) and ultra compact dwarfs (UCDs, star symbols). We overplot the track followed by the NSC in our simulation during the infall events (purple-continue curve) and during relaxation (continue-blue line). The structural properties of the NSC formed in our simulations (blue-filled circle) are in good agreement with those of real NSCs.

From the figure we can see that the faintest nuclei have roughly the same mass as a typical globular cluster. The size distributions for the nuclei and globular clusters also overlap, although the clusters in the Galaxy have half-mass radii of 3 pc, irrespective of mass, while the nuclei follow a relation of the form $r_h \propto \sqrt{M}$. Fainter than a few million solar masses, the nuclei and globular clusters have comparable sizes (Haşegan *et al.*, 2005).

We now consider the merger model for nucleus formation in the absence of a SMBH. In this case one can derive a simple recursive relation between the mass and radius of the NSC during its formation. The radius of the nucleus increases with increasing total mass, or light, as globular clusters merge. After the merger,

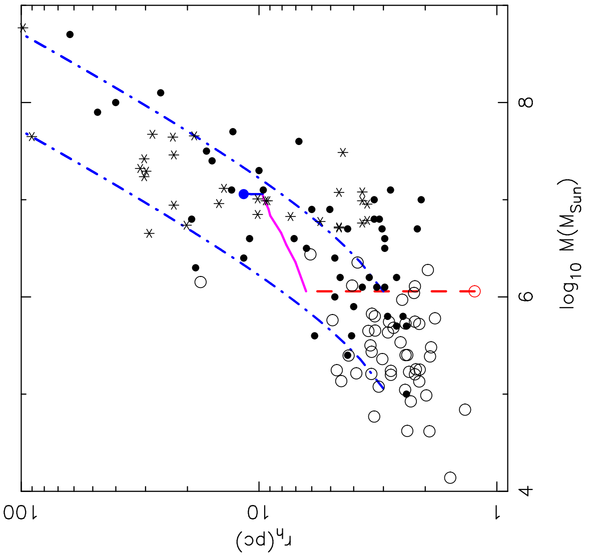

Figure 5.22. The measured mean half-mass radius (or effective radius) plotted against total mass for nuclei (filled circles), globular clusters (empty circles) and UCDs (stars symbols). Data points are from Forbes *et al.* (2008) and Côté *et al.* (2006). Blue dot-dashed curves show the predicted scaling in the merger model without SMBH for two different choices for the mass of merged clusters (see text for details). The red-open circle represents the initial globular cluster model in the N-body simulation. Purple and continue-blue curves are the evolutionary track of the NSC during its formation and during relaxation respectively. The filled blue circle represents the final product of our simulation.

its final energy, E_f, equals the energy of the nucleus before the merger, E_i, plus the energy brought in by the globular cluster. This energy has two components: the internal energy or binding energy E_b, and the orbital energy just before the merger, E_o. From conservation of energy:

$$E_f = E_i + E_o + E_b \ . \tag{5.35}$$

Just before the merger, the orbital energy is $E_o = \alpha GmM_i/2Ri_i$, where M_i and R_i are the mass and radius of the nucleus, respectively, m is the mass of the globular cluster, and α is a constant of order unity (Hausman and Ostriker, 1978) that depends on the radius of the capture orbit - the radius at which the dominant influence on the trajectory of a globular cluster first comes from the nucleus. After the merger, the nucleus reaches a state of dynamical equilibrium quickly; the virial theorem implies $E_f = -GM_f^2$. The equations above permit expressing the mass, energy, and radius of the nucleus recursively as

$$M_{j+1} = (j+1)M_1, \tag{5.36}$$

$$jE_{j+1} = (j+\alpha)\,E_j + jE_1, \tag{5.37}$$

$$(j+1)^2\,R_{j+1}^{-1} = j\,(j+\alpha)\,R_j^{-1} + R_1^{-1}, j = 1,2,3,... \tag{5.38}$$

where the subscript 1 denotes the initial nucleus, and, by assumption, $M_1 = m$. At the time when a nucleus consists of few merged globular clusters, its mass and that of the next infalling globular cluster are comparable. In this case, Equations (5.36,5.38) imply $R \propto M^{0.5}$. However, after many mergers, $M \gg m$, and the relation steepens to $R \propto M$. For $\alpha = 1.2$ and 5(25)100 mergers, Equations (5.36,5.38) imply $R \approx 2(5)10$ and $R \propto M^p$, $p = 0.5(0.6)0.7$. The typical half-mass radius of a globular cluster is about 3 pc (Jordán *et al.*, 2005) so for a nucleus assembled from 25 mergers, $R \sim 15$ pc. This is in reasonable agreement with the measured sizes for the brighter nuclei. For $\alpha = 1.2$, the expected scaling between r_h and mass is shown by the blue dot-dashed curves in Figure 5.22. We show the predicted behavior for two assumptions for the mass, m, of the clusters which merge to form the nucleus: 10^5 and 10^6 $M_\odot$. At least for $m = 10^6$ $M_\odot$, the agreement with the r_h-mass relation for real nuclei is remarkably good.

5.8 Summary

We have used initially large-scale N-body simulations to test the merger model in a generic galactic environment and then, always by means of such kind of simulations, we focussed our attention on the formation of the Milky Way nuclear star cluster (NSC). Our initial conditions consisted of a massive black hole (SMBH) at the center of a nearly homogeneous N-body system representing the nuclear stellar disk. Globular clusters were then added to this system, starting from circular orbits of radius 20 pc. The clusters were tidally limited by the external field to have a mass of $\sim 1.1 \times 10^6$ $\mathrm{M}_\odot$ at the start. Infall was driven by dynamical friction, due to the stellar disk, and later also to the accumulated mass from the previously-merged clusters. The clusters were fully disrupted by the SMBH at a radius of approximately one parsec. After 12 inspiral events, the accumulated mass of the NSC was about $1.5 \times 10^7 M_\odot$, comparable with the actual mass.

The principle results of our study are summarized below.

1 The stellar system resulting from the consecutive mergers has a density that falls off as $\sim r^{-2}$, and a core of radius ~ 1 pc. These properties are similar to those observed in the Milky Way NSC.

2 The morphology of the NSC evolved during the course of the infalls, from an early, strongly triaxial shape toward a more oblate/axisymmetric shape near the end of the merger process. Kinematically, the final system is characterized by a mild tangential anisotropy within the inner 30 pc and a low degree of rotation.

3 In order to investigate the effect of gravitational encounters on the evolution of the NSC, we continued the N-body integrations after the final inspiral was complete. The core that had been created by the SMBH was observed to shrink by roughly a factor of two in 10 Gyr as the stellar density evolved toward a Bahcall-Wolf cusp. This final core size is essentially identical to the size of the core observed at the center of the Milky Way. The density profile

outside the core remained nearly unchanged during this evolution. Gravitational encounters also caused the NSC to evolve toward spherical symmetry in configuration and velocity space.

4 The merger model implies that a large fraction of the stars in the NSC are old. We confronted this prediction with the observed luminosity function (LF) of the Milky Way NSC. Using stellar population models, we showed that the observed LF is consistent with a star formation history in which a large fraction (about 1/2) of the mass consists of old ($\sim$ 10 Gyr) stars and the remainder from continuous star formation.

Chapter 6

Tidal tails and clumpy structures around Globular Clusters

We continued our study of stellar dynamics dealing with the evolutionary mechanisms now dealing with the evolution of GCs in the large scale galactic potential. Globular clusters are the oldest systems found in the Galaxy and they witnessed the Galactic formation epoch (see Chapter 1).

Due to both internal and external dynamical mechanisms GCs lose stars and dissolve with time. The internal two body relaxation mechanism makes stars gradually leave the clusters in a time-scale of a few hundred relaxation times (Binney and Tremaine, 1987). Relaxation through encounters pushes the velocity distribution toward a Maxwellian form and hence places a fraction of the stars on the high-velocity tail beyond the escape velocity (also see Chapter 3). These stars are then removed from the system that evaporates, and at the same time the energetics cause the core of the system to contract (Johnstone, 1993). The approach to equipartition implies that more massive stars sink toward the center of the cluster, while lighter stars move outward (see Section 1.3). Core collapse can be halted by the presence of hard binaries, which, acting as energy sources, heat the central core by three-body encounters (Hénon, 1961; Ostriker, 1985). Internal processes can be enhanced by the perturbation coming from the external galactic field. In particular the external influence may accelerate the dissolution of a GC (Spitzer and Thuan, 1972). While orbiting the host galaxy, a GC experiences a slowly varying external potential, which has little effect on its structure, except when crossing the disc or bulge of the galaxy. On the crossing event the GC potential is rapidly changed, shrinking the tidal radius in a time-scale shorter than the cluster dynamical time, rapidly turning bound stars into unbound ones. This creates a preferential way of escape along the line of action of the tidal forces. Stars that leave through the inside of the GC orbit will leap forward in the cluster path and stars on the outside will lag behind in the orbit. Before the final dissolution of the globular cluster, the stars

escaped form the tidal tails around the clusters. Since the velocity dispersion of the stars in the cluster is much less than the orbital velocity of the cluster, the stars that become loose follow approximately the same orbit. Before the final dissolution of the globular cluster, the stars escaped form the tidal tails around the clusters. In fact stars that leave through the inside of the GC orbit will leap forward in the cluster path and stars on the outside will lag behind in the orbit. We may think of each unbound star as a test particle for the gravitational potential of the MW. Thus, by finding which orbit solution that best fits the observed tail distribution, we may infer the best model for the MW potential (Koposov *et al.*, 2010).
In this Chapter we report the results of an on-going study on tidal tails by mean of high precision N-body simulations. We focused on tail substructure (clumps) origin and evolution.

6.1 Searching for tidal tails in the sky and in simulations: a brief review

The search for tidal tails around GCs started with the Grillmair *et al.* (1995) work where, analysing the spatial distribution of stars in a dozen of Galactic GC, the authors found that the observed density profiles deviate from the prediction of a best-fit King model at the outermost radii and extend beyond the conventional limiting radius set by this model. Although in this work and in other ones (see for example Leon *et al.* 2000) the authors observationally found distinct star count overdensities, the observational technique errors cause a certain degree of uncertainties in the locations and shapes of putative tidal tails (Law *et al.*, 2003; Sollima *et al.*, 2011b). However the tidal tails of three clusters have been detected with high statistical significance: Palomar 5 (Yanny *et al.*, 2003; Grillmair and Dionatos, 2006a), NGC 5466 (Belokurov *et al.*, 2006b) and NGC 2298 (Balbinot *et al.*, 2011). In particular, the orientation of the detected tails in NGC 5466 is also in good agreement with its orbit as derived from proper-motion data. On the contrary of previous works, focused on nearby objects, Sollima *et al.* (2011b) concentrated their attention on Palomar 14, one of the furthest GCs in the Milky Way. As described in Section 4.9, in this work, the authors show the evidences for the presence of tidal tails around Palomar 14, despite its low mass and density and its big distance from the Galactic center.

One of the first numerical investigations of the role played by a galactic tidal field on spherical stellar systems was that of Keenan and Innanen (1975), who studied the effect of realistic, time-varying tidal fields on the stellar orbits in a star cluster. They numerically integrated the equations of motion of three bodies in models of spherically symmetric clusters, which, in turn, move in eccentric orbits in the field of a model galaxy. One of the main conclusions of this work was that star clusters rotating in a retrograde sense are more stable in a tidal field than clusters with either direct rotation or no rotation.

More recent works on weak tidal encounters based on a Fokker-Planck approach (Oh and Lin, 1992; Lee and Goodman, 1995) and self-consistent N-body techniques (Grillmair, 1998) confirmed that the interaction with an external tidal field, combined with two-body relaxation in the core of the cluster and following replenishment of stars near the tidal radius, causes a flow of stars away from the cluster. The stripped stars remain in the vicinity of the cluster for several orbital periods, either migrating ahead of the cluster or falling behind, giving rise to a slow growth of the tidal tails. The effects of a realistic galactic tidal field (including both bulge, halo, and disk) on GCs were investigated few years later by Combes *et al.* (1999). In this work, the authors found that: (i) the stars escaped from the system go to populate two giant tidal tails along the cluster orbit; (ii)these tails present substructures, or clumps, attributed to strong shocks suffered by the cluster and are preferentially formed by low-mass stars. Yim and Lee (2002) performed N-body simulations of GCs orbiting in a two-component galaxy model (with bulge and halo but no disk), using the direct-summation NBODY6 code (Aarseth, 1999) and focusing their attention, in particular, to the correlation between tidal tail direction (described by means of a “position angle”, defined as the angle between the direction of the tail and the galactic center direction) and the cluster orbit. They found that, on circular orbits, tidal tails maintain an almost constant position angle (60°), while GCs on noncircular orbits show a variation of the position angle, according to orbital path and phase. The position angle increases when the cluster heads for perigalacticon. On the other hand, it tends to decrease when the cluster heads for apogalacticon. Finally, some authors also investigated the dynamical evolution of some globular clusters in the tidal field of the Galaxy. In this context Dehnen *et al.* (2004) modeled the disruption of the globular cluster Palomar 5 by galactic tides. Palomar 5 is remarkable not only for its extended and massive tidal tails, but also for its very low mass and velocity dispersion (Capuzzo Dolcetta *et al.*, 2005). In order to understand these extreme properties, they performed many simulations aimed at reproducing the Pal 5 evolution along its orbit across the Milky Way. They explained the very large size of Palomar 5 as the result of an expansion following the heating induced by the last strong disk shock about 150 Myr ago. The clumpy substructures detected in the tidal tails of Palomar 5 are not reproduced in their simulations, so they argued that these overdensities were probably caused by interaction with Galactic substructures, such as giant molecular clouds, spiral arms, and dark matter clumps, which were not considered in their modeling. These simulations also predict the destruction of Palomar 5 at its next disk crossing in about 110 Myr, suggesting that many more similar systems once populated the inner parts of the Milky Way but have been transformed into debris streams by the Galactic tidal field. In this context, it may be interesting to mention recent numerical work devoted to the study of smaller size systems (open clusters) in the MW tidal field (Chumak and Rastorguev, 2006), which confirms the results (already known in the case of the external part of GC tidal tails) regarding the alignment of stars of the tidal stream around a common orbit in the external field (Grillmair, 1998; Combes

Bulge	M_B	$1.41 \times 10^{10} M_{\odot}$
	b_B	387.3 pc
Disk	M_D	$8.56 \times 10^{10} M_{\odot}$
	a_D	5317.8 pc
	b_D	250.00 pc
Halo	M_H	$10.7 \times 10^{10} M_{\odot}$
	a_H	12000 pc

Table 6.1. Parameters for the Galactic model (Allen and Santillan, 1991)

et al., 1999; Capuzzo Dolcetta *et al.*, 2005). A wider study, focused on the dynamics of globular clusters in external tidal fields and more in particular on the morphology and orientation of the tidal tails was performed by Capuzzo Dolcetta *et al.* (2005); Miocchi *et al.* (2006); Montuori *et al.* (2007). The study identified unambiguously the substructure of the tails, i.e. the presence of two clumps in the two tidal tails emanating from the cluster. The authors analysed the kinematics of these clumps showed the latter corresponding to minima of the average velocity of particles. Following these early studies, more developed analyses for the explanation of the structure formation and morphology of tidal tails were proposed by Küpper *et al.* (2008); Just *et al.* (2009); Küpper *et al.* (2010). The theory of tidal tails is based on the two-body equations in an external, analytical, potential and is complemented by several N-body simulations to evaluate the relevance of all the factors present in a realistic model (galaxy and cluster) with respect to the two body idealization. The authors found that, in this approximation, the particles that evaporate from the cluster follow an epicyclic motion. The interesting conclusion is that such simplest description seems to account for the main features of the tail formation. Prompted by such theoretical results and our previous ones we started a deeper analysis of the process by mean of extensive N-body simulations.

6.2 Models and methods

Here we present one of the simulations carried on to study the formation of clumpy tidal tails around a cluster which initial conditions are based on the observational data regarding Palomar 5. In order to simplify the analysis the cluster was put on a circular orbit and embedded in a fixed external potential representing the MW one.

6.2.1 Numerical methods

All the simulations were performed by means of NBSymple run on the 2 TESLA C1060 contained in the workstation described in Chapter 4.

The (fixed) time step was set equal to 1.5×10^3 yr (i.e. $4 \times 10^{-5} t_{cr}$, where, as usual, t_{cr} stands for the internal crossing time of the GC). The system was integrated for

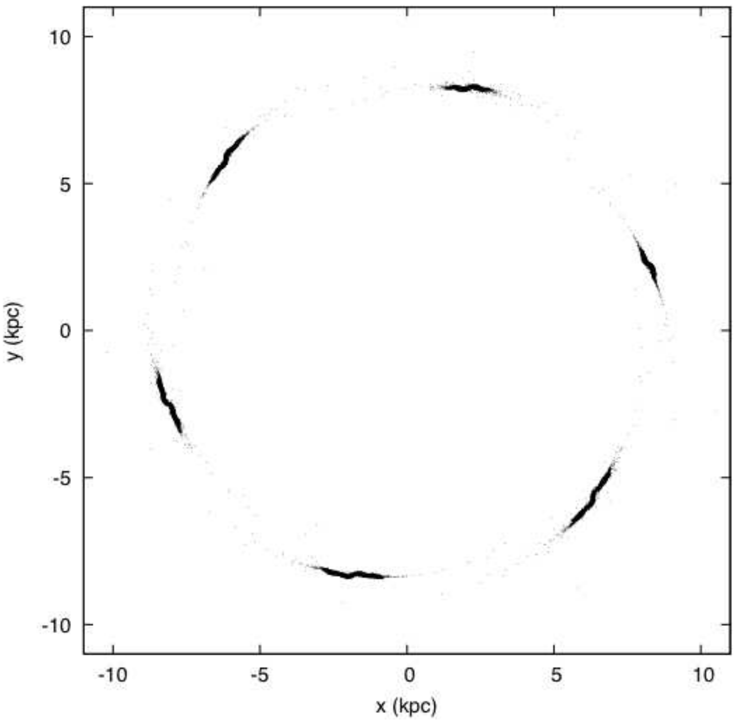

Figure 6.1. Snapshots of the simulation related to the second orbital period of the cluster around the center of the Galaxy.

about 4 Gyr. We set $\varepsilon = 0.004$ pc, after verifying that this value is significantly smaller than the mean first neighbour distance between particles in the cluster.

We chose the second order leapfrog method to perform the time integration of the particles trajectories; this choice is justified by computational time limitations and was done after testing that the same cluster, evolved in isolation, with the same parameters, is well simulated as the energy is conserved at a good level in the same time interval. The relative error in every simulation is indeed less than $\Delta E/E_0 = 10^{-7}$ at the end of the integration both in the isolated and not isolated case.

6.2.2 The Galactic model

The Galaxy is represented by the Allen and Santillan (1991) potential. It consists of a three-component system: a spherical central bulge and a flattened disk, both of Miyamoto and Nagai (1975) form, plus a massive spherical halo (see Section 4.1). The gravitational potential is time-independent, axisymmetric, and given in an analytical form that is continuous together with its spatial derivatives. Choosing a reference frame where the $(x; y)$-plane coincides with the MW equatorial plane, the three components of the potential have, in cylindrical coordinates, the form

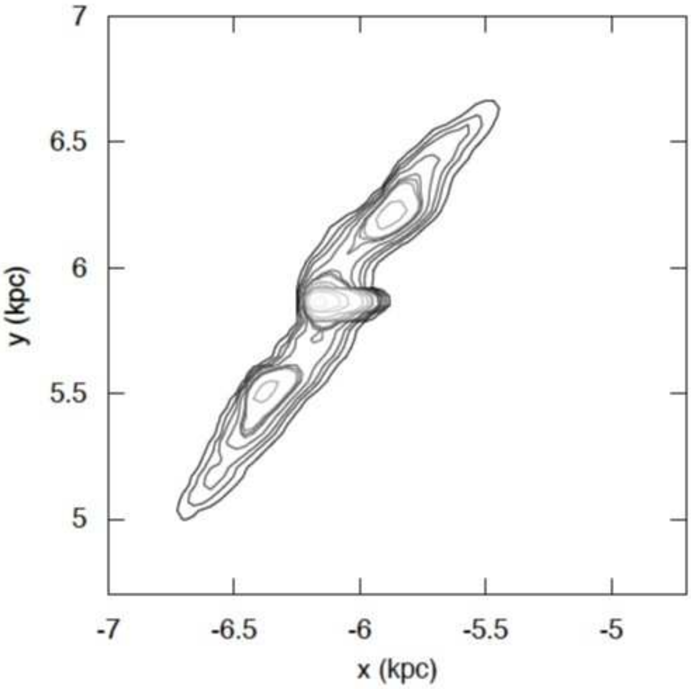

Figure 6.2. Isodensity contours of the GC after one orbit around the Galaxy. The tidal tails with the characteristic S-shape and two clumps (one in each tail) are apparent.

$$\Phi_B(R,z) = -\frac{GM_B}{\sqrt{R^2+z^2+{b_B}^2}}, \tag{6.1}$$

$$\Phi_D(R,z) = -\frac{GM_D}{\sqrt{R^2+\left(a_D+\sqrt{z^2+{b_B}^2}\right)^2}}, \tag{6.2}$$

and

$$\Phi_H(r) = -\frac{GM(r)}{r} - \frac{GM_H}{1.02a_H}\left\{-\frac{1.02}{1+\left(\frac{r}{a_H}\right)^{1.02}} + \ln\left[1+\left(\frac{r}{a_H}\right)^{1.02}\right]\right\}_r^{100}, \tag{6.3}$$

where square brackets indicate the difference of the function evaluated at the 100 kpc and the generic $r = \sqrt{R^2+z^2}$ extremes. The parameters in the formulas above are listed in Table 6.1. At the center of the Galaxy a SMBH of mass 4.0×10^6 $M_\odot$ is located and considered as a fixed particle, giving rise to a Keplerian potential.

6.2.3 Globular cluster model

For the globular cluster we chose a model representative of the Milky Way GC Palomar 5 (Küpper *et al.*, 2010). The GC was initially put on a circular orbit with radius $R_G = 8.5$ kpc; its circular velocity is ~ 220 km/s. As we said previously,

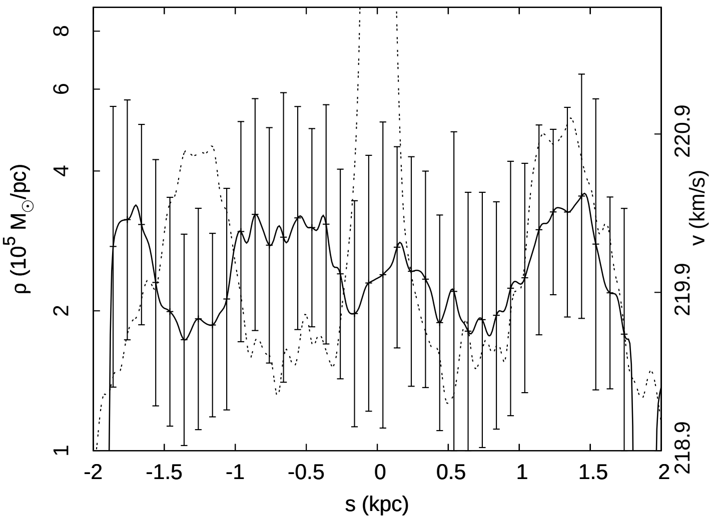

Figure 6.3. The average density ρ of particles (dashed line) and the average velocity v (solid line) vs curvilinear coordinate along the orbit s. The averages are computed in bin of fixed length of 0.034 pc. The error bars are the corresponding root mean square of v in each bin.

this cluster has been widely studied and observed through years and this eventually allows to compare the simulations results with the observational data. Palomar 5 is $\sim$ 10 Gyr old and we planned to simulate its evolution during the last 4 Gyr, i.e. for $\sim$ 15 orbits around the Galactic center. The choice of Palomar 5 is justified by the fact that it is the only GC with prominent tidal tails in which substructures have been clearly identified (Odenkirchen *et al.*, 2003). The mass of the GC is set equal to $20,000\ \mathrm{M}_\odot$ and it is modeled using a Plummer sphere

$$\rho(r) = \frac{3Mr_s}{4\pi\left(r^2 + r_s^2\right)^{5/2}}, \tag{6.4}$$

using the *NEMO* package *mkplummer*, see Teuben (1995). The chosen Plummer profile has an half mass radius to the tidal radius ratio equal to $r_h/r_t = 0.2$ for a circular orbit. The mass within a radius r in a Plummer model is given by

$$M(r) = M_{cl}\frac{r^3}{(r^2 + r_s^2)^{\frac{3}{2}}}, \tag{6.5}$$

where M_{cl} is the total mass of the cluster, and r_s is the Plummer radius, a scale parameter which sets the size of the cluster core. The scale radius (that we need as an input of the *mkplummer* routine) and the half mass radius are connect through the relation

$$r_s = (4^{\frac{1}{3}} - 1)^{\frac{1}{2}} r_h. \tag{6.6}$$

Following Dehnen *et al.* (2004) we have

$$r_{tid} \simeq \left(\frac{GM}{v_c^2}R_G^2\right)^{\frac{1}{3}}, \tag{6.7}$$

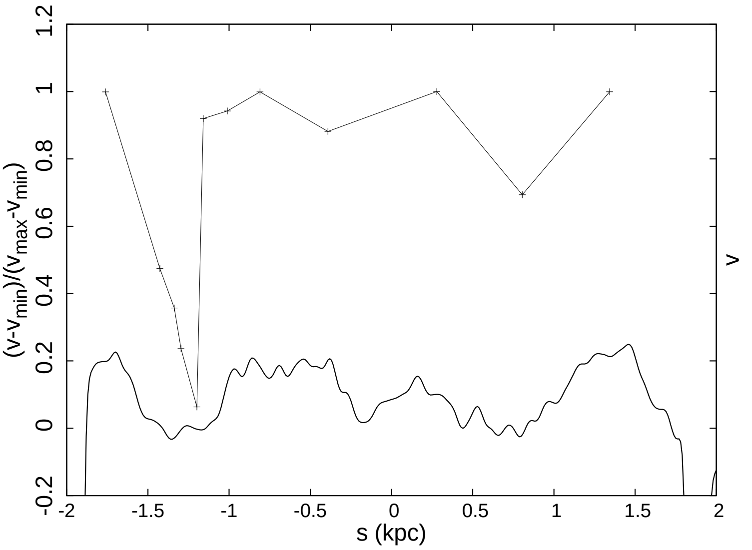

Figure 6.4. v is plotted with the relative difference $\Delta(s) = (v - v_{min})/(v_{max} - v_{min})$ averaged over particles contained in ≈ 0.25 kpc bins in s. Δ gives an indication of the average position of the corresponding particles on their orbit (near apocenter $\Delta = 0$, near pericenter $\Delta = 1$).

where R_G is the galactocentric distance of the cluster and M is its mass. In our case we have $r_t = 50.5$ pc, thus $r_h = 10.1$ pc and $r_s = 7.74$ pc.

The system was then represented by a number of particles $N = 30720$. This number is obviously lower than the number of stars in the real cluster, and this choice is obviously due to computational limitations. All the particles has the same mass, properly rescaled to give a total mass equal to the total mass of the cluster, so we neglected the mass segregation effects.

6.3 Results

According with previous works, we observe the formation of the tidal tails emanating from the GC. In Figure 6.2 we report the isodensity contours of the GC. Tails with characteristic S-shape as well as clumps are well apparent. The figure refers to the situation after an orbital period. We perform a statistical analysis of some kinematical features of the clumps after having identified the escapers.

- Escapers identification

Escapers are identified as particles with positive energy and distance greater than $2r_h$ from the GC center. We checked that such escapers never become bounded again (in the simulation time).

- Orbital path of escapers

The particles escape from the cluster and perform orbits very similar to the circular one made by the cluster barycenter ($e \approx 10^{-3}$). They indeed escape from the system with a speed close to the circular velocity of the GC and at a radius only slightly different from its galactocentric radius, and thus they will move on orbits with very small eccentricities.

- Basic statistical analysis of clumps

In Figure 6.3 we show the average density ρ of particles and the average velocity v vs s (curvilinear coordinate along the orbit) at a given time t (i.e. a snapshot of the GC at time t). For v we show also the corresponding root mean square. Both the density ρ and the average velocity v vary with s, even if the variation for v is tiny while the corresponding r.m.s is quite large.

- Correlations
  The clumps are formed by escapers which have a velocity correlated with the density in the trailing tail and anti-correlated with the density in the leading tail.

- Orbital positions
  In order to understand if clumps are formed by escapers at a particular position of their orbits, we plot in Figure 6.4 the difference $\Delta = (\langle v \rangle - v_{min})/(v_{max} - v_{min})$. $\langle v \rangle$ is the average of v in a group of bins. v_{max}, v_{min} are the maximum and minimum values of $\langle v \rangle$ versus time, corresponding to pericenter and apocenter of an average orbit of the escapers. Δ is simply the fractional distance of an averaged v from his minimum value. If a group of escapers is at time t on average near apocenters of their orbits, $\Delta = 0$; if near pericenters of their orbits, $\Delta = 1$. Figure 6.4 shows that the clumps are located where the escapers are on average at apsides of their orbits. The clump in the leading tail is formed by escapers which are on average at the apocenters of their orbits, while the clump in the trailing tail is composed by those at the pericenters of their orbits.

From this results it is quite apparent that the clumps seems to be caused by the orbital properties of the escapers instead of their kinematical properties as previously stated in the literature. This study deserves further analysis in order to provide a definitive explanation to the on-going processes.

Conclusions

The study of star cluster dynamics has a long history and significant progress has been made in understanding the physics driving their dynamical evolution. Many fundamental problems, however, are still open and new observations continuously present us with new challenges and questions. As clusters evolve, their structural properties and stellar content are modified by evolutionary processes. Clusters in different galaxies and at different galactocentric distances have different dynamical histories.

After a brief discussion of the properties of Globular Clusters and Nuclear Star Clusters we turn our attention to different topics and problems, facing open questions about the evolution of stellar systems on different spatial scales, using observational data and numerical methods.

Here we briefly resume the main results that we achieved. Globular Cluster Systems in galaxies are less concentrated to the center than the halo and bulge stars of the host galaxy. This difference has not yet received a definitive explanation, but a number of works (e.g., Capuzzo-Dolcetta 1993; Capuzzo-Dolcetta and Donnarumma 2001; Capuzzo-Dolcetta and Tesseri 1997) suggested the hypothesis that these systems were born at the same time with the same initial radial profiles, and, afterward, the GCS evolved due to dynamical friction and tidal interaction with the galactic field, while the collisionless stellar halo remained almost unchanged. In this scenario the initial radial profile of the GCS would have been the same of the present density profile of the halo stars, in the same host galaxy. Starting from this hypothesis it has been possible to evaluate the number of GCs lost to the galactic center as the integral of the difference between the two profiles. The results found in the literature have been extended analysing eight new elliptical galaxies (NGC 1400, NGC 1407, NGC 4472, NGC 3268, NGC 3258, NGC 4374, NGC 4406, NGC 4636). We evaluated the mass lost by the GCSs of these galaxies. In this way we found that such systems, during their evolution, may have lost a quantity of mass between $\sim 21\%$ and $\sim 71\%$ of the initial value. The mass lost by the GCS arrives at the galactic center influencing the local dynamics where, it is often found an SMBH and/or a Nuclear Star Cluster. The connection between the orbital evolution of GCs and the formation of the galactic central SMBH is supported by the positive correlation we found between the mass lost by the GCS and the mass of the central SMBH. This positive trend is expected considering that the more massive the SMBH is the more it accretes mass during its evolution, increasing the rate at which GCs decay to the center (Capuzzo-Dolcetta and Tesseri, 1999).

Stellar clusters like GCs can be considered as "dry" N-body systems, and so their dynamics can be studied using N-body methods. A number of methods have been devised in recent years for the numerical simulation of stellar systems. Here we presented a new high-performance and reliable code, NBSymple. Ordinary numerical methods for integrating Newtonian equations of motions are dissipative and exhibit incorrect long term behaviour. This is a serious problem when facing N-body problems, particularly when studying their long term evolution. One possibility is using symplectic integrators. Symplectic integrators are numerical integration schemes for Hamiltonian systems, which describe the exact time evolution of a slightly perturbed Hamiltonian system respect to the original one. Thus they possess the perturbed Hamiltonian as a conserved quantity and this guarantees the absence of any secular change in the error of the total energy. If the integrator is not symplectic, the error on the total energy grows secularly, in general. Thus we introduced the possibility to choose between two different symplectic methods in NBSymple: a leapfrog second order and a sixth order method. We set up 5 versions of the code:

- NBSympleA: fully serial code running on a single processor;
- NBSympleB: single-parallel code which uses Open Multi-Processing (OpenMP) directives, for both the $O(N^2)$ pairwise interactions and the $O(N)$ calculations (i.e. the time integration and evaluation of the Galactic component of the force on the system stars) over all the processors available;
- NBSympleC: single-parallel code, where the $O(N^2)$ all-pairs interactions calculations are demanded to a single GPU, using CUDA while all the remaining tasks are done by a single CPU;
- NBSympleD: double-parallel code, which again uses CUDA to evaluate the $O(N^2)$ portion of the code (as NBSympleC), while the $O(N)$ computations is parallelized sharing work between all the cores of the host, using OpenMP, as NBSympleB;
- NBSympleE: double-parallel code that uses CUDA on one or more GPUs to evaluate the total force over the system stars, i.e. both the all-pairs component and that due to the Galaxy. Only the time integration is demanded to all the CPUs.

We benchmarked the various versions of the code and we found that, using GPU as accelerators, we can obtain a significative speed up (up to 3 orders of magnitude in single precision) respect to the serial version. We also presented a very new version of NBSymple developed using MPI instead of OpenMP; this code was tested on a large CPU+GPU cluster and showed an almost perfect scaling. We tested NBSymple in various applications and we demonstrated its versatility, speed and reliability.

Then we started using numerical methods to face practical astrophysical problems. As said above, Nuclear Star Clusters are observed at the center of many galaxies. In particular, in the Milky Way's center, the Nuclear Star Cluster coexists with a central supermassive black hole. The origin of these clusters is still unknown and can be connected to the evolution of GCs. A possible formation mechanism is indeed the decay of globular clusters and their subsequent merging in the center of the galaxy. Various authors investigated this scenario, known as "merger model", see for example Tremaine *et al.* (1975); Capuzzo-Dolcetta (1993); Capuzzo-Dolcetta and Miocchi (2008a,b). In particular Capuzzo-Dolcetta and Miocchi (2008a,b) found, through self-consistent simulations, that the merging of a number of GCs can give rise to a star cluster similar to the observed NSCs. They reached this conclusion analysing the density profile and the velocity dispersion of the simulated NSC and comparing these data with the observations. In all these works the presence of a central SMBH was neglected and the simulations were not finalized to a specific study of the MW. Our work covers this lack through self-consistent simulations whose initial conditions are set up basing on recent data for the MW (Launhardt *et al.*, 2002), including the presence of its central SMBH. The merging of GCs produces a system which rapidly settles on a quasi-steady state, slowly evolving due to internal relaxation which, in its turn, is affected by the presence of the SMBH. The central and almost flat core characterizing the density profile of the merger product is maintained for a time long enough to justify the core actually observed in the MW NSC. Our results are also supported by that the external slope of the density profile of the NSC remains quite unaltered after the end of the merger events and its value, ~ -1.8, is in optimal agreement with the one inferred from the observations of the Galactic NSC. Moreover, we observe a drift toward velocity isotropy although keeping a slight degree of tangential anisotropy; this peculiarity was found in the observational data and already seen in previous numerical study by Capuzzo Dolcetta *et al.* (2001). As a conclusion, the process of consecutive infalls and merging in the inner region of the MW of a number of the order of 10 massive globular clusters could give an explanation of the observed features of the NSC observed in our Galaxy around the Sgr A* massive black hole.

In the last part of this Thesis we faced more directly the dynamical evolution of GCs in the Galactic field by mean of numerical simulations carried out using NBSymple. During their orbit around the Galactic center GCs lose stars, which form the tidal tails, along a direction resulting from the composition of the direction towards the galactic center and the cluster velocity around the galaxy, thus leading to the peculiar S-shape found in the outermost region of the cluster (Capuzzo Dolcetta *et al.*, 2005). Once formed, tidal tails are elongated such to remain parallel to the cluster orbit, with a trailing tail that lies slightly inside the orbit and a leading tail slightly outside it. Capuzzo Dolcetta *et al.* (2005) found that tails are excellent tracers of the cluster orbit near the pericenter, while, at the apocenter, they tend to deviate from the orbital path.

Tidal tails have a clumpy structure which cannot be associated with an episodic mass loss or tidal shocks with galactic compact sub-structures, since stars are lost from the cluster continuously. These clumps are not bound, self-gravitating, systems, and their formation mechanism is not yet completely known. We modeled a GC using the observed properties of the Galactic GC Palomar 5 and we run some simulations of this cluster on a circular orbit around the Galactic center. The analysis of our simulations showed a correlation among the average velocity and density of escapers. In particular, the clump in the leading tail corresponds to a minimum average velocity and the one in the trailing tail to a maximum average velocity of the escapers along the orbit. Moreover, our preliminary results, suggest that the clumps are located where the escapers are on average at apsides of their orbits. The clump in the leading tail is formed by escapers which are on average at the apocenters of their orbits, while the clump in the trailing tail is composed by those at the pericenters. This study deserves further analysis to achieve a better knowledge of the mechanisms involved; moreover the comparison of these simulations with observations could provide more information on the shape of the Galactic potential and on the Galactic dynamics as a whole.

Conclusioni

Lo studio della dinamica dei sistemi stellari ha una lunga storia e molti sono stati i progressi compiuti nella comprensione della fisica che ne guida l'evoluzione dinamica. Moti problemi fondamentali sono però ancora aperti e le osservazioni continuano a proporci nuove sfide e nuove domande. Quando un ammasso evolve le sue proprietà strutturali e il suo contenuto stellare vengono modificati dai processi evolutivi. Ammassi in galassie diverse e posti a varie distanze dal centro galattico hanno storie dinamiche differenti. Una migliore conoscenza degli effetti dell'evoluzione dinamica è un passo fondamentale nel nostro tentativo di fare luce sulla relazione tra le attuali proprietà degli ammassi

Dopo una breve discussione delle proprietà degli AG e dei NSC abbiamo diretto la nostra attenzione a diversi problemi e argomenti, affrontando questioni aperte sull'evoluzione dei sistemi stellari su diverse scale spaziali ed utilizzando sia l'analisi di dati osservativi, sia metodi numerici. Qui riassumiamo i principali risultati ottenuti in questo lavoro.

I Sistemi di Ammassi Globulari (SAG) nelle galassie osservate risultano essere meno concentrati al centro della galassia rispetto alle stelle di alone e e di bulge. Questa differenza non ha ancora ottenuto una spiegazione definitiva, ma diversi lavori (si vedano ad esempio Capuzzo-Dolcetta 1993; Capuzzo-Dolcetta and Donnarumma 2001; Capuzzo-Dolcetta and Tesseri 1997) hanno suggerito l'ipotesi che questi sistemi siano nati allo stesso tempo con lo stesso profilo radiale iniziale, e che, successivamente il SAG sia evoluto a causa dell'attrito dinamico e dell'interazione con il campo mareale, mentre la componente stellare non collisionale sia rimasta invariata. In questo scenario il profilo radiale iniziale del SAG è dato dall'attuale profilo di densità delle stelle di alone, nella stessa galassia. A partire da questa ipotesi è possibile valutare il numero di AG persi verso il centro della galassia come l'integrale della differenza tra i due profili. Il nostro lavoro è consistito nell'ampliare i risultati trovati in letteratura analizzando 8 nuove galassie ellittiche (NGC 1400, NGC 1407, NGC 4472, NGC 3268, NGC 3258, NGC 4374, NGC 4406, NGC 4636). Abbiamo inoltre valutato la massa persa dai SAG di queste galassie. In questo modo abbiamo trovato che tali sistemi, durante la loro evoluzione, potrebbero aver perso una quantità di massa tra il $\sim 21\%$ e il $\sim 71\%$ del valore iniziale. La massa persa dal SAG arriva al centro della galassia, dove è spesso presente un SMBH e/o un NSC, influenzando la dinamica locale. La connessione tra l'evoluzione orbitale degli AG e la formazione del SMBH centrale è supportato dalla correlazione positiva trovata tra la massa persa dal SAG e la massa del SMBH. Questo andamento è ciò che ci si aspetta considerando che più il SMBH è massiccio piú esso accresce massa durante la sua evoluzione, aumentando il tasso con cui gli AG decadono al centro (Capuzzo-Dolcetta and Tesseri, 1999). Ammassi stellari come gli AG possono essere considerati come sistemi a N-corpi privi di gas, e quindi la loro dinamica può essere studiata impiegando metodi a N-corpi. Recentemente, un certo numero di metodi sono stati sviluppati per simulare numericamente l'evoluzione dei sistemi stellari. In questa Tesi abbiamo presentato un nuovo codice ad alte prestazioni e affidabilità, NBSymple. I metodi numerici ordinari per l'integrazione delle equazioni del moto sono dissipativi e presentano un comportamento non corretto a lungo termine. Questo è un problema grave quando si affronta il problema degli N-corpi, in particolare quando si studia la loro evoluzione a lungo termine. Una possibilità è quella di utilizzare integratori simplettici. Gli integratori simplettici sono schemi di integrazione numerica per sistemi Hamiltoniani, che descrivono l'evoluzione esatta di un sistema Hamiltoniano solo leggermente perturbato rispetto all'originale e che, dunque, possiedono l'Hamiltoniana perturbata come una quantità conservata. Questo garantisce l'assenza di qualsiasi cambiamento secolare nell'errore del totale sull'energia. Se l'integratore non è simplettico, l'errore sull'energia totale, generalmente, cresce in modo secolare. Abbiamo quindi introdotto in NBSymple la possibilità di scegliere tra due diversi metodi simplettici: un metodo del secondo ordine detto "leapfrog" e un metodo del sesto ordine. Abbiamo quindi realizzato 5 versioni del codice:

- NBSympleA: è la versione completamente seriale del codice che viene eseguito su un singolo processore;
- NBSympleB: è un codice a singola parellelizzazione su CPU, che utilizza le direttive Open Multi-Processing (OpenMP), sia per il calcolo delle interazioni a coppie (che scalano come N^2) e sia per i calcoli di ordine N (cioè l'integrazione temporale e la valutazione della componente galattica della forza sulle stelle);
- NBSympleC: qui si sfrutta la parellizzazione solo su GPU, demandando le interazioni a coppie ad una singola GPU, tramite CUDA mentre tutte le attività rimanenti sono svolte da una singola CPU;
- NBSympleD: è un codice doppiamente parallelo, che utilizza ancora una volta CUDA per valutare la porzione di codice di ordine $O(N^2)$ (come NBSympleC), mentre i calcoli di ordine $O(N)$ sono suddivisi tra le CPU a disposizione tramite OpenMP, come NBSympleB;
- NBSympleE: questo codice utilizza codice CUDA su una o due GPU per valutare la forza totale che agisce sul sistema stellare, vale a dire sia le interazioni a coppie sia la forza dovuta al potenziale galattico. Solo l'integrazione temporale è svolta da tutte le CPU a disposizione.

Abbiamo testato le varie versioni del codice trovando che l'utilizzo delle GPU permette un guadagno significativo in velocità di calcolo (fino a 3 ordini di grandezza in singola precisione) rispetto alla versione seriale. Abbiamo inoltre presentato una nuova versione di NBSymple in cui OpenMP è stato sostituito da direttive MPI: questo codice è stato testato su un cluster di CPU+GPU mostrando uno scalamento quasi perfetto. NBSymple è stato testato in varie applicazioni dimostrando versatilità, velocità e affidabilità.

Successivamente abbiamo utilizzato i metodi numerici per affrontare questioni aperte della dinamica stellare. Come affermato in precedenza, i NSC sono osservati al centro di molte galassie. In particolare, nel centro della Via Lattea, il NSC coesiste con un SMBH. L'origine di questi sistemi stellari è ancora sconosciuta ma potrebbe essere collegata all'evoluzione degli AG. Un possibile meccanismo di formazione, infatti, è proprio il decadimento degli ammassi globulari e la loro successiva fusione nel centro della galassia. Vari autori hanno indagato questo scenario, noto come "merger model" (si vedano per esempioTremaine *et al.* (1975); Capuzzo-Dolcetta (1993); Capuzzo-Dolcetta and Miocchi (2008a,b). In particolare Capuzzo-Dolcetta and Miocchi (2008a,b), attraverso simulazioni auto-consistenti, hanno trovato che la fusione di GC può dar luogo ad un ammasso stellare simile ai NSC osservati. Questi autori sono giunti a tale conclusione analizzando il profilo di densità e la dispersione velocità del NSC simulato e confrontando questi risultati con le osservazioni. In tutti questi lavori si è trascurata la presenza di un SMBH centrale e le simulazioni non sono mai state finalizzate ad uno studio specifico della Via Lattea.

Il nostro lavoro ha coperto questa mancanza attraverso simulazioni auto-consistenti le cui condizioni iniziali sono impostate basandosi su dati recenti riguardanti la VL (Launhardt *et al.*, 2002), includendo la presenza dei suoi SMBH centrale. La fusione di AG produce un sistema che si attesta rapidamente su uno stato quasi stazionario, e che evolve lentamente a causa del rilassamento interno che, a sua volta, è influenzato dalla presenza del SMBH. Il nucleo centrale a densità circa costante che caratterizza il prodotto della fusione viene mantenuto per un tempo abbastanza lungo da giustificare il suo analogo effettivamente osservato nel NSC della VL. I nostri risultati sono anche supportati dalla pendenza esterna del profilo di densità del NSC che rimane quasi invariata dopo la fine degli eventi di fusione e il cui valore, ~ -1.8, è in ottimo accordo con quello dedotto dalle osservazioni del NSC galattico. Inoltre il NSC simulato evolve verso l'isotropia delle velocità pur mantenendo un leggero grado di anisotropia tangenziale; questa peculiarità è stata trovata nei dati osservativi ed era stata già notata in precedenti studi numerici da Capuzzo Dolcetta *et al.* (2001). In conclusione, il decadimento consecutivo e la fusione, nella regione interna della Via Lattea, di un numero dell'ordine di 10 ammassi globulari massicci potrebbe spiegare le caratteristiche osservate del NSC che, nella nostra Galassia circonda il SMBH Sgr A^*.

Nell'ultima parte di questa Tesi abbiamo affrontato piú direttamente l'evoluzione dinamica degli AG nel campo galattico per mezzo di simulazioni numeriche effettuate con NBSymple. Durante la loro orbita intorno al centro galattico l'AG perde stelle, che vanno a formare le code mareali, lungo una direzione che deriva dalla composizione della direzione del centro galattico e la velocità orbitale dell'ammasso, determinando in tal modo la peculiare forma a S, osservata nella regione piú esterna dell'ammasso (Capuzzo Dolcetta *et al.*, 2005). Una volta formate, le code mareali si distendono rimanendo parallele all'orbita dell'ammasso, con la coda che precede l'ammasso che viene a trovarsi leggermente all'interno della sua orbita e la coda che segue l'ammasso che si sviluppa leggermente al di fuori della stessa orbita. Capuzzo Dolcetta *et al.* (2005) hanno dimostrato che le code tracciano in modo eccellente l'orbita dell'ammasso vicino al pericentro, mentre, all'apocentro, tendono a deviare dall'orbita stessa. Le code mareali hanno una struttura con sovradensità (clump) che non può essere associata a una perdita di massa episodica o a shock mareali dovuti alle sotto-strutture compatte della galassia, dal momento che le stelle sono perse dal cluster in modo continuo. Queste sovradensità non sono sistemi legati o auto-gravitanti, e il loro meccanismo di formazione non è ancora completamente noto. Abbiamo dunque modellato un GC utilizzando le proprietà osservate dell'AG Galattico Palomar 5 e effettuando alcune simulazioni di questo cluster su un orbita circolare intorno al centro Galattico.

L'analisi delle nostre simulazioni ha mostrato una correlazione tra la velocità media e la densità delle stelle che vengono perse dall'ammasso stesso. In particolare, il clump nella coda che precede l'ammasso corrisponde alla velocità media minima (e quello nella coda che segue alla velocità media massima) delle particelle lungo l'orbita. Inoltre, i nostri risultati preliminari, suggeriscono che le sovradensità si trovino dove le stelle che fuggono sono in media nei punti estremi delle loro orbite. Il clump nella coda che precede l'ammasso è formato da particelle che sono in media all'apocentro delle loro orbite, mentre il clump nella coda che segue l'ammasso è composto da particelle che sono in media al loro pericentro. Questo studio sarà oggetto ulteriori analisi che permetteranno di ottenere una migliore conoscenza dei meccanismi coinvolti; in particolare il confronto tra queste simulazioni e i dati osservativi potrebbe fornire ulteriori informazioni sulla forma del potenziale Galattico e sulla dinamica Galattica nel suo complesso.

Appendix A

The formal error on the estimates of number of lost Globular Clusters

Here we describe how we evaluated the errors, ϵ_l, given in Table 2.4. As explained in Section 2.2, the number of GCs lost in the galaxies of the sample has been evaluated as the integral of the difference between the (estimated) initial and present GCS radial distributions over the radial range $[r_{min}, r_{max}]$ where the two profiles differ. The absolute errors on N_l (ΔN_l) are given by the sum of the error on N_i (ΔN_i) and the error on N (ΔN), yielding the relative error $\epsilon_l = \frac{\Delta N_l}{N_l}$ of Table 2.4. We may estimate ΔN and ΔN_i as follows.

i) estimate of ΔN

For all the galaxies, except for NGC 4472, the number $N(r_{min}, r_{max})$ is given by

$$\begin{aligned} N(r_{min}, r_{max}) &= 2\pi\Sigma_0 \int_{r_{min}}^{r_{max}} \frac{r}{\left[1+\left(\frac{r}{r_c}\right)^2\right]^\gamma} dr = \\ &= \frac{\Sigma_0 \pi (r^2 + r_c^2)}{(1-\gamma)\left[1+\left(\frac{r}{r_c}\right)^2\right]^\gamma}\Bigg|_{r_{min}}^{r_{max}} \end{aligned} \tag{A.1}$$

which is a function of the parameters Σ_0, r_c, γ, r_{min} and r_{max} whose indetermination is

$$\begin{aligned} \Delta N = &\left|\frac{\partial N}{\partial \Sigma_0}\right| \Delta\Sigma_0 + \left|\frac{\partial N}{\partial r_c}\right| \Delta r_c + \left|\frac{\partial N}{\partial \gamma}\right| \Delta\gamma + \\ &+ \left|\frac{\partial N}{\partial r_{min}}\right| \Delta r_{min} + \left|\frac{\partial N}{\partial r_{max}}\right| \Delta r_{max} \end{aligned} \tag{A.2}$$

where:

$$\frac{\partial N}{\partial \Sigma_0} = 2\pi \int_{r_{min}}^{r_{max}} \frac{r}{\left[1+\left(\frac{r}{r_c}\right)^2\right]^{\gamma}} dr = \left.\frac{\pi(r^2+r_c^2)}{(1-\gamma)\left[1+\left(\frac{r}{r_c}\right)^2\right]^{\gamma}}\right|_{r_{min}}^{r_{max}}, \tag{A.3}$$

$$\begin{aligned} \frac{\partial N}{\partial r_c} &= \int_{r_{min}}^{r_{max}} \frac{4\pi\Sigma_0\gamma r^3}{r_c^3\left[1+\left(\frac{r}{r_c}\right)^2\right]^{(1+\gamma)}} dr = \\ &= -\left.\frac{2\pi\Sigma_0(r_c^2+\gamma r^2)}{r_c(\gamma-1)\left[1+\left(\frac{r}{r_c}\right)^2\right]^{\gamma}}\right|_{r_{min}}^{r_{max}}, \end{aligned} \tag{A.4}$$

$$\begin{aligned} \frac{\partial N}{\partial \gamma} &= -2\pi\Sigma_0 \int_{r_{min}}^{r_{max}} r\left[1+\left(\frac{r}{r_c}\right)^2\right]^{-\gamma} \ln\left[1+\left(\frac{r}{r_c}\right)^2\right] dr = \\ &= \left.\frac{\pi\Sigma_0(r^2+r_c^2)\left\{1+(\gamma-1)\ln\left[1+\left(\frac{r}{r_c}\right)^2\right]\right\}}{(\gamma-1)^2\left[1+\left(\frac{r}{r_c}\right)^2\right]^{\gamma}}\right|_{r_{min}}^{r_{max}}, \end{aligned} \tag{A.5}$$

$$\frac{\partial N}{\partial r_{min}} = -2\pi\Sigma_0 \frac{r_{min}}{\left[1+\left(\frac{r_{min}}{r_c}\right)^2\right]^{\gamma}}, \tag{A.6}$$

(we set $r_{min} = 0.1$ arcmin).

$$\frac{\partial N}{\partial r_{max}} = 2\pi\Sigma_0 \frac{r_{max}}{\left[1+\left(\frac{r_{max}}{r_c}\right)^2\right]^{\gamma}}. \tag{A.7}$$

For NGC 4472 we have that:

$$\begin{aligned} N(r_{min}, r_{max}) &= 2\pi\Sigma_0 \int_{r_{min}}^{r_{max}} \left(\frac{r_c}{r}\right)^{\gamma} \frac{r}{\left[1+\frac{r}{r_c}\right]^{4-\gamma}} dr = \\ &= 2\pi\Sigma_0(r_c r)^2\left(\frac{r_c+r}{r}\right)^{\gamma} \left.\frac{(3-\gamma)r_c+r}{(6-5\gamma+\gamma^2)(r_c+r)^3}\right|_{r_{min}}^{r_{max}}. \end{aligned} \tag{A.8}$$

This is a function of the parameters Σ_0, r_c, r_{min} and r_{max} whose indetermination is:

$$\Delta N = \left|\frac{\partial N}{\partial \Sigma_0}\right| \Delta\Sigma_0 + \left|\frac{\partial N}{\partial r_c}\right| \Delta r_c + \left|\frac{\partial N}{\partial \gamma}\right| \Delta\gamma + \left|\frac{\partial N}{\partial r_{min}}\right| \Delta r_{min} + \left|\frac{\partial N}{\partial r_{max}}\right| \Delta r_{max} \tag{A.9}$$

where:

$$\begin{aligned}\frac{\partial N}{\partial \Sigma_0} &= 2\pi \int_{r_{min}}^{r_{max}} \left(\frac{r_c}{r}\right)^{\gamma} \frac{r}{\left[1+\frac{r}{r_c}\right]^{4-\gamma}} dr = \\ &= 2\pi (r_c r)^2 \left(\frac{r_c + r}{r}\right)^{\gamma} \frac{(3-\gamma) r_c + r}{(6-5\gamma+\gamma^2)(r_c+r)^3}\Bigg|_{r_{min}}^{r_{max}} .\end{aligned} \tag{A.10}$$

$$\begin{aligned}\frac{\partial N}{\partial r_c} &= 2\pi\Sigma_0 \int_{r_{min}}^{r_{max}} \left[\frac{(\gamma-4)r^2}{r_c^2}\left(\frac{r_c}{r}\right)^{\gamma}\left(1+\frac{r}{r_c}\right)^{\gamma-5} + \right. \\ &\left. +\gamma\left(\frac{r_c}{r}\right)^{\gamma-1}\left(1+\frac{r}{r_c}\right)^{\gamma-4}\right] dr = \\ &= \frac{2\pi\Sigma_0 r_c r^2}{(6-5\gamma+\gamma^2)(r_c+r)^4}\left(\frac{r_c+r}{r}\right)^{\gamma} \times \\ &\times \left[2r^2(\gamma-1) - 2r_c r(\gamma^2-5\gamma+4) - \gamma r_c^2(\gamma-3)\right]\Big|_{r_{min}}^{r_{max}} ,\end{aligned} \tag{A.11}$$

$$\begin{aligned}\frac{\partial N}{\partial \gamma} &= 2\pi\Sigma_0 \int_{r_{min}}^{r_{max}} \left(\frac{r_c}{r}\right)^{\gamma} r \left(1+\frac{r}{r_c}\right)^{\gamma-4} \ln\left(1+\frac{r_c}{r}\right) dr = \\ &= \frac{2\pi\Sigma_0 (r_c r)^2}{(6-5\gamma+\gamma^2)^2 (r_c+r)^3}\left(\frac{r_c+r}{r}\right)^{\gamma}\Big\{r_c(9-6\gamma+\gamma^2) + \\ &+ r(5-2\gamma) - (6-5\gamma+\gamma^2)[(\gamma-3)r_c - r]\ln\left(1+\frac{r_c}{r}\right)\Big\}\Bigg|_{r_{min}}^{r_{max}} ,\end{aligned} \tag{A.12}$$

$$\frac{\partial N}{\partial r_{min}} = -2\pi\Sigma_0 \left(\frac{r_c}{r_{min}}\right)^{\gamma} \frac{r_{min}}{\left[1+\frac{r_{min}}{r_c}\right]^{4-\gamma}}, \tag{A.13}$$

$$\frac{\partial N}{\partial r_{max}} = 2\pi\Sigma_0 \left(\frac{r_c}{r_{max}}\right)^{\gamma} \frac{r_{max}}{\left[1+\frac{r_{max}}{r_c}\right]^{4-\gamma}}. \tag{A.14}$$

The fitting parameters used to calculate ΔN are summarized in Tab. 2.2.

ii) estimate of ΔN_i

The fitting formulas to the initial distribution of GCs change for the various galaxies studied.
For NGC 1400, NGC 1407, NGC 4374, NGC 4636 we have (see Section 2.3.1, 2.3.2, 2.3.5, 2.3.8 and Tab. 2.3 for the meaning and the values of the parameters)

$$\begin{aligned}N_i(r_{min}, r_{max}) &= 2\pi\eta r_b^{-\alpha} \int_{r_{min}}^{r_b} r dr + 2\pi\eta \int_{r_b}^{r_{max}} r^{1-\alpha} dr = \\ &= \pi\eta r_b^{-\alpha} r^2 \Big|_{r_{min}}^{r_b} + 2\pi\eta \frac{r^{2-\alpha}}{2-\alpha}\Bigg|_{r_b}^{r_{max}} .\end{aligned} \tag{A.15}$$

In Equation A.15, η represents the parameter obtained by the vertical shifting of the luminosity profile.

The error ΔN_i is thus given by:

$$\Delta N_i = \left|\frac{\partial N_i}{\partial \eta}\right| \Delta\eta + \left|\frac{\partial N_i}{\partial r_b}\right| \Delta r_b + \left|\frac{\partial N_i}{\partial \alpha}\right| \Delta\alpha + \left|\frac{\partial N_i}{\partial r_{min}}\right| \Delta r_{min} + \left|\frac{\partial N_i}{\partial r_{max}}\right| \Delta r_{max} \quad \text{(A.16)}$$

where:

$$\begin{aligned} \frac{\partial N_i}{\partial \eta} &= 2\pi r_b^{-\alpha} \int_{r_{min}}^{r_b} r dr + 2\pi \int_{r_b}^{r_{max}} r^{1-\alpha} dr = \\ &= \pi r_b^{-\alpha} r^2 \Big|_{r_{min}}^{r_b} + 2\pi \frac{r^{2-\alpha}}{2-\alpha}\Bigg|_{r_b}^{r_{max}}, \end{aligned} \quad \text{(A.17)}$$

$$\frac{\partial N_i}{\partial r_b} = -2\pi\eta\alpha r_b^{-1-\alpha} \int_{r_{min}}^{r_b} r dr = -\pi\eta r_b^{-1-\alpha} r^2 \Big|_{r_{min}}^{r_b}, \quad \text{(A.18)}$$

$$\begin{aligned} \frac{\partial N_i}{\partial \alpha} &= -2\pi\eta r_b^{-\alpha} \int_{r_{min}}^{r_b} r \ln(r_b) dr - 2\pi\eta \int_{r_b}^{r_{max}} r^{1-\alpha} \ln(r) dr = \\ &= -2\pi r_b^{-\alpha} r^2 \ln(r_b) \Big|_{r_{min}}^{r_b} + \frac{2\pi\eta r^{2-\alpha}\left\{1 + [\alpha - 2]\ln(r)\right\}}{(\gamma-2)^2}\Bigg|_{r_b}^{r_{max}}, \end{aligned} \quad \text{(A.19)}$$

Also in this case we assumed $r_{min} = 0.1$ arcmin. For all the galaxies analysed, $r_{min} > r_b$ and $r_{max} > r_b$; so we have

$$\frac{\partial N_i}{\partial r_{min}} = -2\pi\eta r_{min}^{1-\alpha}, \quad \text{(A.20)}$$

$$\frac{\partial N_i}{\partial r_{max}} = 2\pi\eta r_{max}^{1-\alpha}. \quad \text{(A.21)}$$

For M 49 and NGC 4406 (Section 2.3.7 and Section 2.3.6) we have

$$\begin{aligned} N_i(r_{min}, r_{max}) &= 2\pi\eta \int_{r_{min}}^{r_{max}} r \left\{ \left(\frac{r_b}{r}\right)^{\gamma} \theta(r_b - r) + \mathrm{e}^{b_n\left[\left(\frac{r_b}{r_e}\right)^{\frac{1}{n}} - \left(\frac{r}{r_e}\right)^{\frac{1}{n}}\right]} \theta(r - r_b) \right\} dr = \\ &= \frac{2\pi\eta}{2-\gamma} r^2 \left(\frac{r_b}{r}\right)^{\gamma}\Bigg|_{r_{min}}^{r_b} + 2\pi\eta \int_{r_b}^{r_{max}} r\mathrm{e}^{b_n\left[\left(\frac{r_b}{r_e}\right)^{\frac{1}{n}} - \left(\frac{r}{r_e}\right)^{\frac{1}{n}}\right]} dr \end{aligned} \quad \text{(A.22)}$$

where $b_n = 1.992n - 0.3271$. The second row of the previous expression is justified by the fact that, both for M 49 and NGC 4406, $r_b > r_{min}$. Thus the error on N_l

$$\begin{aligned} \Delta N_i = &\left|\frac{\partial N_i}{\partial \eta}\right| \Delta\eta + \left|\frac{\partial N_i}{\partial b_n}\right| \Delta b_n + \left|\frac{\partial N_i}{\partial r_b}\right| \Delta r_b + \left|\frac{\partial N_i}{\partial \gamma}\right| \Delta\gamma + \\ &+ \left|\frac{\partial N_i}{\partial r_e}\right| \Delta r_e + \left|\frac{\partial N_i}{\partial n}\right| \Delta n + \left|\frac{\partial N_i}{\partial r_{min}}\right| \Delta r_{min} + \left|\frac{\partial N_i}{\partial r_{max}}\right| \Delta r_{max} \end{aligned} \quad \text{(A.23)}$$

where $\Delta b_n = \left|\frac{\partial b_n}{\partial n}\right| \Delta n$, is evaluated by the following expressions of the individual error contribution:

$$\begin{aligned}\frac{\partial N_i}{\partial \eta} &= 2\pi \int_{r_{min}}^{r_b} r\left(\frac{r_b}{r}\right)^{\gamma} dr + 2\pi \int_{r_b}^{r_{max}} r e^{b_n\left[\left(\frac{r_b}{r_e}\right)^{\frac{1}{n}}-\left(\frac{r}{r_e}\right)^{\frac{1}{n}}\right]} dr = \\ &= \frac{2\pi}{2-\gamma} r^2 \left(\frac{r_b}{r}\right)^{\gamma}\Bigg|_{r_{min}}^{r_b} + 2\pi \int_{r_b}^{r_{max}} r e^{b_n\left[\left(\frac{r_b}{r_e}\right)^{\frac{1}{n}}-\left(\frac{r}{r_e}\right)^{\frac{1}{n}}\right]} dr,\end{aligned} \tag{A.24}$$

$$\frac{\partial N_i}{\partial b_n} = 2\pi\eta \int_{r_b}^{r_{max}} r e^{b_n\left[\left(\frac{r_b}{r_e}\right)^{\frac{1}{n}}-\left(\frac{r}{r_e}\right)^{\frac{1}{n}}\right]} \left[\left(\frac{r_b}{r_e}\right)^{\frac{1}{n}} - \left(\frac{r}{r_e}\right)^{\frac{1}{n}}\right] dr, \tag{A.25}$$

$$\begin{aligned}\frac{\partial N_i}{\partial r_b} &= 2\pi\eta\gamma \int_{r_{min}}^{r_b} \left(\frac{r_b}{r}\right)^{\gamma-1} dr + \\ &+ 2\pi\frac{\eta b_n}{n r_e} \int_{r_b}^{r_{max}} r e^{b_n\left[\left(\frac{r_b}{r_e}\right)^{\frac{1}{n}}-\left(\frac{r}{r_e}\right)^{\frac{1}{n}}\right]} \left(\frac{r_b}{r_e}\right)^{\frac{1}{n}-1} dr = \\ &= \frac{2\pi\eta\gamma}{2-\gamma} r\left(\frac{r_b}{r}\right)^{\gamma-1}\Bigg|_{r_{min}}^{r_b} + \\ &+ 2\pi\frac{\eta b_n}{n r_e} \int_{r_b}^{r_{max}} r e^{b_n\left[\left(\frac{r_b}{r_e}\right)^{\frac{1}{n}}-\left(\frac{r}{r_e}\right)^{\frac{1}{n}}\right]} \left(\frac{r_b}{r_e}\right)^{\frac{1}{n}-1} dr,\end{aligned} \tag{A.26}$$

$$\begin{aligned}\frac{\partial N_i}{\partial \gamma} &= 2\pi\eta \int_{r_{min}}^{r_b} r\left(\frac{r_b}{r}\right)^{\gamma} \ln\left(\frac{r_b}{r}\right) dr = \\ &= \frac{2\pi\eta r^2}{(\gamma-2)^2}\left(\frac{r_b}{r}\right)^{\gamma}\left[1+(2-\gamma)\ln\left(\frac{r_b}{r}\right)\right]\Bigg|_{r_{min}}^{r_b}\end{aligned} \tag{A.27}$$

$$\begin{aligned}\frac{\partial N_i}{\partial r_e} &= -2\pi\frac{\eta b_n}{n r_e^2} \int_{r_b}^{r_{max}} r e^{b_n\left[\left(\frac{r_b}{r_e}\right)^{\frac{1}{n}}-\left(\frac{r}{r_e}\right)^{\frac{1}{n}}\right]} \times \\ &\times \left[r_b\left(\frac{r_b}{r_e}\right)^{\frac{1}{n}-1} - r\left(\frac{r}{r_e}\right)^{\frac{1}{n}-1}\right] dr,\end{aligned} \tag{A.28}$$

$$\begin{aligned}\frac{\partial N_i}{\partial n} &= -2\pi\frac{\eta b_n}{n^2} \int_{r_b}^{r_{max}} r e^{b_n\left[\left(\frac{r_b}{r_e}\right)^{\frac{1}{n}}-\left(\frac{r}{r_e}\right)^{\frac{1}{n}}\right]} \times \\ &\times \left[\left(\frac{r_b}{r_e}\right)^{\frac{1}{n}} \ln\left(\frac{r_b}{r_e}\right) - \left(\frac{r}{r_e}\right)^{\frac{1}{n}} \ln\left(\frac{r}{r_e}\right)\right] dr,\end{aligned} \tag{A.29}$$

Remembering that, for both NGC 4472 and NGC 4406, $r_{min} > r_b$ and $r_{max} > r_b$ we can estimate the following contributions

$$\frac{\partial N_i}{\partial r_{min}} = -2\pi\eta r_{min} \exp\left\{b_n\left[\left(\frac{r_b}{r_e}\right)^{\frac{1}{n}} - \left(\frac{r_{min}}{r_e}\right)^{\frac{1}{n}}\right]\right\}, \tag{A.30}$$

$$\frac{\partial N_i}{\partial r_{max}} = 2\pi\eta r_{max} \exp\left\{b_n\left[\left(\frac{r_b}{r_e}\right)^{\frac{1}{n}} - \left(\frac{r_{max}}{r_e}\right)^{\frac{1}{n}}\right]\right\}. \tag{A.31}$$

See Tab. 2.3 for the values of the parameters used in the Equation A.22- Equation A.31.

Last, for NGC 3268 and NGC 3258 (see Section 2.3.4, Section 2.3.3 and Tab. 2.3 for the values of the parameters) we have the same equations obtained for the present profile of all the galaxies, except NGC 4472 (see Equation A.1-A.7). All the integrals from Equation A.22 to Equation A.29 must be calculated numerically using the values of the parameters given in Table 2.3.

The results listed in Table 2.2 are obtained assuming an error of 1% on each independent parameter used. Just in the case of NGC 4472, where we assumed $\gamma = 0$ (Côté *et al.*, 2003), we could not consider a value for $\Delta\gamma$ as obtained by a fixed percentual variation and, thus, we adopted $\Delta\gamma = 0.01$.

Appendix B

A simplified derivation of the relaxation time

To derive an expression of the relaxation time, we can consider a test particle of mass m, moving toward a system composed of N particles of mass M (field stars), from position $\widetilde{\mathbf{r}} \to \infty$ with velocity $\mathbf{v}$ parallel to the x-axis. As we can see in Figure (B.1), the *impact parameter*, respect to a generic field star is b. Each close encounter perturbs the velocity of the test particle by a quantity $\delta v_\perp$ parallel to the y axis. Since the field stars are assumed to be distributed uniformly, the mean value $\langle \Delta \mathbf{v}_\perp \rangle$, is zero. Thus, to derive the relaxation time we set

$$\frac{\langle \Delta v_\perp^2 \rangle}{v^2} \simeq 1 \ ,$$

in such a way we require that the generic test particle completely loses memory of its initial trajectory. The module of the perpendicular force, $F_\perp$, (i.e. the component along the y-axis), acting on the mass m, can be expressed as

$$F_\perp = G\frac{mM}{r^2}\cos\theta \ . \tag{B.1}$$

Assuming that the perturbation to the velocity is small (i.e. $\delta v_\perp / v \ll 1$), we can write

$$\cos\theta \simeq \frac{b}{r} \qquad r^2 \simeq x^2 + b^2 \qquad x = vt$$

and, substituting this expression into Equation (B.1), we get

$$F_\perp = G\frac{mMb}{(v^2t^2+b^2)^{\frac{3}{2}}} = G\frac{mM}{b^2\left[\left(\frac{vt}{b}\right)^2+1\right]^{\frac{3}{2}}} = m\frac{\mathrm{d}}{\mathrm{d}t}v_\perp \tag{B.2}$$

where, in the last passage we used the Newton's second law of motion. Integrating the relation (B.2) with respect to time, we have

$$\delta v_\perp = \frac{GM}{b^2}\int\limits_{-\infty}^{+\infty}\left[\left(\frac{vt}{b}\right)^2+1\right]^{-\frac{3}{2}}\mathrm{d}t = 2\frac{GM}{bv} \ .$$

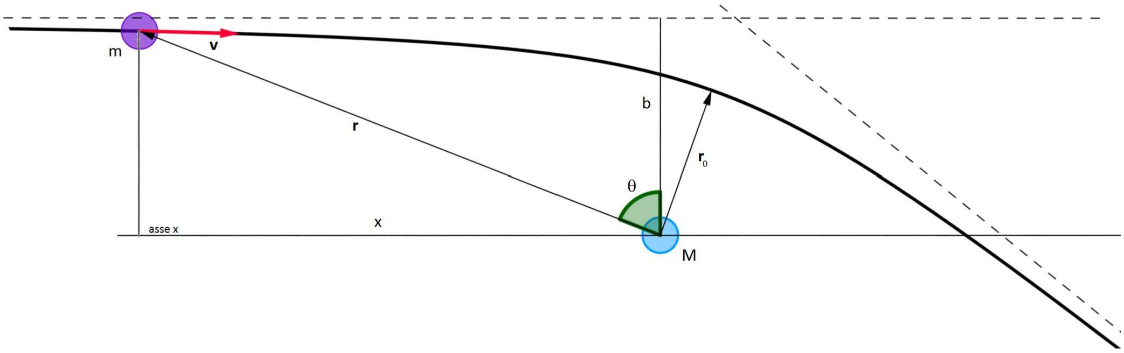

Figure B.1. A simple scheme of a two-body collision with impact parameter b.

The average number of collisions δn_b, with an impact parameter between b and $b + \delta b$, suffered by a particle that crosses a system with a typical dimension equal to R is

$$\delta n_b = P(b, R) \cdot N$$

where the probability of the single close, $P(b, R)$, is equal to the ratio between the geometric cross section of the collision and the geometric cross section of the system. Therefore

$$\delta n_b = \frac{2\pi b \mathrm{d}b}{\pi R^2} N = \frac{2bN}{R^2} \mathrm{d}b$$

and the mean quadratic variation of $v_\perp$, due to the collisions δn_b, can be expressed as

$$\left\langle \Delta v_\perp^2 \right\rangle_b = \delta n_b \delta v_\perp^2 = \frac{8G^2 M^2 N}{v^2 R^2} \mathrm{d} \log b \ . \tag{B.3}$$

Integrating Equation (B.3) over all possible values of b we get $\langle \Delta v_\perp^2 \rangle$. We take he typical dimension of the system, R, as the maximum value of the impact parameter (b_M). To give a correct estimate of the minimum value of the same quantity, b_m, avoiding logarithmic divergence, we use the distance of minimum approach between the two particle involved in the collision, r_0 (see figure (B.1). The total energy must be conserved, thus

$$\frac{1}{2}\mu v^2 = \frac{1}{2}\mu v_0^2 - G\frac{mM}{r_0} \tag{B.4}$$

where v_0 is the velocity at the minimum distance, and $\mu = \frac{mM}{m+M}$ is the reduced mass of the system. From (B.4) we can obtain

$$\frac{1}{2}\mu v_0^2 - G\frac{mM}{r_0} > 0 \Rightarrow r_0 > \frac{2G(M+m)}{v^2 \frac{v_0^2}{v^2}} \simeq \frac{2G(M+m)}{v^2} = b_m$$

where we have used the approximation of small perturbation ($\frac{v_0^2}{v^2} \simeq 1$). In light of this, we can integrate Equation (B.3) between b_m and b_M obtaining

$$\left\langle \Delta v_\perp^2 \right\rangle = \frac{8G^2 M^2 N}{v^2 R^2} \log \Lambda \tag{B.5}$$

where the quantity $\log \Lambda = \log \frac{b_M}{b_m}$ has been introduced and, often, it is called *Coulomb logarithm*. Dividing (B.5) by v^2 we get

$$\frac{\langle \Delta v_\perp^2 \rangle}{v^2} = \frac{8G^2M^2N}{v^4R^2} \log \Lambda \ . \tag{B.6}$$

From (3.22) we can evaluate the typical velocity of a particle in an N-body system, provided that this system is in a stationary state. We have

$$2T - U = M_{tot} v_{typical}^2 - \alpha \frac{GM_{tot}^2}{R} = 0 \Rightarrow v_{typical}^2 = \alpha \frac{GM_{tot}}{R} = \alpha \frac{GMN}{R} \tag{B.7}$$

where α is constant such that $\alpha \lesssim 1$ and $M_{tot} = MN$ is the total mass of the system. Putting $\alpha = 1$ and substituting into (B.6), we obtain

$$\frac{\langle \Delta v_\perp^2 \rangle}{v^2} = \frac{8}{N} \log \Lambda \ \ .$$

Before relaxation, a particle will pass through the system a number of times n_R which can be derived from the condition

$$\frac{\langle \Delta v_\perp^2 \rangle}{v^2} n_R \simeq 1 \Rightarrow n_R \simeq \frac{1}{8} \frac{N}{\log \Lambda}$$

so, finally, we obtain

$$t_r \simeq n_R t_c = \frac{1}{8} \frac{N}{\log \Lambda} t_c \tag{B.8}$$

where t_c is the crossing time given by Equation (3.25) and, generally, $\log \Lambda$ is replaced by $\log N$ because

$$\log \Lambda = \log \frac{Rv^2}{2G(M+m)} \simeq \log \frac{N}{2} \simeq \log N$$

where we have used the expression of the typical velocity given by Equation (B.7) and we have considered $M \gg m$ and $\log N \gg \log 2$.

Appendix C

The distribution of the Globular Clusters orbits

In this appendix we briefly resume how we obtained the different circular orbits of our GCs.

The surface of a sphere can be uniquely tessellated by means of 12 regular pentagons, the centers of which form a regular dodecahedron inscribed in the sphere. Following Gualandris and Merritt (2009) we used the centers of these pentagons to identify the vectors parallel to our GCs angular momentum vectors.

To rotate the positions and velocities of the original N-body model of the cluster we used the inclination i and longitude of ascending node Ω of the centers of the pentagons given in Table C.1.

The positions (as well as the velocities) in the rotated reference frame (x', y', z') can be obtained using the following equations, where (x, y, z) are the coordinates in the original frame

$$\begin{aligned} x' &= \lambda_{x_1} x + \lambda_{x_2} y + \lambda_{x_3} z \\ y' &= \lambda_{y_1} x + \lambda_{y_2} y + \lambda_{y_3} z \\ z' &= \lambda_{z_1} x + \lambda_{z_2} y + \lambda_{z_3} z \end{aligned} \tag{C.1}$$

where

$$\begin{aligned} \lambda_{x_1} &= \cos\Omega\cos\omega - \sin\Omega\cos i\sin\omega \\ \lambda_{x_2} &= \sin\Omega\cos\omega + \cos\Omega\cos i\sin\omega \\ \lambda_{x_3} &= \sin i\sin\omega, \end{aligned} \tag{C.2}$$

$$\begin{aligned} \lambda_{y_1} &= -\cos\Omega\sin\omega - \sin\Omega\cos i\cos\omega \\ \lambda_{y_2} &= -\sin\Omega\sin\omega + \cos\Omega\cos i\cos\omega \\ \lambda_{y_3} &= \sin i\cos\omega \end{aligned} \tag{C.3}$$

and

n	i	Ω
1	0	148.28
2	31.72	90
3	328.28	90
4	0	31.72
5	180	31.72
6	270	58.28
7	180	148.28
8	90	121.72
9	90	58.28
10	270	121.72
11	148.28	90
12	211.72	90

Table C.1. The inclination i and longitude of ascending node Ω.

$$\begin{aligned}\lambda_{z_1} &= \sin i \sin\Omega \\ \lambda_{z_2} &= \sin\Omega\cos\omega + \cos\Omega\cos - \sin i\cos\Omega. \\ \lambda_{z_3} &= \cos i.\end{aligned} \tag{C.4}$$

The value of $\omega \in [0, 2\pi]$, that is needed to evaluate the rotated position and velocities, was picked randomly for each orbit.

Bibliography

Aarseth, S. J. (1999). From NBODY1 to NBODY6: The Growth of an Industry. *PASP*, **111**, 1333–1346.

Aarseth, S. J. (2003). *Gravitational N-Body Simulations.*

Aarseth, S. J. and Heggie, D. C. (1998). Basic N-body modelling of the evolution of globular clusters - I. Time scaling. *MNRAS*, **297**, 794–806.

Aarseth, S. J. and Lecar, M. (1975). Computer simulations of stellar systems. *ARA&A*, **13**, 1–21.

Abadi, M. G., Navarro, J. F., and Steinmetz, M. (2006). Stars beyond galaxies: the origin of extended luminous haloes around galaxies. *MNRAS*, **365**, 747–758.

Abraham, R. and Mardsen, J. E. (1978). Foundations of mechanics. In Abraham, R. & Mardsen, J. E., editor, *London, Amsterdam: Benjamin/Cummings, 1978, 2nd ed.*

Abraham, R. G. and van den Bergh, S. (1995). A Gauss-Hermite expansion of the galactic globular cluster luminosity function. *ApJ*, **438**, 218–222.

Agarwal, M. and Milosavljević, M. (2011). Nuclear Star Clusters from Clustered Star Formation. *ApJ*, **729**, 35.

Allen, C. and Santillan, A. (1991). An improved model of the galactic mass distribution for orbit computations. *RMxAA*, **22**, 255–263.

Allison, R. J., Goodwin, S. P., Parker, R. J., de Grijs, R., Portegies Zwart, S. F., and Kouwenhoven, M. B. N. (2009). Dynamical Mass Segregation on a Very Short Timescale. *ApJL*, **700**, L99–L103.

Ambartsumian, V. A. (1985). On the dynamics of open clusters. In J. Goodman & P. Hut, editor, *Dynamics of Star Clusters*, volume 113 of *IAU Symposium*, page 521.

André, P. (2002). Nearby Protoclusters as Laboratories for Understanding Star Formation on Galactic Scales. *Ap&SS*, **281**, 51–66.

Antonini, F., Capuzzo-Dolcetta, R., and Merritt, D. (2009). A counterpart to the radial-orbit instability in triaxial stellar systems. *MNRAS*, **399**, 671–682.

Antonini, F., Capuzzo-Dolcetta, R., Mastrobuono-Battisti, A., and Merritt, D. (2011). Dissipationless Formation and Evolution of the Milky Way Nuclear Star Cluster. *submitted to ApJ*.

Arca-Sedda, M. and Capuzzo-Dolcetta, R. (2011). *in preparation*.

Ashman, K. M. and Zepf, S. E. (1998). Globular Cluster Systems. In Ashman, K. M. & Zepf, S. E., editor, *Globular cluster systems / Keith M. Ashman, Stephen E. Zepf. Cambridge, U. K. ; New York : Cambridge University Press, 1998. (Cambridge astrophysics series ; 30) QB853.5 .A84 1998 ($69.95)*.

Bahcall, J. N. and Wolf, R. A. (1976). Star distribution around a massive black hole in a globular cluster. *ApJ*, **209**, 214–232.

Balbinot, E., Santiago, B. X., da Costa, L. N., Makler, M., and Maia, M. A. G. (2011). The tidal tails of NGC 2298. *MNRAS*, **416**, 393–402.

Balmaverde, B. and Capetti, A. (2006). The host galaxy/AGN connection in nearby early-type galaxies. Is there a miniature radio-galaxy in every ”core” galaxy? *A&A*, **447**, 97–112, BC06.

Barnes, J. and Hut, P. (1986). A hierarchical O(N log N) force-calculation algorithm. *Nature*, **324**, 446–449.

Barsdell, B. R., Barnes, D. G., and Fluke, C. J. (2010). Advanced Architectures for Astrophysical Supercomputing. In Y. Mizumoto, K.-I. Morita, & M. Ohishi, editor, *Astronomical Data Analysis Software and Systems XIX*, volume 434 of *Astronomical Society of the Pacific Conference Series*, page 209.

Bartko, H. *et al.* (2010). An Extremely Top-Heavy Initial Mass Function in the Galactic Center Stellar Disks. *ApJ*, **708**, 834–840.

Bate, M. R., Bonnell, I. A., and Price, N. M. (1995). Modelling accretion in protobinary systems. *MNRAS*, **277**, 362–376.

Bate, M. R., Bonnell, I. A., and Bromm, V. (2003). The Formation Mechanism and Resulting Properties of Brown Dwarfs. In E. Martín, editor, *Brown Dwarfs*, volume 211 of *IAU Symposium*, page 27.

Battinelli, P. and Capuzzo-Dolcetta, R. (1991). Formation and evolutionary properties of the Galactic open cluster system. *MNRAS*, **249**, 76–83.

Becklin, E. E. and Neugebauer, G. (1968). Infrared Observations of the Galactic Center. *ApJ*, **151**, 145.

Bekki, K. (2007). The Formation of Stellar Galactic Nuclei through Dissipative Gas Dynamics. *PASA*, **24**, 77–94.

Bekki, K. and Forbes, D. A. (2006). On the structure of globular cluster systems in elliptical galaxies. *A&A*, **445**, 485–491.

Bekki, K., Couch, W. J., Drinkwater, M. J., and Shioya, Y. (2004). Cluster Cannibalism and Scaling Relations of Galactic Stellar Nuclei. *ApJL*, **610**, L13–L16.

Bellazzini, M., Ferraro, F. R., and Ibata, R. (2003). Building Up the Globular Cluster System of the Milky Way: The Contribution of the Sagittarius Galaxy. *AJ*, **125**.

Belleman, R. G., Bédorf, J., and Portegies Zwart, S. F. (2008). High performance direct gravitational N-body simulations on graphics processing units II: An implementation in CUDA. *NewA*, **13**, 103–112.

Belokurov, V. *et al.* (2006a). The Field of Streams: Sagittarius and Its Siblings. *ApJL*, **642**, L137–L140.

Belokurov, V. *et al.* (2007). An Orphan in the “Field of Streams”. *ApJ*, **658**, 337–344.

Belokurov, V., Evans, N. W., Irwin, M. J., Hewett, P. C., and Wilkinson, M. I. (2006b). The Discovery of Tidal Tails around the Globular Cluster NGC 5466. *ApJL*, **637**, L29–L32.

Beuther, H., Churchwell, E. B., McKee, C. F., and Tan, J. C. (2007). The Formation of Massive Stars. *Protostars and Planets V*, pages 165–180.

Binney, J. and Tremaine, S. (1987). *Galactic dynamics.*

Bodenheimer, P., Laughlin, G. P., Rózyczka, M., and Yorke, H. W., editors (2007). *Numerical Methods in Astrophysics: An Introduction.*

Böker, T. (2007). Nuclear Star Clusters across the Hubble Sequence. *ArXiv e-prints.*

Böker, T. (2010a). Nuclear star clusters. In R. de Grijs & J. R. D. Lépine, editor, *IAU Symposium*, volume 266 of *IAU Symposium*, pages 58–63.

Böker, T. (2010b). *Nuclear Star Clusters Across the Hubble Sequence*, page 99.

Böker, T., Laine, S., van der Marel, R. P., Sarzi, M., Rix, H.-W., Ho, L. C., and Shields, J. C. (2002a). A Hubble Space Telescope Census of Nuclear Star Clusters in Late-Type Spiral Galaxies. I. Observations and Image Analysis. *AJ*, **123**, 1389–1410.

Böker, T., Laine, S., van der Marel, R. P., Sarzi, M., Rix, H.-W., Ho, L. C., and Shields, J. C. (2002b). A Hubble Space Telescope Census of Nuclear Star Clusters in Late-Type Spiral Galaxies. I. Observations and Image Analysis. *AJ*, **123**, 1389–1410.

Böker, T., Sarzi, M., McLaughlin, D. E., van der Marel, R. P., Rix, H.-W., Ho, L. C., and Shields, J. C. (2004). A Hubble Space Telescope Census of Nuclear Star Clusters in Late-Type Spiral Galaxies. II. Cluster Sizes and Structural Parameter Correlations. *AJ*, **127**, 105–118.

Bolte, M. and Hogan, C. J. (1995). Conflict over the age of the Universe. *Nature*, **376**, 399–402.

Bonnell, I. A. and Davies, M. B. (1998). Mass segregation in young stellar clusters. *MNRAS*, **295**, 691.

Bonnell, I. A., Clarke, C. J., Bate, M. R., and Pringle, J. E. (2001). Accretion in stellar clusters and the initial mass function. *MNRAS*, **324**, 573–579.

Bonnell, I. A., Bate, M. R., and Vine, S. G. (2003). The hierarchical formation of a stellar cluster. *MNRAS*, **343**, 413–418.

Bonnell, I. A., Clark, P., and Bate, M. R. (2008). Gravitational fragmentation and the formation of brown dwarfs in stellar clusters. *MNRAS*, **389**, 1556–1562.

Bryan, G. L. and Norman, M. L. (1998). Statistical Properties of X-Ray Clusters: Analytic and Numerical Comparisons. *ApJ*, **495**, 80.

Buchholz, R. M., Schödel, R., and Eckart, A. (2009). Composition of the galactic center star cluster. Population analysis from adaptive optics narrow band spectral energy distributions. *A&A*, **499**, 483–501.

Bullock, J. S. and Johnston, K. V. (2005). Tracing Galaxy Formation with Stellar Halos. I. Methods. *ApJ*, **635**, 931–949.

Capuzzo-Dolcetta, R. (1993). The Evolution of the Globular Cluster System in a Triaxial Galaxy: Can a Galactic Nucleus Form by Globular Cluster Capture? *ApJ*, **415**, 616–630.

Capuzzo-Dolcetta, R. (2002). Galactic Nuclear Activity Induced By Globular Cluster Merging (Invited). In E. K. Grebel & W. Brandner, editor, *Modes of Star Formation and the Origin of Field Populations*, volume 285 of *Astronomical Society of the Pacific Conference Series*, page 389.

Capuzzo-Dolcetta, R. (2005). High performance computing for self-gravitating systems. *Computer Physics Communications*, **169**, 365–369.

Capuzzo Dolcetta, R. and di Lisio, R. (1994). The Initial Evolution of Open Clusters in their Placental Clouds (Invited paper). *MmSAI*, **65**, 1107.

Capuzzo-Dolcetta, R. and Donnarumma, I. (2001). Evolution of globular cluster systems in three galaxies of the Fornax cluster. *MNRAS*, **328**, 645–652, CDD01.

Capuzzo-Dolcetta, R. and Mastrobuono-Battisti, A. (2009). Globular cluster system erosion in elliptical galaxies. *A&A*, **507**, 183–193.

Capuzzo-Dolcetta, R. and Miocchi, P. (2008a). Merging of Globular Clusters in Inner Galactic Regions. II. Nuclear Star Cluster Formation. *ApJ*, **681**, 1136–1147.

Capuzzo-Dolcetta, R. and Miocchi, P. (2008b). Self-consistent simulations of nuclear cluster formation through globular cluster orbital decay and merging. *MNRAS*, **388**, L69–L73.

Capuzzo-Dolcetta, R. and Tesseri, A. (1997). Evolution of the globular cluster system of a triaxial galaxy. *MNRAS*, **292**, 808–816.

Capuzzo-Dolcetta, R. and Tesseri, A. (1999). Globular cluster system erosion and nucleus formation in elliptical galaxies. *MNRAS*, **308**, 961–968.

Capuzzo-Dolcetta, R. and Vicari, A. (2005). Dynamical friction on globular clusters in core-triaxial galaxies: is it a cause of massive black hole accretion? *MNRAS*, **356**, 899–912.

Capuzzo-Dolcetta, R. and Vignola, L. (1997). Have many globulars disappeared to the galactic centres? The case of the Galaxy, M 31 and M 87. *A&A*, **327**, 130–136.

Capuzzo Dolcetta, R., Pucello, N., Rosato, V., and Saraceni, F. (2001). On the Use of a Heterogeneous MIMD-SIMD Platform to Simulate the Dynamics of Globular Clusters with a Central Massive Object. *Journal of Computational Physics*, **174**, 208–225.

Capuzzo Dolcetta, R., Di Matteo, P., and Miocchi, P. (2005). Formation and Evolution of Clumpy Tidal Tails around Globular Clusters. *AJ*, **129**, 1906–1921.

Capuzzo Dolcetta, R., Arca Sedda, M., Mastrobuono Battisti, A., Montuori, M., Punzo, D., and Spera, M. (2011). High performance astrophysics computing. *To appear in "Advances in Computational Astrophysics: methods, tools and outcomes", ASP Conference Series, R. Capuzzo-Dolcetta, M. Limongi and A. Tornambè eds.*

Capuzzo-Dolcetta, R., Mastrobuono-Battisti, A., and Maschietti, D. (2011a). NBSymple, a double parallel, symplectic N-body code running on graphic processing units. *NewA*, **16**, 284–295.

Capuzzo-Dolcetta, R., Antonini, F., and Mastrobuono-Battisti, A. (2011b). The Milky Way Nuclear Star Cluster. *To appear in proceedings of "Stellar Clusters and Associations - A RIA workshop on GAIA", 23-27 May 2011, Granada, Spain.*

Carollo, C. M., Danziger, I. J., Rich, R. M., and Chen, X. (1997). Nuclear Properties of Kinematically Distinct Cores. *ApJ*, **491**, 545.

Carollo, C. M., Stiavelli, M., and Mack, J. (1998). Spiral Galaxies with WFPC2. II. The Nuclear Properties of 40 Objects. *AJ*, **116**, 68–84.

Carter, D. and Jenkins, C. R. (1993). High-Resolution Kinematic Observations of Rapidly Rotating Spheroidal Components of Galaxies. *MNRAS*, **263**, 1049–1074, CJ93.

Cartwright, J. H. E. and Piro, O. (1992). The Dynamics of Runge–Kutta Methods. *Int. J. Bifurcation and Chaos*, **2**, 427–449.

Casertano, S. and Hut, P. (1985). Core radius and density measurements in N-body experiments Connections with theoretical and observational definitions. *ApJ*, **298**, 80–94.

Casertano, S., Phinney, E. S., and Villumsen, J. V. (1987). Dynamical Friction and Orbit Circularization. In P. T. de Zeeuw, editor, *Structure and Dynamics of Elliptical Galaxies*, volume 127 of *IAU Symposium*, page 475.

Chaboyer, B., Demarque, P., and Sarajedini, A. (1996). Globular Cluster Ages and the Formation of the Galactic Halo. *ApJ*, **459**, 558.

Chandrasekhar, S. (1942). *Principles of stellar dynamics.*

Chandrasekhar, S. (1943). Dynamical Friction. II. The Rate of Escape of Stars from Clusters and the Evidence for the Operation of Dynamical Friction. *ApJ*, **97**, 263.

Chapman, S., Pongracic, H., Disney, M., Nelson, A., Turner, J., and Whitworth, A. (1992). The formation of binary and multiple star systems. *Nature*, **359**, 207–210.

Charbonnel, C., Meynet, G., Maeder, A., Schaller, G., and Schaerer, D. (1993). Grids of Stellar Models - Part Three - from 0.8 to 120-SOLAR-MASSES at Z=0.004. *A&A*, **101**, 415.

Cheng, H., Greengard, L., and Rokhlin, V. (1999). A fast adaptive multipole algorithm in three dimensions. *Journal of Computational Physics*, **155**(2), 468–498.

Chumak, Y. O. and Rastorguev, A. S. (2006). Study of the nearest open clusters and the associated moving clusters by numerical simulations. *Astronomy Letters*, **32**, 446–455.

Clarke, C. (2010). The physics and modes of star cluster formation: simulations. *Royal Society of London Philosophical Transactions Series A*, **368**, 733–754.

Clutton-Brock, M. (1972). The Gravitational Field of Flat Galaxies. *Ap&SS*, **16**, 101–119.

Combes, F., Leon, S., and Meylan, G. (1999). N-body simulations of globular cluster tides. *A&A*, **352**, 149–162.

Côté, P., McLaughlin, D. E., Cohen, J. G., and Blakeslee, J. P. (2003). Dynamics of the Globular Cluster System Associated with M49 (NGC 4472): Cluster Orbital Properties and the Distribution of Dark Matter. *ApJ*, **591**, 850–877.

Côté, P., Piatek, S., Ferrarese, L., Jordán, A., Merritt, D., Peng, E. W., Haşegan, M., Blakeslee, J. P., Mei, S., West, M. J., Milosavljević, M., and Tonry, J. L. (2006). The ACS Virgo Cluster Survey. VIII. The Nuclei of Early-Type Galaxies. *ApJS*, **165**, 57–94.

Cox, A. N. (2000). *Allen's astrophysical quantities*.

de Grijs, R. (2010). A revolution in star cluster research: setting the scene. *Royal Society of London Philosophical Transactions Series A*, **368**, 693–711.

Dehnen, W. (1993). A Family of Potential-Density Pairs for Spherical Galaxies and Bulges. *MNRAS*, **265**, 250–256.

Dehnen, W. (2000). A Very Fast and Momentum-conserving Tree Code. *ApJL*, **536**, L39–L42.

Dehnen, W., Odenkirchen, M., Grebel, E. K., and Rix, H.-W. (2004). Modeling the Disruption of the Globular Cluster Palomar 5 by Galactic Tides. *AJ*, **127**, 2753–2770.

Di Matteo, P., Capuzzo Dolcetta, R., and Miocchi, P. (2005). Clumpy Substructures in Globular Cluster Tidal Tails. *Celestial Mechanics and Dynamical Astronomy*, **91**, 59–73.

Dirsch, B., Richtler, T., and Bassino, L. P. (2003). The globular cluster systems of NGC 3258 and NGC 3268 in the Antlia cluster. *A&A*, **408**, 929–939, D03.

Djorgovski, S. and Meylan, G. (1993). The Galactic Globular Cluster Systems - a List of the Known Clusters and Their Positions. In S. G. Djorgovski & G. Meylan, editor, *Structure and Dynamics of Globular Clusters*, volume 50 of *Astronomical Society of the Pacific Conference Series*, page 325.

Do, T., Ghez, A. M., Morris, M. R., Lu, J. R., Matthews, K., Yelda, S., and Larkin, J. (2009). High Angular Resolution Integral-Field Spectroscopy of the Galaxy's Nuclear Cluster: A Missing Stellar Cusp? *ApJ*, **703**, 1323–1337.

Eisenhauer, F., Genzel, R., Alexander, T., Abuter, R., Paumard, T., Ott, T., Gilbert, A., Gillessen, S., Horrobin, M., Trippe, S., Bonnet, H., Dumas, C., Hubin, N., Kaufer, A., Kissler-Patig, M., Monnet, G., Ströbele, S., Szeifert, T., Eckart, A., Schödel, R., and Zucker, S. (2005). SINFONI in the Galactic Center: Young Stars and Infrared Flares in the Central Light-Month. *ApJ*, **628**, 246–259, E05.

Elmegreen, B. G. (1999). The Specific Frequency of Globular Clusters in Galaxies. *Ap&SS*, **269**, 469–484.

Elsen, E., Houston, M., Vishal, V., Darve, E., Hanrahan, P., and Pande, V. (2006). N-body simulation on gpus. In *SC '06: Proceedings of the 2006 ACM/IEEE conference on Supercomputing*, page 188, New York, NY, USA. ACM.

Emsellem, E. and van de Ven, G. (2008). Formation of Central Massive Objects via Tidal Compression. *ApJ*, **674**, 653–659.

Fall, S. M. and Rees, M. J. (1977). Survival and disruption of galactic substructure. *MNRAS*, **181**, 37P–42P.

Ferrarese, L. and Ford, H. (2005). Supermassive Black Holes in Galactic Nuclei: Past, Present and Future Research. *SSRv*, **116**, 523–624, Fe05.

Ferrarese, L., Côté, P., Dalla Bontà, E., Peng, E. W., Merritt, D., Jordán, A., Blakeslee, J. P., Haşegan, M., Mei, S., Piatek, S., Tonry, J. L., and West, M. J. (2006a). A Fundamental Relation between Compact Stellar Nuclei, Supermassive Black Holes, and Their Host Galaxies. *ApJL*, **644**, L21–L24.

Ferrarese, L., Côté, P., Jordán, A., Peng, E. W., Blakeslee, J. P., Piatek, S., Mei, S., Merritt, D., Milosavljević, M., Tonry, J. L., and West, M. J. (2006b). The ACS Virgo Cluster Survey. VI. Isophotal Analysis and the Structure of Early-Type Galaxies. *ApJS*, **164**, 334–434.

Figer, D. F., Morris, M., Geballe, T. R., Rich, R. M., Serabyn, E., McLean, I. S., Puetter, R. C., and Yahil, A. (1999). High-Resolution Infrared Imaging and Spectroscopy of the Pistol Nebula: Evidence for Ejection. *ApJ*, **525**, 759–771.

Figer, D. F., Rich, R. M., Kim, S. S., Morris, M., and Serabyn, E. (2004). An Extended Star Formation History for the Galactic Center from Hubble Space Telescope NICMOS Observations. *ApJ*, **601**, 319–339.

Filippenko, A. V. and Ho, L. C. (2003). A Low-Mass Central Black Hole in the Bulgeless Seyfert 1 Galaxy NGC 4395. *ApJL*, **588**, L13–L16.

Font, A. S., Johnston, K. V., Bullock, J. S., and Robertson, B. E. (2006). Chemical Abundance Distributions of Galactic Halos and Their Satellite Systems in a ΛCDM Universe. *ApJ*, **638**, 585–595.

Forbes, D. A. and Bridges, T. (2010). Accreted versus in situ Milky Way globular clusters. *MNRAS*, **404**, 1203–1214.

Forbes, D. A., Franx, M., Illingworth, G. D., and Carollo, C. M. (1996). Ellipticals with Kinematically Distinct Cores: WFPC2 Imaging of Globular Clusters. *ApJ*, **467**, 126–144.

Forbes, D. A., Grillmair, C. J., Williger, G. M., Elson, R. A. W., and Brodie, J. P. (1998). HST imaging of the globular clusters in the Fornax cluster - NGC 1399 and NGC 1404. *MNRAS*, **293**, 325.

Forbes, D. A., Sánchez-Blázquez, P., Phan, A. T. T., Brodie, J. P., Strader, J., and Spitler, L. (2006). An imaging study of the globular cluster systems of NGC 1407 and 1400. *MNRAS*, **366**, 1230–1242.

Forbes, D. A., Lasky, P., Graham, A. W., and Spitler, L. (2008). Uniting old stellar systems: from globular clusters to giant ellipticals. *MNRAS*, **389**, 1924–1936.

Forte, J. C., Martinez, R. E., and Muzzio, J. C. (1982). On the origin of the globular cluster system of M87. *AJ*, **87**, 1465–1469.

Gaburov, E., Harfst, S., and Portegies Zwart, S. (2009). SAPPORO: A way to turn your graphics cards into a GRAPE-6. *NewA*, **14**, 630–637.

Geha, M., Guhathakurta, P., and van der Marel, R. P. (2002). Internal Dynamics, Structure, and Formation of Dwarf Elliptical Galaxies. I. A Keck/Hubble Space Telescope Study of Six Virgo Cluster Dwarf Galaxies. *AJ*, **124**, 3073–3087.

Ghez, A. M., Salim, S., Weinberg, N. N., Lu, J. R., Do, T., Dunn, J. K., Matthews, K., Morris, M. R., Yelda, S., Becklin, E. E., Kremenek, T., Milosavljevic, M., and Naiman, J. (2008). Measuring Distance and Properties of the Milky Way's Central Supermassive Black Hole with Stellar Orbits. *ApJ*, **689**, 1044–1062.

Gillessen, S., Eisenhauer, F., Trippe, S., Alexander, T., Genzel, R., Martins, F., and Ott, T. (2009). Monitoring Stellar Orbits Around the Massive Black Hole in the Galactic Center. *ApJ*, **692**, 1075–1109.

Gingold, R. A. and Monaghan, J. J. (1977). Smoothed particle hydrodynamics - Theory and application to non-spherical stars. *MNRAS*, **181**, 375–389.

Gómez, M. and Richtler, T. (2004). The globular cluster system of NGC 4374. *A&A*, **415**, 499–508, GR04.

González Delgado, R. M., Pérez, E., Cid Fernandes, R., and Schmitt, H. (2008). HST/WFPC2 Imaging of the Circumnuclear Structure of Low-Luminosity Active Galactic Nuclei. I. Data and Nuclear Morphology. *AJ*, **135**, 747–765.

Goodwin, S. P. (2009). The effect of the dynamical state of clusters on gas expulsion and infant mortality. *Ap&SS*, **324**, 259–263.

Graham, A. W. and Spitler, L. R. (2009a). Quantifying the coexistence of massive black holes and dense nuclear star clusters. *MNRAS*, **397**, 2148–2162.

Graham, A. W. and Spitler, L. R. (2009b). Quantifying the coexistence of massive black holes and dense nuclear star clusters. *MNRAS*, **397**, 2148–2162.

Gratton, R. G., Fusi Pecci, F., Carretta, E., Clementini, G., Corsi, C. E., and Lattanzi, M. (1997). Ages of Globular Clusters from HIPPARCOS Parallaxes of Local Subdwarfs. *ApJ*, **491**, 749.

Grillmair, C. J. (1998). Probing the Galactic Halo with Globular Cluster Tidal Tails. In D. Zaritsky, editor, *Galactic Halos*, volume 136 of *Astronomical Society of the Pacific Conference Series*, page 45.

Grillmair, C. J. (2006). Detection of a 60deg-long Dwarf Galaxy Debris Stream. *ApJL*, **645**, L37–L40.

Grillmair, C. J. (2009). Four New Stellar Debris Streams in the Galactic Halo. *ApJ*, **693**, 1118–1127.

Grillmair, C. J. and Dionatos, O. (2006a). A 22° Tidal Tail for Palomar 5. *ApJL*, **641**, L37–L39.

Grillmair, C. J. and Dionatos, O. (2006b). Detection of a 63deg Cold Stellar Stream in the Sloan Digital Sky Survey. *ApJL*, **643**, L17–L20.

Grillmair, C. J. and Johnson, R. (2006). The Detection of a 45deg Tidal Stream Associated with the Globular Cluster NGC 5466. *ApJL*, **639**, L17–L20.

Grillmair, C. J., Freeman, K. C., Irwin, M., and Quinn, P. J. (1995). Globular Clusters with Tidal Tails: Deep Two-Color Star Counts. *AJ*, **109**, 2553.

Gualandris, A. and Merritt, D. (2009). Perturbations of Intermediate-mass Black Holes on Stellar Orbits in the Galactic Center. *ApJ*, **705**, 361–371.

Haşegan, M., Jordán, A., Côté, P., Djorgovski, S. G., McLaughlin, D. E., Blakeslee, J. P., Mei, S., West, M. J., Peng, E. W., Ferrarese, L., Milosavljević, M., Tonry, J. L., and Merritt, D. (2005). The ACS Virgo Cluster Survey. VII. Resolving the Connection between Globular Clusters and Ultracompact Dwarf Galaxies. *ApJ*, **627**, 203–223.

Haller, J. W., Rieke, M. J., Rieke, G. H., Tamblyn, P., Close, L., and Melia, F. (1996). Stellar Kinematics and the Black Hole in the Galactic Center. *ApJ*, **456**, 194.

Hamada, T. and Iitaka, T. (2007). The Chamomile Scheme: An Optimized Algorithm for N-body simulations on Programmable Graphics Processing Units. *ArXiv Astrophysics e-prints*.

Harfst, S., Gualandris, A., Merritt, D., Spurzem, R., Portegies Zwart, S., and Berczik, P. (2007). Performance analysis of direct N-body algorithms on special-purpose supercomputers. *NewAst*, **12**, 357–377.

Harris, W. E. (1986). Globular clusters in galaxies beyond the local group. V - The giant ellipticals reconsidered. *AJ*, **91**, 822–841.

Harris, W. E. (1991). Globular cluster systems in galaxies beyond the Local Group. *ARA&A*, **29**, 543–579.

Harris, W. E. (1996a). A Catalog of Parameters for Globular Clusters in the Milky Way. *AJ*, **112**, 1487.

Harris, W. E. (1996b). A Catalog of Parameters for Globular Clusters in the Milky Way. *AJ*, **112**, 1487.

Harris, W. E. and Racine, R. (1979). Globular clusters in galaxies. *ARA&A.*, **17**, 241–274.

Harris, W. E., Kavelaars, J. J., Hanes, D. A., Pritchet, C. J., and Baum, W. A. (2009). The Globular Cluster Systems in the Coma Ellipticals. IV: WFPC2 Photometry for Five Giant Ellipticals. *AJ*, **137**, 3314–3328.

Hartmann, M., Debattista, V. P., Seth, A., Cappellari, M., and Quinn, T. R. (2011). Constraining the role of star cluster mergers in nuclear cluster formation: Simulations confront integral-field data.

Hashimoto, Y., Funato, Y., and Makino, J. (2003). To Circularize or Not To Circularize?-Orbital Evolution of Satellite Galaxies. *ApJ*, **582**, 196–201.

Hausman, M. A. and Ostriker, J. P. (1978). Galactic cannibalism. III - The morphological evolution of galaxies and clusters. *ApJ*, **224**, 320–336.

Heggie, D. and Hut, P. (2003). *The Gravitational Million-Body Problem: A Multidisciplinary Approach to Star Cluster Dynamics.*

Heggie, D. C. (1992). Ecology of globular clusters. *Nature*, **359**, 772–773.

Hénon, M. (1961). Sur l'évolution dynamique des amas globulaires. *Annales d'Astrophysique*, **24**, 369.

Hernquist, L. and Ostriker, J. P. (1992). A self-consistent field method for galactic dynamics. *ApJ*, **386**, 375–397.

Hillenbrand, L. A. and Hartmann, L. W. (1998). A Preliminary Study of the Orion Nebula Cluster Structure and Dynamics. *ApJ*, **492**, 540.

Hockney, R. W. and Eastwood, J. W. (1988). Computer simulation using particles. In Hockney, R. W. & Eastwood, J. W., editor, *Bristol: Hilger, 1988*.

Hopkins, P. F., Cox, T. J., Dutta, S. N., Hernquist, L., Kormendy, J., and Lauer, T. R. (2009). Dissipation and Extra Light in Galactic Nuclei. II. ”Cusp” Ellipticals. *ApJS*, **181**, 135–182.

Ibata, R. A. and Lewis, G. F. (1998). Galactic Indigestion: Numerical Simulations of the Milky Way's Closest Neighbor. *ApJ*, **500**, 575.

Illingworth, G. (1976). The masses of globular clusters. II - Velocity dispersions and mass-to-light ratios. *ApJ*, **204**, 73–93.

Inman, R. T. and Carney, B. W. (1987). AM-4 - The poorest globular cluster? *AJ*, **93**, 1166–1171.

Johnstone, D. (1993). Evaporation of stars from isolated, truncated globular clusters. *AJ*, **105**, 155–167.

Jordán, A., Côté, P., Blakeslee, J. P., Ferrarese, L., McLaughlin, D. E., Mei, S., Peng, E. W., Tonry, J. L., Merritt, D., Milosavljević, M., Sarazin, C. L., Sivakoff, G. R., and West, M. J. (2005). The ACS Virgo Cluster Survey. X. Half-Light Radii of Globular Clusters in Early-Type Galaxies: Environmental Dependencies and a Standard Ruler for Distance Estimation. *ApJ*, **634**, 1002–1019.

Jordi, K., Grebel, E. K., Hilker, M., Baumgardt, H., Frank, M., Kroupa, P., Haghi, H., Côté, P., and Djorgovski, S. G. (2009). Testing Fundamental Physics with Distant Star Clusters: Analysis of Observational Data on Palomar 14. *AJ*, **137**, 4586–4596.

Just, A., Berczik, P., Petrov, M. I., and Ernst, A. (2009). Quantitative analysis of clumps in the tidal tails of star clusters. *MNRAS*, **392**, 969–981.

Katz, N. (1991). Dissipationless collapse in an expanding universe. *ApJ*, **368**, 325–336.

Keenan, D. W. and Innanen, K. A. (1975). Numerical investigation of galactic tidal effects on spherical stellar systems. *AJ*, **80**, 290–302.

King, I. (1962). The structure of star clusters. I. an empirical density law. *AJ*, **67**, 471.

King, I. (1963). Dynamical Models for Spherical Stellar Systems. *AJ*, **68**, 282.

King, I. R. (1966). The structure of star clusters. III. Some simple dynamical models. *AJ*, **71**, 64.

Kinoshita, H., Yoshida, H., and Nakai, H. (1991). Symplectic integrators and their application to dynamical astronomy. *Celestial Mechanics and Dynamical Astronomy*, **50**, 59–71.

Kirk, H., Johnstone, D., and Di Francesco, J. (2006). The Large- and Small-Scale Structures of Dust in the Star-forming Perseus Molecular Cloud. *ApJ*, **646**, 1009–1023.

Kissler, M., Richtler, T., Held, E. V., Grebel, E. K., Wagner, S. J., and Capaccioli, M. (1994). The globular cluster system of NGC 4636: A rich system in an otherwise normal elliptical galaxy? *A&A*, **287**, 463–469, KR94.

Kissler-Patig, M., Ashman, K. M., Zepf, S. E., and Freeman, K. C. (1999). HUBBLE SPACE TELESCOPE Imaging of Globular Clusters in the Edge-on Spiral Galaxies NGC 4565 and NGC 5907. *AJ*, **118**, 197–207.

Kitsionas, S., Federrath, C., Klessen, R. S., Schmidt, W., Price, D. J., Dursi, L. J., Gritschneder, M., Walch, S., Piontek, R., Kim, J., Jappsen, A.-K., Ciecielag, P., and Mac Low, M.-M. (2009). Algorithmic comparisons of decaying, isothermal, supersonic turbulence. *A&A*, **508**, 541–560.

Klessen, R. S., Burkert, A., and Bate, M. R. (1998). Fragmentation of Molecular Clouds: The Initial Phase of a Stellar Cluster. *ApJL*, **501**, L205+.

Koposov, S. E., Rix, H.-W., and Hogg, D. W. (2010). Constraining the Milky Way Potential with a Six-Dimensional Phase-Space Map of the GD-1 Stellar Stream. *ApJ*, **712**, 260–273.

Kormendy, J. and Bender, R. (2009). Correlations between Supermassive Black Holes, Velocity Dispersions, and Mass Deficits in Elliptical Galaxies with Cores. *ApJ*, **691**, L142–L146.

Küpper, A. H. W., MacLeod, A., and Heggie, D. C. (2008). On the structure of tidal tails. *MNRAS*, **387**, 1248–1252.

Küpper, A. H. W., Kroupa, P., Baumgardt, H., and Heggie, D. C. (2010). Tidal tails of star clusters. *MNRAS*, **401**, 105–120.

Lada, C. J. (2010). The physics and modes of star cluster formation: observations. *Royal Society of London Philosophical Transactions Series A*, **368**, 713–731.

Lada, C. J. and Lada, E. A. (2003). Embedded Clusters in Molecular Clouds. *ARA&A*, **41**, 57–115.

Lada, C. J., Margulis, M., and Dearborn, D. (1984). The formation and early dynamical evolution of bound stellar systems. *ApJ*, **285**, 141–152.

Lada, E. A., Depoy, D. L., Evans, II, N. J., and Gatley, I. (1991). A 2.2 micron survey in the L1630 molecular cloud. *ApJ*, **371**, 171–182.

Lauer, T. R. and Kormendy, J. (1986). The core of the M87 globular cluster system. *ApJ*, **303**, L1–L4.

Lauer, T. R., Faber, S. M., Ajhar, E. A., Grillmair, C. J., and Scowen, P. A. (1998). M32 +/- 1. *AJ*, **116**, 2263–2286.

Lauer, T. R., Gebhardt, K., Faber, S. M., Richstone, D., Tremaine, S., Kormendy, J., Aller, M. C., Bender, R., Dressler, A., Filippenko, A. V., Green, R., and Ho, L. C. (2007). The Centers of Early-Type Galaxies with Hubble Space Telescope. VI. Bimodal Central Surface Brightness Profiles. *ApJ*, **664**, 226–256.

Launhardt, R., Zylka, R., and Mezger, P. G. (2002). The nuclear bulge of the Galaxy. III. Large-scale physical characteristics of stars and interstellar matter. *A&A*, **384**, 112–139.

Law, D. R. and Majewski, S. R. (2010). Assessing the Milky Way Satellites Associated with the Sagittarius Dwarf Spheroidal Galaxy. *ApJ*, **718**, 1128–1150.

Law, D. R., Majewski, S. R., Skrutskie, M. F., Carpenter, J. M., and Ayub, H. F. (2003). 2MASS Studies of Differential Reddening across Three Massive Globular Clusters. *AJ*, **126**, 1871–1887.

Lee, H. M. and Goodman, J. (1995). Influence of the stellar mass function of the evaporation rate of tidally limited postcollapse globular clusters. *ApJ*, **443**, 109–116.

Leisawitz, D., Bash, F. N., and Thaddeus, P. (1989). A CO survey of regions around 34 open clusters. *ApJS*, **70**, 731–812.

Lemaster, M. N. and Stone, J. M. (2008). Density Probability Distribution Functions in Supersonic Hydrodynamic and MHD Turbulence. *ApJL*, **682**, L97–L100.

Leon, S., Meylan, G., and Combes, F. (2000). Tidal tails around 20 Galactic globular clusters. Observational evidence for gravitational disk/bulge shocking. *A&A*, **359**, 907–931.

Lienhart, G. Kugel, A. and Männer, R. (2002). Using floating-point arithmetic on fpgas to accelerate scientific n-body simulations. In *10th Annual IEEE Symposium on Field-Programmable Custom Computing Machines (FCCM'02)*, page 182, Los Alamitos, CA, USA. IEEE Computer Society.

Londrillo, P. and Nipoti, C. (2009). N-MODY: a code for collisionless N-body simulations in modified Newtonian dynamics. *Memorie della Societa Astronomica Italiana Supplementi*, **13**, 89.

Lotz, J. M., Miller, B. W., and Ferguson, H. C. (2004). The Colors of Dwarf Elliptical Galaxy Globular Cluster Systems, Nuclei, and Stellar Halos. *ApJ*, **613**, 262–278.

Lucy, L. B. (1977). A numerical approach to the testing of the fission hypothesis. *AJ*, **82**, 1013–1024.

Lynden-Bell, D. and Lynden-Bell, R. M. (1995). Ghostly streams from the formation of the Galaxy's halo. *MNRAS*, **275**, 429–442.

MacKay, R. S. (1990). Some aspects of the dynamics and numerics of Hamiltonian systems. *Dynamics of Numerics and Numerics of Dynamics IMA*.

Mackey, A. D. and Gilmore, G. F. (2004). Comparing the properties of local globular cluster systems: implications for the formation of the Galactic halo. *MNRAS*, **355**, 504–534.

Magorrian, J., Tremaine, S., Richstone, D., Bender, R., Bower, G., Dressler, A., Faber, S. M., Gebhardt, K., Green, R., Grillmair, C., Kormendy, J., and Lauer, T. (1998). The Demography of Massive Dark Objects in Galaxy Centers. *AJ*, **115**, 2285–2305, M98.

Majewski, S. R., Skrutskie, M. F., Weinberg, M. D., and Ostheimer, J. C. (2003). A Two Micron All Sky Survey View of the Sagittarius Dwarf Galaxy. I. Morphology of the Sagittarius Core and Tidal Arms. *ApJ*, **599**, 1082–1115.

Makino, J. and Hut, P. (1990). Bottlenecks in simulations of dense stellar systems. *ApJ*, **365**, 208–218.

Makino, J. and Taiji, M. (1998). *Scientific Simulations with Special-Purpose Computers–the GRAPE Systems.*

Mandushev, G., Staneva, A., and Spasova, N. (1991). Dynamical masses for Galactic globular clusters. *A&A*, **252**, 94–99.

Marín-Franch, A. *et al.* (2009). The ACS Survey of Galactic Globular Clusters. VII. Relative Ages. *ApJ*, **694**, 1498–1516.

Mastrobuono-Battisti, A. and Capuzzo-Dolcetta, R. (2011). The Formation of the Milky Way Nuclear Cluster. *To appear in "Advances in Computational Astrophysics: methods, tools and outcomes", ASP Conference Series, R. Capuzzo-Dolcetta, M. Limongi and A. Tornambè eds.*

Matthews, L. D., Gallagher, III, J. S., and van Driel, W. (1999). The Extraordinary "Superthin" Spiral Galaxy UGC 7321. I. Disk Color Gradients and Global Properties from Multiwavelength Observations. *AJ*, **118**, 2751–2766.

McLaughlin, D. E. (1995). Was the Compact Nucleus in M87 Formed by Destroyed Globular Clusters? *AJ*, **109**, 2034–2037.

McMillan, P. J. and Dehnen, W. (2005). Halo evolution in the presence of a disc bar. *MNRAS*, **363**, 1205–1210.

McMillan, S. L. W. and Aarseth, S. J. (1993). An O(N log N) integration scheme for collisional stellar systems. *ApJ*, **414**, 200–212.

McMillan, S. L. W., Vesperini, E., and Portegies Zwart, S. F. (2007). A Dynamical Origin for Early Mass Segregation in Young Star Clusters. *ApJL*, **655**, L45–L49.

Menyuk, C. R. (1984). Some properties of the discrete Hamiltonian method. *Physica D Nonlinear Phenomena*, **11**, 109–129.

Merritt, D. (2006). Dynamics of galaxy cores and supermassive black holes. *Reports on Progress in Physics*, **69**, 2513–2579.

Merritt, D. (2010). The Distribution of Stars and Stellar Remnants at the Galactic Center. *ApJ*, **718**, 739–761.

Meylan, G. and Heggie, D. C. (1997). Internal dynamics of globular clusters. *A&ARv*, **8**, 1–143.

Meylan, G., Mayor, M., and Dubath, P. (1994). The jumbo galactic globular cluster. In *American Astronomical Society Meeting Abstracts #184*, volume 26 of *Bulletin of the American Astronomical Society*, page 956.

Meylan, G., Mayor, M., Duquennoy, A., and Dubath, P. (1995). Central velocity dispersion in the globular cluster ω Centauri. *A&A*, **303**, 761.

Meynet, G., Maeder, A., Schaller, G., Schaerer, D., and Charbonnel, C. (1994). Grids of massive stars with high mass loss rates. V. From 12 to 120 $M_{sun\_}$ at Z=0.001, 0.004, 0.008, 0.020 and 0.040. *A&AS*, **103**, 97–105.

Michie, R. W. (1963). On the distribution of high energy stars in spherical stellar systems. *MNRAS*, **125**, 127.

Milosavljević, M. (2004). On the Origin of Nuclear Star Clusters in Late-Type Spiral Galaxies. *ApJL*, **605**, L13–L16.

Miocchi, P., Capuzzo Dolcetta, R., Di Matteo, P., and Vicari, A. (2006). Merging of Globular Clusters in Inner Galactic Regions. I. Do They Survive the Tidal Interaction? *ApJ*, **644**, 940–953.

Miyamoto, M. and Nagai, R. (1975). Three-dimensional models for the distribution of mass in galaxies. *PASJ*, **27**, 533–543.

Moeckel, N. and Bonnell, I. A. (2009). Does subcluster merging accelerate mass segregation in local clusters? *MNRAS*, **400**, 657–664.

Monaghan, J. J. (2005). Smoothed particle hydrodynamics. *Reports on Progress in Physics*, **68**, 1703–1759.

Montuori, M., Capuzzo-Dolcetta, R., Di Matteo, P., Lepinette, A., and Miocchi, P. (2007). Tidal Tails around Globular Clusters: Are They a Good Tracer of Cluster Orbits? *ApJ*, **659**, 1212–1221.

Moore, B., Kazantzidis, S., Diemand, J., and Stadel, J. (2004). The origin and tidal evolution of cuspy triaxial haloes. *MNRAS*, **354**, 522–528.

Muzzio, J. C. (1987). Dynamical evolution of globular-cluster systems in clusters of galaxies. *PASP*, **99**, 245–264.

Navarro, J. F., Frenk, C. S., and White, S. D. M. (1996). The Structure of Cold Dark Matter Halos. *ApJ*, **462**, 563.

Newberg, H. J., Yanny, B., and Willett, B. A. (2009). Discovery of a New, Polar-Orbiting Debris Stream in the Milky Way Stellar Halo. *ApJL*, **700**, L61–L64.

Nitadori, K. and Makino, J. (2008). Sixth- and eighth-order Hermite integrator for N-body simulations. *NewAstr*, **13**, 498–507.

Nyland, L., Harris, M., and Prins, J. (2007). Fast N-Body Simulation with CUDA. *GPU Gems*, **3**, H Nguyen, ed., Prentice–Hall 2007.

Odenkirchen, M., Grebel, E. K., Dehnen, W., Rix, H.-W., Yanny, B., Newberg, H. J., Rockosi, C. M., Martínez-Delgado, D., Brinkmann, J., and Pier, J. R. (2003). The Extended Tails of Palomar 5: A 10° Arc of Globular Cluster Tidal Debris. *AJ*, **126**, 2385–2407.

Oh, K. S. and Lin, D. N. C. (1992). Tidal evolution of globular clusters. II - The effects of Galactic tidal field and diffusion. *ApJ*, **386**, 519–538.

Oh, S., Kim, S. S., and Figer, D. F. (2009). Mass Distribution in the Central Few Parsecs of our Galaxy. *Journal of Korean Astronomical Society*, **42**, 17–26.

Ostriker, J. P. (1985). Physical interactions between stars. In J. Goodman & P. Hut, editor, *Dynamics of Star Clusters*, volume 113 of *IAU Symposium*, pages 347–357.

Ostriker, J. P. (1988). The evolution of the system of globular clusters. In J. E. Grindlay & A. G. D. Philip, editor, *The Harlow-Shapley Symposium on Globular Cluster Systems in Galaxies*, volume 126 of *IAU Symposium*, pages 271–279.

Ostriker, J. P., Binney, J., and Saha, P. (1989). The effect of galaxy triaxiality on globular clusters. *MNRAS*, **241**, 849–871.

Owens, J., Houston, M. Luebke, D., Green, S., Stone, J. E., and Phillips, J. (2008). Gpu computing. In *Proc. of the IEEE*, volume 96, page 859.

Padoan, P., Nordlund, A., and Jones, B. J. T. (1997). The universality of the stellar initial mass function. *MNRAS*, **288**, 145–152.

Peretto, N., André, P., and Belloche, A. (2006). Probing the formation of intermediate- to high-mass stars in protoclusters. A detailed millimeter study of the NGC 2264 clumps. *A&A*, **445**, 979–998.

Pesce, E., Capuzzo-Dolcetta, R., and Vietri, M. (1992). Erratum - Dynamical Friction in a Non-Rotating Triaxial Galaxy - the Effect on Box Orbits. *MNRAS*, **256**, 368.

Plummer, H. C. (1911). On the problem of distribution in globular star clusters. *MNRAS*, **71**, 460–470.

Poon, M. Y. and Merritt, D. (2004). A Self-Consistent Study of Triaxial Black Hole Nuclei. *ApJ*, **606**, 774–787.

Portegies Zwart, S. F., Belleman, R. G., and Geldof, P. M. (2007). High-performance direct gravitational N-body simulations on graphics processing units. *NewA*, **12**, 641–650.

Preibisch, T. and Feigelson, E. D. (2005). The Evolution of X-Ray Emission in Young Stars. *ApJS*, **160**, 390–400.

Preto, M., Berentzen, I., Berczik, P., and Spurzem, R. (2011). Fast Coalescence of Massive Black Hole Binaries from Mergers of Galactic Nuclei: Implications for Low-frequency Gravitational-wave Astrophysics. *ApJL*, **732**, L26+.

Racine, R. (1991). Globular clusters in the halo of M31. *AJ*, **101**, 865–872.

Rhode, K. L. and Zepf, S. E. (2001). The Globular Cluster System in the Outer Regions of NGC 4472. *AJ*, **121**, 210–224.

Rhode, K. L. and Zepf, S. E. (2004). The Globular Cluster Systems of the Early-Type Galaxies NGC 3379, NGC 4406, and NGC 4594 and Implications for Galaxy Formation. *AJ*, **127**, 302–317, RZ04.

Richstone, D., Ajhar, E. A., Bender, R., Bower, G., Dressler, A., Faber, S. M., Filippenko, A. V., Gebhardt, K., Green, R., Ho, L. C., Kormendy, J., Lauer, T. R., Magorrian, J., and Tremaine, S. (1998). Supermassive black holes and the evolution of galaxies. *Nature*, **395**, A14–A19, R98.

Richstone, D. O. and Tremaine, S. (1986). Measuring mass-to-light ratios of spherical stellar systems by core fitting. *AJ*, **92**, 72–74.

Rood, H. J., Page, T. L., Kintner, E. C., and King, I. R. (1972a). The Structure of the Coma Cluster of Galaxies. *ApJ*, **175**, 627.

Rood, H. J., Page, T. L., Kintner, E. C., and King, I. R. (1972b). The Structure of the Coma Cluster of Galaxies. *ApJ*, **175**, 627.

Rossa, J., van der Marel, R. P., Böker, T., Gerssen, J., Ho, L. C., Rix, H.-W., Shields, J. C., and Walcher, C.-J. (2006). Hubble Space Telescope STIS Spectra of Nuclear Star Clusters in Spiral Galaxies: Dependence of Age and Mass on Hubble Type. *AJ*, **132**, 1074–1099.

Rosseland, S. (1928). On the time of relaxation of closed stellar systems. *MNRAS*, **88**, 208–.

Saha, P. (1992). Constructing stable spherical galaxy models. *MNRAS*, **254**, 132–138.

Sakari, C. M., Venn, K. A., Irwin, M., Aoki, W., Arimoto, N., and Dotter, A. (2011). Detailed Chemical Abundances of Four Stars in the Unusual Globular Cluster Palomar 1. *ApJ*, **740**, 106.

Salpeter, E. E. (1955). The Luminosity Function and Stellar Evolution. *ApJ*, **121**, 161.

Schaerer, D., Charbonnel, C., Meynet, G., Maeder, A., and Schaller, G. (1993a). Grids of Stellar Models - Part Four - from 0.8-SOLAR-MASS to 120-SOLAR-MASSES at Z=0.040. *A&AS*, **102**, 339.

Schaerer, D., Meynet, G., Maeder, A., and Schaller, G. (1993b). Grids of stellar models. II - From 0.8 to 120 solar masses at Z = 0.008. *A&AS*, **98**, 523–527.

Schaller, G., Schaerer, D., Meynet, G., and Maeder, A. (1992). New grids of stellar models from 0.8 to 120 solar masses at Z = 0.020 and Z = 0.001. *A&AS*, **96**, 269–331.

Schinnerer, E., Böker, T., Emsellem, E., and Lisenfeld, U. (2006). Molecular Gas Dynamics in NGC 6946: A Bar-driven Nuclear Starburst “Caught in the Act”. *ApJ*, **649**, 181–200.

Schinnerer, E., Böker, T., Meier, D. S., and Calzetti, D. (2008). Self-Regulated Fueling of Galaxy Centers: Evidence for Star Formation Feedback in IC 342’s Nucleus. *ApJL*, **684**, L21–L24.

Schmeja, S. and Klessen, R. S. (2004). Protostellar mass accretion rates from gravoturbulent fragmentation. *A&A*, **419**, 405–417.

Schmidt, M. (1959). The Rate of Star Formation. *ApJ*, **129**, 243.

Schödel, R. (2011). The Milky Way Nuclear Star Cluster in Context. In M. R. Morris, Q. D. Wang, & F. Yuan, editor, *The Galactic Center: a Window to the Nuclear Environment of Disk Galaxies*, volume 439 of *Astronomical Society of the Pacific Conference Series*, page 222.

Schödel, R., Eckart, A., Alexander, T., Merritt, D., Genzel, R., Sternberg, A., Meyer, L., Kul, F., Moultaka, J., Ott, T., and Straubmeier, C. (2007). The structure of the nuclear stellar cluster of the Milky Way. *A&A*, **469**, 125–146.

Schödel, R., Merritt, D., and Eckart, A. (2008). The nuclear star cluster of the Milky Way. *Journal of Physics Conference Series*, **131**(1), 012044.

Schödel, R., Merritt, D., and Eckart, A. (2009). The nuclear star cluster of the Milky Way: proper motions and mass. *A&A*, **502**, 91–111.

Schwarzschild, M. (1979). A numerical model for a triaxial stellar system in dynamical equilibrium. *ApJ*, **232**, 236–247.

Serabyn, E. and Morris, M. (1996). Sustained star formation in the central stellar cluster of the Milky Way. *Nature*, **382**, 602–604.

Sérsic, J. L. (1963). Influence of the atmospheric and instrumental dispersion on the brightness distribution in a galaxy. *Boletin de la Asociacion Argentina de Astronomia La Plata Argentina*, **6**, 41.

Seth, A., Agüeros, M., Lee, D., and Basu-Zych, A. (2008a). The Coincidence of Nuclear Star Clusters and Active Galactic Nuclei. *ApJ*, **678**, 116–130.

Seth, A., Agüeros, M., Lee, D., and Basu-Zych, A. (2008b). The Coincidence of Nuclear Star Clusters and Active Galactic Nuclei. *ApJ*, **678**, 116–130.

Seth, A. C., Dalcanton, J. J., Hodge, P. W., and Debattista, V. P. (2006). Clues to Nuclear Star Cluster Formation from Edge-on Spirals. *AJ*, **132**, 2539–2555.

Seth, A. C., Blum, R. D., Bastian, N., Caldwell, N., and Debattista, V. P. (2008c). The Rotating Nuclear Star Cluster in NGC 4244. *ApJ*, **687**, 997–1003.

Shlosman, I. and Begelman, M. C. (1989). Evolution of self-gravitating accretion disks in active galactic nuclei. *ApJ*, **341**, 685–691.

Sjouwerman, L. O., Habing, H. J., Lindqvist, M., van Langevelde, H. J., and Winnberg, A. (1999). OH/IR Stars as Signposts for Ancient Starburst Activity in the Galactic Center. In H. Falcke, A. Cotera, W. J. Duschl, F. Melia, & M. J. Rieke, editor, *The Central Parsecs of the Galaxy*, volume 186 of *Astronomical Society of the Pacific Conference Series*, page 379.

Smith, B. F. and Miller, R. H. (1982). On the stability of Schwarzschild's triaxial galaxy model. *ApJ*, **257**, 103–109.

Sollima, A., Nipoti, C., Mastrobuono-Battisti, A., Montuori, M., and Capuzzo-Dolcetta, R. (2011a). A Monte Carlo analysis of the velocity dispersion of the globular cluster Palomar 14. *accepted for publication by ApJ*.

Sollima, A., Martínez-Delgado, D., Valls-Gabaud, D., and Peñarrubia, J. (2011b). Discovery of Tidal Tails Around the Distant Globular Cluster Palomar 14. *ApJ*, **726**, 47.

Spera, M. (2010). *Using a Hybrid Computational Architecture to Study Self-Gravitating N-Body Systems*. Master's thesis, Master degree in Astronomy and Astrophysics.

Spitzer, L. (1987). *Dynamical evolution of globular clusters*.

Spitzer, L. J. (1940). The stability of isolated clusters. *MNRAS*, **100**, 396.

Spitzer, L. J. and Thuan, T. X. (1972). Random Gravitational Encounters and the Evolution of Spherical Systems. IV Isolated Systems of Identical Stars. *ApJ*, **175**, 31.

Spolaor, M., Forbes, D. A., Hau, G. K. T., Proctor, R. N., and Brough, S. (2008). The early-type galaxies NGC 1407 and NGC 1400 - I. Spatially resolved radial kinematics and surface photometry. *MNRAS*, **385**, 667–674.

Springel, V. (2005). The cosmological simulation code GADGET-2. *MNRAS*, **364**, 1105–1134.

Szell, A., Merritt, D., and Kevrekidis, I. G. (2005). Core Collapse via Coarse Dynamic Renormalization. *Physical Review Letters*, **95**(8), 081102.

Teuben, P. (1995). The Stellar Dynamics Toolbox NEMO. In R. A. Shaw, H. E. Payne, & J. J. E. Hayes, editor, *Astronomical Data Analysis Software and Systems IV*, volume 77 of *Astronomical Society of the Pacific Conference Series*, page 398.

Theis, C. and Spurzem, R. (1999). On the evolution of shape in N-body simulations. *A&A*, **341**, 361–370.

Tremaine, S. D., Ostriker, J. P., and Spitzer, L. J. (1975). The formation of the nuclei of galaxies. I - M31. *ApJ*, **196**, 407–411.

Trippe, S., Gillessen, S., Gerhard, O. E., Bartko, H., Fritz, T. K., Maness, H. L., Eisenhauer, F., Martins, F., Ott, T., Dodds-Eden, K., and Genzel, R. (2008). Kinematics of the old stellar population at the Galactic centre. *A&A*, **492**, 419–439.

Trujillo, I., Erwin, P., Asensio Ramos, A., and Graham, A. W. (2004). Evidence for a New Elliptical-Galaxy Paradigm: Sérsic and Core Galaxies. *AJ*, **127**, 1917–1942.

van der Marel, R. P. (1999). The Black Hole Mass Distribution in Early-Type Galaxies: Cusps in Hubble Space Telescope Photometry Interpreted through Adiabatic Black Hole Growth. *AJ*, **117**, 744–763, VM99.

van der Marel, R. P., Rossa, J., Walcher, C. J., Böker, T., Ho, L. C., Rix, H.-W., and Shields, J. C. (2007). Nuclear Star Clusters (Nuclei) in Spirals and Connection to Supermassive Black Holes. In A. Vazdekis & R. F. Peletier, editor, *IAU Symposium*, volume 241 of *IAU Symposium*, pages 475–479.

Vietri, M. and Schwarzschild, M. (1983). Analysis of box orbits in a triaxial galaxy. *ApJ*, **269**, 487–499.

Walcher, C. J., van der Marel, R. P., McLaughlin, D., Rix, H.-W., Böker, T., Häring, N., Ho, L. C., Sarzi, M., and Shields, J. C. (2005). Masses of Star Clusters in the Nuclei of Bulgeless Spiral Galaxies. *ApJ*, **618**, 237–246.

Walsh, A. J., Myers, P. C., and Burton, M. G. (2004). Star Formation on the Move? *ApJ*, **614**, 194–202.

Wehner, E. H. and Harris, W. E. (2006a). From Supermassive Black Holes to Dwarf Elliptical Nuclei: A Mass Continuum. *ApJL*, **644**, L17–L20.

Wehner, E. H. and Harris, W. E. (2006b). From Supermassive Black Holes to Dwarf Elliptical Nuclei: A Mass Continuum. *ApJL*, **644**, L17–L20.

White, R. E. and Shawl, S. J. (1987). Axial ratios and orientations for 100 Galactic globular star clusters. *ApJ*, **317**, 246–263.

Yanny, B., Newberg, H. J., Grebel, E. K., Kent, S., Odenkirchen, M., Rockosi, C. M., Schlegel, D., Subbarao, M., Brinkmann, J., Fukugita, M., Ivezic, Ž., Lamb, D. Q., Schneider, D. P., and York, D. G. (2003). A Low-Latitude Halo Stream around the Milky Way. *ApJ*, **588**, 824–841.

Yim, K.-J. and Lee, H. M. (2002). Tidal Tails of Globular Clusters. *Journal of Korean Astronomical Society*, **35**, 75–85.

York, D. G., Adelman, J., Anderson, Jr., J. E., *et al.* (2000). The Sloan Digital Sky Survey: Technical Summary. *AJ*, **120**, 1579–1587.

Yoshida, H. (1990). Conserved quantities of symplectic integrators. In H. Kinoshita & H. Yoshida, editor, *Twenty-Third Symposium on Celestial Mechanics*, pages 16–19.

Yoshida, H. (1991). Construction of higher order symplectic integrators. In H. Kinoshita & H. Yoshida, editor, *24th Symposium on Celestial Mechanics,*, page 132.

Zhang, Z., Xu, H., Wang, Y., An, T., Xu, Y., and Wu, X.-P. (2007). Probing the Mass Distributions in NGC 1407 and Its Associated Group with the X-Ray Imaging Spectroscopic and Optical Photometric and Line-Strength Indices Data. *ApJ*, **656**, 805–817, Z07.

Zhao, H. (1996). Analytical models for galactic nuclei. *MNRAS*, **278**, 488–496.